# Prototype Interferometry in the Era of Gravitational Wave Astronomy

Thesis by
Gautam Venugopalan

In Partial Fulfillment of the Requirements for the
Degree of
Doctor of Philosophy


CALIFORNIA INSTITUTE OF TECHNOLOGY
Pasadena, California

2022
Defended 17 June 2021

Gautam Venugopalan
ORCID: 0000-0003-4414-9918

# ACKNOWLEDGEMENTS

The time I spent with LIGO was special, with many spectacular discoveries along the way. There were too many people who made me feel like I was part of a family to single out, but I thank Rana for giving me the keys to the 40m, Koji for teaching and supporting me through the day-to-day, Steve for setting the pulse of the lab, Chub and Jordan who worked with me through a pandemic, and my grad student and postdoc colleagues who worked on the interferometer with me. My short stint at LLO was an excellent learning experience thanks to the excellent mentorship I received. I thank the folks in Downs who were happy to chat even when I walked in unannounced, and the Strong Fielders for letting me be a part of their softball exploits.

I was lucky to have made many great friends along the way. In particular, I enjoyed the many epic trips and torturous trail runs with Simon, Johan, and Daniel. Magnus, Vin, Marcel and Craig were great housemates and friends. The shows I got to perform at with Vin, Anthony, and Chris as part of the Clowns of Nabla were epic! Motorcycling in Southern California was a dream come true, I'll have many great memories of those rides. There are several others who made my time in Pasadena great fun, I hope our paths cross again at some point in the future.

Finally, I'd like to thank my family for their love, support, and encouragement. I could not have become the person I am today without you.

*Nil Sine Labore.*

# ABSTRACT

Since the first direct detection of gravitational wave signals from the coalescence of a pair of stella-mass black holes on 14 September 2015, a global network of terrestrial interferometric detectors, with kilometer-scale arms, have opened a new window through which the astrophysical universe can be probed. This success was the result of decades of exploratory work done on smaller-scale prototype interferometers. Even though the detection of astrophysical gravitational wave signals has become almost a routine event, prototype interferometers remain an essential tool in developing technologies for future generations of kilometer-scale detectors. They are unique in that they are large enough to probe physics that cannot be easily investigated on the table-top, but have no obligation to function as an observatory, and so can be readily modified for a wide variety of experiments. This thesis focuses on one direction in which prototype interferometry can be taken, serving as a testbed for testing the laws of quantum mechanics at the macroscopic scale. While this is in itself an interesting experimental program, it can make a direct contribution to the field of gravitational wave astronomy since future generations of terrestrial detectors are expected to be limited in their sensitivity due to measurement limits set by the Heisenberg uncertainty principle. Techniques to evade these limits can be demonstrated on a prototype interferometer, before embarking on an expensive program to implement them at the scale necessary for kilometer-scale observatories.

# PUBLISHED CONTENT AND CONTRIBUTIONS

Yuntao Bai, **Venugopalan, Gautam**, Kevin Kuns, Christopher Wipf, Aaron Markowitz, Andrew R. Wade, Yanbei Chen, and Rana X. Adhikari. Phase-sensitive optomechanical amplifier for quantum noise reduction in laser interferometers. *Phys. Rev. A*, 102:023507, Aug 2020. doi: 10.1103/PhysRevA.102.023507. URL https://link.aps.org/doi/10.1103/PhysRevA.102.023507. G.V. participated in the conception of the idea, performed the technical feasibility analysis, and led the writing of the manuscript.

# TABLE OF CONTENTS

# LIST OF ILLUSTRATIONS

# LIST OF TABLES

*Chapter 1*

# PROTOTYPE INTERFEROMETRY IN THE ERA OF GRAVITATIONAL WAVE ASTRONOMY

## 1.1 Introduction

Decades of work put into improving the sensitivity of the LIGO interferometers led to the spectacular first direct measurement of gravitational waves in September 2015 [1]. In August 2017, gravitational wave signals from a pair of neutron stars coalescing were observed by LIGO [2], with an electromagnetic counterpart from the same event recorded shortly after by several telescopes across the electromagnetic spectrum. These events marked the dawn[1] of "Multi-Messenger Astronomy" (MMA), and with it, the opportunity to perform tests of general relativity [3], cosmology [4], and extreme matter physics [5] that were not previously possible. While the first detection was a triumph for the field, several technical challenges remain in achieving the design sensitivity of the instrument. Therefore, improving the detector sensitivity and increasing the volume of the universe probed (and hence the detection rate of astrophysical signals) remains a primary goal of the collaboration.

In addition to their astrophysical value, the LIGO interferometers are among the most sensitive precision measurement devices ever built, and allow testing various quantum-limited metrology schemes. Such experiments can be valuable to other communities who are operating in the quantum-limited sensing regime as well, such as dark matter detection experiments. The size and mass scales of the interferometers also offer a unique environment in which the laws of quantum mechanics can be tested.

Much of the work described in this thesis was performed at the 40m prototype interferometer at Caltech (known as the C1 interferometer). Prototype interferometers have historically been central to developing technologies that are then transferred to the kilometer scale observatories. In the MMA era, prototypes around the world continue to play an important role in supporting the observatories as low-risk test environments for exploratory noise-mitigation studies - for the C1 interferometer in particular, there are many excellent references [6–8]. Among the fully instrumented

[1] At the time of writing, gravitational wave signals from more than 50 binary coalescence events have been measured, with the bulk of them being from binary black hole systems.

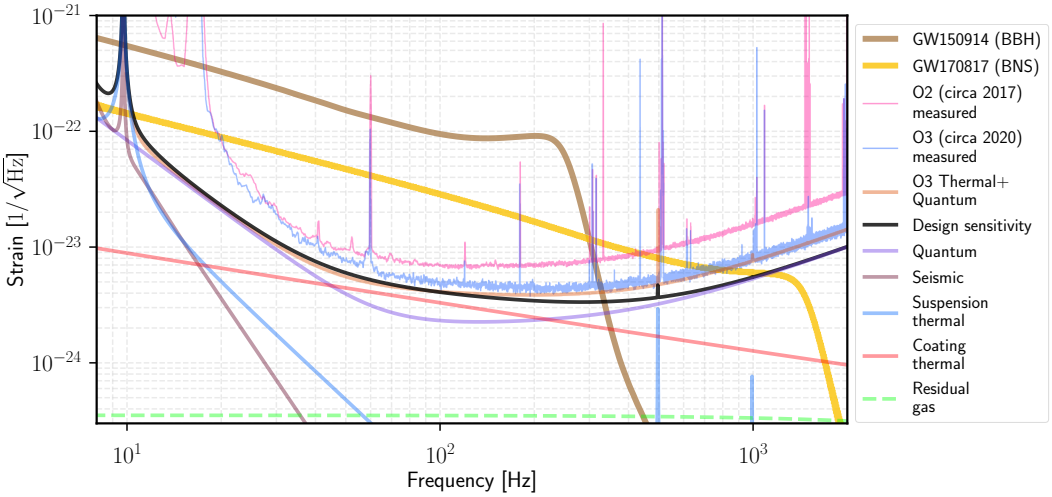


Figure 1.1: Sensitivity of the Advanced LIGO interferometers. Both noise models (smooth curves) and the *measured* detector sensitivities (fuzzy traces) during two of three LIGO observing runs are plotted. The signals from two key gravitational-wave events are overlaid as (smooth thick bands) to give an indication of how much SNR they were sensed with at each frequency.

prototypes in the world, C1 is closest in optical topology to the LIGO interferometers, and also provides the longest (in-vacuum) baseline arm length[2]. Perhaps most importantly, there is no obligation on C1 to observe astrophysical signals, making it ideal for the experimental work described in this thesis.

## 1.2 Sensitivity of the Advanced LIGO interferometers

Fig. 1.1 illustrates how the sensitivity of the LIGO interferometers are typically presented, in a "noise budget". The quantity plotted in each of the noise traces are the amplitude spectral densities (ASDs), and individual noise contributions are summed in quadrature to generate the trace labelled "Design sensitivity". This noise budget is highly simplified - a more comprehensive noise budget includes several tens of noise sources. The ones plotted here are "facility limits" (e.g. seismic and residual gas) or fundamental (e.g. quantum). At high frequencies >100 Hz, O2 and O3 sensitivities differ because squeezed vacuum injection was used in O3 (but not O2) to reduce the quantum noise at those frequencies. The design sensitivity for LIGO assumes higher laser power and frequency dependent squeezed vacuum injection for broadband quantum noise reduction, which explains the difference between O3 sensitivity and the black trace - in fact, above $\approx$ 100 Hz, thermal and quantum noises

[2]The Gingin observatory complex in Australia has an L-shaped vacuum envelope with the arms of the "L" being 80 m long. At the time of writing, it does not have the optical infrastructure installed to configure it as a DRFPMI.

limit O3 sensitivity, with the latter calculated with parameters used in the observing run. At lower frequencies, the measured noise exceed the "fundamental" noises due to residual couplings from the control systems used to keep the interferometers at their linear operating point and stabilize the angular motion of the suspended mirrors (the explicit coupling is not plotted here as a separate the contribution). Also included are the frequency content of gravitational wave signals from two important binary coalescence events (the characteristic strains are multiplied by $\sqrt{f}$ for comparison with the other ASDs on this plot).

The individual noise contributions are explained in greater detail in Chapter 3 and also in [9, 10] - the main point of Fig. 1.1 is to say that (i) the terrestrial interferometers are still being improved, and (ii) even at design sensitivity, the SNR for a typical BNS coalescence will be too small at frequencies $\sim 2\,\mathrm{kHz}$, which is where interesting information about the neutron star equation of state is expected to be encoded (this is just one example, higher order modes of the post binary black hole merger ringdown is another). The work in thesis aims to contribute to the general goal of enabling the terrestrial gravitational wave detectors to reach their design sensitivity, and eventually, surpass it using schemes to circumvent the quantum noise limitations imposed by Heisenberg's uncertainty principle.

### 1.3 LIGO interferometers as a cavity optomechanics experiment

The optical cavity is the fundamental building block of the LIGO interferometers. They amplify the effect of a gravitational wave interacting with the test masses forming the cavity, in addition to providing filtering that makes it possible to make a measurement at the level of $10^{-12}\,\mathrm{rad}/\sqrt{\mathrm{Hz}}$. In order to isolate the mirrors of the cavity from seismic motion, the mirrors are suspended from pendulums, which make them behave like free-masses above the resonant frequency of the suspensions. The laser power circulating in the resonant cavities is also large, O(300 kW). At these powers, the radiation pressure force imparted on the mirrors during the process of reflection are significant enough that the motions of mirrors at either ends of the cavity become coupled. These dynamics make the LIGO interferometers a large optomechanical device, and allows us to test if the rules of quantum mechanics remain valid in a unique region of the mass-frequency parameter space, since the LIGO cavity mirrors weigh $\approx 40\,\mathrm{kg}$ and the detector is most sensitive in the $20\,\mathrm{Hz} - 2\,\mathrm{kHz}$ frequency range. In the last decade, there were multiple landmark demonstrations in the field of cavity optomechanics, but these were largely at ng $-$ $\mu$g mass scales, and at frequencies in the MHz $-$ GHz range [11]. Probing

a complementary region in the mass-frequency space is, therefore, of interest to the precision measurement community.

The optomechanical interaction also raises the interesting possibility of generating squeezed states of light, using which it is possible to make measurements with lower variance than one would naively expect from the Poissonian statistics associated with photon arrival on a detector. The idea has been extensively modelled, and recently, experimentally demonstrated [12] in the $30-60$ kHz regime. One of the goals of this thesis was to improve the noise performance of the C1 interferometer to a level that would allow the measurement of an optomechanically squeezed state at $\approx 100$ Hz. The C1 interferometer has a very similar optical topology to the Advanced LIGO interferometers, but lighter mirrors (250 g in C1 vs 40 kg at LIGO). We believe this to be in a sweet spot, light enough to have significant optomechanical coupling, but large enough that they can be manufactured and handled while maintaining high mechanical quality factors essential for reducing the coupling of thermal noise into the measurement band.

### 1.4 Structure of this thesis

This thesis aims to contribute to the following domains: (i) improve the sensitivity of the current generation of terrestrial gravitational wave detectors, (ii) investigate how interferometers (both prototype and kilometer-scale ones) can be used as quantum-limited force sensors, and (iii) study schemes that can potentially improve the sensitivity of future terrestrial gravitational wave detectors. With these aims in mind, the rest of this thesis is organized as follows:

*Chapters 2* and *3* are focused on documenting the current status of the C1 interferometer. The former is focused on the Arm Length Stabilization (ALS) system. The latter describes in detail the commissioning efforts at the C1 interferometer, which may serve as a useful sequence of steps to follow in characterization efforts after upgrades that are in progress at the time of writing.

*Chapter 4* is a study into how the C1 interferometer can be used to generate an optomechanically squeezed vacuum state. Optomechanical squeezing can potentially be a valuable complement to the non-linear crystal-based squeezers routinely used in terrestrial interferometers today.

*Chapter 5* details an upgrade currently underway at the C1 interferometer that will allow the interferometer's output field to be read out using a technique known as Balanced Homodyne Detection (BHD). The work at C1 is meant to be a proof-of-

concept for a similar planned upgrade for the two LIGO observatories.

*Chapter 6* presents a study of how a phase-sensitive optomechanical amplifier can help future interferometers operated at cryogenic temperatures leverage strongly squeezed vacuum injection in the presence of non-negligible optical losses in the readout chain, a challenge that is anticipated at the planned operating wavelength of $\approx 2\mu$m.

*Chapter 7* describes an algorithm that can be used to design dielectric coatings that satisfy multiple requirements typical of those used in gravitational wave interferometers, but also more broadly applicable to precision metrology experiments that employ optical cavities.

*Chapter 2*

# ARM LENGTH STABILIZATION (ALS) SYSTEM

The ALS system at the 40m is able to control the CARM degree of freedom with $\approx$ 10 pm RMS residual displacement noise (measured from 10 mHz – 1 kHz). At the time of writing, this is among the best performance in suspended interferometers operated around the world that utilize the ALS scheme, and therefore, allows unprecedented repeatable and reliable lock acquisition at the 40m.

The use of auxiliary laser fields phase-locked to the main laser field has been demonstrated on multiple suspended interferometer systems [13–15]. The system used at the 40m has a few differences, which I outline in this section. Figure 2.1 shows a schematic overview of the setup while Figure 2.2 shows the feedback loop topology, for the case of a single arm cavity. In both diagrams, the important subsystems are grouped together with shaded rectangles, and in Figure 2.2, important points in the feedback loop where noise enters the system are indicated. It is instructive to understand the function of each block, and then, how they fit together. Finally, I briefly describe how the ALS system is a valuable diagnostic tool for characterizing the interferometer.

## 2.1 AUX-PDH loop

*This subsystem makes the* AUX *laser frequency follow the (seismically and thermally driven) arm cavity length with high fidelity.*

The ALS approach uses an auxiliary (AUX) laser field to sense the length of the arm cavity. The PDH technique is still the manner in which the error signal is generated. This raises a practical concern - the system needs to work when both the PSL and AUX laser fields are resonating in the arm cavity, so how can we distinguish between these two fields, so that PDH sensing of only the AUX laser field can be done? One possibility is to assign orthogonal polarizations to the two fields, and then rely on polarizing beamsplitters to separate the fields. The 40m ALS system adopts a different approach - the AUX laser field is first frequency doubled (to 532nm, hence the term "green-locking" is also sometimes used to refer to this system), and then injected into the cavity. This approach works because the parametric upconversion process of wavelength doubling adds a negligible amount

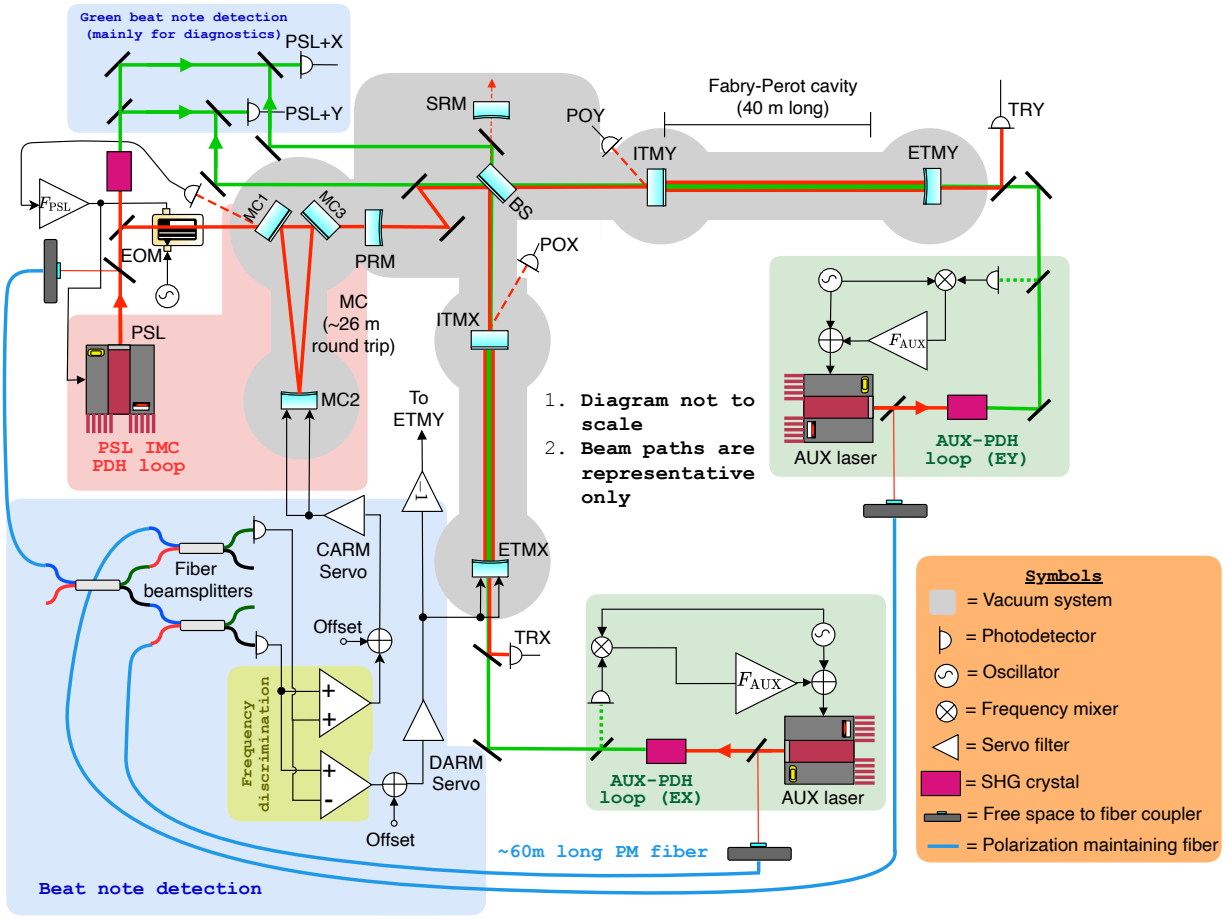


Figure 2.1: Schematic overview of the optical and electrical components of the ALS system used at the 40m. This figure should be interpreted along with Figure 2.2. The layout is adapted from [15], but updated to highlight the major change in the setup, which is that the error signal is now constructed using fiber coupled pickoffs of the 1064 nm laser fields from each NPRO (c.f. the old setup where the beat was constructed by interfering the transmitted green beam from each arm with a frequency-doubled pickoff from the PSL). The latter system is retained for diagnostic purposes, but the new system yields significantly better noise performance, and hence, is used in the lock acquisition process.

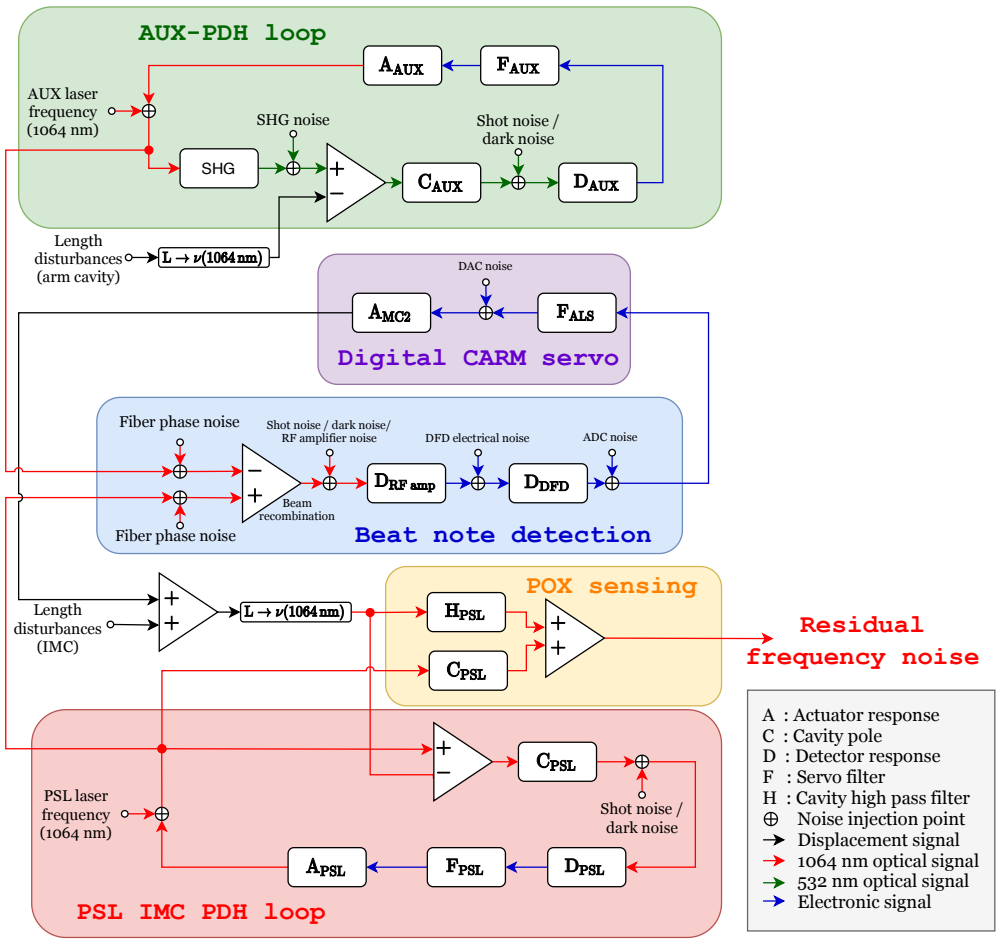


Figure 2.2: Feedback control topology of the IR ALS scheme. See Figure 2.1 for a more schematic overview of the setup. Assuming the system behaves like an LTI one, such a diagram can be used to write out the one-hop noise transfer functions from node to node. By enforcing self consistency on the resulting matrix equation, the closed-loop noise couplings of the various noise sources can be evaluated.

of noise. This field is then injected into the arm cavity from the ETM. At the 40m, this choice of injecting from the ETM side of the cavity is to maintain consistency with what is done at the aLIGO sites - the AUX field can also be injected into the arm cavity from the ITM side of the cavity, and indeed, this approach is adopted at some other interferometers, such as KAGRA [13].

To generate the PDH error signal, phase modulation sidebands have to be imprinted on the AUX field being injected into the arm cavity. For simplifying the complexity of the opto-electronic system, the choice was made at the 40m to do this by directly modulating the PZT element fitted on the (commercial) AUX NPRO laser for frequency control. Compared to the more traditional approach of using an EOM

for this purpose, there are fewer electro-optic components involved in the approach taken at the 40m. However, the PZT actuator has the drawback of having a much lower bandwidth than an EOM, and therefore, limits the overall bandwidth (and hence frequency noise suppression) of the PDH loop used to stabilize the AUX laser frequency to the arm cavity length. Additionally, being an electro-mechanical transducer, the PZT has several resonant features that lead to amplitude (rather than phase) modulation of the AUX laser field. These have to be carefully mapped out and avoided when choosing a modulation frequency. At the 40m, a frequency of $\approx 232\,\mathrm{kHz}$ was chosen as it yields the maximum PM/AM ratio ($\approx 5\times10^5$) [16] in the range $100\,\mathrm{kHz} - 1\,\mathrm{MHz}$. Frequencies $< 100\,\mathrm{kHz}$ are excluded as the reflectivities of the arm cavity mirrors set a cavity pole frequency of 19 kHz (denoted as $C_{\mathrm{AUX}}$ in Figure 2.2) for 532 nm and the PDH technique relies on the PM sidebands being reflected when the carrier is resonant, which requires at least a few linewidths of separation from the resonance of the carrier. Moreover, we do not want too low a modulation frequency to limit the servo bandwidth. Frequencies $> 1\,\mathrm{MHz}$ are excluded as the NPRO's PZT actuator becomes ineffective at those frequencies.

Before injection into the cavity the beam has to be well matched to the cavity's eigenmode, in order to couple maximum power from the injected beam to the cavity. This is important in order to realize a low-noise PDH error signal - any injected light that is not well matched to the cavity's eigenmode will be rejected (reflected) onto the PDH sensing photodiode in reflection. This light would contain no information about length fluctuations of the cavity, but would contribute shot noise at the PDH loop's error point, thereby degrading the quality of the frequency stabilization. In fact, the 40m arm cavity mirrors' dielectric coatings have reflectivities at 532 nm that make the cavity overcoupled - that is, when the cavity is resonant, even assuming perfect mode-matching, part of the resonant field leaks through the input coupling mirror (the ETM, since the beam is injected there), and hence, constitutes a constant level of light on the reflection PDH photodiode that contributes shot noise without any information about cavity length fluctuations. Given that these are the mirrors we have, the task was to identify a series of lenses that could be placed in the injection path in order to realize good mode-matching between the AUX laser's eigenmode and the cavity's eigenmode. A numerical optimization routine was used to identify a solution that uses commonly available focal lengths for the mode-matching lenses, and also to identify lens placement locations in the propagation path that are maximally tolerant to human errors in lens placement (i.e. the resultant mode-matching efficiency to the cavity is negligibly degraded if the actual positions

of the lenses or their focal lengths differ from the assumed values by $\approx$ 5%). Two of the lenses are also mounted on translation stages to permit in-situ optimization of the mode-matching. While the calculated mode-overlap was $>$ 99% [17], the realized mode-overlap was estimated to be $\approx$ 90%. While future higher-precision applications may require this number to be improved, 90% was deemed sufficient for lock acquistion at the 40m, and hence, this was not further optimized.

The final part of this subsystem is the feedback loop, consisting of a detection photodiode ($D_{\mathrm{AUX}}$), servo electronics ($F_{\mathrm{AUX}}$) and actuator ($A_{\mathrm{AUX}}$). For the 40m ALS system, $A_{\mathrm{AUX}}$, which is the NPRO's PZT actuator, may be assumed to have a flat frequency response. In reality, there are several parasitic resonances at frequencies near 100 kHz as revealed in the AM/PM measurements of the NPRO [16], though it is expected that these can be neglected for realizing a servo with a UGF of $\approx$ 10 kHz. Future applications that call for higher bandwidth feedback loops may require either a separate high frequency actuator such as an EOM, or inversion of the frequency-domain poles and zeros characterizing these parasitic resonances using fast digital electronics (e.g. an FPGA based controller [18], being digital, allows easy tuning of the parameters of these resonances as opposed to building an analog electronics circuit). A Thorlabs PDA36A photodiode serves as $D_{\mathrm{AUX}}$. Being a broadband photodiode, it too can be considered as a transimpedance ($I \rightarrow V$) amplifier with flat frequency response. The choice of using a broadband photodiode, as opposed to the typical LIGO approach of using a custom design tuned to have a resonant response at the PDH modulation frequency (and notch frequency at its second harmonic), was motivated by keeping the setup as simple as possible. The servo electronics, $C_{\mathrm{AUX}}$, perform a number of operations, starting with demodulation of the PDH error signal, low-pass filtering the $2f$ frequency component associated with demodulation by a mixer, and finally, producing a low-noise control signal that efficiently rejects frequency fluctuations of the AUX laser frequency relative to the arm cavity length with the desired control bandwidth. The loop transfer functions for the EX AUX PDH loop at the 40m are shown in Figure 2.3. The loop has $\approx$ 10 kHz bandwidth, with a phase-margin of $\approx$ 60°. The purple curve, labeled "other electronics (model)", is instructive in understanding why higher bandwidths are not possible with this setup. It represents the total effect of (i) a post-mixer, fourth$^{\mathrm{th}}$−order low-pass filter with corner frequency $f_c \approx 70$ kHz that attenuates the signal content at $2f_{\mathrm{mod}}$ associated with demodulation using a mixer, (ii) a summing box with a pole at $\approx$ 100 kHz that is used to sum both the control signal and the PDH phase modulation signal before the NPRO PZT, and (iii) a pole associated with the

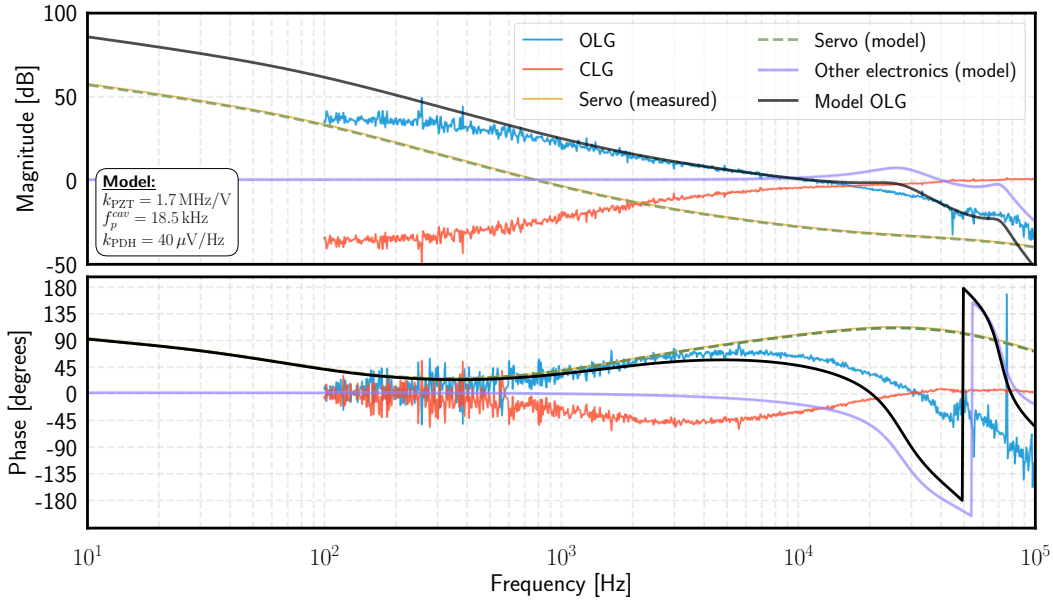


Figure 2.3: Open-loop (measured) and closed-loop (inferred) transfer functions for the AUX PDH loop. Measurements / models for the constituent parts are also included. At $f < 1\,\text{kHz}$ the transfer-function measurement technique used does not yield reliable results since the excitation injected to make the measurement is suppressed by the large loop gain at those frequencies below the noise floor of the measurement apparatus.

NPRO PZT actuator at $\approx$ 200 kHz.

As a result of the phase-lag caused by these components, a higher bandwidth feedback loop is not possible with the existing servo electronics and PDH modulation scheme.

## 2.2 PSL IMC PDH loop

*This subsystem makes the PSL laser follow the Input Mode Cleaner (IMC) cavity length with high fidelity. The system has sufficient gain at low frequencies to suppress the frequency noise of a free-running* NPRO *to the level required for precision interferometry.*

Just as the arm cavity length is the reference to which the AUX laser frequency is stabilized, the IMC cavity serves as the reference to which the PSL frequency is locked. The PDH technique is used. Unlike the system used for the AUX laser frequency stabilization, the IMC loop uses a dedicated EOM to imprint the PM sidebands used for PDH locking. Furthermore, the feedback controller, $F_{\text{IMC}}$ and actuator, $A_{\text{IMC}}$ have a more complicated structure relative to the AUX-PDH loop.

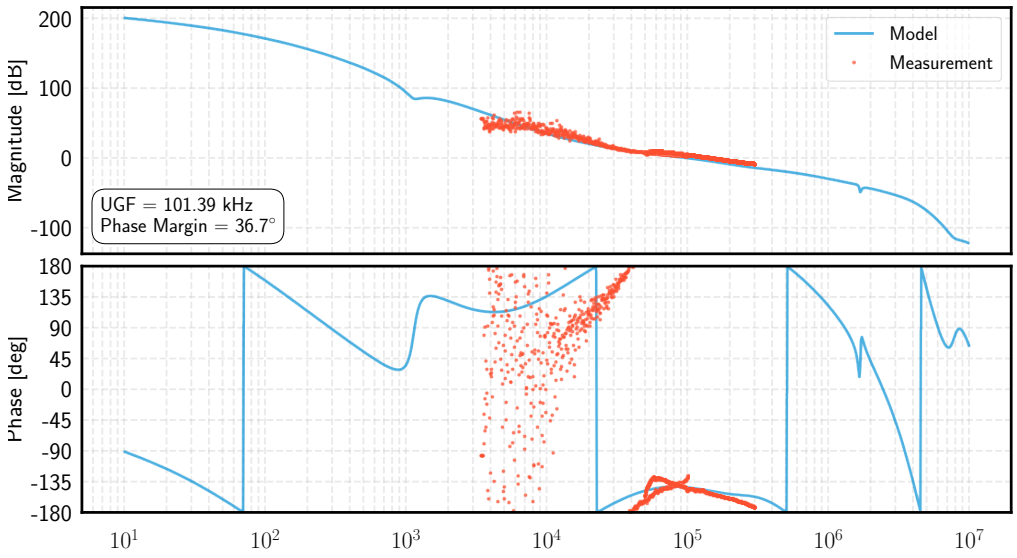


Figure 2.4: Open loop measured and modelled transfer functions for the PSL IMC PDH loop.

This is because the requirements on frequency stability are more stringent for the PSL - a high bandwidth feedback loop is required to meet these requirements. At the 40m, the IMC PDH loop is designed to be able to realize a UGF of $\approx 100\,\text{kHz}$, and a comparison of the measured OLTF compared to the model is shown in Figure 2.4. There is good agreement between model and measurement around the UGF. At $f < 50\,\text{kHz}$ the transfer-function measurement technique used does not yield reliable results since the excitation injected to make the measurement is suppressed by the large loop gain. Furthermore, only one stability margin (phase) is indicated - in reality, there are others that must be considered as well in order to realize a stable loop. Nevertheless, this feedback loop functioned with sufficient reliability to allow locking the interferometer.

## 2.3 Beat note detection

*This subsystem tracks fluctuations in the beat frequency between two lasers with low noise. Assuming each laser is faithfully tracking a cavity length (by the feedback loops described in Sections 2.1 and 2.2), these fluctuations are then a proxy for relative length fluctuations in the two cavity lengths.*

As the lengths of the IMC and arm cavities are disturbed by seismic noise, the feedback loops described in the preceeding two subsections servo the PSL and AUX laser frequency respectively such that they stay resonant in the respective

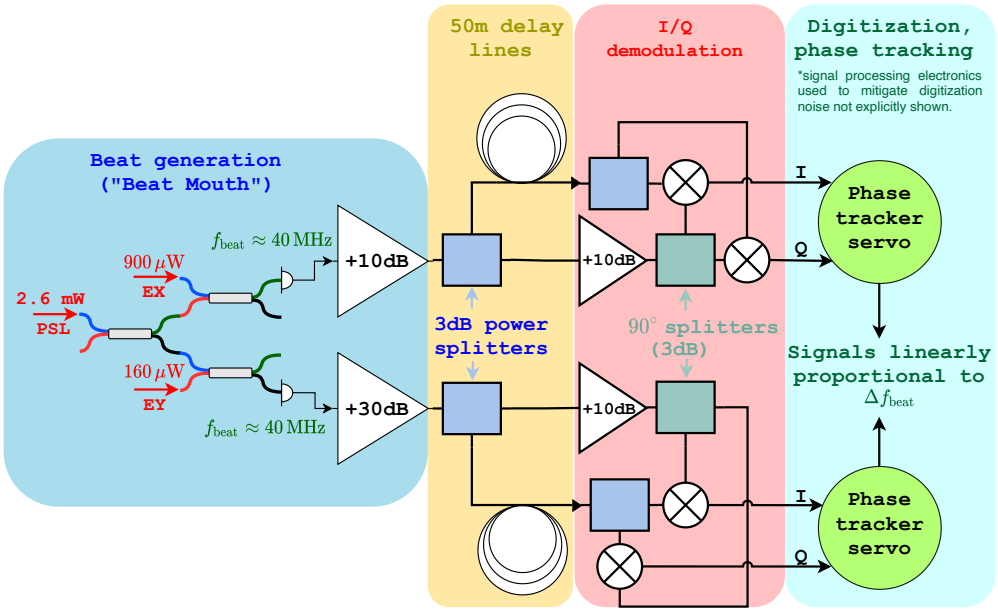


Figure 2.5: Schematic overview of the DFD system. The optical beat is generated in a unit called the "Beat Mouth". Damage thresholds of the fiber coupled photodiodes limit the signal power - therefore, the signals are preamplified before transmission over $\approx$ 20 m coaxial cable to the DFD electronics. Each beat signal is then split equally, with one half sent through a 50m low-losscoaxial delay line, before being mixed with the undelayed version of itself in an RF I/Q demodulator, part # LIGO-D0902745. The demodulated signals are digitized, and a "phase-tracker" servo is used to digitally rotate the demodulated quadratures to derive a signal that is always *linearly* proportional to fluctuations in the beat frequency.

optical cavities. The goal of the ALS system is to eliminate *differential* length fluctuations between these two cavities. Therefore, we need to derive an error signal proportional to these fluctuations that we can drive to zero by a suitable feedback loop. A candidate error signal is the optical beat generated when small pickoffs of the PSL and AUX laser fields are mixed (interfered) on a photodiode. Then, if the length of either cavity changes (well within the bandwidth of the PDH loops stabilizing the laser frequency to the cavity length), the beat frequency will also change. Therefore, in addition to a sufficiently high bandwidth photodiode that can detect the optical beat, we need a low-noise system that can detect fluctuations in the beat frequency with.

At the 40m, a Delay-line Frequency Discriminator (DFD) is used to generate an error signal that is *linearly proportional* to fluctuations in the beat frequency. Once such a signal is available, a linear feedback loop can be used to change the frequency of one of the two lasers generating the beat to null this error signal and thereby, keep

the beat frequency constant. The detailed theory of operation is described in [19], while Appendix A of [8] describes the phase-tracker algorithm used to extend the linear range of the DFD and permit tracking of larger low-frequency variations than would be possible with a traditional DFD. The coaxial cables used for the delay lines are $\approx$ 50 m lengths of LMR-195 by Times Microwave Systems, chosen for their low loss (8.4 dB/100m[20]).

Compared to previous incarnations of the system at the 40m, careful characterization of the signal levels and noise sources in the electronics associated with the DFD readout resulted in an overall lowering of the measurement noise floor of this system. Figure 2.6 shows the dependence of the frequency discriminant as a function of the RF power of the beat signal, using the parameters of the 40m DFD setup. While a naïve analysis suggests that increasing the delay improves sensitivity monotonically, there is no benefit to increasing the delay line length above the point where the loss in the cable exceeds $\approx$ 8.7 dB [8]. Therefore, the limitation of this technique of reading out frequency fluctuations is that high signal powers and low-noise electronics are required to achieve low sensing noise. For instance, with 10 dBm of RF beat signal power, sensing electronics with input referred noise $< 10\,\mathrm{nV}/\sqrt{\mathrm{Hz}}$ would be required to realize a sensing noise floor of $1\,\mathrm{mHz}/\sqrt{\mathrm{Hz}}$. While lock acquisition does not require such low sensing noise levels, future high precision applications, such as calibrating the DARM DoF, may place even more stringent requirements, necessitating a re-think of the way changes in the beat frequency are detected.

A major change in the setup from 2016 is that the way in which the beat signal is generated was changed. Previously [8, 15], the beat was generated by mixing the transmitted green beam from each arm cavity (extracted at the vertex area of the interferometer using a mixture of polarization-separating optics) with a frequency-doubled pickoff from the PSL. Because the mixing was done in free-space, the two beams had to be frequently aligned onto the detection photodiode to compensate for drifts in the alignment of the interferometer's arm cavities. Furthermore, it was suspected that low frequency alignment modulations associated with the complex system of polarization-separating optics in the vertex area of the interferometer, and scattered light fields generated in the process, were contributing excess noise to the DFD system at low ($f < 30\,\mathrm{Hz}$) frequencies.

To improve the situation, I decided to use long ($\approx 60\,\mathrm{m}$) polarization-maintaining fibers to route a pickoff of the AUX laser from each arm cavity to the vertex area of the interferometer, where it was mixed on a high-bandwidth fiber coupled

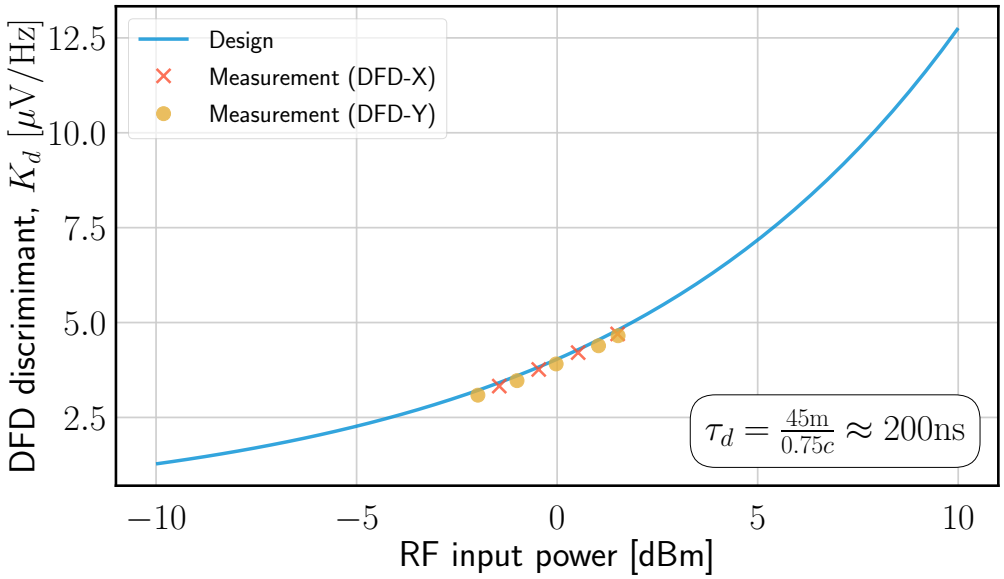


Figure 2.6: The frequency discriminant, i.e. the voltage output of the DFD for a unit change in input frequency, is dependant on both the length of the delay line and the signal power. The latter affects the noise performance of the system, since a *given* electronics noise level will translate to a larger frequency sensing noise.

photodiode (NewFocus 1611-FC) with a pickoff of the PSL. It was hypothesized that compared to the old technique, if the coupling of light from each AUX laser and the PSL could be done using high-quality free-space to fiber couplers mounted on optical tables with stable optomechanics, problems associated with alignment drifts and scattered light could be mitigated to a large degree. Indeed, after the change was made, the alignment did not need adjustment for year-long timescales. Furthermore, the low-frequency noise of the ALS readout was improved. As a result of all these improvements, the procedure of locking the 40m interferometer was greatly simplified, allowing repeatable, reliable locking of various complex interferometer configurations. The old system was not completely dismantled, and now serves as a useful diagnostic tool (though it is no longer used in the lock acquisition sequence).

## 2.4 Digital CARM servo

*This subsystem keeps the beat frequency between the PSL and AUX lasers, as sensed by the DFD described in Section 2.3 at a fixed value.*

The ultimate goal of the ALS system is to allow the PSL frequency to be maintained at arbitary offsets relative to when it becomes resonant in the arm cavity. Sections 2.1, 2.2 and 2.3 describe how relative frequency fluctuations between the PSL and arm

cavity length are sensed, and an error signal is derived. The final step in the chain is to close a feedback loop, driving this error signal to zero.

The procedure starts by first locking the X(Y) arm cavity's length to the PSL frequency with PDH error signals derived from the POX(POY) photodiodes respectively. Simultaneously, the AUX laser frequency is locked to the arm cavity length. The high-range actuator controlling the temperature of the AUX NPRO's lasing crystal is adjusted such that the average value of the beat frequency between the PSL and AUX laser in this condition (simultaneous resonance in the arm cavity) is $f_{\mathrm{ALS}} \approx 40\,\mathrm{MHz}$ [1].

The digital phase tracker servo is then tuned such that the I-phase output is (on average) zero. A simple integrator is used to adjust the digital demodulation phase in a feedback loop with bandwidth $\approx$ 2 kHz (limited by the sampling rate of the system, 16 kHz) - then, within the bandwidth of this loop, fluctuations in the digital demodulation phase can be mapped to frequency fluctuations of the beat frequency, using the calibration factor $\frac{d\phi}{df} = 71.291 \pm 0.024\,^{\circ}/\mathrm{MHz}$ [2]. A feedback loop (with $\approx$ 120 Hz bandwidth) is then closed by actuating on the position of the suspended MC2 mirror of the triangular IMC cavity - as described in Section 2.2, the PSL frequency follows the length of this cavity with $\approx$ 100 kHz bandwidth, and therefore, by changing the length of the IMC cavity, the frequency of the PSL can be changed. Once this feedback loop has been closed, the POX and POY sensors are no longer required to keep the PSL resonant in the arm cavities. Finally, by adding an offset to the error-point of this servo ("CARM offset" in Figure 2.2), arbitrary offsets can be maintained between the PSL frequency and the arm cavity's resonant frequency. For lock acquisition at the 40m, an offset of $\approx$ 4 nm (c.f. the CARM linewidth of $\approx$ 28 pm) is used to allow locking of the vertex area of the interferometer.

## 2.5 ALS noise budget

In order to assess the noise performance, a single arm cavity length was controlled using the ALS system. The DC setpoint of the cavity length was such that the

[1] This value is chosen given the FSR of the 40 m long arm cavity is $\approx$ 4MHz, and ambient levels of seismic activity can disturb the round-trip length of the cavity by greater than one wavelength (equivalently, one FSR). If this were to happen, the sign of the servo that would maintian a fixed offset between PSL and AUX laser frequencies would be inverted. To avoid such complications, the beat frequency chosen to be several FSRs away. Much larger values are avoided to remain well within the operating bandwidths of various RF components composing the beat-detection chain.

[2] This calibration factor is for the one of the two delay lines used - the other has a very similar calibration of $70.973 \pm 0.024^{\circ}/\mathrm{MHz}$. This is purely a function of the delay line length, and it is reasonable that the two delay lines are of slightly different lengths.

main PSL beam was resonant in the arm cavity (though it was not directly used for controlling the cavity length). In this state, the POX photodiode (see Figure 2.1) is a linear, out-of-loop sensor [3] of the residual motion of the arm cavity relative to the PSL frequency. The POX photodiode's voltage readout, digitized by an ADC, was separately calibrated into physical units of meters[4].

In order to estimate the contribution of the various technical noise sources, a model of the system as shown in Figure 2.2 was implemented in MATLAB's SIMULINK toolbox. By linearizing the system, the transfer functions from various points of noises coupling into the closed feedback loop to the residual arm cavity motion can be evaluated. Then, knowing the spectra of the noise sources themselves, a noise budget can be constructed, which gives insight into what is limiting the performance of the ALS system. Such a noise budget is shown in Figure 2.7. While the budgeting done here is not as comprehensive as that in Fig. 7 of [15], the total measured noise is largely explained by (i) residual seismic motion due to finite gain of the feedback loop suppressing it, (ii) unsuppressed frequency fluctuations of the AUX laser relative to the arm cavity length (also due to finite gain of the feedback loop), and (iii) ADC noise.

Between 10-100 Hz, the measured noise is in excess of the budgeted ones. One noise source that is known to be poorly modelled is the noise introduced due to phase fluctuations introduced in the optical fibers involved in generating the beat signal between PSL and AUX lasers. At the 40m, some minimal isolation of the fibers from environmental perturbations (for example,vibrations due to air currents and spinning fans in the laboratory, thermally driven length changes of the fiber etc.) is provided by housing the fibers inside thick foam tubes. In Figure 2.7, the curve for "Fiber phase noise" is for the fundamental thermodynamic limit [21, 22]. However, empirically, it is known that the length (i.e. phase) fluctuations of the fibers are far in excess of this fundamental limit - for example, turning fans associated with the lab's HEPA system off and on revealed a difference in the measured ALS noise. Improving the isolation of the fibers, by suspending the shielded fibers instead of laying it out on a cable tray for example, could improve the overall ALS noise performance. The contribution can be quantified by performing a test analogous to that described in [23].

A point worth noting is that all of the "fundamental" noise sources are several orders

[3] In the usual PDH sense, since the main PSL beam still has PM sidebands imprinted on it.

[4] The PDH optical gain in reflection for the arm cavity associated with a misaligned PRM had a value of $\approx 800\,\mathrm{kW/m}$.

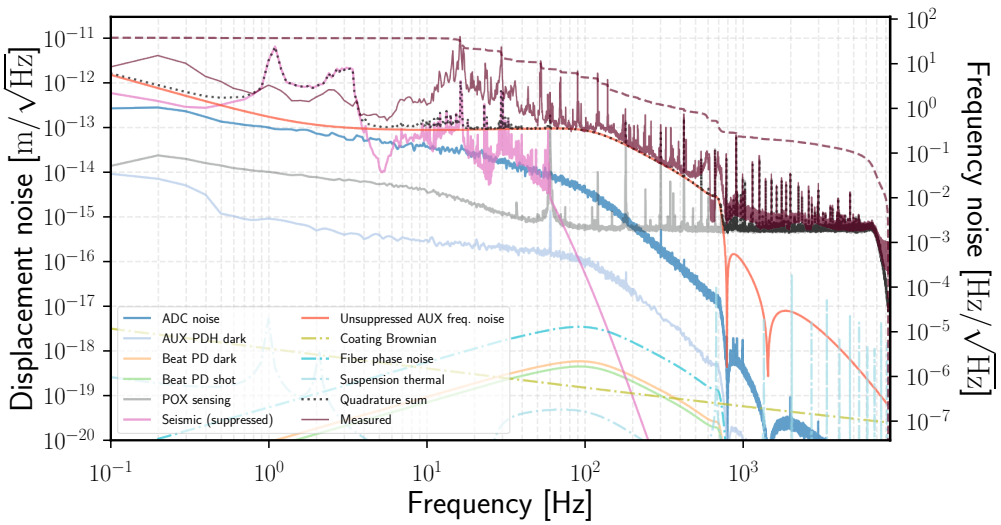


Figure 2.7: Fundamental (dash-dot lines) and technical (solid lines) noise sources contributing to residual motion when a *single* arm cavity's length is controlled using the ALS system. Here and elsewhere in this thesis, dashed lines of the same color as a corresponding ASD is the *cumulative* RMS, computed by integrating the squared ASD from high frequencies to low, and then taking the square root. From the dashed lines, we can evaluate the relative contribution from different frequency bands to the total RMS noise, and hence, come up with mitigation strategies. The technique of using the POX photodiode as an out-of-loop sensor of residual motion is limited by its inherent sensing noise, labeled "POX sensing".

of magnitude away from limiting the noise performance. By solving the engineering challenges that make these noise sources problematic, the existing interferometric infrastructure can be used to realize an RMS residual noise that is at least 100 times better than the current best value of $\approx 8\,\mathrm{pm}/\sqrt{\mathrm{Hz}}$.

Finally, the evolution of the noise performance of the ALS system at the 40m over time is shown in Figure 2.8.

On the basis of Fig. 2.7, some improvements that can be made to improve the noise performance of the ALS system are:

1. Better suppression of AUX laser frequency noise - above $\approx 100\,\mathrm{Hz}$, this is the dominant noise source. The suppression is limited by finite gain of the AUX PDH loop at these frequencies. The dark noise of the AUX PDH sensing photodiode lies a few orders of magnitude below the unsuppressed frequency noise, but if a dramatic improvement is desired, a custom photodetector with better noise may also have to be designed.

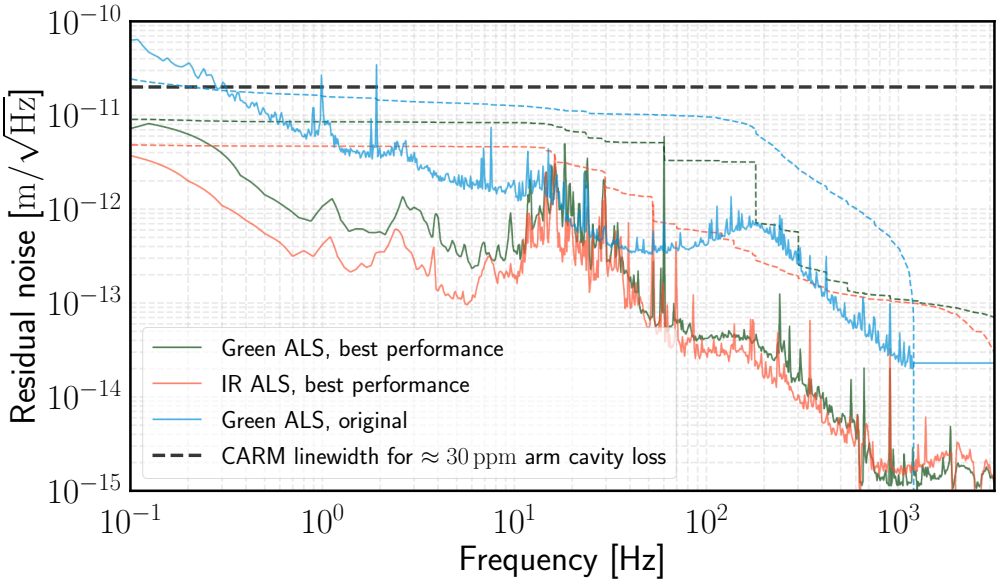


Figure 2.8: Evolution of ALS noise performance. The main difference between the current system (red curve) and previous iterations shown in the blue ([15]) and green ([8]) curves is that the beat between the PSL and AUX lasers is generated using 1064 nm pickoffs from each laser (i.e. before they are frequency doubled to 532 nm) coupled into fibers, while the cited works optically mixed the *transmitted* 532 nm beams from each arm cavity with a frequency doubled pickoff of the PSL. The improvement between the red and green curves may look marginal, but with the new system, lock acquisition of the interferometer is more repeatable and reliable.

2. Better suppression of seismic noise. The finite bandwidth of the feedback loop used to suppress relative frequency fluctuations between the PSL and arm cavity length limits achievable suppression, particularly in the 10-100 Hz band. It is difficult to achieve much higher gain in this frequency band with a stable digital feedback loop - so this problem may be best tackled by reducing the *unsuppressed* relative seismic noise by implementing better passive / active vibration isolation systems. In particular, the MC2 suspension sits on a seismic isolation stack different from those used elsewhere at the 40m, with relatively worse isolation performance.

3. Better whitening filters to pre-process the signal before digitization and hence reduce the ADC noise. The DFD scheme would also benefit from a digitization path that better matches the signal to the dynamic range of the ADC. Unlike the PDH locking scheme, the ALS feedback loop does not suppress the *amplitude* of the beat signal. The resultant large DC component that must be digitized limits the amount of front-end gain we can apply to the beat signal. If a

custom circuit can be designed that separately digitizes the DC part and AC frequency fluctuations with different gains, we could further boost the signal amplitude going into the DFD using a low noise RF amplifier. This improves the frequency discriminant (see Fig. 2.6), while still allowing us to track both DC and AC variations of the beat frequency.

4. Redesign the digital feedback loop to better roll-off the noise at high frequencies. In Fig. 2.7, an ad-hoc 700 Hz elliptic low pass filter is used, but a systematic procedure may lead to better noise rejection in the 100-700 Hz band.

5. Taking the PSL pickoff for the ALS beat from closer to where it is injected into the main interferometer (i.e. after transmission through the IMC). The core idea of multi-wavelength sensing is frequency comparison between two laser beams. *However, any noise imposed on these beams between where they sense cavity length and where they are optically mixed, such as phase noise due to path length modulations of optical fibers carrying these beams, will manifest as frequency noise*. Therefore, every reasonable effort must be taken to eliminate such couplings. By generating the beat signal using pickoff beams "close" to where they sense cavity lengths, the requirement on isolation of the fibers from the environment (for example) is relaxed.

## 2.6 ALS as an arm cavity diagnostic tool

Compared to PDH locking, which is the only other low-noise feedback control technique available at the 40m, the ALS system has the advantage of providing a linear error signal over a much larger range of frequency offsets between the PSL frequency and the arm cavity's resonant frequency. The PDH signal can only be used for linear feedback control over the arm cavity's linewidth of $\approx 8.8$ kHz, and while some tricks such as normalizing the PDH error signal by the arm cavity's transmission can broaden the linear range, it does not permit scanning the arm cavity length in a controlled manner through several free spectral ranges, as the ALS system allows. Performing such a scan allows the 40m long arm cavity to be used as a spectrum analyzer, and several parameters of the interferometer can be measured *with high precision* since the measurement is interferometric*, and in-situ*. From a single scan over multiple FSRs, a non-exhaustive list of information that can be extracted includes (i) The arm cavity FSR (and hence length), with as good as to 1 mm precision, (ii) Modulation depths of the RF sidebands on the main

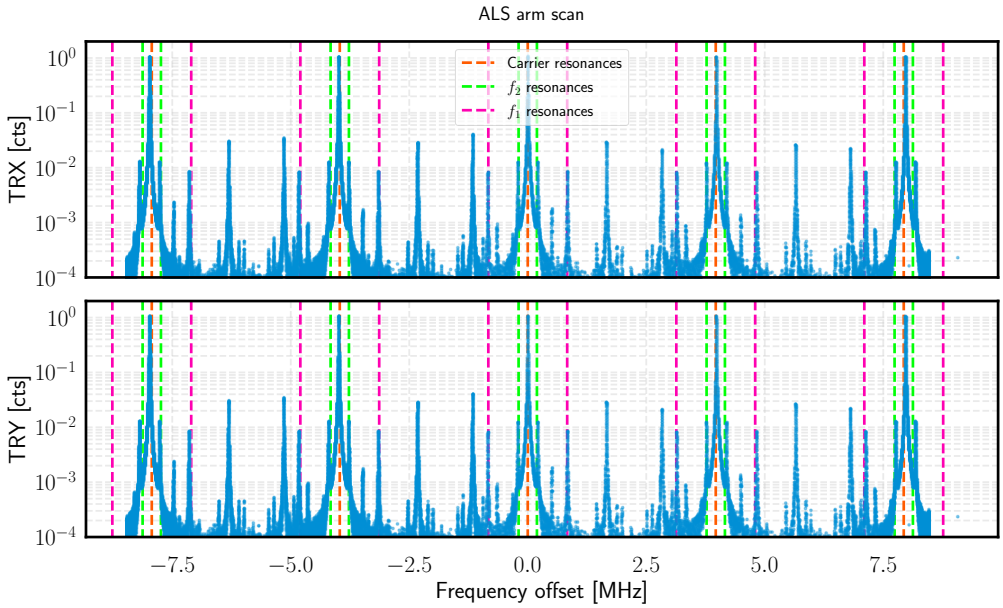


Figure 2.9: Time series of power transmitted (TRX and TRY) through the arm cavities while under ALS control. The scan is effected by changing the offset between the PSL frequency, and the arm cavity's resonant frequency.

interferometer beam, (iii) Large RF sideband asymmetry (symptomatic of possible detuning of the IMC), (iv) Mode-matching of the main interferometer beam to the arm cavity, and (v) $g$ − factor of the arm cavity.

A time series of the transmitted power through the arm cavity during one such scan is shown in Figure 2.9. It can be deduced from this scan that there isn't any significant detuning of the IMC cavity as the RF sidebands on either side of a carrier resonance are approximately equal in height. The principal advantage of this system as a diagnostic tool is that it does not require any significant additional setup to do the scan, since the ALS system is required for regular operation of the interferometer. One source of uncertainty in such scans comes about because of uncertainty in the calibration of the digital phase tracker servo into physical units of frequency. Separate calibration of this parameter using a function generator[5] locked to a Rubidium clock[6] suggests that the phase tracker provides a highly linear readout for beat frequencies in the range 30 − 200 MHz[24]. Another source of error is the noisy transmitted light readout - these photodiodes have to operate over a range of incident light intensities spanning a few orders of magnitude, and hence,

[5] IFR2023B.

[6] Stanford Research FS725, itself synchronized to a 1 PPS signal from a EndRun Technologies Tempus LX GPS receiver.

the SNR for the weak resonances (of higher order modes for example) will be sensed with lower SNR than the main carrier resonances. This problem is mitigated by a combination of (i) Fitting lorentzians to the resonances rather than simply reading off the frequency of the peak value, and (ii) Scanning over multiple FSRs to reduce the statistical uncertainty in the positions of those resonances.

The range of frequency offsets over which the arm length can be scanned is limited by practical factors such as (i) Limited actuation range on moving the position of the mirror, (ii) Low frequency drift of the error point of the ALS system, and (iii) Angle–to-length coupling of the actuator, which leads to the suspended optic's alignment being disturbed when a large DC length offset is applied, due to imbalances in the coil-magnet actuators used.

## 2.7 ALS at H1 and L1

Both the LIGO observatories (H1 and L1) employ a system similar to that described in this chapter, to aid in the lock acquisition process. The specific implementations (the frequency stabilization system used to lock the AUX laser frequency to the arm cavity length, for example) at H1 and L1 differ from that at C1. Nevertheless, in this section, I briefly consider if the experience with the ALS system at C1 can inform improvements at H1 and L1. The original implementation of the ALS system at H1 and L1 was hindered by erroneous dielectric coating of the ETM, as detailed in Table 4.1 of [25]. The offending ETMs were replaced at both sites in 2019, dramatically improving the performance [26]. At the time of writing, the RMS length noise of a single Fabry-Pérot arm cavity under ALS control (measured at H1, see [26]) is 40 pm in the 10 mHz—1 kHz frequency band, c.f. the CARM linewidth of $\approx$ 6 pm. Therefore, the IR PDH signal is expected to stray outside its linear regime when the CARM DoF is controlled using the ALS system, making a direct transition of CARM from ALS control to IR PDH control (as is done at C1) difficult to implement. Instead, the lock acquisition sequence at H1/L1 consists of an intermediate step where CARM is controlled using the DC transmission signals (at 1064 nm) from the arm cavities, see Sec. 3.3.1 of [27]. Close to the cavity resonance, the DC transmission signals are less noisy than the ALS system, and allow CARM fluctuations to be suppressed to a level such that the PDH error signal remains in its linear regime for long enough that control can be handed over to it.

A reasonable question to ask is: how challenging is it to improve the ALS noise at H1 and L1, and will such improvements yield benefits that justify the effort put

into such an exercise? Let us first consider the case for improving the noise such that a direct handoff of CARM control from ALS error signals to IR PDH error signals can be implemented. A detailed noise budget of the ALS system at the sites is not presented here. However, the measurement presented in [26], suggests that the overall RMS noise must be improved by a factor of $\approx 5$, particularly at low frequencies $f < 100\,\mathrm{Hz}$ (as is done at C1, the noise contribution from higher frequencies can be low-pass filtered so as to not get re-injected as cavity length noise under closed loop feedback). At these frequencies, past noise budgeting efforts (Chapter 6 of [25] for example) suggest that the dominant noise contributions come from (i) unsuppressed, seismically driven, cavity length and angular noise, (ii) phase noise due to acoustic noise disturbing the positions of various optics used to route beams outside the vacuum envelope, and (iii) phase noise on the transmitted green beam from the arm cavity used to generate a beat signal, due to motion of suspended mirrors used to extract this beam from the vacuum system. After confirming that these are indeed the limiting noise sources, mitigation strategies for each can be developed. While some improvement may be possible with relatively little hardware interference (such as better feedback loop frequency response design), eliminating other noise coupling mechanisms may require considerable re-working of various parts of the ALS system. So, we must determine if a direct handoff of CARM control from ALS signals to IR PDH signals will significantly speed up the aLIGO lock acquisition process? There is large variability in the time taken to lock H1 and L1, but a representative sequence is shown in Fig. 2.10. The dashed lines indicate the time spent in transferring CARM control from ALS error signals to IR PDH signals, via the intermediary step of using DC transmission signals from the arm cavities. This particular step in the process takes $\approx 1$ minute. It is difficult to make a direct comparison between Fig. 2.10 and Fig. 3.12, because the former includes multiple steps related to angular control of and thermal transients in the H1 and L1 interferometers that do not have to be dealt with at C1. Nevertheless, considering that the CARM transition step at H1 accounts for $< 5\%$ of the total time spent in the lock acquisition process, it is difficult to justify the ALS noise performance limiting the duty cycle of the observatories. Furthermore, an analysis of over 1000 individual times when the L1 interferometer "lost lock" (i.e. fell out of the operating state where all the optical cavities have their lengths controlled to satisfy appropriate resonance conditions) suggests that the CARM transition step accounted for $< 0.1\%$ of the total lock losses.

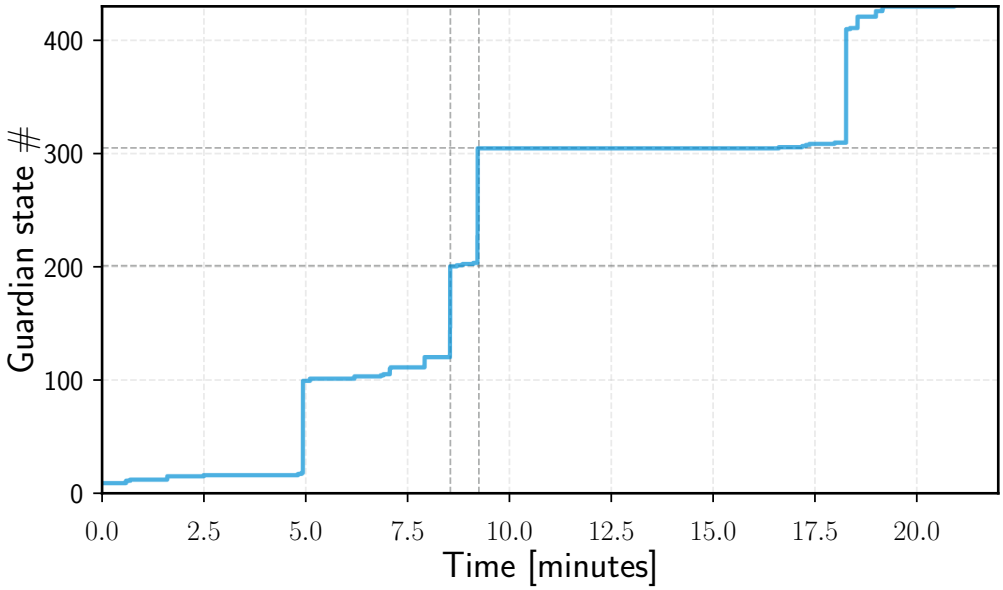


Figure 2.10: Lock acquisition sequence at the H1 interferometer. The vertical axis indexes different states of the interferometer during the lock acquisition process with an integer - the exact mapping is unimportant, but the dashed vertical and horizontal lines indicate the time spent in transferring control of the CARM DoF from ALS error signals to IR PDH error signals.

## 2.8 Conclusions and future work

This chapter described the current implementation of the ALS system at the C1 interferometer. The primary purpose of this system is to aid the lock acquisition process, described in greater detail in Chapter 3. The work described in the preceding sections greatly improved the noise performance of this system relative to previous generations, and eased the process of lock acquisition. Section 2.5 analyzes the noise performance of the system in detail, and lays out some possible improvements that can be made in the near term to further improve it. The GW interferometer community is looking at using the ALS system as a tool for precise calibration of the DARM DoF when the interferometer is locked, and C1 will serve as a testbed for such a scheme. This, and other metrology using multiple laser wavelengths resonating in the interferometer's optical cavities, will demand an improved ALS system, for which this work can serve as a starting point.

*Chapter 3*

# LOCK ACQUISITION AND NOISE PERFORMANCE

The suspended mirrors composing the multiple coupled optical cavities of the interferometer, when uncontrolled, are driven by seismic and thermal fluctuations. Consequently, their positions relative to each other are changing by up to several wavelengths (depending on the effectiveness of seismic isolation and seismic environment, for example). In order for the interferometer to be used as a precision measurement device, the cavity lengths have to be matched to the laser wavelength. The process of bringing the initially uncontrolled mirrors to a state where the resonance conditions for the optical cavities is satisfied is known as *lock acquisition*.

The procedure followed at the 40m prototype is largely similar to that adopted at the LIGO sites, where lock acquisition is largely regarded as a solved problem. However, the seismic environment on the Caltech campus and the less sophisticated seismic isolation systems at the 40m throw up a different set of challenges that have to be overcome. The work presented in this thesis has made repeatable and reliable lock acquisition possible. Without this important step, it would be impossible to characterize and mitigate various noise couplings, eventually reaching sufficient sensitivity to probe the quantum-mechanical nature of the interferometer.

While all the cavities of the interferometer need to have their lengths controlled to maintain the appropriate resonance condition for maximum sensitivity, locking simpler configurations are useful in developing mitigation strategies for certain noise sources. In this chapter, I describe a few such configurations.

## 3.1 Fabry-Pérot arm cavities

*In this configuration, the lengths of the individual arm cavities are controlled to be resonant for the PSL frequency, which is itself locked to the length of the Input Mode Cleaner cavity.*

### 3.1.1 Length control

This is the simplest interferometric configuration that involves an optical cavity (c.f. locking a simple Michelson interferometer which doesn't involve any cavities). It is also the first step in locking more complex interferometer configurations like a

PRFPMI (Section 3.4) - the cavity alignment is optimized using the dither alignment technique [28]. The PRM and SRM are misaligned such that they don't form optical cavities that interact with the rest of the interferometer. Since the beam still has to pass through these optics, the power incident on the beamsplitter and exiting the AS port of the interferometer are attenuated by the PRM and SRM transmissivities of 5.637% and 9.903% respectively[1].

The optical gains for PDH sensing of the arm cavity lengths are consequently reduced - however, the SNR is still sufficient to be able to suppress the residual relative length fluctuations between the PSL frequency and arm cavity's resonant frequency to well below the cavity linewidth of $\approx 9\,\mathrm{kHz}$. At the 40m, individual photodiodes are available that monitor the reflected light from each arm cavity - these are called POX11 and POY11[2] for the X- and Y-arms respectively. Other sensors can also be used for locking each arm cavity - for example, if only one cavity is to be controlled, a photodiode at the AS port can serve as the PDH sensor once the other arm cavity is completely misaligned (to avoid contamination by signal from the unwanted arm cavity) - this is the scheme used for the measurement described in Section 3.1.4. There is negligible contamination ($< -60\,\mathrm{dB}$) due to Y-arm cavity motion in the POX sensor (and similarly for X-arm cavity motion in the POY sensor), such that a single arm cavity, or both at the same time, can be locked relatively easily. A feedback loop with $\approx 100\,\mathrm{Hz}$ bandwidth is closed by filtering the PDH error signals from the POX / POY photodiode by a digital servo filter, and then actuating on the position of the suspended cavity optics (the choice is made to only actuate on the ETM for each arm cavity). The PDH error signal is only linear within the cavity linewidth, whereas the cavity length can be driven by seismic disturbances over multiple FSRs. To ensure that the feedback loop only actuates on the ETM position when the PDH error signal is in the linear regime, and hence a valid readback of the cavity length, *triggering* logic is employed. The transmitted power through the arm

[1] One could imagine a scheme where there would be some remote actuation capability that allows us to move optics in and out of the beam path from outside the vacuum envelope, without having to vent the system to atmospheric pressure. However, such a system would be extremely complex, and the reproducibility of optical configuration to the levels necessary for precision interferometry is questionable. The suspensions are also clamped down to the optical tables for the best vibration isolation - any remote actuation system would also need to have this capability.

[2] It is worth explaining the naming convention of the PDH error signals, since they come up frequently in this chapter. The general notation is the catenation of the port at which the photodiode is located, the demodulation frequency (in MHz), and signal quadrature, in that order. For example, REFL11 I refers to the quadrature signal in phase with the *electrical* LO signal used for demodulation, derived from a photodiode at the REFL port of the interferometer, demodulating the photocurrent at 11 MHz. The *DC signal* from the same photodiode would be called REFLDC.

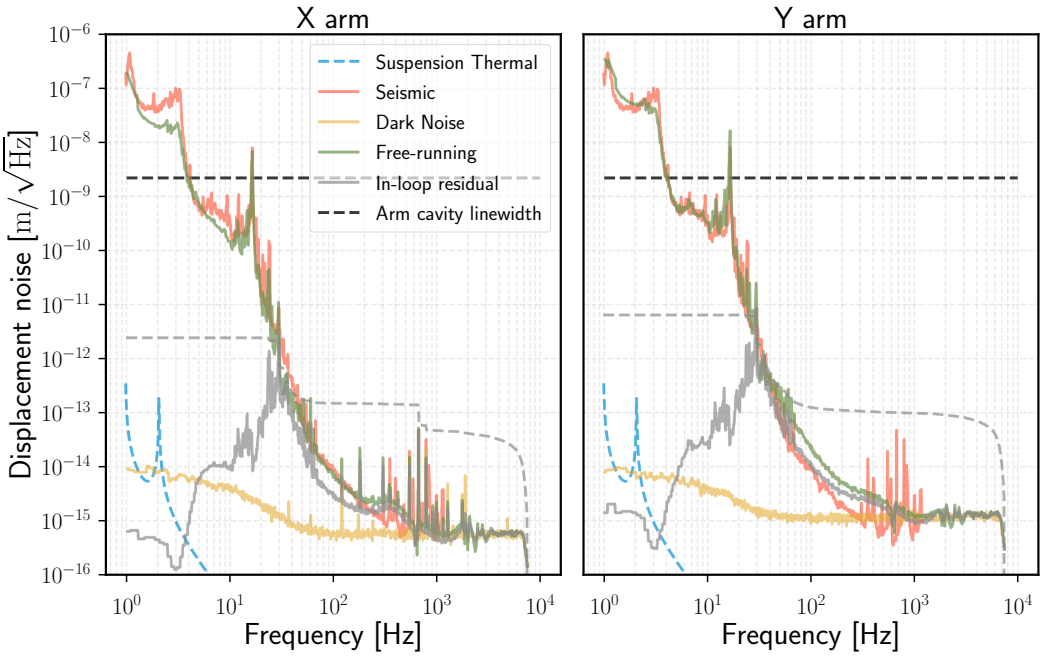


Figure 3.1: Noise budget of the 40m arm cavity when locked to the PSL frequency. Only a few noise sources are budgeted and this is not meant to be a comprehensive noise budget. The "Seismic" noise is only an estimate, which is why it appears to exceed the measured noise at certain frequencies. The residual relative length fluctuation between the arm cavity's resonant frequency and the PSL frequency under closed loop feedback is suppressed to $\approx 0.1\%$ of the cavity linewidth.

cavity is monitored. When this exceeds some threshold value (empirically chosen to be 30% of the value when the arm cavity is on resonance and well aligned), we have high confidence that the PDH error signal is in the linear regime since the intracavity buildup is large. Additionally, normalizing the PDH error signal in reflection by the transmitted power has the effect of broadening the linear regime (see, for example, Figure 8.1 of [6]). For typical seismic velocities at the 40m, the cavity spends $\approx 500\,\mu$s in the linear regime, during which time sufficient force can be applied on the ETM to bring it under control. The linewidth of the arm cavity is large enough that the arm cavities can be locked within a few seconds even during the daytime, when the seismic activity levels (particularly in the anthropogenic band of $1 - 10\,$Hz) on the campus are elevated by a factor of a few in RMS compared to their levels after 10 PM local time.

The free-running displacement noise, and in-loop residual, are summarized in Figure 3.1.

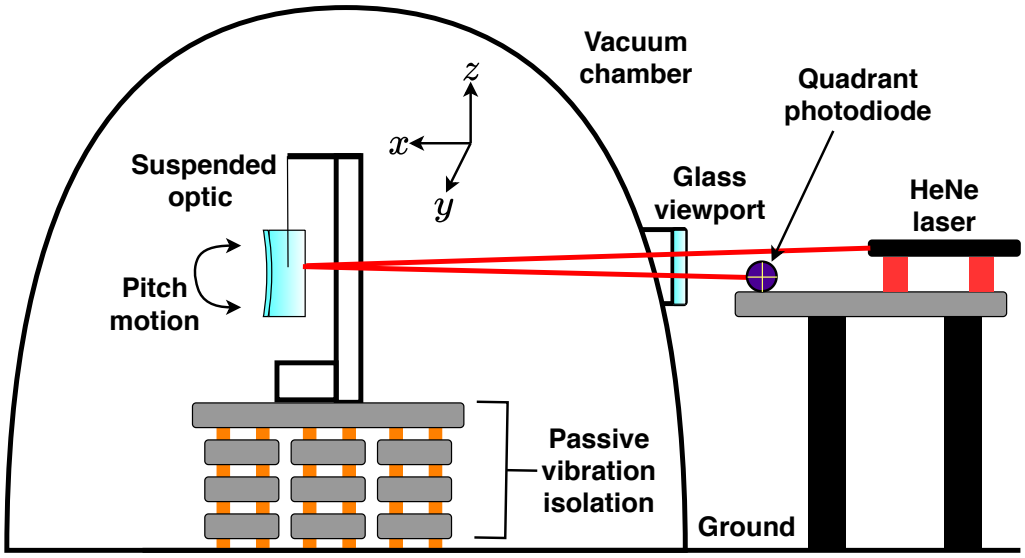


Figure 3.2: Conceptual diagram (not to scale) of an optical lever. Two angular degrees of freedom are controlled using the Oplev, namely "Pitch" (rotation about the $y-$axis) and "Yaw" (rotation about the $z-$axis). A segmented photodiode (split into 4 quadrants) is used to read out the position of the beam reflected from the suspended optic, which carries information about the angular motion of the optic.

### 3.1.2 Angular control

Fluctuations in the *angular* positions of the suspended optics, driven by ambient seismic motion, impede the ability to maintain stable power buildup with the PSL resonant in the arm cavity. Therefore, a feedback loop needs to be implemented to stabilize the angular positions of the ITMs and ETMs as well. Several candidate sensors are available, and indeed, there are multiple feedback loops in operation that stabilize angular motion of the optic. Around the Pitch and Yaw eigenmode frequencies of $\approx 0.6 - 0.8$ Hz, OSEMs installed on the suspension cage damp the angular motion of the optic to $\approx 2\,\mu\text{rad}/\sqrt{\text{Hz}}$. The OSEM signals, however, do not allow sensing angular motion in the $1 - 5$ Hz band, which contributes nearly half of the total RMS angular motion in the 40m seismic environment, because of the sensor noise levels. Optical levers (Oplevs) provide the next layer of angular stabilization, at least in the lock acquisition process, until lower noise alternatives like wavefront-sensing (WFS) become feasible. The concept of operation is illustrated in Figure 3.2.

One advantage of the system is that it doens't require any optical cavities to be locked - the angular position of a suspended optic is simply sensed by tracking the motion of the beam spot from a beam that is injected into the vacuum enclosure

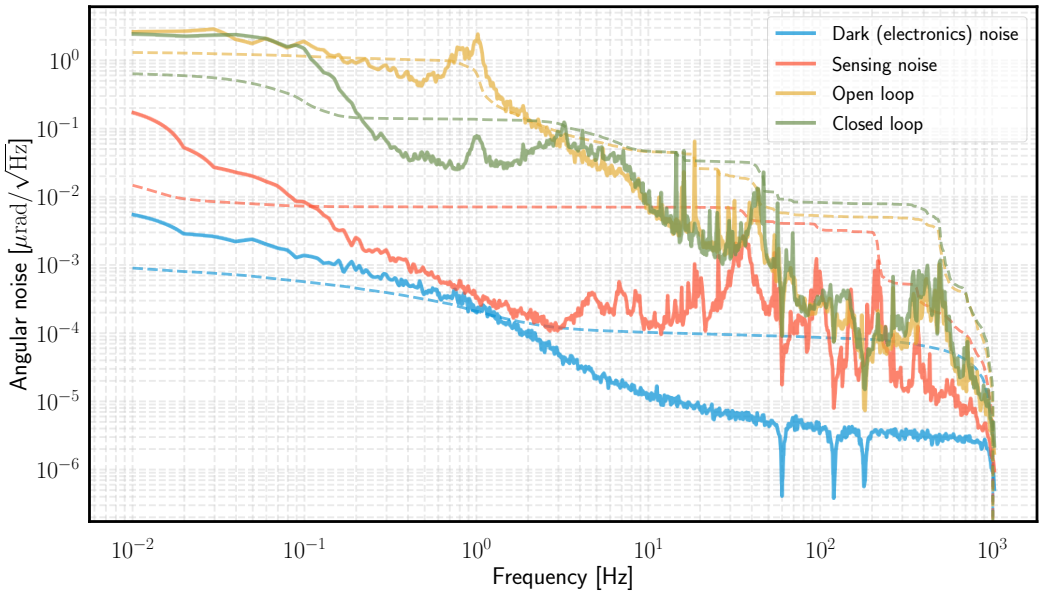


Figure 3.3: Optical lever performance and noise budget. The loop is designed to suppress noise between $\approx 0.1 - 4$ Hz, as for frequencies much outside of this range, the Oplev system is deemed to not sense the angular motion of the optic w.r.t. an inertial coordinate system with sufficient SNR.

and reflected off a suspended optic, imaged on a segmented photodiode (since the photodiodes used have 4 segments, they are also referred to as QPDs.). The lever arm is $\approx 2 - 3$ m, mapping 1 $\mu$rad of angular displacement to $\approx 2 - 3\mu$m of spot motion on the QPD, which is easily sensed with the appropriate transimpedance amplifier. A rough noise budget for an optical lever loop is presented in Figure 3.3. The "sensing noise" is difficult to estimate for the Oplev system - we have to measure the apparent motion measured at the Oplev loop's error point of a hypothetical optic that is fixed relative to the inertial coordinate system. Instead, the sensing noise level in Figure 3.3 was estimated by directly pointing the HeNe beam at the QPD on a stable optical bench, and converting the power fluctuations reported in this configuration to equivalent test mass angular motion. The various sharp features in the spectra above $\approx 30$ Hz are hypothesized to come from some combination of pointing jitter due to mechanical resonances of mounts used for components like the HeNe and steering mirrors in the Oplev beam path. While these are outside the bandwidth of the Oplev feedback loop, the high-frequency content of the *control* signal for this loop must be sufficiently low-pass filtered to 1. avoid impressing this apparent motion onto the optic, and 2. not un-necessarily consume the finite DAC actuation range of the digital control system.

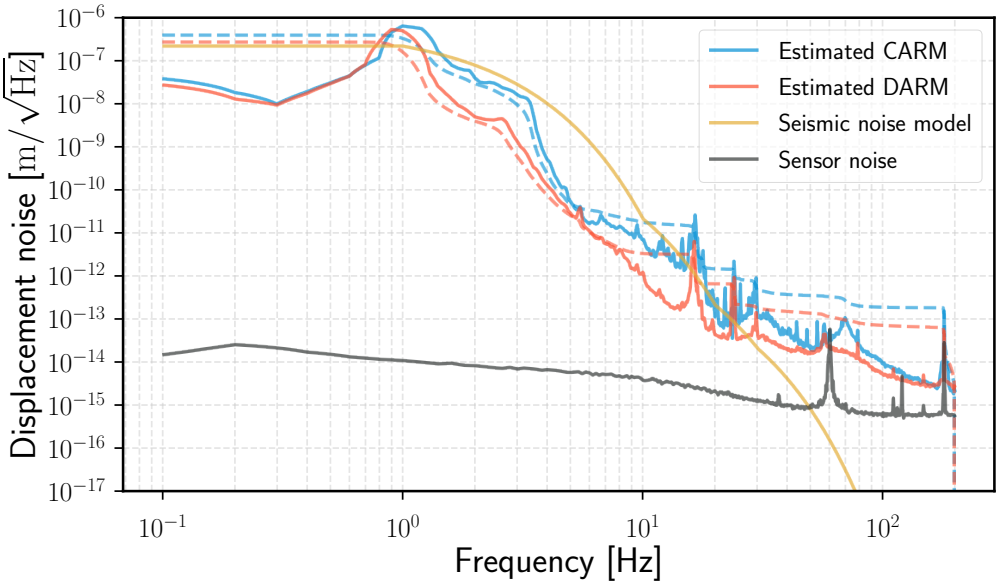


Figure 3.4: Estimation of free-running CARM and DARM noise. Such a measurement is reflective of the seismic environment at the 40m. The IMC cavity has less effective seismic isolation compared to the arm cavities, particularly in the $1-3$ Hz band. Hence, the dominant contribution to CARM in that band is laser frequency noise, since the PSL frequency is locked to the IMC length. Dashed lines indicate the RMS contribution of the like-colored trace. For the range of frequencies shown in the measurement, the measured signal was above the sensing noise (electronics noise of the PDH sensing chain) level. Also overlaid is a model of the seismic noise - the agreement with the measurement is qualitatively reasonable, with deviations below 30 Hz attributable to errors in the assumed transfer functions of the seismic isolation stacks and changing levels of seismic activity at different times. Above 50 Hz, the sensing noise of this technique does not allow reliable measurement of the seismic motion.

### 3.1.3 Estimating CARM and DARM

By definition, the DoFs CARM and DARM are *defined* as $\frac{L_X+L_Y}{2}$ and $L_X - L_Y$ where $L_{X,Y}$ is the length of the respective arm cavity. These have to be matched to the PSL frequency for resonance. We can therefore get an estimate of the *free-running* CARM and DARM noise levels from when the two arm cavities are locked (without needing other DoFs like PRCL locked). Such a measurement is important in designing the feedback loops that must stabilize these DoFs to well within the linewidths of the PDH error signals in more complex configurations like the PRFPMI. A measurement is shown in Figure 3.4.

Each Fabry-Pérot arm cavity length was locked to the PSL frequency. The modelled frequency response of this locking loop, validated against a measurement, was used

to convert the *in-loop* error signal spectra to free-running (i.e. open-loop) estimates. Frequency-dependent Wiener filtering [29] was then used to estimate CARM as the coherent motion of the two arms, while DARM was the incoherent contribution.

The main motivation behind this measurement was to decide whether we would benefit from installing some *passive* vibration isolation device[3] in addition to the existing isolation stacks. On the basis of Figure 3.4, it was determined that there would be negligible benefit at low frequencies, as the pneumatic style isolators being considered have a resonant frequency in the $3 - 5\,\mathrm{Hz}$ range, below which the isolation is negligible (with motion even being amplified at and around the resonant frequency). The dominant contribution to the RMS free-running CARM and DARM motion, however, is below 5 Hz. Nevertheless, installation of additional passive vibration isolation would improve the *in-loop* DARM RMS above $\approx 100\,\mathrm{Hz}$. Non-pneumatic isolators (such a solid rubber blocks like those used in the existing passive vibration isolation stacks at C1), with a resonant frequency of $\approx 20 - 30\,\mathrm{Hz}$, may prove sufficient.

### 3.1.4 Estimating Schnupp asymmetry

The single-arm configuration offers an interferometric probe of the Schnupp asymmetry , defined as $l_{\mathrm{schnupp}} = l_X - l_Y$, with $l_{X,Y}$ being the optical path lengths between the beamsplitter and ITMX / ITMY respectively. The ability to robustly sense PDH error signals for more complex interferometer configurations depends on setting this length accurately. At the 40m, $l_{\mathrm{schnupp}} \approx 3.5\,\mathrm{cm}$[4], while the distance between the BS and the ITMs are $O(2\,\mathrm{m})$. It is difficult to verify $l_{\mathrm{schnupp}}$ by measuring the distance in the vacuum envelope. The arm cavities, however, offer a convenient, in-situ probe of $l_{\mathrm{schnupp}}$. Due to the additional propagation through $2l_{\mathrm{schnupp}}$ (the factor of 2 is to account for the round-trip between BS and cavity) for one of the arm cavities, there will be a phase difference between the reflected RF sideband fields arriving at a photodiode at the AS port. By measuring this phase difference, which is expected to be $\Delta\Phi = 360^\circ \frac{2l_{\mathrm{schnupp}}}{c/f_2} \approx 4.6^\circ$, with $f_2 \approx 55\,\mathrm{MHz}$ being the modulation frequency for PM imprinted on the input beam, $l_{\mathrm{schnupp}}$ can be inferred.

The phase of the field arriving at the AS port photodiode (which also serves as the PDH sensor for this experiment) can be measured because the photocurrent is *electronically* demodulated, after which the demodulated quadrature signals are

[3] The candidate being considered was the SLM series mount from Barry Controls [30].

[4] The target Schnupp asymmetry in the SR configuration proposed for measuring Ponderomotive Squeezing at the 40m is $\approx 2.3\,\mathrm{cm}$.

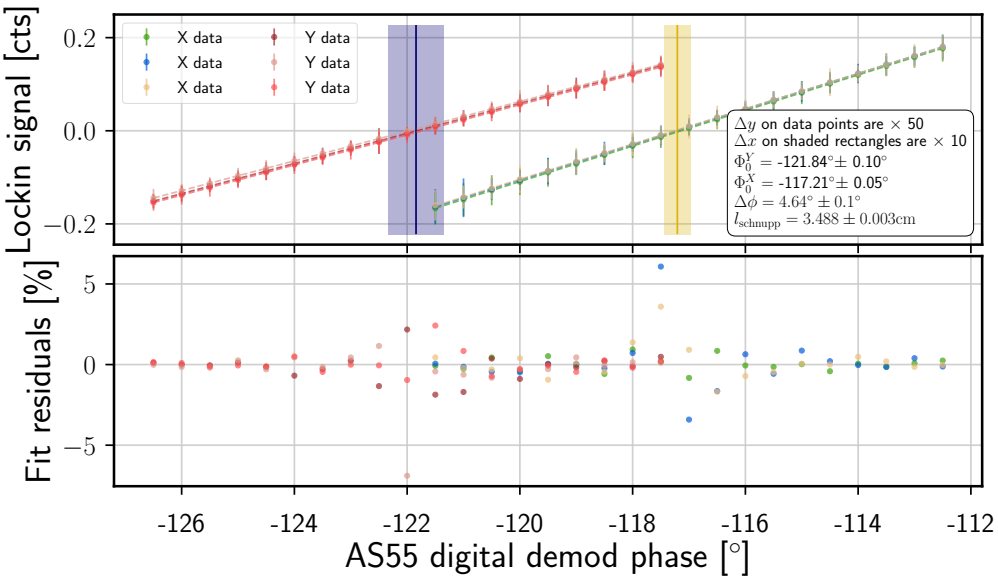


Figure 3.5: Measurement of Schnupp asymmetry. For each arm cavity, the "digital demodulation phase" was swept through a range of values. For each arm cavity, the phase of the reflected field was measured a few times, so as to be able to estimate a statistical uncertainty on the measurement. Subtle systematic effects, like possible *differential* detuning between the arm cavities, are not included but are expected to be small.

digitized. The phase of the LO field for this electronic demodulation step is assumed to be constant. Therefore, if the phase of the optical field is shifted, the projection onto the demodulated quadratures will also change. This change is easily measured in the digital data acquisition system. The arm cavity length is driven at a single frequency, $\approx 300$ Hz (chosen to be outside the bandwidth of the PDH loop that locks the arm cavity length to the PSL frequency). Then, a "digital demodulation phase" is used to track the appearance of this $\approx 300$ Hz signal in the digitized, demodulated quadratures. Such a measurement is shown in Figure 3.5.

## 3.2 Power-Recycled Michelson Interferometer (PRMI)

This configuration corresponds to the ETMX, ETMY and SRM optics being misaligned. This is a useful configuration to fine tune the alignment of the suspended PRM optic in preparation for locking more complex interferometer configurations.

### 3.2.1 Length sensing and control

The standard PDH locking technique is used. With the ETMs misaligned, either the carrier or sideband fields can be made to be resonant in the PRC (but not both at the same time, which is what is required in more complex configurations like the

PRFPMI). For a resonant carrier, the DC signal from the POP photodiode, which is a proxy for the intracavity power buildup, is used to trigger the PDH loops only in their linear regimes. Photocurrent from the POP photodiode demodulated at $2f_1$ serves the same purpose for the resonant sideband configuration, since both the $\pm f_1$ sideband powers will build up in the PRC, generating a signal at $2f_1$. Since the modulation depths are $< 0.2$, the power circulating in the PRC when the carrier is resonant is much greater than when the sidebands are resonant, making that configuration more useful for optimizing cavity alignment (since the signals used by the dither alignment system will be stronger). The POP QPD signals for training feedforward filters as described in Section 3.2.2 also have higher SNR in the resonant carrier configuration. The resonant sideband configuration on the other hand is useful for determining the correct settings for locking more complex configurations like the PRFPMI - the PDH error signals derived from photocurrent demodulated at $3f_{1,2}$ are largely insensitive to the state of the arm cavities, and therefore, the settings that allow easy lock acquisition with the ETMs misaligned are also, at the very least, a good starting point for acquiring lock with the arm cavities present but offset from resonance as described in Section 3.4.

Photocurrent demodulated at either $f_{1,2}$ or $3f_{1,2}$ at the REFL, POP or AS port of the interferometer are candidate PDH error signals. In practice, the following quadratures of error signals were used to control {PRCL, MICH} respectively: {REFL11 I, AS55 Q} for resonant carrier, {REFL55 I,REFL55 Q} for resonant sideband and $1f_{1,2}$ PDH error signals, and {REFL165 I, REFL165Q} for resonant sidebands and $3f_{1,2}$ PDH error signals. These combinations do not represent an exhaustive list of the possible combinations - they are simply what numerical simulations suggested would be feasible and empirically found to work well.

### 3.2.2 Angular sensing and control

One of the main challenges in locking more complex interferometer configurations at the 40m was that the angular stability of the folding mirrors PR2 and PR3 was a factor of a few worse than the other suspended optics. These optics (and the corresponding optics SR2 and SR3 in the SRC) are suspended using a different flavor of suspensions, called TTs [31] compared to the rest of the optics, which are called SOSs[32]. The shorter pendulum length meant the resonant frequency was higher, and was close to one of the resonant modes of the passive isolation stacks on which all the in vacuum optics are mounted. This coincidence is responsible for the broad hump between $2-4$ Hz seen in many noise spectra in this thesis.

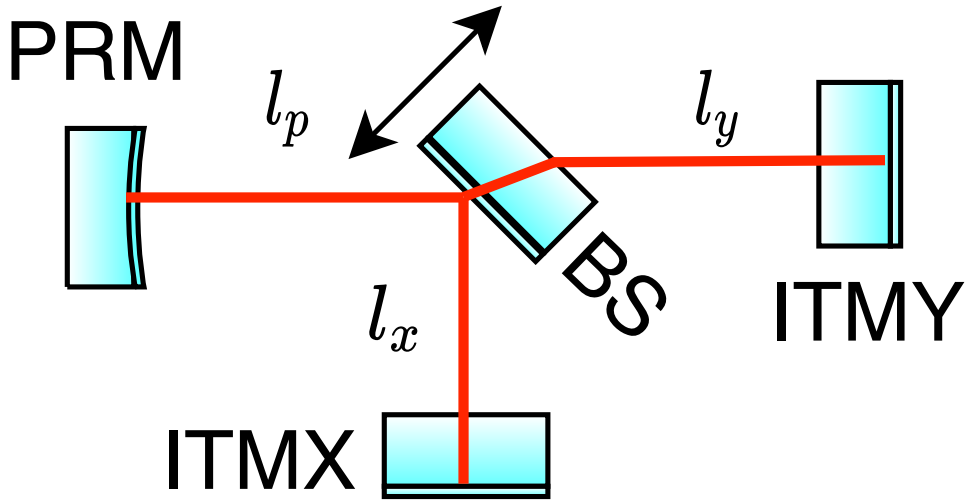


Figure 3.6: Geometric MICH to PRCL coupling from beamsplitter motion. PRCL is defined as $l_p + \frac{l_x+l_y}{2}$, while MICH is defined as $l_y - l_x$, where all distances are between the HR surfaces of the optic. Since the angle of incidence is $45^{circ}$, +1 unit of displacement of the BS along its normal (as indicated by the arrow) changes $l_p$, $l_x$ by $-\sqrt{2}$ units and $l_y$ by $+\sqrt{2}$ units, resulting in an overall change to PRCL by $-\frac{\sqrt{2}}{2}$ units. Therefore, to change *only* MICH and not PRCL by moving the beamsplitter, the PRM also has to be moved to compensate for this effect.

Furthermore, the TTs are not actively damped - the only damping implemented is passive eddy-current feedback, with the damping force being provided by eddy currents generated when magnets attached to the optics changes the flux through copper-wound coils. The net result was that the success rate in locking the PRMI was very low, with only the PRM, BS and ITMs being actively damped.

A solution to this problem was to implement an angular *feedforward* loop to stabilize the angular orientation of the cavity axis. The technique used is an extension of that described in [33]. When the PRMI locked, the POP QPD signals, monitoring the position of the beam transmitted through the PR2 optic, are a proxy for the angular motion of the cavity axis. Simultaneously, signals from a 3-axis seismometer located near the vertex of the interferometer are recorded. It is then possible to find the optimal filter that predicts cavity axis motion from the seismometer signals (effectively, this filter is the transfer function between ground motion and PRC angular motion).

It was found that the $x-$ and $y-$axes signals of the seismometer had highest coherence with the POP QPD signals, while the $z-$axis signal had negligible coherence, and

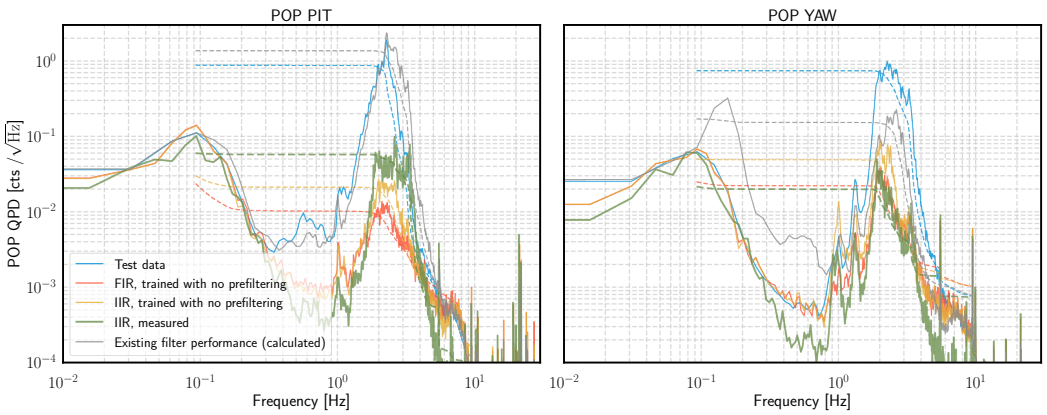


Figure 3.7: Angular stabilization of the PRC with feedforward engaged. The distinction between FIR and IIR filters is made because during the training phase, the filters are calculated in the FIR representation, while implementing them in the realtime digital control system that is responsible for controlling the interferometer requires them to be in the IIR representation (for computational efficiency). Note that the data shown in this plot was not used in the training process. There is some performance trade off in going from the FIR to IIR representation (red vs yellow curve), and a further reduction in the subtraction when the feedforward is implemented in realtime as opposed to offline (green vs yellow), but even so, the RMS angular fluctuations are reduced by a factor of 10. The grey trace is an old filter from $\approx 4$ years ago - it is included to show that the filters do need to be re-trained from time to time.

therefore, was dropped. A MISO feedback topology, with these two signals as inputs and the PRM optic as output, was constructed. The actuation is done on PRM (even though PR2 and PR3 anuglar motion is what we are trying to mitigate) since the PRM is the only optic in the PRC that can be actuated, PR2 and PR3 are not controllable from outside the vacuum envelope. To "train" the filter, a 20-minute segment of data from a locked PRC was used, and a separate 20-minute segment was used to validate the data *offline* before testing the filter out on the live system. The results are shown in Figure 3.7 - both the POP QPD signals and the power buildup (Figure 3.8) in the cavity are stabilized in the $1 - 3$ Hz band when the feedforward filters are engaged. The filter was designed to have negligible gain at frequencies $< 1$ Hz and $> 10$ Hz, to avoid impressing sensing noise from the seismometer onto the optic. This increased both the ease of lock acquisition of the PRMI, as well as the duty cycle of the lock once it was acquired.

A big advantage with the feed*forward* approach, compared to the alternative strategy of closing a feed*back* using the POP QPD signals, is that the former does not require the PRMI to be locked to be effective - therefore, the feedforward approach can

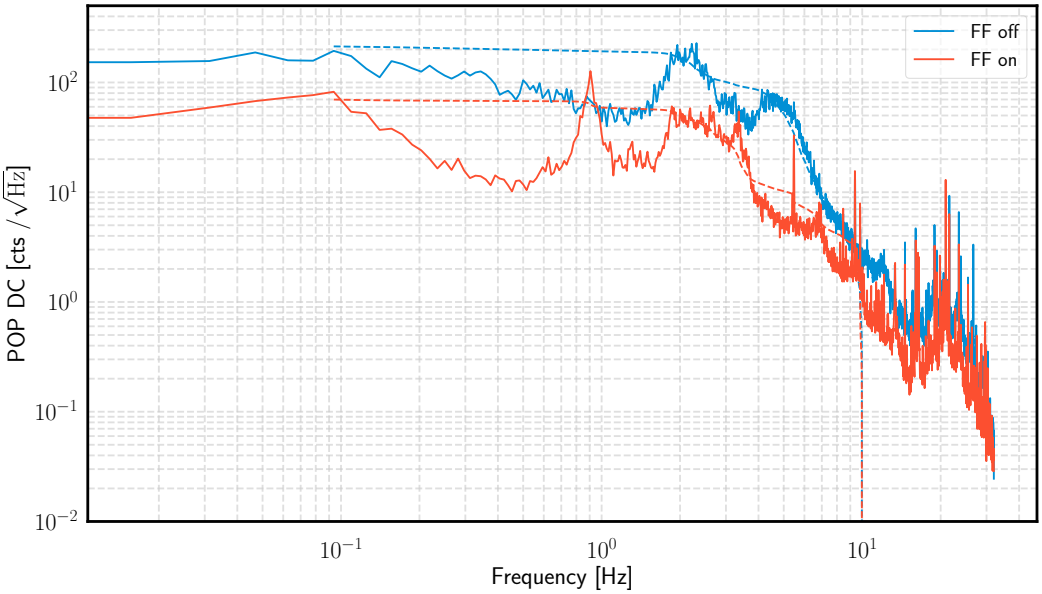


Figure 3.8: Stabilization of the PRC power buildup with feedforward engaged. This signal was never used in the training process, and this observation increases confidence that the angular stability of the cavity is in fact improved.

help in the lock acquisiton process. When the arm cavities are also brought into resonance for the PRFPMI / DRFPMI configurations, the field content in the PRC also changes, such that the POP QPD signals witness angular motion of the *arm cavities* much more strongly than the PRC - any feedback loop using the POP QPD signals would therefore need to be carefully designed to take this effect into account. No such care is needed for the feedforward filters. The feedforward filters, once trained, do not need to be updated very often - empirically, it was determined that over a year long timescale, the performance of the filters in stabilizing the angular motion of the PRC did not degrade.

The planned upgrade of the 40m for the BHD and Ponderomotive Squeezing measurement experiments will eliminate the TTs, and replace them with SOSs. While this is expected to improve the seismic isolation of the optics, if the seismometer signals still show high coherence with a diagnostic signal of the arm cavity motion (e.g. POP QPD), then it will be advantageous to keep the feedforward loop in place.

## 3.3 Dual-Recycled Michelson Interferometer (DRMI)

Going up the complexity ladder, there are 3 length DoFs that need to be controlled to lock the DRMI. Like the PRMI, the ETMs are misaligned, but the SRM is aligned so that the SRC exists. An important difference between the PRMI and DRMI is

that the latter can only be locked with the sidebands resonant in the PRC (assuming the Michelson is still tuned to null the carrier field at the AS port). SRC length sensing using the PDH scheme requires the $f_2$ sideband field to reach the SRM - but if the PRC is made resonant for the carrier (with no Fabry-Pérot arm cavities present), then the sideband field power reaching the SRC is strongly attenuated by the PRC which has a finesse of $\approx 70$[5]. The small leakage field ($\approx 1\%$ of what is incident on the PRM) that does make it to the SRC makes low noise length sensing prohibitively difficult[6]. The DRMI configuration was used to study various noise coupling mechanisms before attempting the PRFPMI/DRFPMI configurations.

### 3.3.1 Michelson noise budget

In the DRMI, the MICH DoF is the analog to DARM, since it is the DoF that is sensitive to differential motion of the Michelson arms. This was the DoF that was studied and budgeted in most detail. For PDH locking of the 3 length DoFs, the sensors and quadratures used are: REFL11 I for PRCL, REFL55 I for SRCL and AS55 Q for MICH. The noise budget is shown in Figure 3.9.

As is the convention, the noise budget is plotted in terms of the *free-running* displacement noise of the degree of freedom. Many quantities are measured while the DRMI is locked - the suppression of the feedback loop, whose frequency response is modelled and validated with a measurement, is undone to convert the in-loop quantities to what they would be open-loop. This noise budget contains several terms that generalize easily to a noise budget for the DARM DoF, which is the ultimate goal of interferometer characterization. Therefore, it is worth it to briefly review what they represent:

1. **Shot noise** - the Poissonian statistics of light arriving at the AS55 photodiode causes power fluctuations, which is indistinguishable from that caused by Michelson motion. This curve corresponds to the shot noise of the DC light level incident on the AS55 photodiode while the DRMI is locked ($\approx 700\mu$W), converted to displacement noise units with the measured optical gain of $4.3 \times 10^5$ W/m. A correction factor is applied for this noise being cyclostationary (see Equation 2.17 of [34]).

[5] The PRC finesse will increase to $\approx 90$ once the excess intracavity loss due to flipped folding mirrors PR2 and PR3 is mitigated

[6] The possibility of locking the DRMI with the carrier resonant in the PRC is not ruled out, but since the DRMI could be repeatedly and reliably locked in the resonant sideband configuration, I did not spend much time trying to implement this configuration.

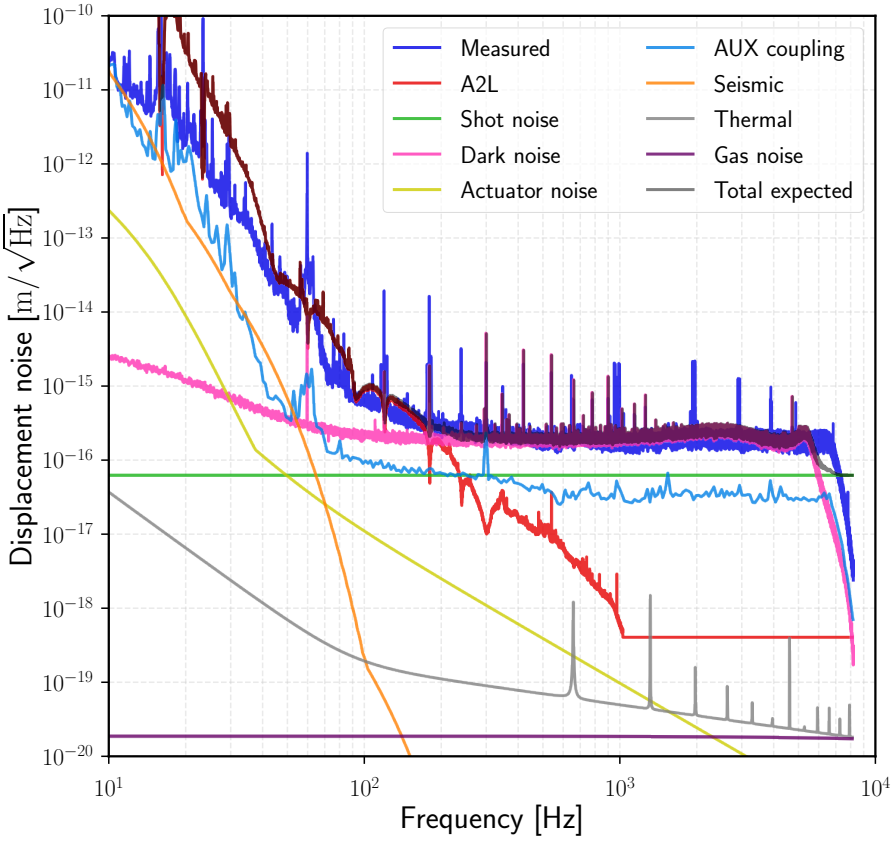


Figure 3.9: Noise budget for the Michelson DoF in the DRMI configuration. The measured quantities are "fuzzy" lines, while those calculated using analytic formulae are smooth solid lines. See text for more explanation on the terms in the legend.

2. **Dark noise** - this represents the contribution of the electronics noise of the various components involved in converting power fluctuations on the AS55 photodiode to an error signal (in counts) in the CDS system. It is the quadrature sum of the photodiode dark current, transimpedance amplifier noise, and digitization electronics noise. It is measured simply by configuring the control system as if the DRMI were locked, but blocking the light incident on the AS55 photodiode. The optical gain of the PDH signal is used to scale this noise to equivalent displacement noise units.

3. **Actuator noise** - also referred to as "coil driver noise". this represents the noise imprinted on the suspended optics by virtue of our installing some mechanism to control their position. Since the optics are suspended as simple pendulums, above the pendulums' resonant frequency, the optics behave like a free mass, weighing 250 g. In the absence of any mechanism to apply a force on the suspended optics, the only forces acting on it would be ambient

electromagnetic and gravitational fields. To facilitate controlling the lengths of optical cavities, permanent magnets[7] are glued onto the optic and coils of copper wire are placed with the solenoid axis lined up with the magnet to allow a force to be applied on the optic by modifying the current through the coil. At the very minimum, the Johnson noise associated with the current driver always flows through the coils, perturbing the position of the optic. At lower frequencies, the noise associated with the DAC that converts the digital control signal from the CDS system to a voltage input to the current driver[8] is the dominant contribution to current noise in the coils. The gold curve corresponds to the quadrature sum of these effects from the four face-mounted actuators on the optic. More detailed models for the DAC noise and coil driver noise, as well as mitigation strategies, can be found in [36–38].

4. **AUX coupling** - in general, fluctuations in all interferometer length DoFs produce an optical response at all ports of the interferometer, making any feedback system used to control these systems inherently MIMO. We approximately diagonalize and approximate it as a SISO system by choosing those sensors where a DoF produces the largest response to derive an error signal for feedback control. Nevertheless, some residual amount of cross-coupling usually remains, due to asymmetries or geometric effects like that described in Figure 3.6. While it is possible to estimate these couplings analytically, it is prohibitively difficult to build a model of the MIMO interferometer that captures all the inherent imperfections. Therefore, the contamination to MICH due to the PRCL and SRCL feedback loops is usually estimated empirically. The procedure involves driving the error point of the PRCL / SRCL loops with broadband white noise (I chose to do this outside the control bandwidth of the MICH loop so as to avoid accounting for the loop suppression), and looking for the coherent contribution at the MICH error point. The cross-coupling from PRCL to MICH is then given by

$$\left|H_{\mathrm{cpl}}^{\mathrm{AUX}}\right| \equiv \sqrt{\frac{\mathrm{MICH}_{\mathrm{exc}}^2 - \mathrm{MICH}_{\mathrm{quiet}}^2}{\mathrm{PRCL}_{\mathrm{exc}}^2 - \mathrm{PRCL}_{\mathrm{quiet}}^2}}, \tag{3.1}$$

[7] Ni-plated SmCo magnets conforming to specifications determined by the LIGO engineering group [35] are used. Each optic, which is roughly cylindrical with a diameter of 3" and thickness of 1", has four magnets arranged on its AR-coated face around its circumference, and two additional ones on the barrels, to allow actuation on various DoFs.

[8] The voltage-to-current conversion is done by a resistor. Each DRMI optic, i.e. the PRM, BS, ITMX and ITMY, used $R = 400\,\Omega$ for each coil, causing a minimum noise current of $\approx 6\,\mathrm{pA}/\sqrt{\mathrm{Hz}}$. At frequencies $\lesssim 100\,\mathrm{Hz}$, other noises exceed this lower bound.

where $\mathrm{MICH}_{\mathrm{exc,quiet}}$ represent the *amplitude* spectral densities of the MICH error point with and without an excitation injected at the PRCL error point respectively, and similarly for PRCL. The form of the SRCL $\rightarrow$ MICH coupling is identical, with SRCL substituting PRCL in Equation (3.1). This technique of measuring noise couplings is very useful for measuring other noise couplings as well, such as laser intensity noise $\rightarrow$ MICH (although it was not done for the DRMI). Knowing $\left|H_{\mathrm{cpl}}^{\mathrm{AUX}}\right|$, the contribution of this coupling to the measured MICH noise is estimated as $\left|H_{\mathrm{cpl}}^{\mathrm{AUX}}\right| \mathrm{PRCL}_{\mathrm{quiet}}$ for example. The curve plotted is the quadrature sum of the cross-coupling from SRCL and PRCL. It is possible to mitigate such cross couplings to an extent by employing a feedforward technique - rather than the coherent power technique described, the *complex-valued* quantity $H_{\mathrm{cpl}}^{\mathrm{AUX}}$ can be measured using a swept-sine measurement. Then, the AUX cross coupling can be nulled by summing the quantity $-H_{\mathrm{cpl}}^{\mathrm{AUX}} \times \mathrm{AUX}_{\mathrm{quiet}}$ to the MICH error point (with appropriate bandpass filtering to ensure that the cancellation is only done at frequencies where this coupling is dominant). Such a feedforward loop was not implemented for the DRMI, though it will be required to achieve low noise in the PRFPMI / DRFPMI configurations, where the MICH $\rightarrow$ DARM cross coupling is significant at low frequencies.

5. **Angle-to-length coupling (A2L)** - if the beam spot position on an optic does not coincide with the center of actuation for Pitch and Yaw motion (which in general it will not), then perturbing the angle of an optic will also change the length of the cavity that is sensed by this beam (this is a purely geometric effect, see Figure 3.10). Even with a perfectly centered beam, if the four actuators on the optic are not perfectly balanced (which in general they are not), there will be some cross coupling between length and angle actuation. As with the AUX coupling term, it is possible to measure the beam spot position and actuator imbalance, and then calculate the A2L coupling. Practically, the same broadband noise injection technique used to estimate $\left|H_{\mathrm{cpl}}^{\mathrm{AUX}}\right|$ can be used. In the DRMI lock, the only relevant angular stabilization loop are the Oplev loops on the BS, PRM and SRM optics (each optic has 2 active loops, one each for Pitch and Yaw motion). The curve plotted is the quadrature sum of the coupling from these 6 loops. The fact that this trace exceeds the total measured noise at low frequencies suggests that the contributions may be correlated to some extent at low frequencies (or the coupling is frequency

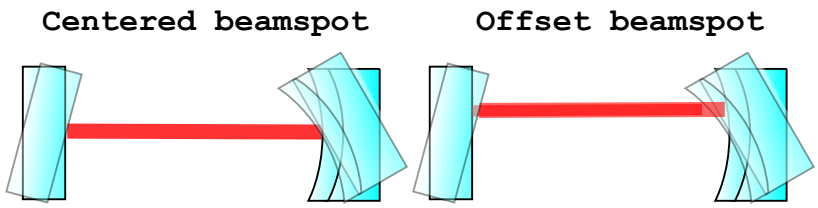


Figure 3.10: Angle-to-length coupling due to an off-centered beam. The apparent length of the cavity sensed by the beam changes with the angular position of one or both optics if the center of rotation does not coincide with the beam axis. The effect is greatly exaggerated for illustration here.

dependent and not flat as assumed), but this was just meant to be an estimate, and so the issue was not pursued further.

6. **Seismic** - this trace is an estimate of how much the suspended optics are moving due to ambient seismic motion, filtered by the passive isolation stacks and pendulum transfer function. The plotted curve is the quadrature sum of the motion of 3 SOS type optics (BS, ITMX, ITMY). The transfer functions of the passive seismic isolation stacks used at the 40m are well characterized [39], but this noise budget uses a coarse model, hence the discontinuous appearance of the curve.

7. **Thermal** - this curve is the quadrature sum of two contributions - suspension thermal noise and coating thermal noise. Coating thermal noise has three contributions, known as thermoelastic, thermorefractive, and Brownian. The first two come about as a result of thermal dissipation in the dielectric layers that compose the HR coatings on the ITMs [40]. These two effects act coherently, and therefore, with appropriate design of the dielectric coating structure, can cancel each other to a large extent. Brownian noise is due to mechanical dissipation in the dielectric layers [41]. This is typically the dominant contribution to coating thermal noise in the LIGO interferometers. Suspension thermal noise arises due to Brownian fluctuations in the suspension wire on which the optic hangs. In Figure 3.9, the standard formulation given in the cited references are used to calculate these noises for the 40m parameters. For the MICH DoF in the DRMI configuration, all of these noises are at least a factor of 1000 below the measured noise - they are included by matter of convention, and are calculated. For the PRFPMI and DRFPMI, the increased optical gain of DARM relative to MICH will start to make these "fundamental" noise terms more important.

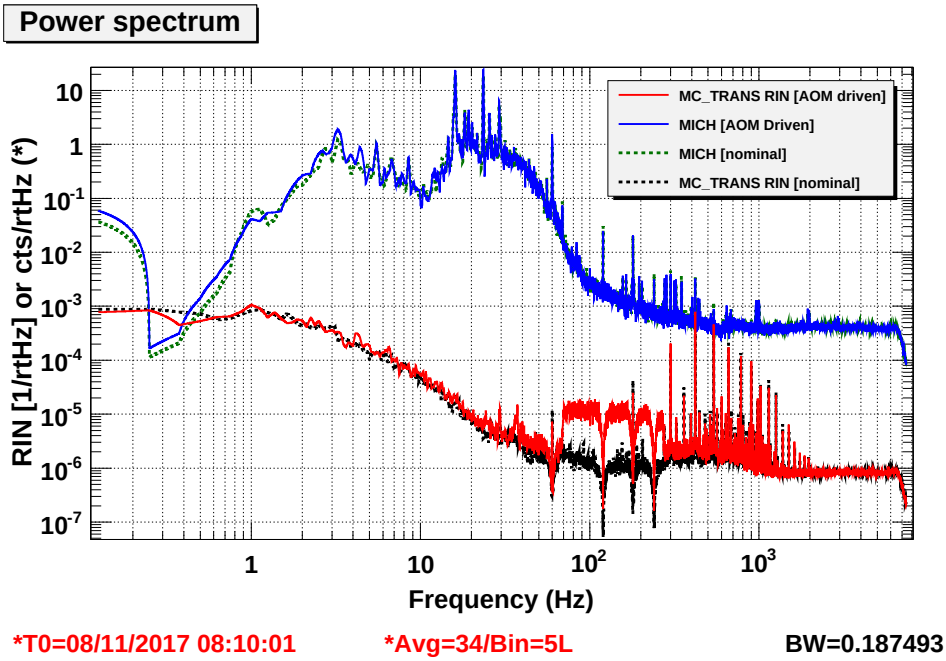


Figure 3.11: Measurement of laser intensity noise coupling to MICH in the DRMI configuration. "MC_TRANS RIN" is a measure of RIN in the beam injected into the interferometer - when the broadband noise injection is turned on, the RIN increases by a factor of 10 at the excited frequencies. There is no measurable effect at the MICH error point. The units of the MICH error signal are in arbitrary units of cts/$\sqrt{\text{Hz}}$, which does not affect the conclusion.

8. **Gas noise** - this term is expected to be completely negligible at the 40m, and like thermal noise, is included in the DRMI noise budget because it is easily generated by calculation. The noise mechanism being accounted for is random phase fluctuations being caused in the path traversed by the laser inside the vacuum envelope, due to residual gas molecules. A simplified model is assumed with only $H_2$, $N_2$ and $H_2O$ molecules contributing phase noise. The partial pressures used to generate the plotted curve are, $P_{H_2} = 10^{-8}$ torr, $P_{N_2} = 3 \times 10^{-7}$ torr and $P_{H_2O} = 5 \times 10^{-7}$ torr, and the calculation is based on [42].

The listed noise sources are by no means a complete set of noises. Notable omissions are laser frequency and intensity noise. An attempt was made to measure the intensity noise coupling, by driving an AOM in the input beam path to the interferometer with broadband noise. However, there was no measurable coherent

coupling to the MICH error point, even when the broadband noise increased the relative intensity noise (RIN) to the interferometer by a factor of 10 above the ambient level, see Figure 3.11. The measured noise appears to be explainable by the A2L, AUX coupling, dark noise, and seismic contributions. The first three are easier to address than improving the seismic isolation. The cross coupling can be reduced by appropriate actuator balancing and filter design (if the Oplev control signal is more aggressively low-pass filtered above its upper UGF of $\approx 5$ Hz, then the contribution will be reduced). As for the dark noise, the transimpedance electronics for the AS55 photodiode were designed to handle the $\approx 100\times$ higher light levels incident on the photodiode when the DRFPMI configuration is locked. Moreover, the DARM optical gain is $\approx 300\times$ greater than the MICH optical gain, and the effective input power to the interferometer in the PRFPMI / DRFPMI configurations is increased by power-recycling. So, the expectation was that the dark noise would be less limiting in those configurations, and the decision to modify the electronics was deferred for later, after determining if it was really required.

Armed with the experience of working with the DRMI, it was decided to tackle the PRFPMI configuration for the next steps in noise budgeting and coming up with mitigation strategies.

## 3.4 Power-Recycled Fabry-Pérot Michelson Interferometer (PRFPMI)

This configuration is simpler to lock and control, (because there is one less length DoF, SRCL, and fewer angular DoFs as well) compared to the DRFPMI configuration. While the measurement of Ponderomotive Squeezing calls for the DRFPMI configuration, the simpler PRFPMI allows many of the important noise sources to be characterized and mitigated before attempting a low noise measurement. Note that the SRM remained installed in its nominal position in the vacuum system - therefore, the field at the AS port of the interferometer was attenuated to the transmissivity of the SRM, $\approx 10\%$. However, by misaligning the SRM in angle, it was ensured that no *optical cavity* (i.e. SRC) was formed, thereby realizing the PRFPMI configuration even with the SRM optic in the beam path. This way, lock acquisition and noise mitigation studies could be undertaken without repeatedly venting the vacuum system to change the optical topology of the interferometer.

### 3.4.1 Control topology

Table 3.1 summarizes the error signals and actuators used for sensing and controlling various *length* DoFs in the PRFPMI.

| DoF | Error signal | Actuator | Remarks |
|---|---|---|---|
| PRCL ($3f$) | REFL165[9] I | PRM | For acquisition. |
| MICH ($3f$) | REFL165 Q | BS + $\alpha$ PRM | For acquisition. |
| CARM (ALS) | $\frac{1}{2}$(ALSX + ALSY) | IMC length (MC2) | For acquisition. |
| DARM (ALS) | (ALSX - ALSY) | ETMX - ETMY | For acquisition. |
| CARM (RF) | REFL11 I | IMC length (MC2) and IMC error point | Low noise operation. |
| DARM (RF) | AS55 Q | ETMX-ETMY | Low noise operation. |
| PRCL ($1f$) | REFL11 I | PRM | Low noise operation (not implemented yet). |
| MICH ($1f$) | REFL55 Q | BS + $\alpha$ PRM | Low noise operation (not implemented yet). |

Table 3.1: Summary of error signals used to sense and control length fluctuations in the PRFPMI DoFs. This particular mapping between DoF and sensor was determined through a combination of simulations to see which photodiodes are able to sense which DoFs with the best SNR, and then experimental verification. For locking acquisition, sensors demodulating the photocurrent at 3 times the modulation frequency are used, due to their insensitivity to other DoFs, as described in [43] - the "penalty" is that the optical gain is smaller by $\approx 100\times$ for modulation depths of $\approx 0.2$, but is still sufficiently large for robust locking. "ALSX" ("ALSY") refers to the frequency of the beat between the PSL and the AUX laser for the X (Y) arm, derived as described in Chapter 2. Note that each RFPD has two demodulated quadratures - in some cases, this allows different signals to be sensed using the same physical photodiode, if the DoF being sensed manifests a response in the cosine (I) quadrature or the sine (Q) quadrature, as in Equation (C.2). For the Michelson actuation, an empirically determined fraction $\alpha$ of the control signal is fed to the PRM to cancel the geometric coupling between MICH and PRCL that arises from changing the BS position, see Figure 3.6.

### 3.4.2 Lock acquisition sequence

The process by which the PRFPMI is locked is best understood by looking at some important signals indicating the resonance conditions of various optical cavities. One such sequence is shown in Figure 3.12. The important steps in the sequence, marked in the upper left plot (with the same time in the sequence indicated by dashed vertical lines in all of the other plots) are described below.

- (A) The procedure begins with the PRM misaligned. Each arm cavity length is locked to the PSL frequency, as described in Section 3.1. At the same time, the green AUX laser beams for each cavity have their frequencies locked to the arm cavity length such that they are resonant. This is to prepare for transitioning control of the arm cavity lengths from the POX and POY PDH signals to the ALS system.

- (B) The transition to ALS control has been realized. The arm cavities are once again resonant for the PSL field, but the length is now controlled using ALS error signals rather than the IR PDH signals from the POX and POY photodiodes. Right after, in preparation for locking the PRMI, the CARM DoF is offset from the point where the PSL resonates in the arm cavities by 4 nm.

- (C) The misaligned PRM is slowly re-aligned. It is not shown in this sequence, but as described in Section 3.2, before commencing the lock acquisition sequence, the PRMI is locked and the cavity alignment optimized. The optimal alignment of the PRM, thus set, can be recovered once the arm cavity lengths are under ALS control. Photodiodes with a demodulation frequency that is $3 \times f_{1,2}$ (REFL165 for this sequence, although it is also possible to use REFL33 signals) is used to lock the PRMI, where $f_{1,2}$ are the PM frequencies used to modulate the input beam to the interferometer.

- (D) The PRMI is locked. Between "C" and "D", the Optical Lever servos for the ITMs are also transitioned from their nominal configuration to having DC control authority (see Section 3.1 for more details about the Oplevs). The arm cavities are ready to be brought into resonance.

- (E) The intentional CARM offset applied in "B" is reduced to 0. The error-points of the *ALS paths* for CARM and DARM control (referred to as "CARM_A"

[9] The exact modulation frequencies are $f_1 = 11.066194$ MHz and $f_2 = 5f_1$. Even thoguh $3f_2$ is closer to 166 MHz than 165 MHz, the latter label is used.

and "DARM_A" in Figure 3.12) are adjusted about their nominal zero-points to *maximize* the power buildup in the arm cavities (for which the TRX and TRY signals are proxies). This is to account for any offsets that may have occurred in the intervening minutes from when the arms were resonant for the PSL in "A" (e.g. due to a *slow* drift of the ALS error signals). Between "E" and "F", the arm cavity power experiences large fluctuations between $\approx 10 - 100$, even though the residual CARM fluctuations with the arms under ALS control should be well within the CARM linewidth. A possible hypothesis as to why this is happening is discussed in Section 3.4.5.

F The "CARM_B" and "DARM_B" paths are engaged. These use conventional PDH signals from the REFL11 and AS55 photodiodes, respectively, to control CARM and DARM. So these DoFs are under hybrid control between the ALS paths, and the PDH paths for a short period of time. Between "F" and "G", the ALS path gains are ramped down to 0 (using a 10 second ramp time over which the gain is smoothly adjusted with a sigmoid-like profile).

G The interferometer *length* DoFs are now all under PDH control (also known as RF control, to distinguish from ALS control). In the inset axes in the second row of Figure 3.12, the CARM_A and DARM_A signals are seen to go to 0. The CARM_B signal settles at a non-zero value in this plot as a small digital offset was introduced to transition from ALS to RF control - this is not consequential, and indeed, was removed in subsequent locks.

H Rudimentary ASC is enabled. The ITMs are already running with DC coupled Oplev servos, and for the ETMs, DC QPDs imaging the transmitted beam from the cavity are used to implement a feedback loop. Some improvement in the stability of the power buildup in the arm cavities is seen. Note that in "A", the power measured by the TRX/TRY photodiodes is normalized to 1, so that the *Power Recycling Gain* can easily be estimated when the full PRFPMI is locked. For example, TRX/TRY $\approx 300$ in the full lock suggests a recycling gain of $300 \times T_{\mathrm{PRM}} \approx 17$.

### 3.4.3 CARM loop characterization

For stable buildup of power in the Fabry-Pérot arm cavities of the interferometer, which is essential for realizing the best possible sensitivity, the laser frequency must be matched to the CARM coupled cavity length to within a fraction of the linewidth,

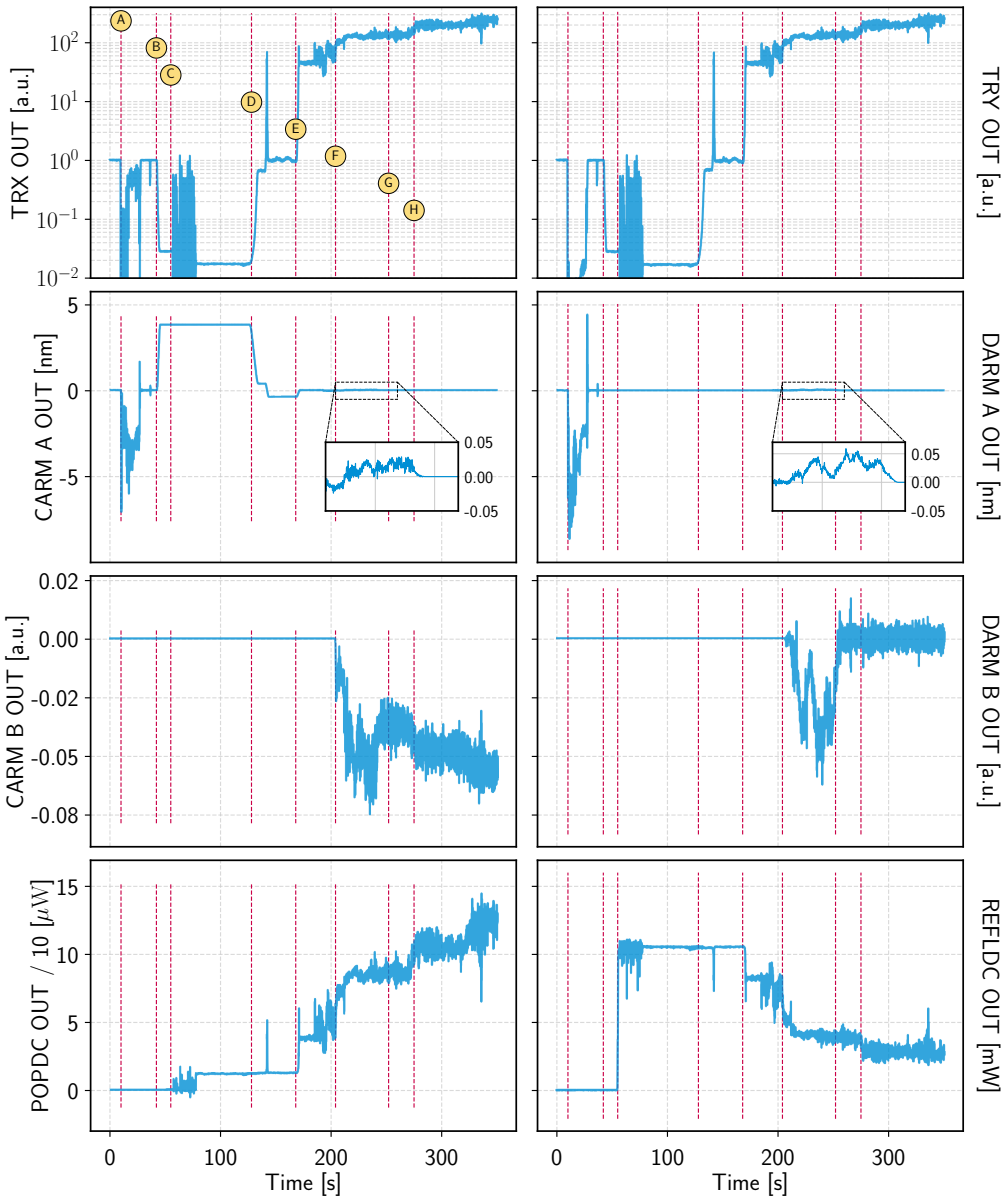


Figure 3.12: A typical PRFPMI lock acquisition sequence. Where available, the y-axes (shared for rows) are indicated in physical units, but are otherwise in arbitrary units (analysis in physical units is deferred to later subsections that discuss individual signals in detail). At the 40m, the entire process takes $\approx$ 5 minutes. While not discussed in this thesis, the DRFPMI configuration can be locked in a similar amount of time. See the text for more discussion about the sequence, and some important ways in which the procedure at the 40m differs from that adopted at the LIGO sites.

which at the time of writing is ≈ 28 pm[10]. The CARM loop (the terms "Common Mode Servo" or "CM servo" are also used) is responsible for suppressing the noise of the free-running NPRO (i.e. the PSL) to a level that meets this requirement.

The CARM loop is actually composed of two nested feedback loops, as shown in Figure 3.13. From this, a models for the OLTF of each path, as well as the overall composite transfer function can be constructed,a s shown in Figure 3.14. The models are then validated against measurements using the techniques described in Appendix B. Such measurements are shown in Figure 3.15(a). At the time of writing, the final state of the CARM servo has a bandwidth of ≈ 12 kHz, with a phase margin of ≈ 60°. This configuration allowed the interferometer to remain locked for stretches several minutes long, so that other characterization tasks could be done - however, the coupling of laser frequency noise to the DARM readout was not directly measured, and so, it may be that the shape of the CARM loop needs to be modified at some point in the future to improve the interferometer noise performance. Figure 3.15(b) shows the another important measurement in characterizing the stability of the CARM loop - the frequency at which the control authority is transferred from the "Slow path" to the "Fast path". At this crossover frequency of ≈ 120 Hz, the relative phase between the two actuation paths is ≈ 40°, which ensures the two loops aren't canceling each other out (which would be the case if the relative phase were 0° per the convention followed in this plot), thereby destabilizing the system.

### 3.4.4 DARM loop characterization

The DARM feedback loop is responsible for suppressing *differential* changes in the lengths of the two arm cavities, due to environmental disturbances, to a level well below the DARM linewidth, which is ≈ 1.2 nm for the 40m in the PRFPMI configuration[11]. If the *residual* (i.e. under closed loop feedback control ) DARM motion were significantly larger than the DARM linewidth, then the PDH error signal response at the AS55 photodiode will no longer remain linear, and hence,

[10] The CARM linewidth is strongly dependent on the losses in the interferometer. The quoted number is assuming an average round-trip arm cavity loss of 50 ppm and ≈ 2% losses in the PRC (on accounted of the flipped folding mirrors, see Appendix D.2). Once new optics are installed in the interferometer vertex to solve the geometric instability problems (see Appendix D.3), the CARM linewidth is expected to decrease to ≈ 15 pm.

[11] In the dual-recycled configuration, the linewidth is ≈ 45 nm in the Resonant Sideband Extraction tuning of the SRC, and ≈ 36 pm in the Signal Recycled tuning of the SRC. For measuring Ponderomotive squeezing, the SRC tuning will be *very close to* Signal Recycled, which will have to be taken into account when designing the DARM control loop for that configuration.

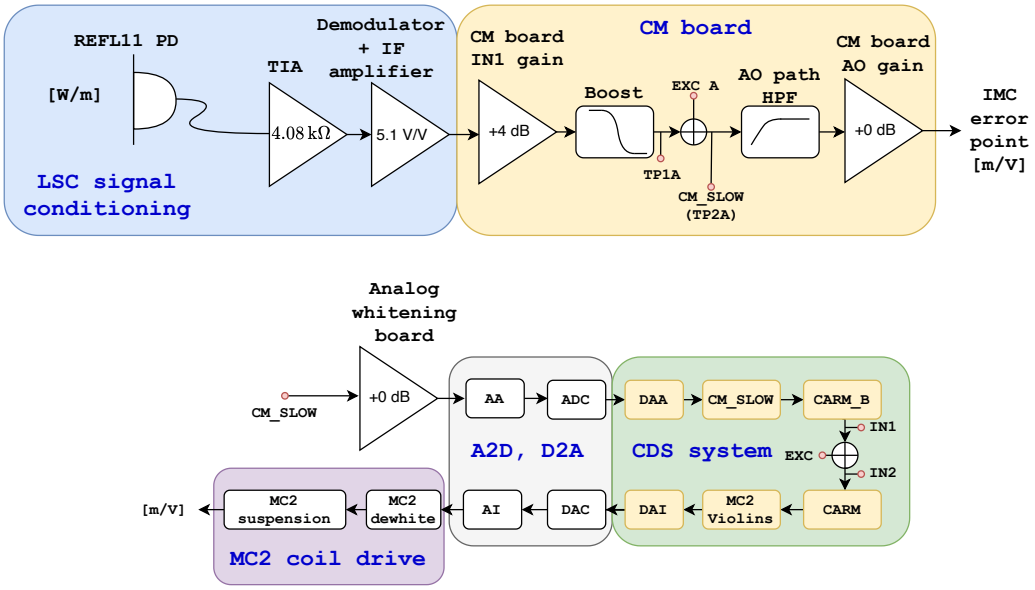


Figure 3.13: Common mode servo topology. The REFL11 photodiode senses fluctuations in CARM. This error signal is then split into two feedback paths. One uses the suspended MC2 mirror as a frequency actuator - it modifies the length of the IMC cavity, and the high bandwidth ($\approx$ 100 kHz UGF) IMC servo then ensures that the PSL frequency is modified to keep the beam resonant in the IMC, and hence, matched to CARM. The bandwidth of this path is $\approx$ 150 Hz, limited by delays in the digital feedback system and the mechanical susceptibility of the suspended MC2 mirror. The second path modifies the error point of the IMC servo, thereby modifying the PSL frequency (with the total RMS frequency actuation being much less than the IMC linewidth of $\approx$ 7.6 kHz). This path allows higher bandwidth control - the transfer function from modifying the IMC servo error point to the laser frequency is flat up to $\approx$ 30 kHz.

the interferometer cannot be kept at its operating point using the linear feedback loops available. This requirement can be satisfied by a purely digital feedback loop - unlike the CARM loop, parallel low and high bandwidth feedback paths are not required. As with all of the interferometer feedback loops, implementing them as digital filters (as opposed to analog electronic filters) means that the frequency response of the servo filter can be easily changed simply by recompiling a piece of C-code (as opposed to having to change various analog electronic components).

As was the case with the CARM loop, the DARM loop was characterized using techniques described in Appendix B.2. The results are summarized in Figure 3.16. The measured DARM loop had a bandwidth of $\approx$ 150 Hz and a phase margin of $\approx 30^\circ$. This loop design allowed the interferometer to remain locked for several tens of minutes at a time, permitting other characterization activities to be carried out,

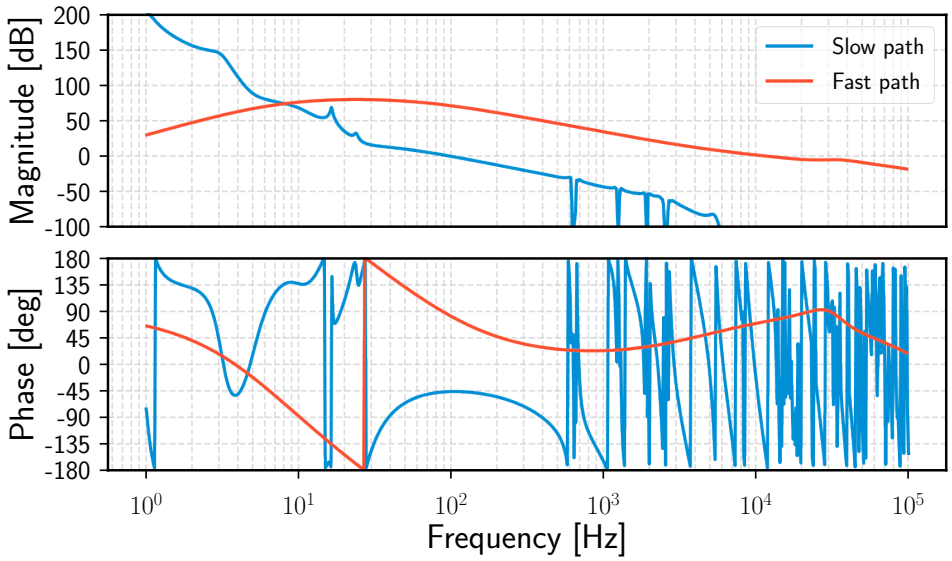


(a)

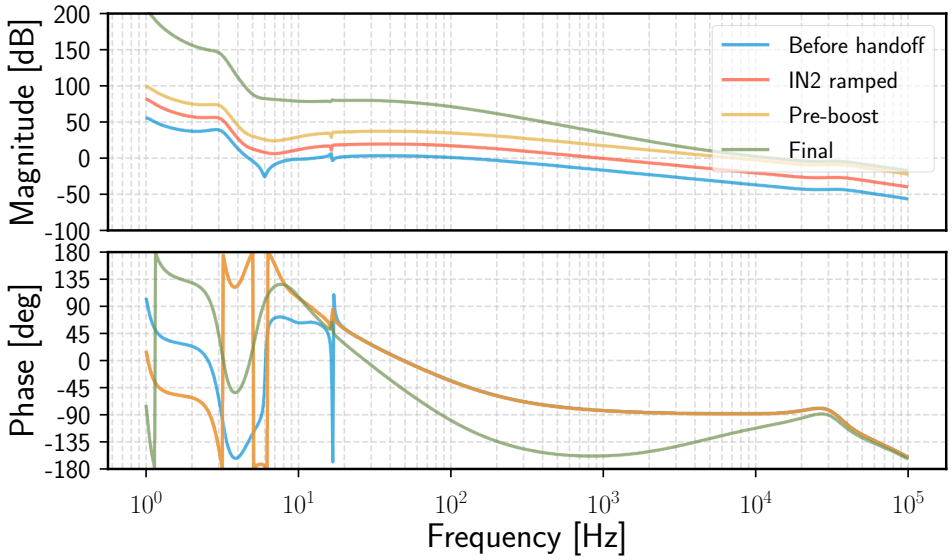


(b)

Figure 3.14: Models of the CARM feedback loop. Figure 3.14(a) shows the transfer functions of the two paths - the "Slow path" involves the digital feedback system and uses the IMC length as a frequency actuator. Due to delays and the mechanical susceptibility of the suspended optic, this loop is limited to a bandwidth of $\approx$ 100 Hz. The "Fast path" actuates on the PSL frequency by modifying the IMC servo's error point - this path allows higher bandwidth, with the overall loop UGF being $\approx$ 12 kHz. In the lock acquisition process, the CARM loop is continually modified, first to facilitate smooth transition between ALS and RF control paths, and finally, to have very large DC gain for effective suppression of laser frequency noise. This evolution is shown in Figure 3.14(b).

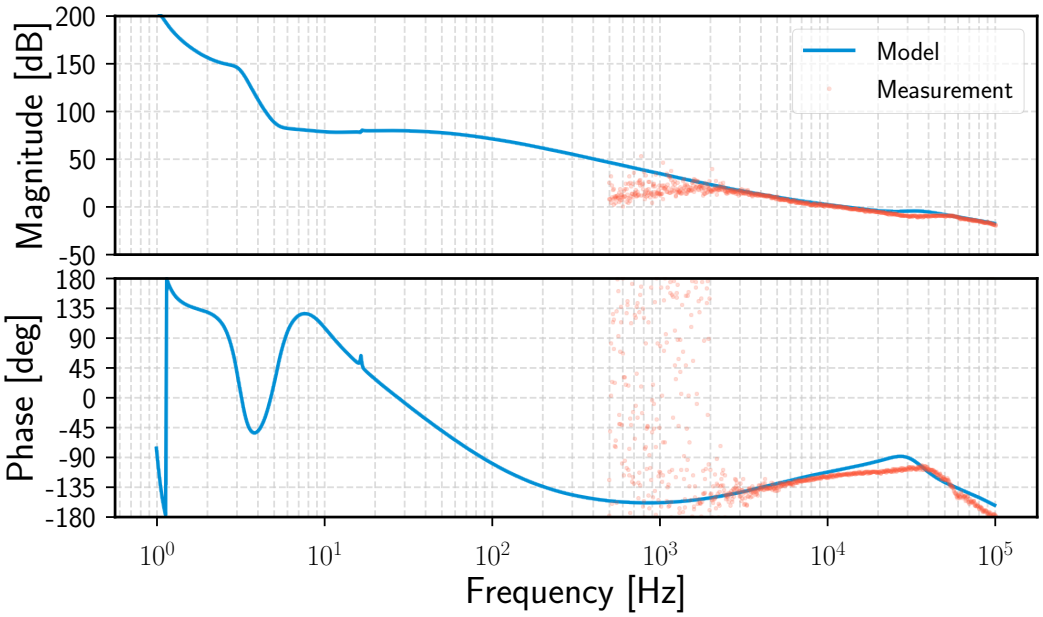


(a)

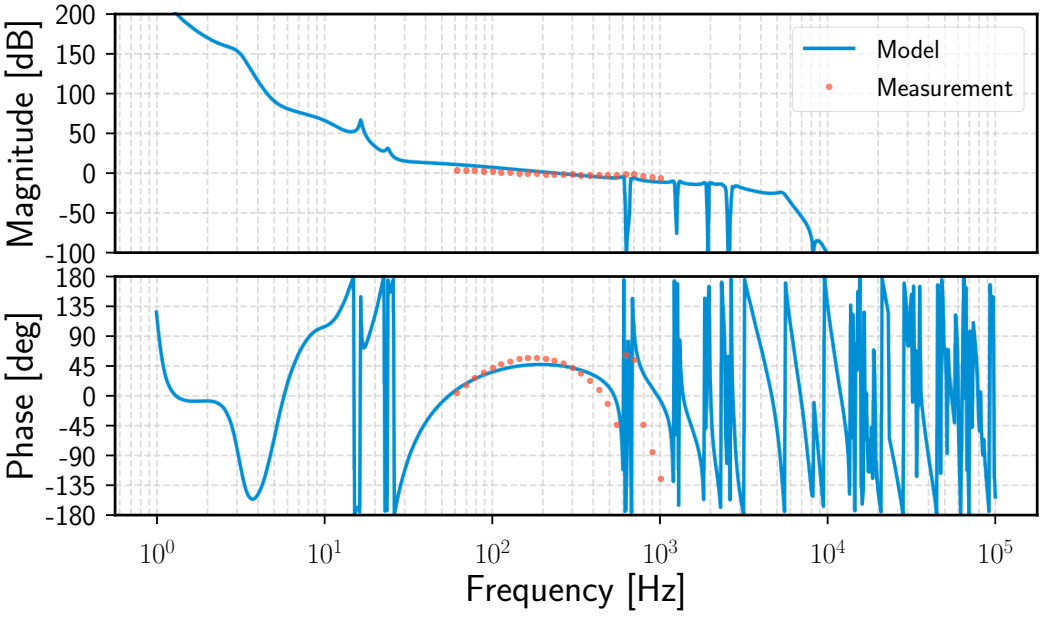


(b)

Figure 3.15: Measurements of the CARM feedback loop. For the overall OLTF shown in Figure 3.15(a), a signal is injected at "EXC A" and the loop OLTF is given by the ratio $\frac{\text{TP1A}}{\text{TP2A}}$. In Figure 3.15(b) a signal is injected at "EXC" in the CDS system and the crossover transfer function is read out as $\frac{\text{IN1}}{\text{IN2}}$ (see Figure 3.13 for the signal injection and readback points). The measurement cannot be done over the full range of modelled frequencies for the reasons described in Appendix B.2. Nevertheless, the overall gain and delay of the model can be fit to the measurement.

but was not optimized to yield the best possible noise performance - to improve the sensitivity to DARM displacement, the frequency response of this loop will likely have to be modified. In Figure 3.16(a), the overall *modelled* gain scaling and time delay in the loop are left as free parameters, which are then fit to match the measured data. The measurement does not extend over the full frequency range plotted for the reasons described in Appendix B.2. Nevertheless, the model and measurement do agree in the region where they overlap, giving confidence in the accuracy of the model.

### 3.4.5 Optomechanics during CARM offset reduction

It was hypothesized that with the improvements to the ALS system at the 40m (described in Chapter 2), the residual length noise in the CARM DoF would be less than the CARM linewidth, allowing the transition of CARM control from ALS signals to RF PDH signals to be easily effected. An interesting feature that was revealed during the PRFPMI lock acquisition studies was that when the CARM offset was brought to 0 in step "E" of Section 3.4.2, the arm powers did *not* remain stable - rather, it appeared that the CARM DoF was "buzzing" in and out of resonance, with the power buildup fluctuating between $\approx 10 - 200\times$ the buildup during POX / POY locking. This range of fluctuation is commensurate with a residual CARM motion of $\gg 1$ CARM linewidth.

Some numerical modeling suggests that the origin of this effect could be optomechanical in nature. With the high power buildup in the arm cavities, the motion of the ITMs and ETMs become coupled due to the radiation pressure force acting on those optics. Consequently, the mechanical susceptibility of the suspended optic gets modified from that of a free mass, which is what it is above the resonant frequency of the pendulum when radiation-pressure effects are neglected. The modified mechanical susceptibilities are shown in Figure 3.17. The key feature in these plots is that near a CARM offset of 0, the *phase* of the transfer function deviates from the simple pendulum response significantly around 100 Hz, which also happens to be the UGF of the digital feedback loop that suppresses CARM motion. That loop is designed assuming that the mechanical plants are simple pendulums, and does not take into account the CARM offset dependent plant variation - so, while the loop is stable with a phase margin of $\approx 30^\circ$ for large values of the CARM offset, it was hypothesized that the modified mechanical susceptibility was causing a transient instability in the CARM feedback loop, but only for small CARM offsets. As the excess CARM motion caused by this instability pushed the CARM offset away from

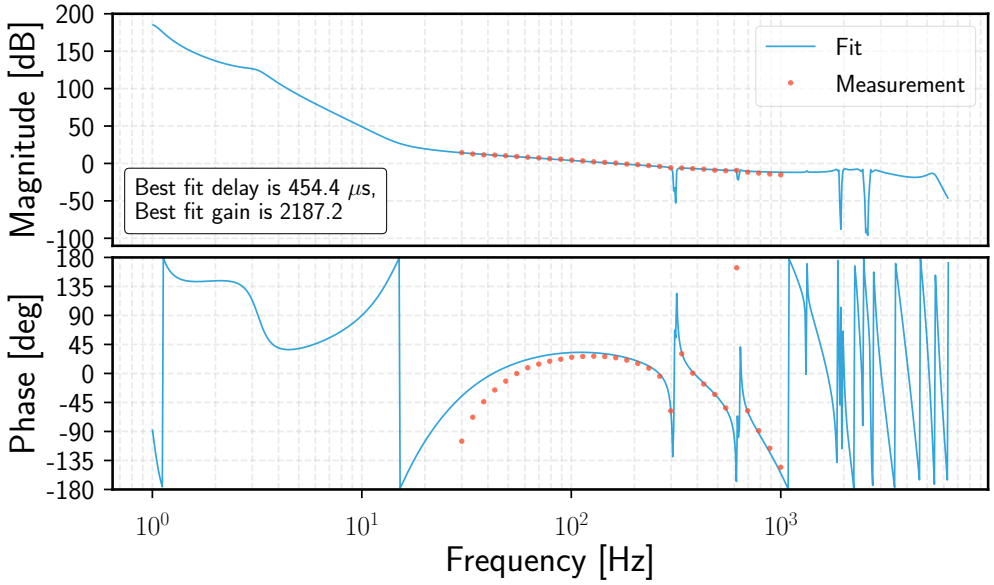


(a)

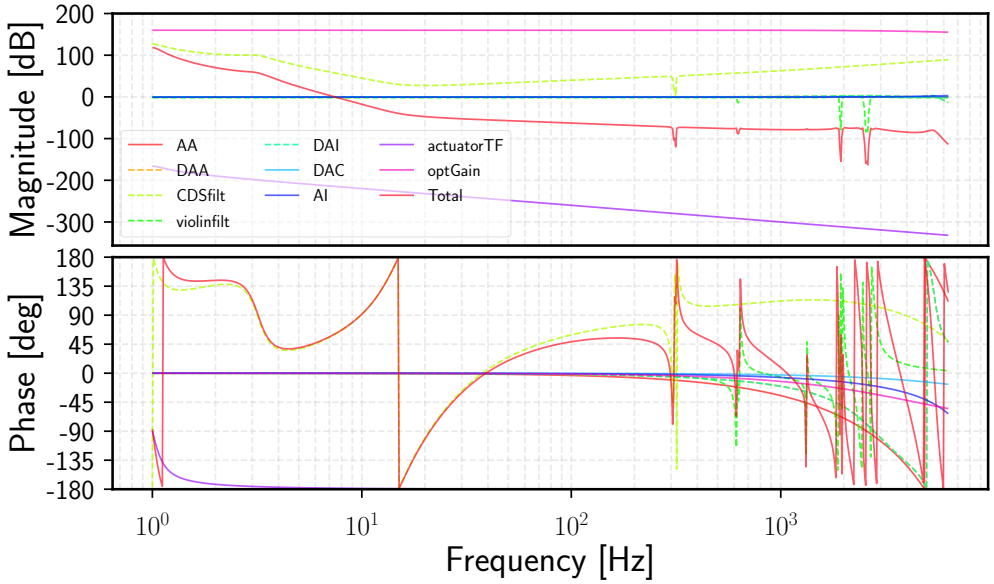


(b)

Figure 3.16: Model and measurement of the DARM feedback loop. In Figure 3.16(b), the frequency response of the various constituent components of the DARM feedback loop are plotted. The dashed lines are for filters that are implemented digitally, while the others are for actual devices (electrical circuits, pendula, and optical fields). The terms in the legend have the following meaning: "AA"→ anti-aliasing filter, "DAA"→ *digital* anti-aliasing filter, "CDSfilt"→ digital feedback control filter, "violinfilt"→ notch filters for suspension violin modes, "DAI"→ *digital* anti-imaging filter, "DAC"→ digital to analog converter, "AI"→ anti-imaging filter, "actuatorTF"→ mechanical susceptibility of the suspended pendulum, "optGain"→ frequency-dependent optical response DARM motion produces in the AS55 photodiode.

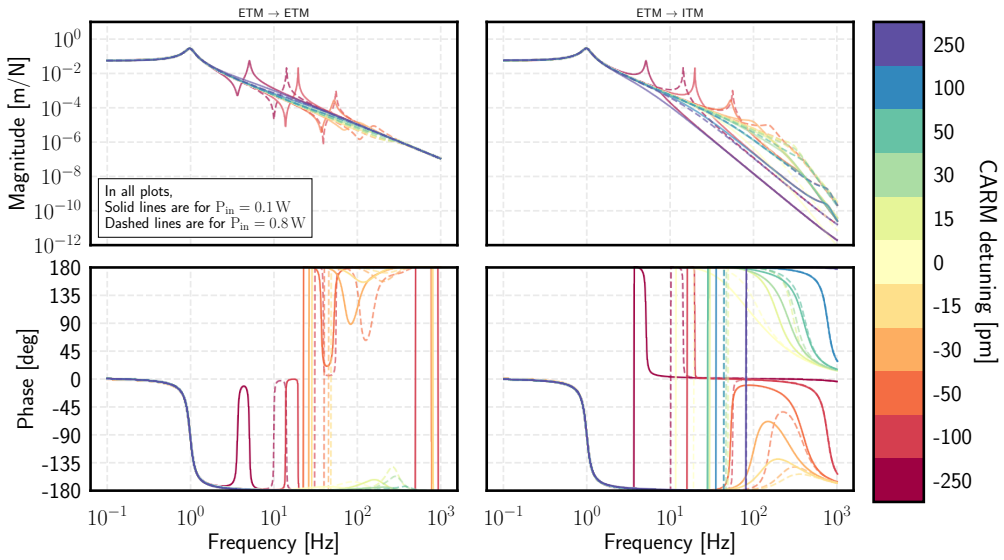


Figure 3.17: Modified mechanical susceptibility of ITM and ETM due to optomechanical effects. See text for more details.

0, the loop once again became stable and was able to bring the system under control, but any attempt to approach 0 CARM offset would result in the same instability occuring again.

To put this hypothesis to the test, I attempted to lock the interferometer with the input power cut to roughly half the nominal value. However, this did not improve the situation. Going back to the model, for the 250 g mirrors at the 40m, it appears that the modified phase close to the CARM loop UGF consumes a non-negligible amount of phase near 0 CARM offset for input powers as low as 100 mW, c.f. the nominal input power of $\approx 0.8$ W. Reducing the input power to the interferometer to much less than $\approx 500$ mW was empirically determined to be infeasible, as it made sensing and control of the other degrees of freedom difficult.

While this effect was unanticipated, it did not adversely affect the lock acquisition procedure - despite CARM not remaining entirely in its linear range when the CARM offset under ALS control was zeroed, it was possible to *directly* hand over control to the RF path, by first blending the two paths in a frequency-dependent way (with the RF path having authority at DC), and then gradually ramping up the gain of the RF path to the final state while simultaneously ramping the gain of the ALS path to 0.

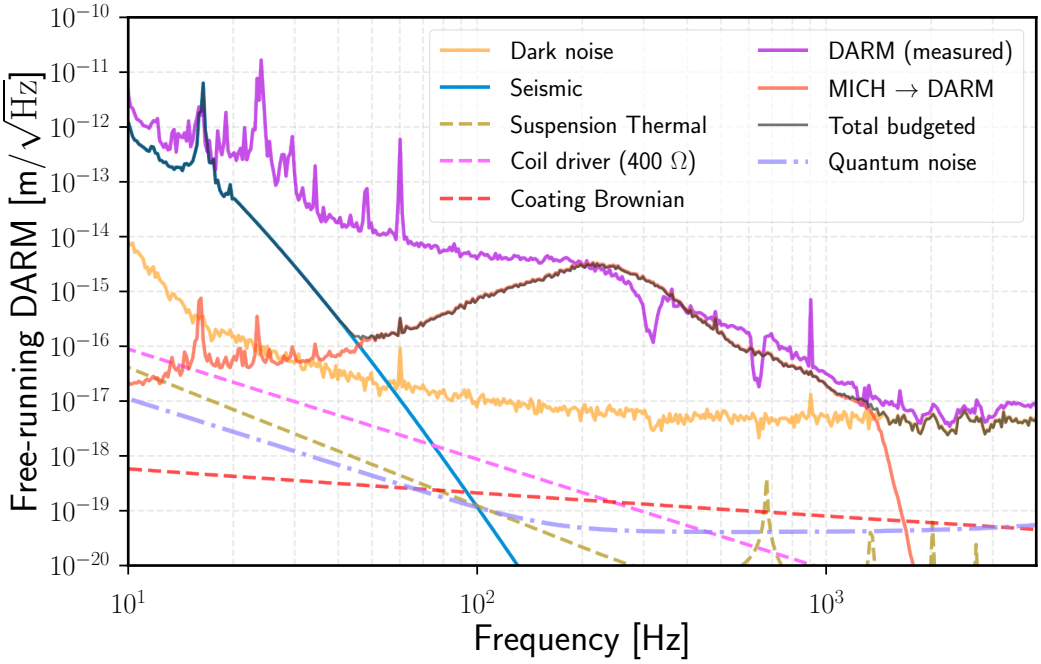


Figure 3.18: Preliminary DARM noise budget in PRFPMI lock. See text for more details on the budgeted noise sources.

### 3.4.6 DARM noise budget

The DARM loop model from Section 3.4.4 is used to infer the *free-running* DARM displacement noise by undoing the effect of the loop suppression. This noise budget is shown in Figure 3.18. This budget is in a very preliminary, but in the early stages of successfully locking the PRFPMI, DARM sensitivity is limited by seismic noise noise below $\approx 30\,\mathrm{Hz}$, cross coupling from MICH from $\approx 200\,\mathrm{Hz} - 2\,\mathrm{kHz}$, and the dark noise of the AS55 sensing chain above 2 kHz. The seismic noise plotted here is adapted from Figure 3.4 below $\approx 30\,\mathrm{Hz}$, where that measurement isn't dominated by sensing noise, and falls off as $f^{-10}$ above (the seismic isolation stacks provide $\approx f^{-8}$ isolation at high frequencies with the pendulum providing additional $f^{-2}$ isolation). At the time this measurement was taken, the vertex degrees of freedom are controlled using $3f_{1,2}$ PDH error signals (see Figure 3.19 for the in-loop noise spectra), which are inherently noisier than their $1f$ counterparts due to the $\approx 100\times$ lower optical gain. The sensing noise of the MICH control loop gets impressed on DARM because MICH actuation also produces a signal in the DARM sensor that is indistinguishable from any DARM signal (even though it is smaller than the DARM signal by $\approx 300\times$ because the latter gets enhanced by the arm cavities). It is this coupling that is labelled "MICH→DARM". The coupling was measured by performing a swept-sine injection at the control point of the MICH

loop, and coherently demodulating the response at the DARM error point, as shown in Figure 3.20. Knowing this transfer function, this contribution can be nulled by implementing a feedforward filter [44] which would have the same magnitude response but 180° phase relative to the measured coupling path. Initial attempts to do this cancellation did not work (transient signals when the feedforward filter was engaged destroyed the PRFPMI lock). The limited available commissioning time had to be used to mitigate other noise sources and improve the robustness of the lock, and so the feedforward approach was not pursued further. It is anticipated that MICH and PRCL control will get less noisy once transferred to $1f$ PDH error signals, but this transition was not successfully executed at the time of writing. Any residual cross-coupling will be nulled by implementing a more carefully tuned feedforward filter. The "PRCL→DARM" contribution was not explicitly measured and may account for some of the un-budgeted noise in the $30-200$ Hz band. Above $\approx 2$ kHz, the dark noise of the AS55 photodiode and demodulator electronics are the dominant noise contributions. In this early stage of characterization, this was not deemed a high-priority noise source and so no effort was made to modify the electronics to have lower noise. The excess in the measured DARM noise above the dark noise at high frequencies may be due to un-modelled laser noise (intensity and frequency) coupling. Other traces are included in the budget to get an idea of how much the aforementioned three noise sources need to be suppressed, before problems like the coil driver noise start limiting DARM sensitivity.

### 3.4.7 Sensing matrix measurement

In order to convert the measurements made in the digital control system to meaningful noise spectral densities in physical units, the optical response of the interferometer (i.e. Watts of signal power produced per meter of displacement of a DoF) has to be known. This is measured by driving one or more of the suspended optics with single-frequency sine wave, and coherently demodulating the response produced in the digital control system (usually in units of ADC "counts"). The actuators are calibrated a priori (using the methods in [45] for example), so we know how many meters of motion is being produced as a result of the applied drive. Taking the ratio of these two quantities, we get the desired "cts/m" calibration factor. The collection of such factors can be arranged into a matrix with shape $m_{\text{sensors}} \times n_{\text{DoF}}$ - this is known as a sensing matrix. A convenient way to visualize the sensing matrix is in a series of radar plots, like that shown in Figure 3.21. Such a measurement can then be validated against numerical models of the system. By looking at such a set

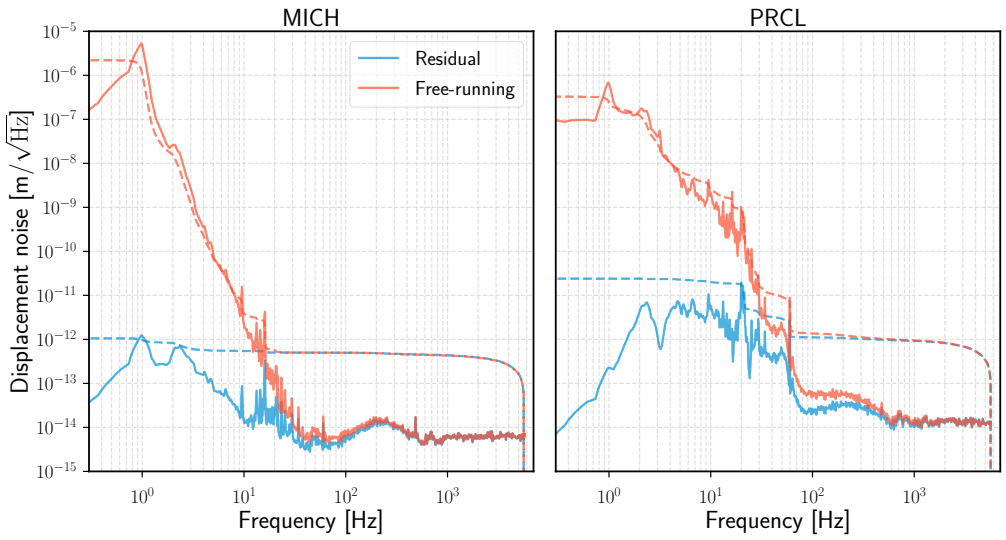


Figure 3.19: Residual (measured) and free-running (inferred) MICH and PRCL noise in PRFPMI lock. The free-running quantities are inferred from the in-loop measurements by undoing the effects of loop suppression using a model of the OLG. The inferior seismic isolation provided by the TT type suspension (relative to their SOS counterparts) affects PRCL, but not MICH, and this excess is visible between $\approx 3 - 30$ Hz.

of radar plots, one can attempt to "diagonalize" the system in the sensor-actuator space. However, one of the main problems plaguing the 40m is the poorly understood sensing response of the interferometer. For instance, analytic calculations and numerical modeling both suggest that the PRCL and MICH DoFs should produce responses in orthogonal quadratures. However, the measurements suggest that there is negligible separation in almost all of the sensors - the REFL165 sensor offers the best separation between these two DoFs, and hence, is used for control. Part of the problem is that even in simpler configurations like the PRMI, the cross coupling between the PRCL and MICH DoFs described in Figure 3.6 cannot be nulled simply by the usual technique of feeding back a portion of the MICH control signal to the PRM - at the time of writing, a satisfactory explanation has not been arrived at as to why. Problems with the RF phase modulation sidebands applied on the input beam (for example, unreasonably large sideband imbalance or excessive RAM) were ruled out by direct characterization (see Figure C.2(a)), and because the expected orthogonality was recovered if the MICH actuation was applied differentially on the ITMs instead of the beamsplitter (in which case there is no geometric coupling between MICH and PRCL). The working hypothesis is that either or both of the BS and PRM suspensions are problematic - it is hoped that a planned vent of the

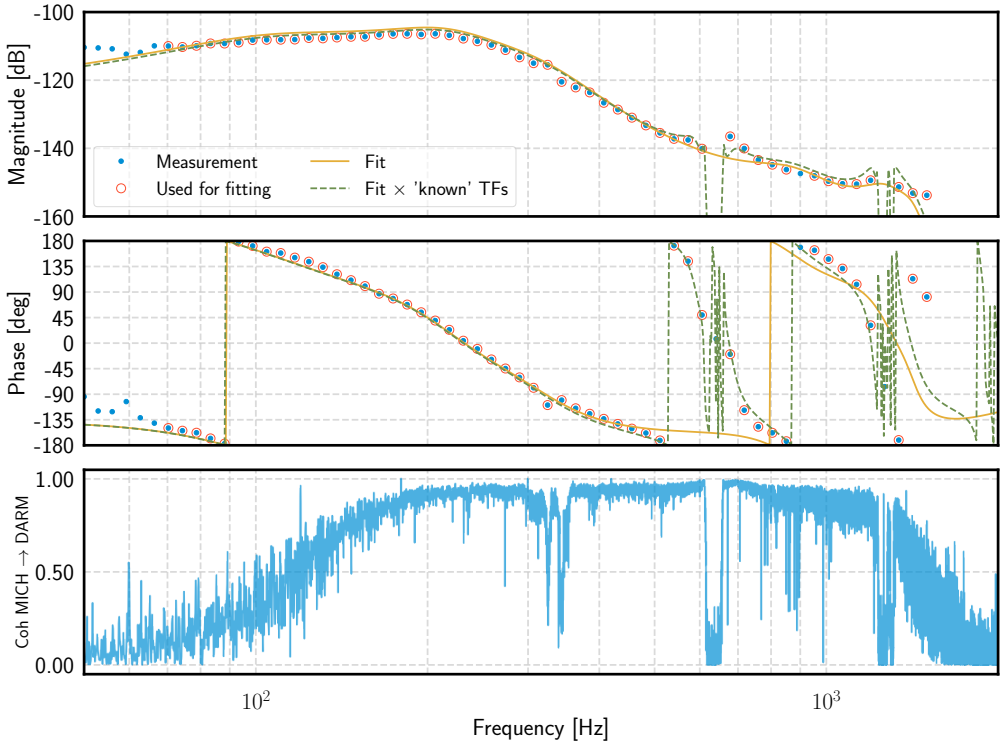


Figure 3.20: Measured and modelled coupling from the MICH *control* signal to DARM error point. Frequencies at which the coherence between the MICH control signal and the DARM error signal is near unity are those where this coupling is strongest, and limits the DARM sensitivity. This transfer function is measured using the swept-sine technique at some discrete frequencies, and extended to continuous frequency by fittin, weighted by coherence. The fundamental and second-harmonic violin modes of the suspended optics at the 40m are at $\approx$ 600 Hz and $\approx$ 1.2 kHz - to avoid exciting these modes while actuating on the optics, bandstop filters are implemented at these frequencies, which explains the abrupt loss of coherence (these are the "known" transfer functions alluded to in the legend).

vacuum system will allow further debugging.

### 3.4.8 Angular sensing and control (ASC)

The high circulating laser power in the IFO's Fabry-Pérot arm cavities couple the motion of the two constituent mirrors due to radiation pressure. In particular, the angular models of the ITM and ETM, which in the absence of radiation pressure are defined purely by the mechanical susceptibility of the pendulums they are suspended on, get modified and coupled. For sufficiently high powers, one of these coupled eigenmodes of the cavity become open-loop unstable (see for example Equations 5-16 and 5-17 of [46]), necessitating a feedback loop to maintain a locked IFO.

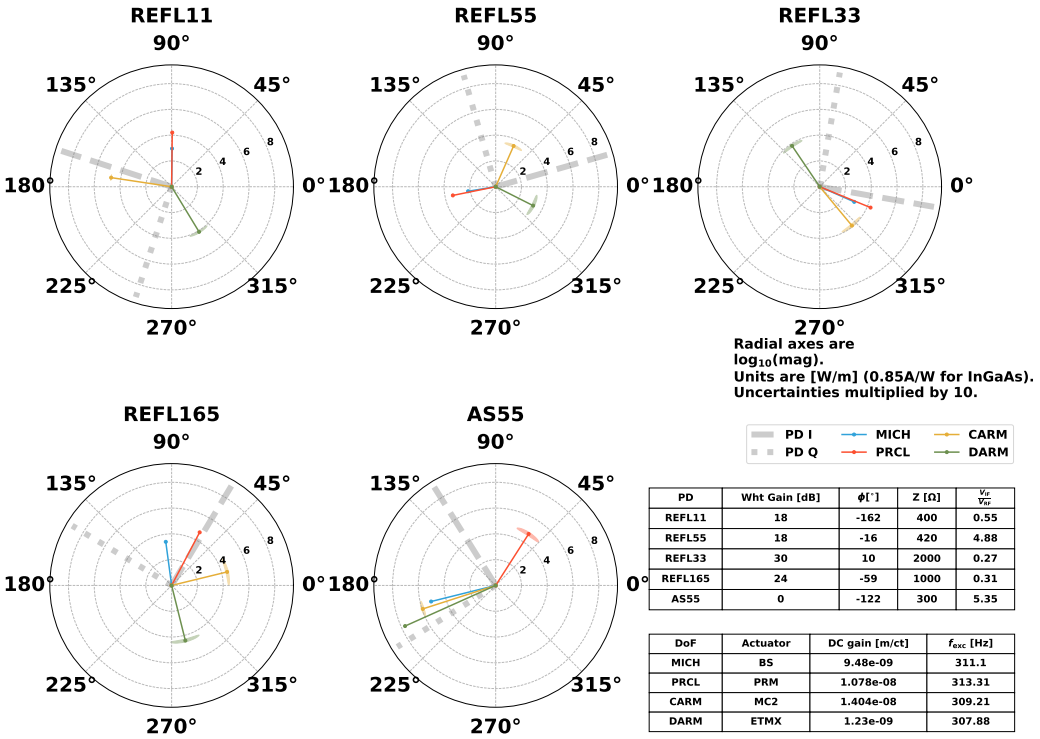


| PD | Wht Gain [dB] | $\phi$[°] | Z [Ω] | $\frac{V_{rf}}{V_{dc}}$ |
|---|---|---|---|---|
| REFL11 | 18 | -162 | 400 | 0.55 |
| REFL55 | 18 | -16 | 420 | 4.88 |
| REFL33 | 30 | 10 | 2000 | 0.27 |
| REFL165 | 24 | -59 | 1000 | 0.31 |
| AS55 | 0 | -122 | 300 | 5.35 |

| DoF | Actuator | DC gain [m/ct] | $f_{exc}$ [Hz] |
|---|---|---|---|
| MICH | BS | 9.48e-09 | 311.1 |
| PRCL | PRM | 1.078e-08 | 313.31 |
| CARM | MC2 | 1.404e-08 | 309.21 |
| DARM | ETMX | 1.23e-09 | 307.88 |

Figure 3.21: Sensing matrix in PRFPMI lock. This measurement is from a 5-minute stretch of data, segmented into 10-second long sections for some statistical averaging. Shaded ellipses around the tips of the stems are indicative of the statistical uncertainty from the 30 samples. Two demodulated quadratures per photodiode are indicated - their naming is arbitrary, but the convention is to orient (i.e. define) the quadratures, by adjusting a digital demodulation phase, such that "Common" interferometer DoFs like CARM and PRCL produce a response in the "I" quadrature, while "Differential" DoFs like MICH and DARM produce a response in the "Q" quadrature. The reflected beam from the IFO is *not* equally split among the REFL photodiodes, which has to be taken into account when comparing the measurement to numerical simulations.

For the geometry of the 40m arm cavity, this critical power level is $\approx 3.5\,\mathrm{kW}$[12]. While there is some uncertainty, it is estimated that the circulating power in the arm cavities is limited to $\approx 2 - 2.5\,\mathrm{kW}$[13] due to the excess losses in the PRC. Therefore,

[12]This effect applies to the IMC as well - for the cavity geometry, with the input and output couplers being flat and the folding mirror having an RoC of $\approx 18.4\,\mathrm{m}$, the critical circulating power is estimated to be $\approx 11.2\,\mathrm{kW}$. Since the power gain of the cavity is $\approx 500$, angular instabilities are not expected for input powers less than 20 W into the IMC

[13]Interestingly, this makes the power-to-mass ratio at the 40m, with 250 g mirrors, comparable to that in the aLIGO interferometers at Hanford and Livingston, with $\approx 200\,\mathrm{kW}$ circulating in the arm cavities whose mirrors weigh 40 kg. However, the classical noise levels at the 40m are also much higher than at the LIGO sites, making it much more difficult to probe optomechanical effects and noise evasion schemes, like in [47].

the IFO is not yet in the regime of dynamical angular instability, though planned upgrades for the Ponderomotive Squeezing measurement experiment will certainly push it over the threshold. Even so, implementing feedback loops to stabilize the angular positions of the various optics allows higher and more stable power buildup in the IFO (see after "H" in Figure 3.12), which in turn improves DARM sensitivity.

For the inital phase of work presented in this chapter, a very rudimentary ASC scheme was implemented. Error signals were derived from single QPDs monitoring the transmitted beam from each arm cavity, and after an appropriate basis change to go from the X-arm and Y-arm basis to the "Common" and "Differential" basis and filtering, the control signal was fed back to the ETMs. The ITMs had their angular positions controlled by a different strategy - their Oplev loops were DC-coupled, so the spot positions on the Oplev QPDs were deemed a good enough reference. This scheme is almost certainly sub-optimal - where possible, we should always be using interferometric signals in favor of local sensors like the Oplev. However, this feedback scheme allowed the interferometer to remain locked for a few tens of minutes at a time, which was deemed sufficient. Neither the cross-couplings between the Oplev based and Transmon QPD based ASC servos, nor the coupling to the DARM error point due to A2L, were characterized. The feedback loops had a bandwidth of $\approx 10\,\mathrm{Hz}$ - with a low-frequency boost implemented, the loop shape was able to effectively suppress angular fluctuations in the $0.5 - 3\,\mathrm{Hz}$ band, which makes the dominant contribution to RMS angular motion. Angular fluctuations in the PRC also degrade the power buildup in the arm cavities. As mentioned in Section 3.2.2, seismometer-based feedforward control was able to stabilize the buildup in the PRC. These loops were left engaged during the PRFPMI lock. A single QPD is also available at the POP port of the IFO. However, it is not a good candidate sensor to stabilize PRC angular motion with a feedback loop, as the ITM and ETM produce much larger signals in the POP QPD. The *simulated* sensitivity of the available angular sensors at the 40m to motion of various suspended optics is summarized in Figure 3.22. These could be validated against measurements using the same technique as in Section 3.4.7 - efforts to do so were hampered by lock losses when the measuring excitations were injected. While this could have indicated some instabilities in the ASC loops implemented, a more detailed characterization of the ASC system was deferred for future work.

The preferred technique of stabilizing angular motion in a locked interferometer is to use Wavefront Sensors (WFS). These detect angular misalignment by measuring

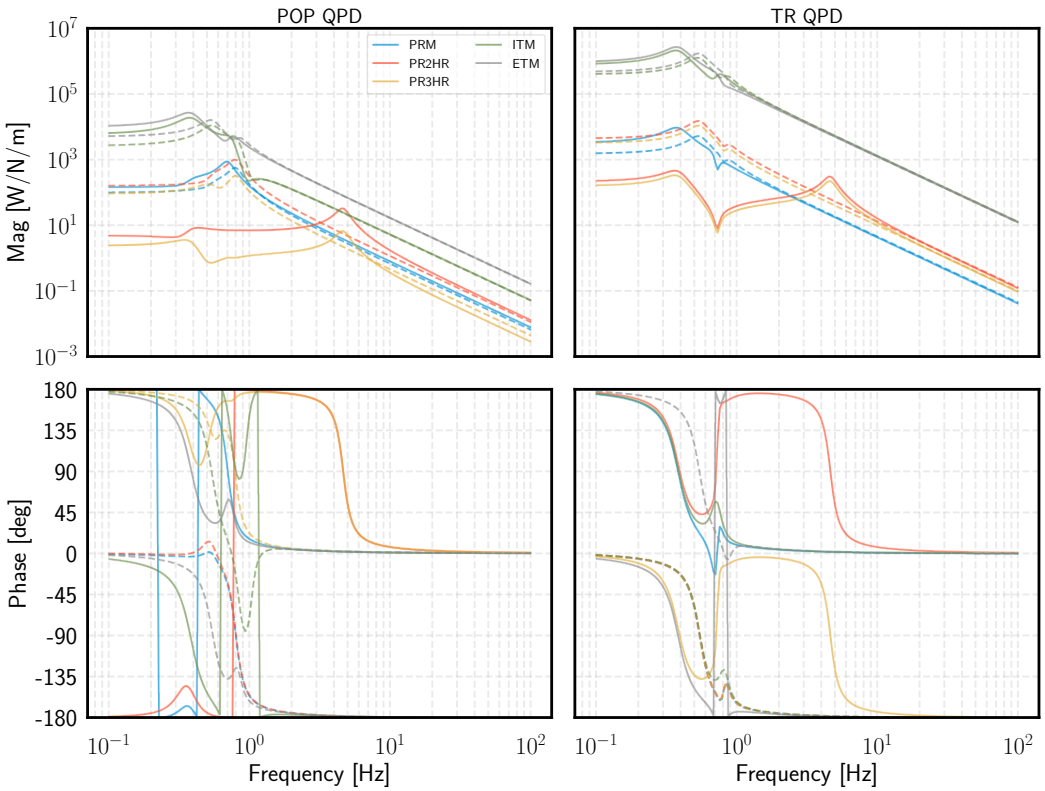


Figure 3.22: Sensing responses of the available angular sensors to torques on various suspended optics. Although only a single column is included for the "TR QPD", it is understood that there is an individual TR QPD monitoring the transmission of *each* arm cavity.

(on a QPD) the beat between the $\mathrm{TEM}_{00}$ spatial mode of an LO field either at the carrier frequency or one of the PM sideband frequencies $f_{1,2}$, and $\mathrm{TEM}_{01}$ or $\mathrm{TEM}_{10}$ spatial modes at the other frequency, which get generated due to misalignment [48]. Note that the error signal generated from a WFS QPD is at an RF frequency offset from the carrier, unlike the signal generated on a DC QPD, and therefore, must be electrically demodulated like PDH error signals to pick out the quadrature signal that has maximum sensitivity to the angular motions we are trying to sense. Polluting noise sources such as laser RIN or electronics noise are typically much lower at RF frequencies than at DC, making WFS a lower noise sensor than their DC QPD counterparts. However, they are also much more complex systems, consuming significant commissioning time to implement correctly. For the data presented in this chapter, there was no WFS available to sense fields from the IFO. A single WFS has recently been installed at the AS port of the IFO, and has been verified to work correctly from an electrical standpoint. However, it has still not been used for any angular stabilization of the interferometer.

### 3.4.9 Power recycling gain (PRG)

With both the Fabry-Pérot arm cavities and the PRC aligned, the PRFPMI configuration allows a direct measurement of the PRG (interchangably used with $G_{\mathrm{PRC}}$), which is a measure of how much the input power to the interferometer is enhanced by the presence of the PRM. Since the arm cavity transmissions are normalized to 1 with the PRM misaligned, the PRG is given by $\mathrm{TR}_{\mathrm{X,Y}} \times T_{\mathrm{PRM}}$, where $\mathrm{TR}_{\mathrm{X,Y}}$ denotes the average transmission of the arm cavities when the PRFPMI is locked. Sub-optimal ASC loops dominate fluctuations in $\mathrm{TR}_{\mathrm{X,Y}}$, but we assume an average value for a rough estimate of the PRG. After careful optimization of the alignment of various optics, the arm cavity transmission was observed to go as high as $\approx 425$ - this is consistent with a PRG of $\approx 24$, which is the highest that has been observed at the 40m. The achievable recycling gain is largely determined by round-trip optical losses in the arm cavity, since this sets the reflectivity of the compound mirror forming the PRC together with the PRM - $G_{\mathrm{PRC}} \times G_{\mathrm{arm}} \lesssim \frac{1}{2\mathcal{L}_{\mathrm{rt}}}$, where $\mathcal{L}_{\mathrm{rt}}$ is the average *round-trip* loss of the arm cavities. This simplistic model assumes negligible intracavity losses in the PRC. However, due to the folding mirrors in the PRC being flipped to ensure geometric stability (with the AR coated side and substrate being inside the cavity), there is an estimated $1-3\%$ additional loss introduced. A good test of this model was to compare the recycling gains before and after the arm cavity mirrors were cleaned - the results are summarized in Figure 3.23.

Both before and after cleaning[14], the loss of the arm cavities was measured using independent techniques such as measuring the DC reflection from the ITM with the ETM aligned (so a compound mirror is formed) and misaligned (so just a single bounce off the ITM) - these measurements are indicated as vertical shaded bands. Similarly, the measured PRG in PRFPMI lock are indicated as horizontal shaded bands. There is considerable uncertainty on what the actual loss inside the PRC is, but we can bound it between $1.3-2.6\%$[15] with reasonably high confidence.

Such low measured losses in the arm cavities were a bit surprising - the PRM transmissivity of 5.637% was chosen such that we would have a slightly overcoupled[16]

[14] A commercial polymer-based cleaning agent, First Contact, is used as per the guidance of the LIGO engineering group [50].

[15] Because the *optical* loss is so high, it is impossible to deconvolve losses due to mode-mismatch between the interferometer's spatial common-mode and optical losses. Nevertheless, we can place an upper-bound on the *total* loss, since high recycling gain cannot be realized if the effective loss were higher.

[16] The IFO is "overcoupled" when the compound arm cavity reflectivity as per Equation (D.1) is greater than the PRM reflectivity, and "undercoupled" when the reverse is true. Critical coupling refers to the case where the two reflectivities are equal. At critical coupling, the PRG is $\frac{1}{T_{\mathrm{PRM}}} \approx 18$.

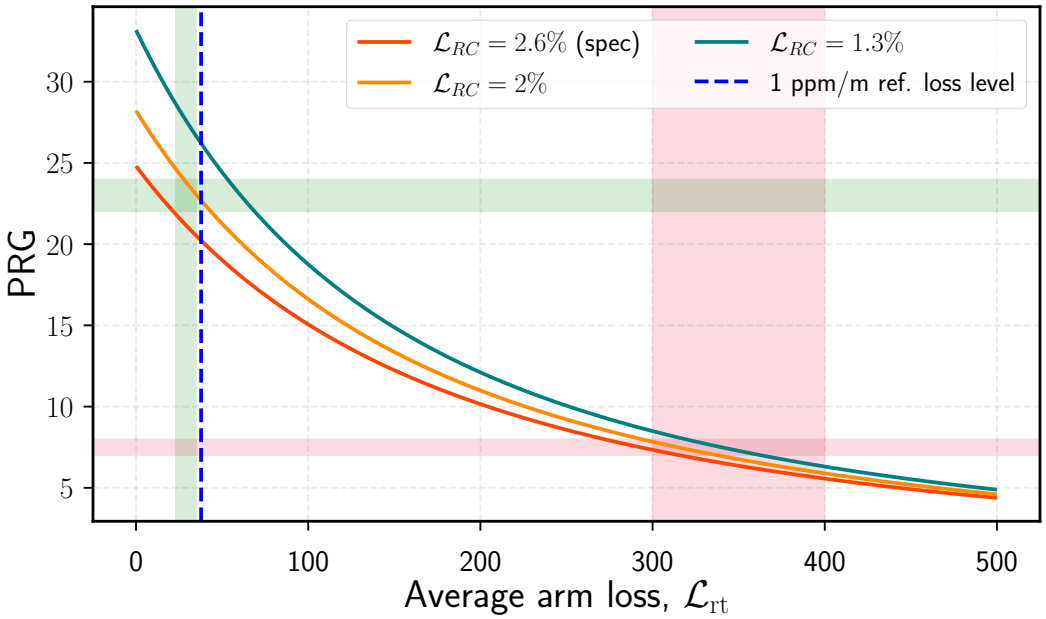


Figure 3.23: Inferred arm cavity losses from PRG measurements, before (red shaded bands) and after (green shaded bands) cleaning the 40m arm cavity mirrors (see Appendix E). Each of the three plotted lines are PRG as a function of arm cavity loss, assuming a fixed loss in the PRC (indicated in the legend). The shaded bands are meant to indicate $1\sigma$ statistical uncertainties on $\mathcal{L}_{\mathrm{rt}}$ and PRG *measurements*. A "1ppm/m" reference loss level is indicated to show that it is possible to realize losses below this target value for $\approx$ centimeter-sized beams. This is a target for proposed long-storage time filter cavities, that can inject frequency-dependent squeezed vacuum into the LIGO interferometers and improve their sensitivity [49].

IFO for $\mathcal{L}_{\mathrm{rt}} \approx 100 - 150$ ppm. With the measured loss levels, a well-aligned 40m is virtually guaranteed to be overcoupled. However, that is a strong caveat - until the interferometer is well aligned, angular motion causes large power fluctuations in the arm cavities and the PRC, changing the field content arriving at various detection ports. Whether the IFO is undercoupled or overcoupled has implications on the PDH error signals at the REFL and POP ports. As per Equation (C.2), the PDH error signal can, in general, have contributions from a static sideband field beating with a dynamic carrier field, or vice-versa. For the CARM, DARM and MICH DoFs, one of these combinations is dominant over the other, to a good approximation. However, for sensing PRCL using $1f_{1,2}$ PDH signals, both contributions can have comparable magnitude (see, for example, Equation 15 of [51]). There is a relative $-1$ sign between *field* reflectivities for undercoupled and overcoupled cavities - so the correct sign of a servo filter for suppressing fluctuations in a DoF can end up enhancing them if the coupling changes. If the interferometer happens to go through

the point of critical coupling, due to angular fluctuations, then the PDH error signal could vanish entirely. In both cases, the PRFPMI lock will be lost, because one or more DoFs will stray outside the range where the PDH signals remain linear. Fortunately, sensing PRCL using the $3f_{1,2}$ scheme is immune to these effects, which allows the interferometer to remain locked until the alignment can be improved to a point where the coupling is not in danger of changing or vanishing. Once the folding mirrors in the PRC are replaced and the intracavity loss becomes $\approx 0.1\%$, it is expected that the IFO will move even further into the firmly overcoupled regime, allowing transition of the vertex DoFs from $3f_{1,2}$ control to lower-noise $1f_{1,2}$ control.

### 3.5 Conclusions and future work

In this section, I have presented various configurations in which the 40m IFO can be locked, thereby becoming a precision measurement instrument. The reliability of lock acquisition was improved to the point where the IFO could remain locked for up to an hour, while the measured PRG was the highest seen at the 40m in its current incarnation with 250 g mirrors. This work represents but the first step in realizing the prototype's true value as a testbed for quantum-limited sensing measurements, as well as new technologies that could improve the current and next generation of GW detectors. A pathway to this dream is outlined in the following non-exhaustive list. Many of these steps are planned for, or are already being undertaken, as part of the ongoing upgrade of the 40m lab.

- **Improve the suspensions and electronics** - the TT type suspension, as well as most of the $\approx$ 20 year old electronics in the lab will be phased out and replaced with modern equivalents. This will hopefully facilitate commissioning time to be spent on tasks that improve nosie performance, as well as allow more interferometry to be done during times of slightly elevated seismic activity (due to improved seismic isolation).

- **Improve the duty cycle of the IMC**. Without a locked IMC, no other IFO configuration can be locked. The multiple coupled cavities of the LIGO interferometers have been demonstrated to stay locked for times in excess of 1 week, so there is no reason a single optical cavity cannot remain locked for comparable periods of time. At the 40m, there are periods, sometimes as long as 30 minutes, when the IMC fails to re-acquire a stable lock. This has been a problem that has plagued the 40m for $\approx$ a decade - the exact cause is unknown

despite repeated characterization efforts, but is likely due to flaky electronics and/or a degrading laser.

- **Fix the geometric stability issues with the recycling cavities**. Apart from the obvious higher circualting gain in the arm cavities, it is anticipated that this will lead to better agreement between numerical models and measurements, and fewer higher-order-mode related problems in LSC and ASC. The replacement mirrors per Appendix D are already in hand, and suspensions are being designed for them.

- **Install more sensors that monitor environmental noise sources** - e.g. seismic, thermal, and acoustic. Then, design feedforward filters using these to subtract the coupling of these noises to the interferometer. Currently, only the vertex seismometer signals are used to stabilize the PRC angular motion and the IMC length. Accelerometers and seismometers are already installed elsewhere in the lab, and microphones to monitor acoustic couplings could also greatly improve the situation.

- **Improve the LSC and ASC loops.** Better characterize the noise couplings between them. In particular, the ASC system has not received much attention. Clever loop design will allow for much more stable power buildup in the arm cavities.

- **Perform more detailed characterization of unmodelled noise sources.** In particular, the laser noise couplings (frequency noise and intensity noise). An intensity stabilization servo will likely need to be implemented to improve the DARM sensitivity at some point in the near future.

- **Clean the IMC mirrors and re-optimize the transmission / isolation of the Input Faraday Isolator (IFI)**. It is estimated that we lose $\approx 20\%$ of the light injected into the vacuum envelope before it reaches the PRM. Increasing this throughput will increase the optical gain on various sensors, leading to better noise performance. This will be a critical step in moving to high power operations in preparation for the Ponderomotive Squeezing measurement experiment, described in the next chapter.

- **Implement more, and preferably automated, interferometer diagnostic routines**. This can help pinpoint the time when a particular system's performance degraded. Often, a particular subsystem of the interferometer (e.g. the

ALS system) doesn’t receive any attention from a human for several weeks or months at a time while other systems are being worked on. If automated diagnostics could be run at a time when the lab is unused (e.g. 6 AM in the morning), the health of these "neglected" systems could be constantly monitored, and immediate action can be taken if a problem is reported.

The list above addresses "known" problems - there are many new challenges that will arise when the IFO moves to high power operation and a BHD readout - which are the subject of the next two chapters.

*Chapter 4*

# AN EXPERIMENT TO MEASURE OPTOMECHANICAL SQUEEZING AT THE 40M PROTOTYPE INTERFEROMETER

The theory of optomechanical interactions modifying the noise properties of the output field of GW interferometers has been extensively studied [52–54]. Making a *direct* measurement of squeezed vacuum states generated by optomechanical interactions at (i) room-temperature, (ii) kilogram mass scales, (iii) audio-band frequencies of $\approx$ 200 Hz that are relevant to terrestrial GW detectors has been a long-standing goal in the field [55–57]. In the last two decades, there have been multiple demonstrations of cavity optomechanical phenomena, see Figure 3 of [11] for a good, but dated, summary - but the region with experiments in mass-frequency space relevant for GW detectors remains sparsely populated. Classical noise sources, and fluctuations due to coupling from the environmental thermal bath, have posed a formidable challenge. While I have been working on the projects described in this thesis, there has been significant progress [47, 58, 59], and several exciting new proposals made to push the optomechanical, quantum-limited sensing regime even further.

In this chapter, I will describe an experiment to measure squeezed vacuum states generated by the 40m interferometer. Chapter 3 described efforts to characterize and improve the sensitivity of the 40m - the ultimate goal was to improve the noise performance to a level that would enable us to carry out the measurement described in this chapter. Much of the design work was done in collaboration with K. Kuns and is described in detail in Chapter 3 of [60], so after a brief conceptual review, I will try and focus on some practical challenges of implementing the design, which are not covered there.

## 4.1 Conceptual overview of "quantum noise" in an interferometer

In the LIGO parlance, "quantum noise" is a blanket term describing imprecision at the interferometer readout caused by the quantum-mechanical nature of the interferometer. There are two contributing physical pathways. One is the uncertainty caused by the Poissonian statistics of photon arrival at the detection photodiode, called "shot noise". The other, "radiation pressure noise", has to do with the random momentum impulses imparted on the mirrors of the interferometer by individual

photons during the process of reflection. For the dual-recycled optical topology adopted by the LIGO interferometers, radiation pressure noise is the dominant contributor at low frequencies, while shot noise dominates at high frequencies, although the specific parameters of the interferometer such as the laser power circulating in the Fabry-Pérot arm cavities and the type of readout (i.e. DC readout / RF readout / BHD) must be known to quantify these statements. The insight of [53, 54] was that a proper analysis of these two noise sources must take into account any correlations that exist between them.

A convenient technique to analyze the quantum noise of a particular optical configuration is to use the Input-Output (I/O) relations. "Inputs" refer to optical fields that enter open ports, such as the symmetric port where the PSL beam pumps the interferometer, while "Outputs" refer to fields that are read out at various open ports, such as the field exiting the AS port. Being a MIMO device, each output field can in general have contributions from multiple inputs. These can be derived using the Adjacency matrix approach described in Appendix C.1, but using the two-photon representation of the fields described in [61]. For LIGO-like optical topologies, the pertinent I/O relation is that for the output field at the AS port (which is where the gravitational wave signal is expected). In the two-photon formalism notation [62, 63], this will take the general form

$$\underbrace{\begin{bmatrix} b_1 \\ b_2 \end{bmatrix}}_{\substack{\text{output} \\ \text{field}}} = \underbrace{\begin{bmatrix} C_{11} & C_{12} \\ C_{21} & C_{22} \end{bmatrix}}_{\substack{\text{Optomechanics,} \\ \boldsymbol{C}}} \underbrace{\begin{bmatrix} a_1 \\ a_2 \end{bmatrix}}_{\substack{\text{input} \\ \text{vacuum} \\ \text{noise}}} + \underbrace{\begin{bmatrix} D_1 \\ D_2 \end{bmatrix}}_{\substack{\text{optical} \\ \text{gain,} \\ \boldsymbol{D}}} \underbrace{\frac{h}{h_{\mathrm{SQL}}}}_{\substack{\text{DARM} \\ \text{signal}}}, \tag{4.1}$$

where $h \equiv \frac{\delta L}{L}$ is the differential arm strain and $h_{\mathrm{SQL}} \equiv \sqrt{\frac{8\hbar}{m\Omega^2 L^2}}$ is the Standard Quantum Limit (SQL) for an interferometer with test masses of mass $m$ and arm cavity length of $L$ at the signal frequency $\Omega$. The generalized version of Eq. (4.1) taking into account optical losses entering the interferometer at various ports, ignored in the above, can be found as Eqs. 5.6-5.12 in [54]. The *frequency-dependent* matrix coefficients $C_{ij}(\Omega)$ and $D_i(\Omega)$ are functions of the interferometer parameters, such as injected laser power, arm cavity bandwidth etc. Eq. (4.1) may be interpreted as follows: the output field at the AS port is the sum of the vacuum noise entering the AS port (which may be squeezed or unsqueezed), modified by the optomechanical properties of the interferometer, and the DARM signal scaled by the optomechanical gain of the interferometer.

It is conventional manipulate such I/O relations in units where unsqueezed vacuum has unit variance, and is represented as $\begin{bmatrix} a_1 \\ a_2 \end{bmatrix} = \begin{bmatrix} 1 \\ 1 \end{bmatrix}$. In general, we will measure some linear combination of the quadrature fields $b_1$ and $b_2$, with $b_\zeta \equiv b_1 \sin\zeta + b_2 \cos\zeta$, with $\zeta$ being the "homodyne angle", discussed in greater detail in Chapter 5. Therefore, if $|b_\zeta| < 1$, the variance of the measured field is below that of the vacuum, and is, therefore, squeezed. The dimensions of the fields in these normalized units is $\sqrt{n_{\text{photons}}/\text{Hz}}$. However, LIGO noise budgets are usually plotted as "signal-referred" - i.e. the transfer function of the interferometer, in units of $\sqrt{\text{W}}/\text{h}$ or $\sqrt{\text{W}}/\text{m}$ where $h$ is the differential arm strain, is used to convert a measured noise to the equivalent DARM displacement (or strain) which would have produced the same output field (it is convenient to represent electric fields in units of $\sqrt{W}$ rather than S.I. units). To convert $b_\zeta$ from units of $\sqrt{n_{\text{photons}}/\text{Hz}}$ to $\sqrt{\text{W}}/\text{h}$, we multiply the former by a factor of $\sqrt{2\hbar\omega_0}$, where $\omega_0$ is the laser frequency - the detailed derivation may be found in Appendix A of [64].

In order to use the interferometer as a *source* of squeezed vacuum[1], the goal is to determine the optical configuration such that $|b_\zeta| < 1$ for some $\zeta$, over some appreciable range of frequencies $\Omega$. Note that the squeezing is generated by the elements $C_{12}$ or $C_{21}$, which convert phase quadrature fluctuations into the amplitude quadrature or vice-versa (depending on the configuration of the interferometer). For us to be able to measure this generated squeezing, all other noise sources, such as differential arm motion due to Brownian noise of the dielectric coatings which contribute to $b_\zeta$ via the matrix elements $D_1$ and $D_2$, must be low enough that the noise variance of $b_\zeta$ remains lower than that of unsqueezed vacuum. For the 40m, at $f = \Omega/2\pi < 100\,\text{Hz}$, the displacement noises are typically so large that they far exceed the quantum noise (which is the input vacuum transformed by the matrix $\boldsymbol{C}$). The systematic optimization study to determine the configuration that gives the best chance of measuring optomechanical squeezing is described in detail in Chapter 3

[1] A reasonable question is why we would want to generate squeezed vacuum in this way. At the time of writing, squeezed vacuum generation using non-linear crystals is a mature technology, and both LIGO observatories have been operating with $\approx 2\,\text{dB}$ of squeezed vacuum injected into their AS ports for the entire O3 observing run [65]. However, using the optomechanical interaction may offer some advantages - for example, the losses due to imperfect polishing of the non-linear crystals far exceed that of super-polished mirrors, and it is known that losses limit the amount of squeezing that can be realized. Therefore, an ultra-low-loss optical cavity may allow even stronger squeezed fields to be generated. One reason non-linear crystals are the preferred technology is because the optomechanical interaction is inherently weak, and other classical noise sources would swamp any generated squeezing. However, recent technological advances have made it possible to mitigate many of these, making the idea worth pursuing.

of [60].

It is worth emphasizing that the goal of this particular experiment is *not* to maximize the signal-to-noise ratio of the DARM signal (which is the primary objective at terrestrial observatories, since better SNR would presumably lead to more precise astrophysical measurements and probes of deviations from General Relativity). The quadrature which should be selected for that purpose is different from what is selected for the optomechanical squeezing experiment. We seek the quadrature at which the ratio of noise variance in $b_\zeta$ to unsqueezed vacuum is minimized. Other ways of validating the quantum-mechanical nature of the interferometer, encoded in the matrix $\boldsymbol{C}$, include injecting well-characterized *squeezed* vacuum into the AS port, measure the output field, and inferring the *optomechanical* squeezing operation by mapping the relationship between the two - this was the approach adopted in [47].

## 4.2 Optical loss

There are numerous sources of optical loss within the interferometer. There are at least two reasons why this is undesirable for the measurement we are trying to make, which are briefly discussed in this section.

### 4.2.1 Degradation of squeezed states

As detailed in Sec. V of [54], each point at which optical loss occurs in the interferometer represents a point where some amount of unsqueezed vacuum gets coupled into the measurement. In Eq. (4.1), only the contribution of the unsqueezed vacuum entering the interferometer through the AS port is included - in most cases, the transmission of the SRM is usually such that this contribution is indeed the dominant contribution. However, a more complete analysis requires that we account for unsqueezed vacuum that enters the interferometer from other "open ports" as well. Assuming we are still reading out the field that exits the AS port, the relevant open ports include (i) losses in the arm cavity due to scattering, absorption in the dielectric coatings, and transmission through the ETMs, (ii) losses in the SRC due to scattering and transmission through the folding mirrors[2], (iii) possible clipping on the BS[3], (iv) mode-mismatch between the arm cavities and the SRC, and (v) losses in the photodetection chain (consisting of an OFI, OMC, and detection

[2]The optical power in the SRC is usually very low and so absorption in the dielectric coatings can be neglected.

[3]The finite apertures of all the optics can lead to clipping - the BS's contribution is expected to dominant because of the lateral shift the beam experiences while travelling through the 1-inch substrate.

photodiodess), due to scattering, mode-mismatch between the OMC's and the IFO's cavity eigenmodes, and imperfect quantum efficiency of the detection photodiodes. These sources of loss can be accounted for in the same way as the $\boldsymbol{C}$ matrix accounts for unsqueezed vacuum entering the AS port. I have listed the sources of loss in this way to indicate that there are different mechanisms at play, but from an analysis point of view, (ii),(iii), and (iv) are grouped together as "SRC losses". So Eq. (4.1) would have additional terms, which are $2\times2$ matrices - letters $\boldsymbol{P}$, $\boldsymbol{Q}$, and $\boldsymbol{N}$ are used in [54] to refer to "SRC losses", photodetection chain losses, and arm cavity losses respectively. This more complete version of Eq. (4.1), with the effects of optical loss on the quadrature noise included, was what was explored numerically to identify the interferometer configuration that would allow us to measure an optomechanically squeezed field in the presence of classical noise sources. For this analysis, losses due to mode-mismatch between optical cavities is treated in a simplified way that does not account for cavity enhancement effects in the SRC.

### 4.2.2 Limited optical power buildup

We are relying on the optomechanical interaction between the high circulating power in the arm cavities and the suspended mirrors to generate a squeezed state. The stronger this interaction, the greater the squeezing, and hence, we will have better immunity to degradation of the generated squeezed state due to imperfections elsewhere in the interferometer and the photodetection chain. The radiation pressure force exerted by a beam with power $P$ is $2P/c$, and so it is desirable to have as high a power resonate in the arm cavity as is practically feasible. We rely on the resonant enhancement in the PRC and arm cavities to realize this high power buildup, with $O(10\,\mathrm{kW})$ power in the 40m resonant arm cavities whose mirrors weigh 250 g, for $O(10\,\mathrm{W})$ amount of power input to the IFO[4]. Furthermore, there are at least two high-finesse cavities, the PMC and the IMC, in addition to the Input Faraday Isolator (IFI), between the amplifier output housed in an enclosure outside the vacuum envelope, and the PRM, which is inside the vacuum envelope. The transmissivity of these cavities is strongly dependent on the intracavity losses. The relationship between the power in the arm cavities, $P_{\mathrm{arm}}$ and the laser amplifier output, $P_{\mathrm{amp}}$ may be written as

[4] At the time of writing, compact fiber-pumped amplifier units are available that can generate $O(10\,\mathrm{W})$ of light with sufficient frequency and intensity stability, with $O(100\,\mathrm{mW})$ input from a stable source such as an NPRO [66].

$$P_{\mathrm{arm}} = P_{\mathrm{amp}} \cdot T_{\mathrm{PMC}} \cdot T_{\mathrm{IMC}} \cdot T_{\mathrm{IFI}} \cdot \alpha \cdot G_{\mathrm{PRC}} \cdot T_{\mathrm{BS}} \cdot G_{\mathrm{arm}}, \tag{4.2}$$

where $G_i$ denotes the power gain of the cavity $i$, $T_j$ denotes the power transmissivity of the element $j$, and $\alpha$ denotes an effective mode-matching between the input beam and the arm cavity's spatial eigenmodes. Using multiple different measurement techniques, we have verified that it is possible to get the *round-trip* loss in the 40m arm cavities to be as low as 20-30 ppm, so we expect $G_{\mathrm{arm}} \approx 270$. As discussed in Section 3.4.9, $G_{\mathrm{PRC}}$ is currently limited to $\approx 20$ due to the internal losses in the PRC - once we replace the folding mirrors, we expect that we can realize $G_{\mathrm{PRC}} \approx 40$. $T_{\mathrm{BS}}$ is 50%, while $T_{\mathrm{PMC}} \approx 85\%$. From the arm cavity scans discussed in Section 2.6, the mode-matching efficiency between the input beam and the arm cavity's eigenmode is $\approx 93\%$, but this number does not account for possible mismatches between the PRC and arm cavity eigenmode. Finally, the product $T_{\mathrm{IMC}} \cdot T_{\mathrm{IFI}}$ is estimated to be $\approx 50\,\%$. Putting all these numbers together, I estimate $P_{\mathrm{arm}} \approx 2200 P_{\mathrm{amp}}$. We expect to be able to improve this to $P_{\mathrm{arm}} \approx 4000 P_{\mathrm{amp}}$, if we can increase the product $T_{\mathrm{IMC}} \cdot T_{\mathrm{IFI}}$ to 0.9, which we expect to be able to do with a vent of the vacuum system to clean the IMC optics and tune the polarization optics in the IFI. The numbers related to optical loss used for the modeling results presented in this thesis are summarized in Table 4.1.

| **Parameter** | **Value** |
|---|---|
| Arm cavity losses $\mathcal{L}_{\mathrm{arm}}$ | 20 ppm |
| PRC losses, $\mathcal{L}_{\mathrm{PRC}}$ | **1000** ppm |
| SRC losses, $\mathcal{L}_{\mathrm{SRC}}$ | **1000** ppm |
| PMC transmission, $T_{\mathrm{PMC}}$ | 85% |
| IMC transmission, $T_{\mathrm{IMC}}$ | **95**% |
| IFI transmission, $T_{\mathrm{IFI}}$ | **95**% |
| Effective mode-matching, $\alpha$ | 93% |
| Power recycling gain, $G_{\mathrm{PRC}}$ | **40** |
| Arm cavity gain, $G_{\mathrm{arm}}$ | 280 |
| Photodetection chain losses, $\mathcal{L}_{\mathrm{PD}}$ | 5% |

Table 4.1: Optical losses at various points in the 40m interferometer. Numbers in **bold** are optimistic projections of what will be achievable, while other numbers have been measured in the current 40m interferometer.

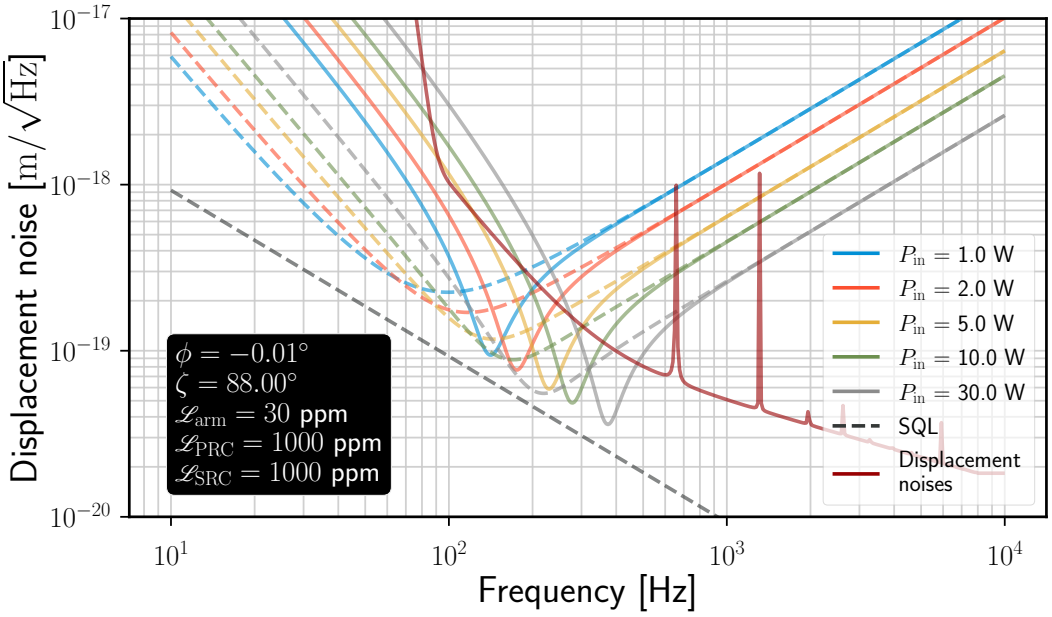


Figure 4.1: Quantum noise as a function of input power for the 40m. The parameters in Table 4.1 can be used together with Eq. (4.2) to map $P_{\rm in}$ in the legend to circulating power in the arm cavities. See text for what the solid and dashed lines indicate.

### 4.3 The need for high laser power and anticipated challenges

The full functional forms of the matrix elements in Eq. (4.1) are complicated algebraic functions of the interferometer's optomechanical parameters, and so are best explored numerically. Intuitively, we expect that high laser power is required in order to have appreciable optomechanical coupling, which is after all the physical mechanism responsible for generating the squeezed state in the arm cavity. To get an order of magnitude estimate, the shot noise of $P_{\rm arm} = 22\,\mathrm{kW}$ is $\approx 90\,\mathrm{nN}/\sqrt{\mathrm{Hz}}$. The radiation pressure from this generates an AC force on the mirror of $\approx 0.6\,\mathrm{fN}/\sqrt{\mathrm{Hz}}$ which in turn modulates the position of the mirror by $\approx 6\times10^{-21}\,\mathrm{m}/\sqrt{\mathrm{Hz}}$, and the phase of the light reflected off it by $\approx 10^{-14}\,\mathrm{rad}/\sqrt{\mathrm{Hz}}$. This simplistic analysis ignores the cavity enhancement effects that strengthen the optomechanical interaction - nevertheless, the result was a small number, even by interferometric standards.

Fig. 4.1 is a more quantitative visualization of how the input vacuum is transformed by the interferometer. Some notes on how this plot should be interpreted:

1. The *dashed* lines of the same color indicate the signal-referred, *unsqueezed* vacuum levels. Explicitly, following [54] but with $t_{\rm s}$ denoting the SRM amplitude transmissivity, the output field of the interferometer in response to

*unit strain* is given by

$$E_\zeta(\Omega) = \sqrt{2\hbar\omega_0}\frac{t_s e^{i\beta}\sqrt{2\mathcal{K}}\left[D_1 \sin\zeta + D_2\cos\zeta\right]}{M h_{\mathrm{SQL}}}. \tag{4.3}$$

Therefore, to refer the vacuum field with unit variance to equivalent DARM displacement, we simply divide it by this transfer function, and scale by the arm cavity length to convert from strain to displacement, i.e.

$$S^{\mathrm{sig-ref}}_{\mathrm{quantum}} = \sqrt{2\hbar\omega_0}\frac{L_{\mathrm{arm}}}{|E_\zeta(\Omega)|}. \tag{4.4}$$

2. The quantum noise, plotted as *solid* lines with the same color as their dashed counterparts, are also signal-referred, by dividing it with the optical transfer function of the interferometer. The procedure is the same as in Eqs. (4.3) and (4.4), except that the field divided by the DARM transfer function is the unsqueezed input vacuum field transformed by the interferometer. Explicitly,

$$S^{\mathrm{sig-ref}}_{\mathrm{vac}} = \sqrt{2\hbar\omega_0}\frac{L_{\mathrm{arm}}}{|E_\zeta(\Omega)|}\boldsymbol{C}\times\begin{bmatrix} a_1 \\ a_2. \end{bmatrix}. \tag{4.5}$$

3. Therefore, the vacuum state is "squeezed" wherever the solid lines dip below the dashed ones, and anti-squeezed when the reverse is true.

4. The "resonant dips" in the solid lines relative to dashed, which turn over more smoothly, are indicative of the optomechanical resonance caused by a small detuning of the SRC from $\phi = 0$. Note that these dips shift to higher frequencies as the laser power is increased, consistent with an optical spring of increasing rigidity being formed with higher powers.

5. Asymptotically, all the solid lines approach their dashed counterparts - this is consistent with the optomechanical coupling becoming negligible at high frequencies, due to the mechanical susceptibility of the suspended optics falling off as $f^{-2}$.

6. "Displacement noises" are the quadrature sum of (i) seismic noise (dominant below 100 Hz), (ii) coil driver noise (dominant between 100 – 500 Hz), (iii) suspension thermal noise (dominant at the resonant peaks at 650 Hz and harmonics thereof), and (iv) coating brownian noise (dominant above $\approx$ 500 Hz), which are considered as a minimal set of noises that limit the displacement noise sensitivity of the interferometer (in reality, we will likely have to deal with many other unaccounted noise sources).

7. Laser noises (i.e. intensity noise and frequency noise) on the field pumping the interferometer from the symmetric port are not included in this plot.

8. The SQL is just plotted for illustrative purposes. if the goal were to demonstrate a sub-SQL measurement, the optical configuration of the interferometer would again have to be modified.

While there is a significant range of frequencies for which the solid line dips below the dashed for even the lowest power plotted, suggesting we don't need 10 W of input power to the interferometer to measure optomechanical squeezing, the presence of classical noises leave very little margin. The errors between modelled displacement noises and what they are in reality also tend to be larger at lower frequencies. Furthermore, the likelihood of some un-modelled noise source coupling to the measurement is also higher at lower frequencies. Therefore, it is advantageous to try and make this measurement at as high a frequency as possible. Fig. 4.1 also raises the interesting possibility of being able to access a regime where the test-mass motion is dominated by radiation-pressure - these are when the green and grey lines are greater than the dark red "displacement noises". While this is undoubtedly an interesting regime, the fact that we need the "classical" noise of the interferometer to be at the level of $10^{-18}\,\mathrm{m}/\sqrt{\mathrm{Hz}}$ at 100 Hz makes it an exceedingly challenging prospect.

A brief word on some of the anticipated difficulties in working with such high laser powers resonant in the arm cavities: as described in Chapter 3, the highest powers achieved in the 40m interferometer's arm cavities at the time of writing is $O(1\,\mathrm{kW})$, which is at least one order of magnitude below what we need, to have a good chance of measuring a squeezed state. While the aLIGO interferometers have extensive experience dealing with thermal absorption (both in the substrates and dielectric coatings), as well as dynamical instabilities (both of the angular modes as well as dynamic parametric instabilities [67]), these are unexplored at the 40m. Unlike the LIGO sites, the 40m does not have any thermal actuators to correct for radius of curvature mismatches or thermally induced lenses, and there are no plans to install these - so there will be limited mitigation strategies available, and these effects are expected to pose a formidable challenge. There will, of course, be many other challenges, like implementing the BHD system necessary to read out arbitrary quadratures of the IFO's output field described in Chapter 5, and improving the sensitivity at $\approx 100\,\mathrm{Hz}$ by 4 orders of magnitude relative to what is shown in Fig. 3.18.

## 4.4 Prospects for measuring optomechanical squeezing in aLIGO

As illustrated in Fig. 4.1, the principal difficulty in making a *direct* measurement of an optomechanically squeezed field is to suppress all the other classical noise sources (such as thermal noise) in the measurement apparatus to a level low enough that the quantum noise becomes measurable. Some clever experimental techniques[5] can be used to relax the requirements on the required technical noise levels, but even so, they remain challenging to realize in the audio frequency band at room temperature, particularly in a table-top experiment. The Advanced LIGO interferometers at Hanford (H1) and Livingston (L1), on the other hand, can be reasonably considered as the state-of-the-art when it comes to suppression of technical noise levels, both displacement noises as well as laser frequency and intensity noise on the pump beam. So, will am attempt to measure an optomechanically squeezed state at L1 or H1 be significantly easier than at the 40m (C1)?

In attempting to answer this question, we must keep in mind that the primary objective of the H1 and L1 observatories is to measure astrophysical signals, and so we must restrict ourselves to the existing in-vacuum optical topology. In particular, the SRC is configured for operation in the RSE. Even though the difference between the RSE ($\phi_{\rm SRC} = 90°$) and ESR ($\phi_{\rm SRC} = 0°$) configurations is a $\lambda/4 \approx 250\,$nm change in the position of the SRM, which is easily within the available range by which the SRM can be actuated from outside the vacuum envelope, the problem is in sensing the SRC length using the PDH technique. As detailed in Eqs. (D.4) and (D.5), the macroscopic length of the SRC for each of these modes of operation differ by $O(1\,\text{m})$. Therefore, we restrict the analysis to $\phi \approx 90°$, allowing $\pm 10°$ of detuning around this nominal point, which is still within the regime where the SRCL PDH signal remains linear (i.e. within the SRC cavity linewidth of $\approx 33\,$nm for $T_{\rm SRM} = 32.5\%$). Another important difference between C1 and H1/L1 is that the mirrors of the arm cavities weigh $\approx 250\,$g in the former and $\approx 40\,$kg in the latter[6]. The optical power resonant in the arm cavities at H1/L1 is O(10)× that in the C1 arm cavities, but the important quantity is the optomechanical coupling $\mathcal{K}$, which depends on the ratio $P_{\rm arm}/m_{\rm TM}$, with $m_{\rm TM}$ being the mass of the mirrors. We expect that $\mathcal{K}_{C1} \approx 100\mathcal{K}_{H1/L1}$ at 100 Hz - the question is if the reduced optomechanical coupling will still generate a measurable optomechanically squeezed state.

[5] Measuring the output field of the IFO in a quadrature that is not the one most sensitive to DARM displacements is one such trick.

[6] One of the reasons the aLIGO design chose heavier mirrors relative to earlier generations of the detector was to make it more immune to radiation pressure effects, which ironically, is what we are trying to exploit in this discussion.

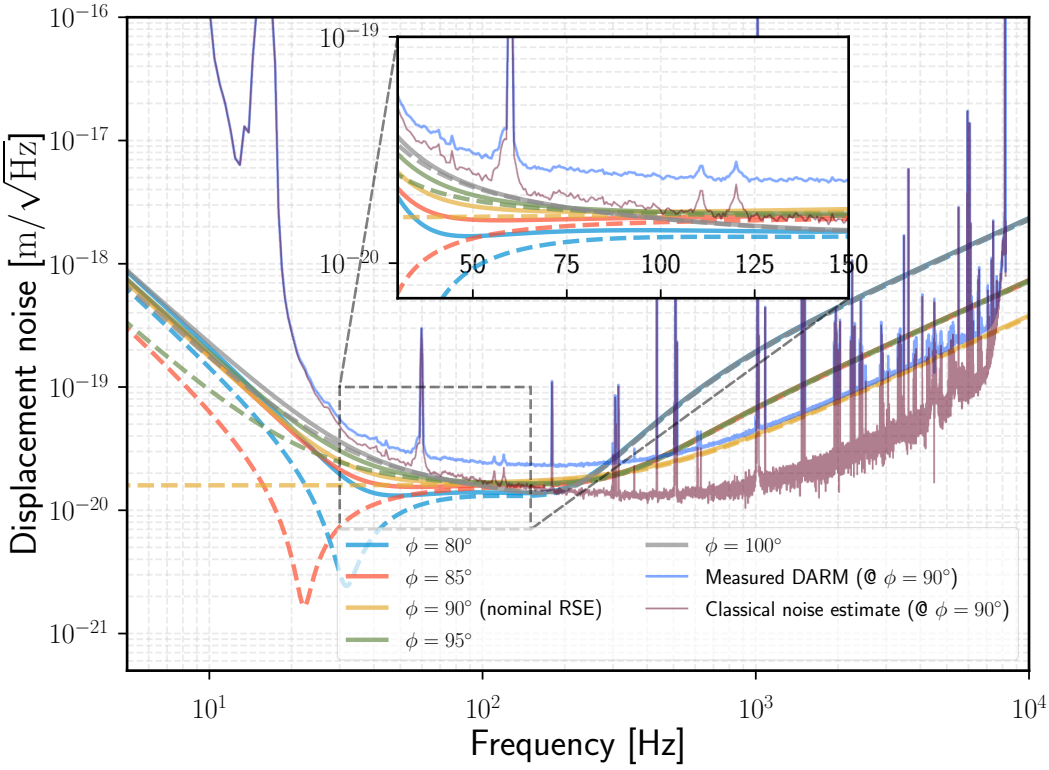


Figure 4.2: Modelled quantum noise in aLIGO as a function of SRC detuning. The "classical noise estimate" trace is reproduced from [47] - unlike Fig. 4.1 which plots only the displacement noises, this trace includes *all* noise sources other than quantum noise. The "masured DARM" curve is included to show that below $\approx$ 30 Hz, classical noises dominate the total measured noise. As in Fig. 4.1, solid lines indicate unsqueezed vacuum injected from the dark port transformed by optomechanical interaction with the interferometer, while dashed lines are signal-referred unsqueezed vacuum levels (plotted in the same color for a given $\phi$).

### 4.4.1 Prospects with DC readout

First, let us consider the case where the field is read out using a special type of homodyne readout, called "DC readout". This is the system currently implemented at H1 and L1 to measure the gravitational wave signal. It differs from a traditional homodyne detection setup in that the LO field used to measure the IFO's output field is sourced by introducing a deliberate *small* asymmetry in DARM, allowing a small amount of carrier light to leak out at the AS port. While this scheme offers many advantages, we are constrained to reading out fields at a fixed quadrature, namely $\zeta = \phi_{\mathrm{SRC}}$. As shown in Fig. 4.2, there aren't any clear frequency bands where the solid lines dip below the dashed - indeed, the classical noises can only be considered negligible relative to quantum noise above $\approx$ 200 Hz. This is not a surprising conclusion - as explained in Sec 3.2 of [60], in the RSE configuration with $\phi_{\mathrm{SRC}} \approx 90°$,

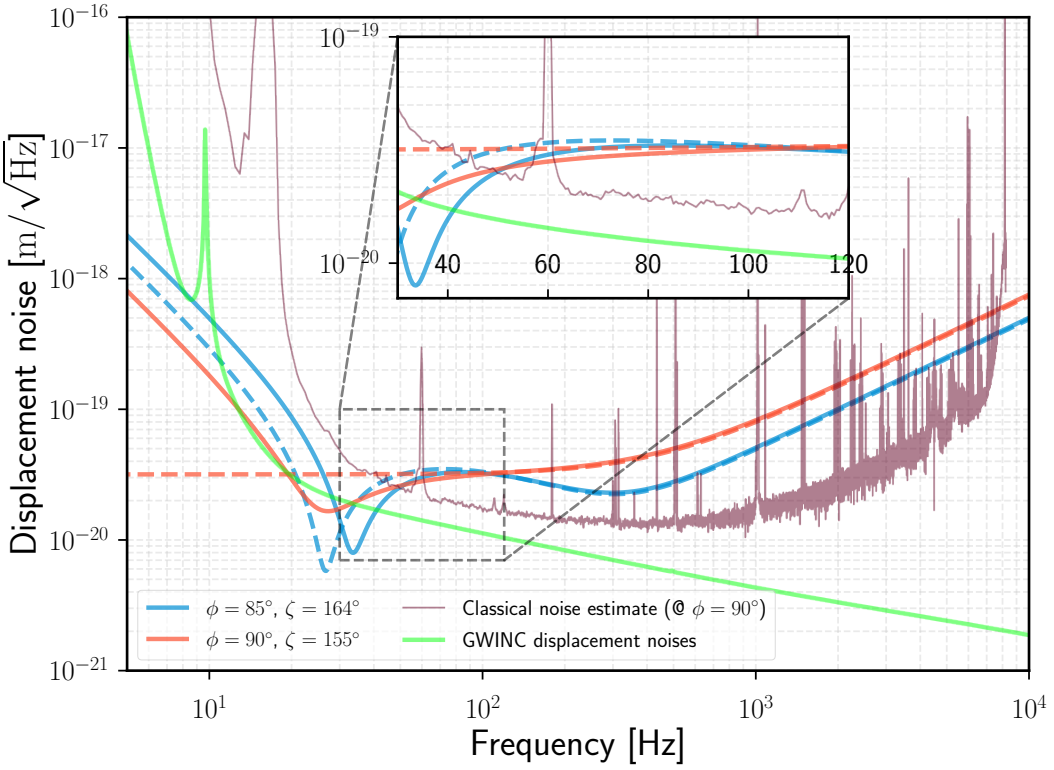


Figure 4.3: Modelled quantum noise in aLIGO as a function of SRC detuning, with BHD. Since the BHD system is a planned future upgrade, I have also assumed slightly different interferometer parameters in calculating these curves relative to Fig. 4.2. The input power to the interferometer is increased from ≈ 35 W to ≈ 50 W, and that the losses in the arm cavity are improved to $\mathcal{L}_{\rm rt}$ = 50 ppm. The net effect of these is to increase the circulating power in the arm cavities to ≈ 350 kW compared to ≈ 200 kW in Fig. 4.2. A "GWINC displacement noises" curve is included to indicate what the expected level of displacement noises should be, based on our best models and measurements of seismic and thermal noises.

readout quadratures $\zeta \approx 90°$ will exhibit varying amounts of *anti*-squeezing. For an interferometer configured close to the RSE state, our best chance of measuring an optomechanically squeezed state is in fact close to $\zeta = 0°$ or $\zeta = 180°$. With standard DC readout, we cannot access arbitrary quadratures. Therefore, we conclude that in its current configuration, measuring an optomechanically squeezed state is not possible at H1 or L1.

### 4.4.2 Prospects with BHD readout

Fortunately, H1 and L1 are undergoing an upgrade in the near future that will see both interferometers fitted with Balanced Homodyne Readout (see Chapter 5 for more details). There is still some uncertainty about the exact control scheme that

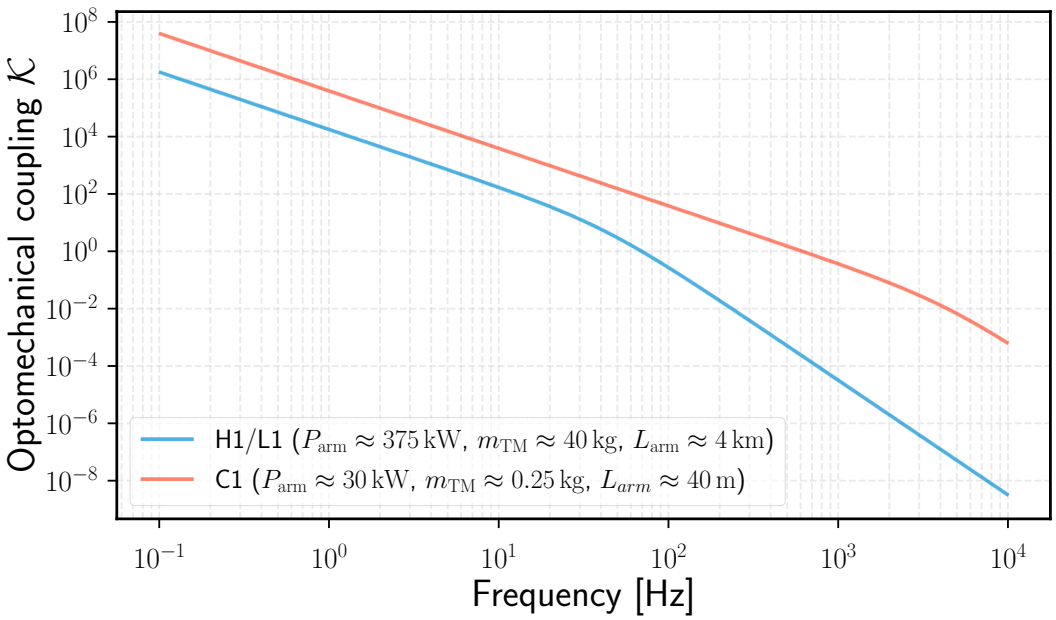


Figure 4.4: Optomechanical coupling coefficient for the C1 and H1/L1 interferometers. This parameter is only a function of the measurement frequency, arm cavity bandwidth, power in the arm cavity, and mirror mass.

will be used to keep the homodyne phase $\zeta$ fixed (i.e. the relative phase between the LO and IFO fields must be kept fixed), and what levels of RMS stability in $\zeta$ can be realistically achieved. Nevertheless, the BHD technique offers, at least in-principle, the ability to read out arbitrary quadratures of the IFO's output field. So, we repeat the analysis of Section 4.4.1, but explore homodyne angles near $\zeta = 0°$ or $\zeta = 180°$ instead. Fig. 4.3 shows the result of such a modeling effort. Two representative traces are shown here, with the $\phi = 90°$ trace showing that it may be possible to measure an optomechanically squeezed state even at the nominal SRC operating point, once we have access to arbitrary quadratures of the output field. The classical noise trace from [47] is included again, to show that above $\approx 50\,{\rm Hz}$, quantum noise will be the largest contributor to the readout, and indeed, the solid lines are lower than their dashed counterparts over some range of frequencies.

While the technical noise levels at 100 Hz are $\approx 100\times$ lower in the H1/L1 interferometers compared to C1, the factor by which the unsqueezed input vacuum field is optomechanically squeezed by H1/L1 is also smaller as shown in Fig. 4.4. The H1/L1 interferometers have $\approx 10\times$ smaller $P_{\rm arm}/m_{\rm TM}$ ratio than the *planned* C1 configuration, and the arm cavity bandwidth is also $\approx 100\times$ smaller. The net effect is that the optomechanical coupling strength at H1/L1, which is physically responsible for generating optomechanical squeezing, is $\approx 10\times$ smaller below the arm

cavity pole frequency of $\approx 40\,\mathrm{Hz}$, and drops off even more at higher frequencies. This is also the reason why the dips in the quantum noise curves in Fig. 4.1 are at higher frequencies than in Figs. 4.2 and 4.3 - since C1 has larger $\mathcal{K}$ out to higher frequencies than H1/L1, we can then try and find $\phi_{\mathrm{SRC}}, \zeta$ which allow measuring a squeezed state at those frequencies, where technical noise contributions are typically smaller than at lower frequencies. Therefore, it is difficult to make a definitive case that measuring even modest squeeze factors of $\approx 2\,\mathrm{dB}$ below vacuum will be significantly easier at H1/L1 than at C1.

## 4.5 Summary and future work

A planned experiment at the C1 interferometer to make a direct measurement of an optomechanically squeezed vacuum state was reviewed, with emphasis on why high laser powers and light test masses generate a more strongly squeezed state. The possibility of making this measurement at the H1/L1 interferometers *without significantly detracting from their primary objective of measuring astrophysical gravitational waves* was also considered - the conclusion was that the heavier mirrors at H1/L1 make it difficult to conclusively say that it will be easier than at C1. The experiment has been extensively simulated, and the C1 interferometer is currently undergoing an upgrade to fit it with BHD readout, an essential capability for measuring optomechanical squeezing. A laser amplifier is also being installed, to allow approx 10 W of laser power to be injected into the interferometer (c.f. the maximum of $\approx 1\,\mathrm{W}$ that is available at the time of writing). Many technical challenges remain in commissioning the interferometer and improving the noise performance, which will only become apparent once we start working with the upgraded configuration.

One may reasonably ask what the point is of using the C1 interferometer as an optomechanical squeezer. While the system as described in this chapter cannot reasonably be considered as an alternative to the non-linear crystal based squeezers currently employed at H1/L1, the optomechanical approach has a few notable advantages:

1. Current technology allows manufacture of super-polished mirrors with much lower optical loss than non-linear crystals.

2. An optomechanical squeezer generates an inherently frequency-dependent squeezed state. While it is not extensively analyzed in this thesis, this raises the possibility of tweaking the available degrees of freedom (various cavity detunings, transmissivities and mechanical susceptibilities of the mirrors) to

generate a squeezed field, which if injected into the AS port of a GW detector, already has the frequency dependence which minimizes quantum noise at all frequencies in the detection band. For the non-linear crystal squeezers, this functionality is achieved by starting with a field in only one quadrature (this is what is generated by the non-linear crystal), and reflecting it off a detuned filter cavity [49] to realize the appropriate frequency-dependent squeezed quadrature fields.

3. Optomechanical squeezing is in principle more wavelength agnostic than a non-linear crystal. An optomechanical squeezer designed to work at 1064 nm can be converted to work at other wavelengths (e.g. $\approx 2\,\mu$m that is the planned operating wavelength for future cryogenic interferometers [68]) by changing the dielectric coatings on the optics to have the appropriate reflectivity at the new operating wavelength. For a nonlinear crystal, the $\chi^{(2)}$ coefficient responsible for squeezed state generation can have strong wavelength dependence, and hence, a new operating wavelength may call for a new material.

4. Advances in material science might make it possible to realize suspensions for cavity mirrors that have arbitrary mechanical transfer functions. This would then offer great flexibility in tuning the frequency dependence of the optomechanically generated squeezed state.

The DRFPMI topology of C1 is almost certainly not the optimal one to serve as an optomechanical squeezer, but it is one that has received decades of attention from the modeling community, and so represents a reasonable starting point. In order to be considered a viable alternative to non-linear crystal squeezers for future GW detectors, substantial changes to the optical topology may have to be made.

*Chapter 5*

# BALANCED HOMODYNE DETECTION

Design studies for near term as well as long term upgrades to terrestrial gravitational wave detectors assume that the output field of the interferometer will be read out using a technique known as BHD. This technique itself is not new - however, applying it to gravitational wave detectors with suspended optics brings about a unique set of challenges, which will have to be overcome in A+ and future detectors. Getting practical experience on mitigating these problems in a prototype interferometer is, therefore, crucial.

This chapter is an abridged version of [69], which contains a detailed report of the requirements on the various subsystems in order to successfully implement a BHD readout - rather than reproduce that document in its entirety, I focus instead on some important noise considerations. At the time of writing, a major infrastructural upgrade is being prepared, so that the scheme can be tested out with the full complexity of a dual-recycled, suspended interferometer. This chapter also describes a proof-of-concept experiment that was done in the meantime, using the available infrastructure.

## 5.1 Optical beats for electric field detection

An interferometer appropriately configured produces an *electric field* at the AS port that is linearly proportional to the deviation (from 0) of the DARM degree of freedom. Physical detectors like photodiodes are sensitive to *intensity* rather than the electric field itself. Moreover, present-day photodiodes are incapable of responding to changes at the optical frequency of the laser field used ($\approx 282\,\mathrm{THz}$). The technique commonly used to circumvent this problem involves optical beats, where the weak signal field from the IFO is optically mixed (interfered) with a strong LO field (see Appendix C for more discussion on this subject). This process is mathematically described as

$$
\begin{aligned}
i_{\mathrm{PD}} &\propto \left|E_{\mathrm{LO}}\cos(\omega_{\mathrm{LO}}t) + E_{\mathrm{sig}}\cos(\omega_{\mathrm{sig}}t+\zeta)\right|^2 \\
&= E_{\mathrm{LO}}^2\cos^2(\omega_{\mathrm{LO}}t) + E_{\mathrm{sig}}^2\cos^2(\omega_{\mathrm{sig}}t+\zeta) \\
&+ E_{\mathrm{LO}}E_{\mathrm{sig}}\cos(\left[\omega_{\mathrm{LO}}+\omega_{\mathrm{sig}}+\zeta\right]t) \\
&+ E_{\mathrm{LO}}E_{\mathrm{sig}}\cos(\left[\omega_{\mathrm{LO}}-\omega_{\mathrm{sig}}-\zeta\right]t),
\end{aligned}
\tag{5.1}
$$

where $i_{\mathrm{PD}}$ is the photocurrent generated in a detection photodiode, $\omega_{\mathrm{LO}}$ and $\omega_{\mathrm{sig}}$ are the angular frequencies of the LO and signal fields respectively, and $\zeta$ is represents a relative phase between the two fields. For a laser wavelength of 1064 nm, $\omega_{\mathrm{LO}}$ and $\omega_{\mathrm{sig}}$ are $\approx 1.8\times10^{15}$ rad/s ($\omega_{sig}$ are audio frequency sidebands around the carrier frequency created by DARM fluctuations).

The last term in Equation (5.1) shows how phase fluctuations of the AS port field can be converted to lower frequencies ($\sim \omega_{\mathrm{LO}}-\omega_{\mathrm{sig}}$) at which photodetectors can respond directly to intensity fluctuations. Furthermore, the weak signal field $E_{\mathrm{sig}}$ can be amplified by the strong LO field $E_{\mathrm{LO}}$. Depending on the frequency of the LO field used, the detection scheme is referred to as homodyne (where the LO and signal fields have the same frequency) or heterodyne (where the LO and signal fields are offset by some amount, in the case of LIGO-like interferometers a few tens of MHz). In practise, the choice between the two available schemes is dictated by noise considerations.

## 5.2 RF readout, DC readout and motivation for BHD

The first generation of terrestrial interferometers used a heterodyne detection scheme, known as 'RF readout'. The LO field in this scheme consisted of a pair of phase-modulation RF sidebands around the carrier frequency, generated by an EOM. This scheme necessitates a second (electronic) demodulation of the photocurrent, since the optical beat frequency is $\approx$ 50 MHz while the GW signal information typically lies in the range 10 Hz – 5 kHz. The appeal of this scheme lay in the fact that the amplitude and phase noise in the LO field, offset from the carrier by a few MHz, could be stabilized to levels better than the carrier frequency itself, using passive filtering and active feedback loops.

However, because of technical noise considerations (a good summary may be found in [34]) and advances in laser frequency stabilization techniques, modern GW interferometers employ a form of homodyne detection known as 'DC readout'. A comprehensive discussion of the *fundamental* noise limitations associated with

heterodyne readout may be found in [70]. Although the shot-noise (due to the Poissonian statistics of photon arrival on a photodetector) associated with homodyne schemes is lower than heterodyne schemes, technical noise couplings, such as amplitude and phase noise of the local oscillator field, typically dominate. The DC readout scheme benefits from strong passive filtering by the narrow linewidth CARM cavity of the interferometer, and the resulting LO field has sufficiently low amplitude and phase noise so as to allow quantum noise limited sensing at high frequencies $f \gtrsim 100\,\mathrm{Hz}$.

While 'DC readout' is a form of homodyne detection, it requires a deliberate asymmetry to be introduced to the IFO's operating point in order to generate the LO field. This introduces additional noise couplings (a discussion of a recent study on one such coupling mechanism is [71]) that would be absent if the IFO were operated at a perfect dark fringe. In order to realize significant sensitivity improvement, these couplings will need to be minimized. Moreover, neither the DC nor RF readout schemes allows the phase $\zeta$ to be varied arbitrarily (at least, not without additional complexities being introduced, like a deliberate asymmetry in the upper and lower RF sideband amplitudes), which may be required for more exotic IFO configurations. For these reasons (discussed in more detail in [72]), there is an interest in investigating in detail the noise performance of a true homodyne readout scheme, in which the AS port is maintained dark for the carrier, and an LO field is sourced separately.

### 5.3 Noise requirements on fields

This chapter makes references to the "two-photon formalism", developed in [62, 63]. Since an electric field can be represented as a complex-valued quantity, it can be expressed as the sum of two modulations, one $\propto \cos(\omega t)$ and one $\propto \sin(\omega t)$ - in the literature, these are assigned the names "amplitude quadrature" and "phase quadrature", because an amplitude (phase) modulation applied to a hypothetical ideal, noiseless input field will create modulation sidebands exclusively in the amplitude (phase) quadrature (the detailed derivation may be found in Sec. 2.2.2 of [73] for example). This distinction is significant because it represents two different physical mechanisms of creating modulation sidebands - furthermore, an interferometer is capable of *converting* amplitude modulations to phase modulation, and vice-versa, due to radiation pressure effects and complex-valued reflectivities of optical cavities. While exact calculations are required to derive accurate noise models and couplings, there is a very useful diagrammatic way of representing the quadrature

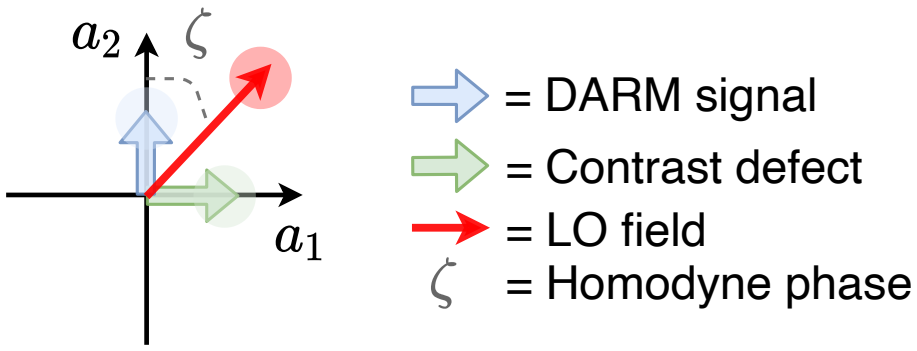


Figure 5.1: Quadrature fields for a DRFPMI operated in ESR mode. $a_1$ is usually referred to as the "amplitude quadrature", and $a_2$ the "phase quadrature". The lengths of the arrows denote the coherent amplitude $\propto \sqrt{P_i}$ where $P_i$ in the $i^{\text{th}}$ field, not drawn to scale here since typically $P_{\text{LO}} \gg P_{sig}$. The shaded circles at the ends of each arrow denote uncorrelated amplitude (axis along the arrow) and phase noise (axis perpendicular to the arrow) on each field - again, the sizes of the circles are for illustration purposes only. The angle $\zeta$, drawn here following Eq. 2.26 of [54] determines the projections of various signal and noise components to the readout.

fields as phasors, which provide some intuition and serves as the starting point for a detailed calculation. An example of such a diagram for the case of a DRFPMI operated in the Signal-Recycled ($\phi_{\text{SRC}} = 0°$) mode [54], with some important fields, is shown in Figure 5.1. This configuration is sometimes also referred to in the literature using the acronym ESR, which stands for Extreme Signal Recycling.

In a practical BHD implementation, the photocurrent readout scheme is different from what is stated in Eq. (5.1) - the signal and LO fields are optically mixed on a 50:50 beamsplitter, and the photocurrent at each output port, $i_{1,2}$ are read out. Following the derivation in Appendix A of [74], the difference photocurrent, $i_- \equiv i_1 - i_2$, has the form

$$i_- \propto 2E_{\text{LO}}E_{\text{sig}} \cos\zeta + 2E_{\text{LO}}\delta E^{\zeta}_{\text{sig}} + 2E_{\text{sig}}\delta E^{\zeta}_{\text{LO}}, \tag{5.2}$$

where the LO and signal fields have been decomposed into a DC component, $E_{\text{LO,sig}}$, and a time-dependent component, $\delta E^{\zeta}_{\text{LO,sig}}$, with the angle $\zeta$ defined as before to be the relative phase between the two fields (so $\zeta$ "picks out" the quadrature noise components of $\delta E_{\text{LO,sig}}$ that get amplified by the coherent amplitudes $E_{\text{LO,sig}}$). In a perfectly balanced interferometer, $E_{\text{sig}} = 0$, and so only the second term in Eq. (5.2) survives, with the signal field getting amplified by the coherent amplitude of the LO field.

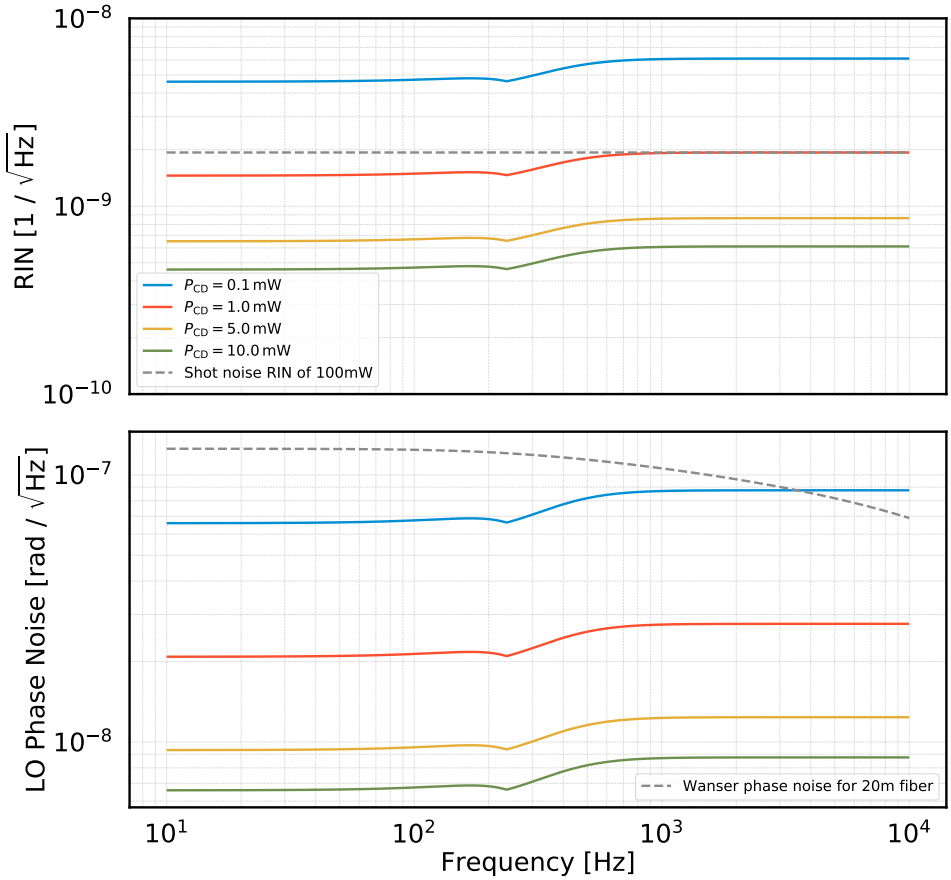


Figure 5.2: Requirements on the LO field noises for measuring optomechanical squeezing at the 40m. An arbitrarily chosen safety factor of 10 is assumed in these plots (i.e. if these noise levels are achieved, the LO noise contribution to the readout will be $< 10\%$ of the next highest noise contribution).

In practice, small asymmetries can lead to a non-zero power in the signal beam. For concreteness, let us consider the example of the "contrast defect" field shown in Figure 5.1 - this can arise due to reflectivity imbalances between the two arm cavities of the DRFPMI. If the coherent amplitude of this field is non-zero, then its projection onto the "LO field" phasor can amplify amplitude and phase fluctuations in the LO field, and the third term in Eq. (5.2) can become non-negligible. If we were only interested in the "DARM signal", which for the ESR configuration shows up entirely in the $a_2$ quadrature, we would choose $\zeta$ such that the red and blue arrows are collinear. In this case, the contrast defect field amplifies *phase fluctuations* in the LO field and adds a noise term to the readout. If, on the other hand, we want to make a measurement very close to the $a_1$ quadrature and choose $\zeta$ accordingly, then the contrast defect would amplify *amplitude fluctuations* in the LO field and contribute noise to the readout.

The requirements for the case of phase quadrature readout $\zeta = 0°$ is analyzed in detail in [69], so I will focus here on the near-amplitude-quadrature readout case, with $\zeta \approx 88°$, which is what is proposed for the optomechanical squeezing experiment at the 40m. Results from numerical modeling are shown in Fig. 5.2. The requirement was that the contribution of the LO noises to the readout was a factor of 10 below the next-dominant noise source at each frequency, which was assumed to be coil-driver noise at mid frequencies and quantum noise at high frequencies - this is why the graph has a discontinuous profile around $\approx 200$ Hz, as the envelope of the next-dominant noise source follows this profile. Assuming we have 1 mW of contrast defect light, and focusing on a frequency of $\approx 200$ Hz (which is where we expect to be able to be sufficiently sensitive to have any chance of measuring a squeezed output field from the interferometer), the requirements on the LO field may be summarized as $\underline{\text{RIN} < 2 \times 10^{-9}/\sqrt{\text{Hz}}}$ and $\underline{\delta\phi \lesssim 3 \times 10^{-8}\text{rad}/\sqrt{\text{Hz}}}$.

These, and in particular the requirement on the RIN, are extremely challenging. Any intensity stabilization servo (ISS) will be limited to stabilizing the intensity to the level of the sensing photodiodes, and to achieve the required stabilization, we need to sense $\approx 100$ mW of light (dashed grey line in upper plot of Fig. 5.2). Handling such high power levels with low-noise sensing photodiodes will require considerable engineering. One possible way to relax the requirements on an external ISS is to pick off the LO field from the PRC - once the interferometer is locked, the laser frequency is stabilized to the CARM DoF. The *passive* filtering offered by the CARM cavity, whose linewidth is $\approx 20$ nm at C1, has a $1/f$ corner frequency of $\approx 100$ Hz. As a result, the stabilization of intensity fluctuations due to the passive filtering action at C1 is insufficient to meet the intensity noise requirements on the LO field - an active stabilization servo will be needed to supplement the passive filtering. For comparison, the aLIGO interferometers with 4 km long arm cavities move this corner frequency down by a factor of 100, and the CARM linewidth is $\approx 0.7$ Hz - so there is significant *passive* filtering even at the low end of the detector's bandwidth of $\approx 20$ Hz. Nevertheless, even at H1 and L1, an active intensity stabilization servo will be needed to meet the requirements on the main interferometer beam's intensity noise.

It is expected that the phase noise requirement will be easier to satisfy (at least, at 200 Hz), provided all the optics are suspended. $30\,\text{nrad}/\sqrt{\text{Hz}}$ corresponds to $\approx 3 \times 10^{-15}\,\text{m}/\sqrt{\text{Hz}}$ of displacement noise, and the isolation provided by the suspensions and passive seismic isolation stacks available at the 40m are expected to provide

$>$ 200 dB of isolation from ambient ground motion at 200 Hz. A dashed grey line labelled "Wanser phase noise for 20m fiber" is included in the lower plot in Fig. 5.2 - an in-air length of optical fiber was being considered as an option to deliver the LO field to the photodetection chain, but as this modeling shows, it is not a feasible option for any reasonable amount of contrast defect light expected at the 40m. Furthermore, it is extremely unlikely that the fundamental thermo-optic noise of the optical fiber quantified by the Wanser model [21, 22] will in fact be the dominant noise source if such a delivery mechanism were pursued - acoustic vibrations due to imperfect shielding is likely to manifest at a much higher level. This reveals an important advantage of other length sensing techniques, such as heterodyne PDH locking or DC readout [34], which inherently have the LO field and signal field co-propagate along the same optical path to a sensing photodiode - no significant effort has to be made to stabilize the *relative* phase between the LO and signal fields. One of the questions being studied in detail at the time of writing is whether all the extra engineering complexities brought about by changing the readout scheme of the aLIGO interferometers from DC readout to BHD is justified[1], and offers a *measurable* performance improvement.

## 5.4 Interferometer contrast defect

There is considerable uncertainty on what is a realistic amount of contrast defect light we can expect at the 40m. It is not easily directly measured because (i) we lack an OMC, which would allow the output field of the interferometer to be scanned, (ii) the current configuration of the PRC and SRC, with the flipped folding mirrors, are a *known* source of degradation of the mode-matching, and (iii) the angular fluctuations of optics in the locked interferometer has not been stabilized at the time of writing. Nevertheless, the discussion of the previous section has made it clear that is is an important parameter in setting the requirements on the LO field. In this section, an attempt is made to numerically model the expected amount of contrast defect light, based on reasonable guesses.

### 5.4.1 Definitions

The term "contrast defect" is confusingly used to refer to several different effects in the LIGO literature. For the purposes of this section, I define the contrast defect, $C$, as the ratio of the amount of light leaking to the dark port of the interferometer to

[1] Although the discussion in this section has been focused on the $\zeta = 88°$ case, the LO phase stability requirements for a BHD system at aLIGO are also extremely challenging.

the power circulating in the interferometer. Mathematically,

$$C = \frac{\int_S dS(E_x - E_y)}{\int_S dS(E_x + E_y)}, \tag{5.3}$$

where the integrals are over the spatial coordinates of the detecting element, while $E_x$ and $E_y$ denote the electric fields from the X and Y arm cavities at the beam splitter. Adding a signal recycling mirror will merely scale this number.

Clearly, there are a number of factors that determine the amount of contrast defect light. These are:

1. Imbalance between the ITM transmissivities.
2. Imbalance between the ETM transmissivities.
3. Imbalance between the round-trip arm cavity loss (finesse imbalance).
4. Imbalance between the reflectivity and transmissivity of the beamsplitter (e.g. due to an AR coating).
5. Imperfect spatial overlap of the modes from the two arm cavities at the beamsplitter.

The first three collectively result in an asymmetry of the reflectivities of the arm cavities. In the following subsections, we analyze these effects quantitatively. It is evident from Eq. (5.3) that in the absence of any asymmetries between the arm cavities, when the interferometer is locked on a dark fringe, there is no (carrier) light at the antisymmetric port. Moreover, the frequency dependence of a given asymmetry on the interferometer noise is dependent on where the asymmetry enters the system.

### 5.4.2 DC analysis

Fluctuations in the LO field are amplified by the DC contrast defect light. Hence, we would like to know how much asymmetry is permissible such that we end up with less than 1 mW of DC contrast defect light at the antisymmetric port, *in the TEM00 mode of the OMC*. Let us first consider the first three sources of asymmetry listed in Section 5.4.1. We allow the test mass transmissivities and intracavity loss to vary about their nominal value by some realistic amount, and look at the variation in the arm cavity power reflectivity. The results are summarized in Fig. 5.3, while

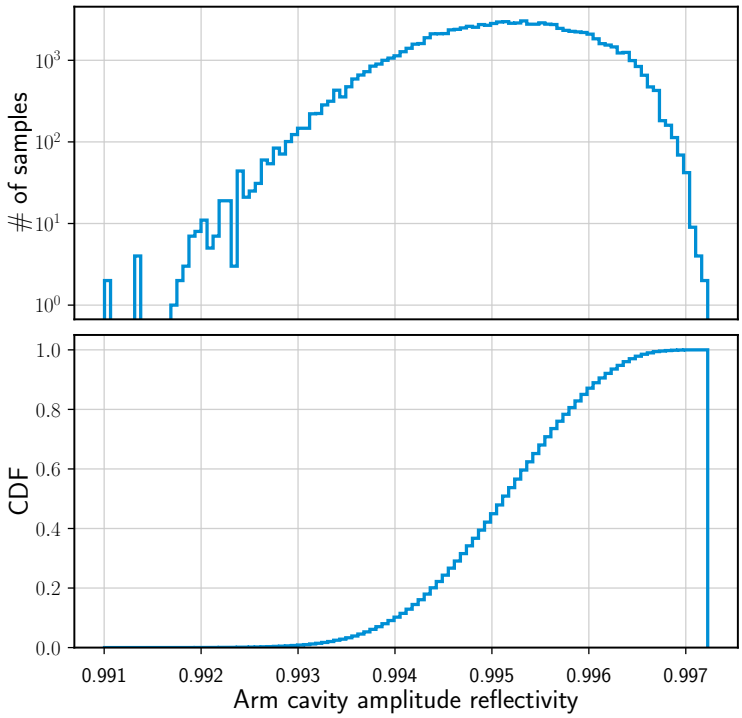


Figure 5.3: Variation in the arm cavity reflectivity as a result of introducing some asymmetry to the test mass transmissivities and the intracavity loss. Perturbations are applied about the nominal values of these parameters, namely $T_{\mathrm{ITM}} = 1.384\%$, $T_{\mathrm{ETM}} = 13\,\mathrm{ppm}$, $\mathcal{L}_{\mathrm{rt}} = 20\,\mathrm{ppm}$. The distributions of the applied perturbations are shown in Fig. 5.4.

.

the range of parameters scanned are shown in Figure 5.4. The $1\sigma$ ($3\sigma$) level of variation in the arm cavity reflectivity is found to be 800 ppm (2400 ppm). The amount of light that leaks from the symmetric port to the AS port as a function of the arm cavity reflectivity imbalance is shown in Fig. 5.5.

To translate this to the amount of light at the antisymmetric port, we need to know the transmissivity from the symmetric port to the antisymmetric port. This is given by

$$t_{\mathrm{DRFPMI}}^{\mathrm{sym}\to\mathrm{AS}} = \frac{e^{i(\phi_{PRC}+\phi_{SRC})}e^{2i\phi_-}(r_X - r_Y)t_P t_S}{2e^{2i(\phi_{\mathrm{PRC}}+\phi_{\mathrm{SRC}})} + 2r_P r_S r_X r_Y e^{4i\phi_-} - e^{2i\phi_-}(r_X + r_Y)(r_S e^{2i\phi_{\mathrm{PRC}}} + r_P e^{2i\phi_{\mathrm{SRC}}})}\,. \tag{5.4}$$

Here, $\phi_-$ is the Schnupp asymmetry. The phases $\phi$ are one-way phases. Since we have the PRC resonant for the carrier, and the SRC nearly so (a slight detuning of $\approx 1^\circ$ of the SRC is proposed to enhance the measurable squeezing), we can simplify

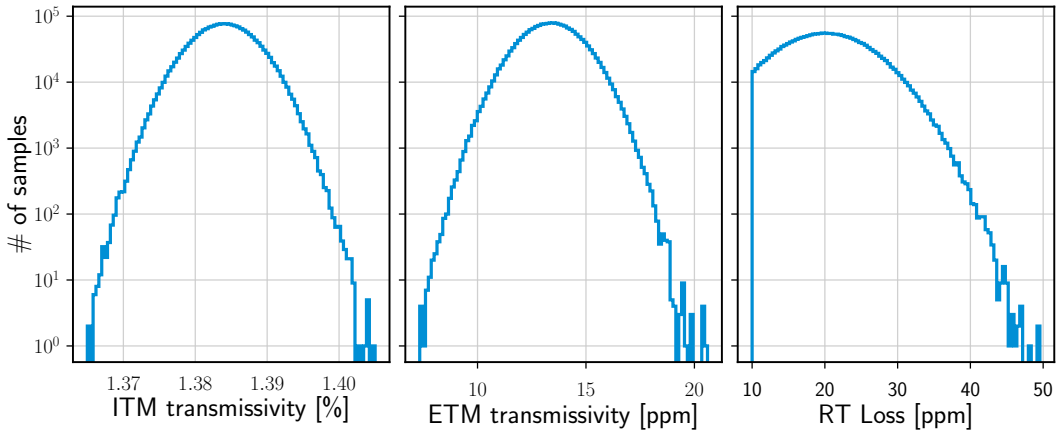


Figure 5.4: Distribution of the parameters sampled to investigate the effect of asymmetry in the test mass transmissivities and intracavity loss on the arm cavity transmissivity. Note that the round trip loss is constrained to be $> 10$ ppm in the sampling process.

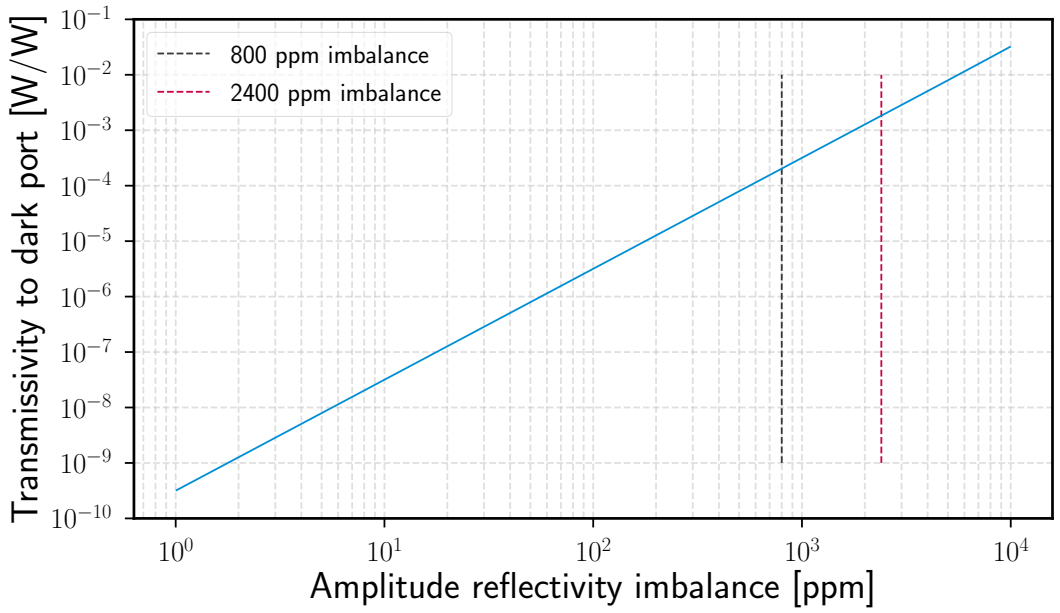


Figure 5.5: Contrast defect as a function of arm cavity reflectivity imbalance.

the above expression somewhat (for the carrier field) to

$$t_{\mathrm{DRFPMI}}^{\mathrm{sym}\to\mathrm{AS}} \approx \frac{t_P t_S (r_X - r_Y)}{2 + 2 r_P r_S r_X r_Y - (r_P + r_S)(r_X + r_Y)} \,. \tag{5.5}$$

The amount of carrier light that leaks from the symmetric to AS port of the IFO as a function of the arm cavity reflectivity is shown in Fig. 5.5, with the $1\sigma$ and $3\sigma$ levels inferred from the MCMC simulation indicated. From this admittedly

simplistic analysis, assuming 10 W of power is incident on the PRM, it appears very likely that $> 1$ mW of contrast defect light will be present at the AS port.

Next, we consider the contribution to the contrast defect from the mismatched RoCs of the two ETMs (since the 40m ITMs are flat). In other words, HOM generation due to misalignments are neglected. Hence, per [28], we only need to consider the $\mathrm{TEM}_{02}$ and $\mathrm{TEM}_{20}$ modes (to lowest order). [75] derives the analytic form of this by analyzing the reflectivity of the arm cavity for an input beam whose waist size differs from that of an arm cavity eigenmode (the assumption being that it is perfectly matched to the other arm). We adapt this analysis, incorporating

1. SRC cavity gain for the 00 and 02/20 modes.
2. Lossy arm cavities.
3. Complex reflectivities based on Gouy Phase (i.e. fields are not assumed to be exactly resonant / anti-resonant).

The relevant relation for this analysis from [75]:

$$C = 1 - \frac{2\Re[r_a \alpha_{00}]}{|r_a|^2 + |\alpha_{00}|^2 + 2|\alpha_{02}|^2}, \text{ where} \alpha_{00} \equiv r_a c_{00}^2 + 2\hat{r}_a c_{02}^2, \quad \alpha_{02} \equiv r_a c_{00} c_{02} - \hat{r}_a c_{02} c_{22}. \tag{5.6}$$

For this analysis, we are more interested in the actual amount of power leaking to the dark port when locked on the dark fringe, in the IFO $\mathrm{TEM}_{00}$mode. The power at the dark port is given by

$$P_{\mathrm{dark}} = g_s^2 P_{\mathrm{in}} \left( \frac{|r_a|^2}{4} + \frac{|\alpha_{00}|^2}{4} - \frac{1}{2}\Re[r_a \alpha_{00}] \right) + \hat{g}_s^2 P_{\mathrm{in}} \left( \frac{|\alpha_{02}|^2}{2} \right), \tag{5.7}$$

where we have allowed for $\alpha$ terms to be complex. The first term contributing to the $\mathrm{TEM}_{00}$ mode, and the second term being in the $\mathrm{TEM}_{02}$ and $\mathrm{TEM}_{20}$ modes, and $g_s$, $\hat{g}_s$ signify the mode healing/harming due to the SRC (for the fundamental and higher order modes respectively). For a first pass, $r_a = 1$, $\hat{r}_a = -1$ (for a more realistic calculation, we will need to take into account the arm cavity losses and the non-perfect rejection of the $m + n = 2$ mode). Of the contrast defect light, only the $\mathrm{TEM}_{00}$ part will pass through the OMC with high transmission, and hence, contribute to shot noise on the BHD photodetectors (for a first pass, we assume OMC completely rejects the other junk light). The coupling coefficients $c_{ij}$ are

given in the appendix of [75]. There are only 3 unique ones, the other coefficients are all related to these three by a sign change. The three relevant ones are

$$c_{00} = \frac{2\omega_0\omega_1}{\omega_0^2+\omega_1^2}, \quad c_{02} = -\frac{\sqrt{2}\omega_0\omega_1(\omega_0^2-\omega_1^2)}{(\omega_0^2+\omega_1^2)^2}, \quad c_{22} = -\frac{\omega_0\omega_1(\omega_0^4-10\omega_0^2\omega_1^2+\omega_1^4)}{(\omega_0^2+\omega_1^2)^3}, \tag{5.8}$$

where $\omega_0$ is the input beam waist (assumed to be matched to one of the arms) while $\omega_1$ is that for the other arm.

The last piece is to define the waist size for the $\mathrm{TEM}_{00}$ eigenmode of a linear two-mirror cavity of length $L$, with mirrors whose RoCs are $R_1$ and $R_2$, given by

$$\omega_0 = \sqrt{\frac{\lambda L}{\pi}}\left(\frac{g_1 g_2(1-g_1 g_2)}{(g_1+g_2-2g_1g_2)^2}\right)^{\frac{1}{4}}, \text{ where} g_i = 1-\frac{L}{R_i},\ i = 1,2\ . \tag{5.9}$$

Figure 5.6 shows the amount of contrast defect, as defined in Equation (5.3), as a function of the RoC of one of the test masses, with that of the other held fixed at 60.2 m. A dashed vertical line is used to indicate the ex-situ measured value of the RoC of the other optic.

To summarize, the requirement that the contrast defect be less than 1 mW of power at the AS port will be a very challenging one to satisfy. A measurement of the IFO's output field needs to be performed to refine these estimates further, and in the process, revise the requirements on the LO field quadrature noises described in Section 5.3 ias necessary.

## 5.5 Output mode cleaner cavities

The OMC that we used for the 40m BHD experiment is based on the aLIGO design: a bowtie configuration with two flat mirrors and two curved mirrors, a finesse of $\sim 400$, and an angle of incidence of $\sim 4°$. This section reviews design considerations for the OMCs.

### 5.5.1 OMC cavity functions

The OMC is a cavity that is installed between the IFO output and the readout DCPDs. The functions of the OMC are:

1. To filter out the RF sideband frequency content from the AS and LO fields.
2. To filter out higher-order HG modes of the carrier field, that may be generated due to mismatched optical cavities and/or misalignments.
3. Transmit the DARM signal to the DCPDs with as little optical loss as possible.

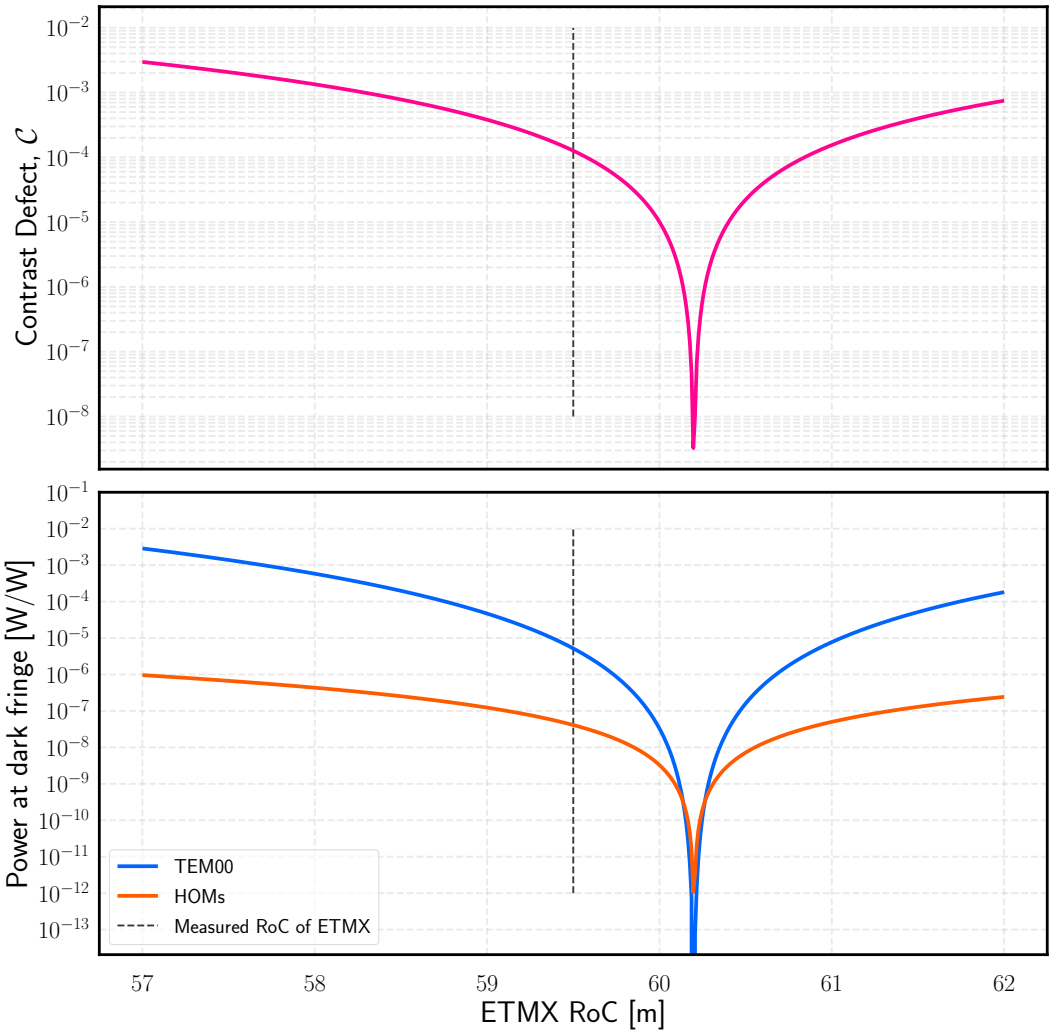


Figure 5.6: Contrast defect as a function of the RoC of the ETMs. The simulation is done with a numerical model where the RoC of ETMY is fixed to 60.2 m, while the RoC of ETMX is varied.

### 5.5.2 Design considerations

This is a brief overview of the design thought process.

Why does the OMC have four (and not fewer or more) mirrors? We need at least two mirrors to form an optical cavity. The simplest cavity one can imagine is the linear two mirror cavity. This is not a good choice for the OMC because the amount of backscattered light increases exponentially with smaller angles of incidence. Even with state-of-the-art AR coatings, a linear cavity would result in large backscatter into the IFO AS port, which would create additional noise.

The next simplest option is the three-mirror folded cavity, like the IMC. However, an optical cavity with an odd number of mirrors has a complicated HOM resonance

structure (relative to its even number mirror counterpart). Since one of the purposes of the OMC is to filter out unwanted HOMs, such an extra complication is undesirable. Which brings us to the choice of four-mirror optical cavity where the additional complexity of the HOM resonance structure is avoided.

By having a small but non-zero angle of incidence, $\theta_i$, the direct backscatter can be attenuated, since the BRDF of super-polished mirrors is expected to fall off as $1/\theta_i^2$. Finally, with super-polished mirrors each having optical loss at the level of 5 ppm per bounce for a 500 $\mu$m beam, it is possible to have a cavity with a finesse of $\approx 400$ for sufficient filtering of unwanted fields, while still achieving $\geq 99$ % transmission of the DARM signal field.

Having decided on the number of mirrors forming the OMC cavity, the design problem is then to decide the geometry of the cavity, and the power transmissivities of the mirrors. A schematic drawing of the OMC optical layout is shown in Figure 5.7. For simplicity, we stick to the aLIGO OMC design [76], with two flat mirrors and two curved mirrors. Furthermore, for a start, we preserve the aLIGO OMC choice of cavity finesse, $\mathcal{F} \approx 400$, and angle of incidence, $\theta_i \approx 4°$. The design problem then amounts to the following: what should the values of the parameters $L_1$ and RoC be, such that the functions outlined in Section 5.5.1 are satisfied?

*For cost and timeline-related reasons, a decision was made to use the spare OMC cavity optics (originally manufactured with specs for the aLIGO IFOs) for the 40m BHD experiment*. This removed an additional degree of freedom, RoC, from the design space. The problem then amounts to determining the round-trip cavity length for the OMC which provides adequate filtering of the RF sidebands and HOM content of the 40m IFO, as described in Section 5.5.3.

### 5.5.3 OMC cavity filtering performance

#### Incident mode spectrum

The filtering performance of the OMC is determined by the cavity finesse. However, the actual amount of junk light that makes it onto the OMC DCPDs is dependent on the amount incident as well.

For the aLIGO OMC, the filtering requirement is principally on the AS beam from the IFO. The recycling cavity lengths are chosen in such a way that the $f_2$ sideband is critically coupled to the dark port, while the $f_1$ sideband mostly remains in the symmetric side (though the leakage to the dark port isn't zero). Consequently, the

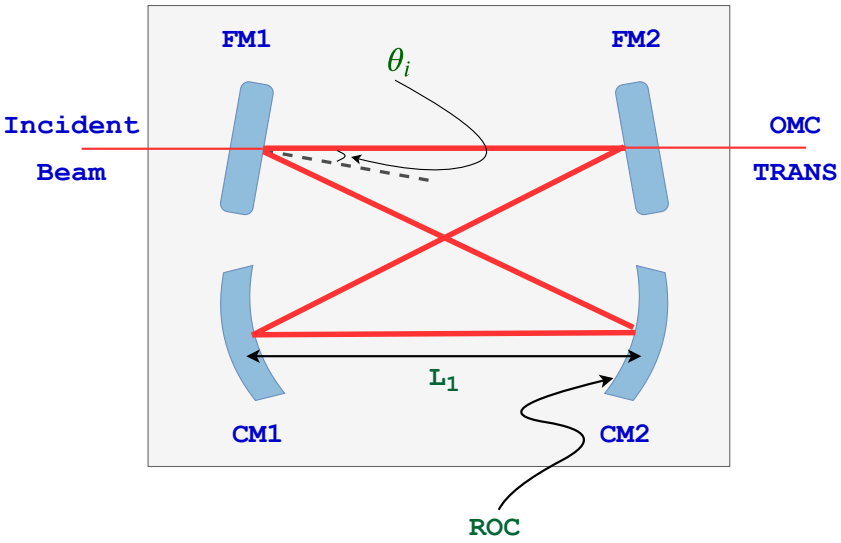


Figure 5.7: Proposed OMC optical layout. To preserve symmetry, the mirrors labelled FM1 and FM2 are flat, and CM1 and CM2 have identical curvatures. The geometrical design parameters, namely the angle of incidence $\theta_i$, the length $L_1$, and the radius of curvature of the curved mirrors, ROC, are indicated in green. In addition to these, the OMC design has to determine the power transmissivities of the FMs, $t_{\mathrm{F}}^2$ and CMs, $t_{\mathrm{C}}^2$.

following power law model was assumed for the power fraction in various carrier HOMs:

$$P_{f_0}(n)\,[\mathrm{W/W}] = \begin{cases} 0 & n = 0, \\ 7 \times 10^{-5} & n = 1, \\ 1.8 \times 10^{-(3+\frac{n}{4.8})} & n \geq 2. \end{cases} \tag{5.10}$$

For the $f_2$ sideband, the following model was assumed for transmission from the PRC to the SRC (the SRC cavity's resonance structure is neglected):

$$T_{f_2}(n) = \begin{cases} 1 & n = 0, \\ 1.7 \times 10^{-1} & n = 1, \\ 7 \times 10^{-(1+\frac{n}{2})} & n \geq 2. \end{cases} \tag{5.11}$$

Finally, for the $f_1$ sideband, it was assumed that $T_{f_1} = T_{f_2}/1000$. This model neglects (i) mode-healing / mode-harming effects of the SRC, and (ii) the actual transmissivity of the $f_1$ sideband with the SRC included. For the BHD setup, the OMC also needs to clean up the LO field, which is in fact picked off from the

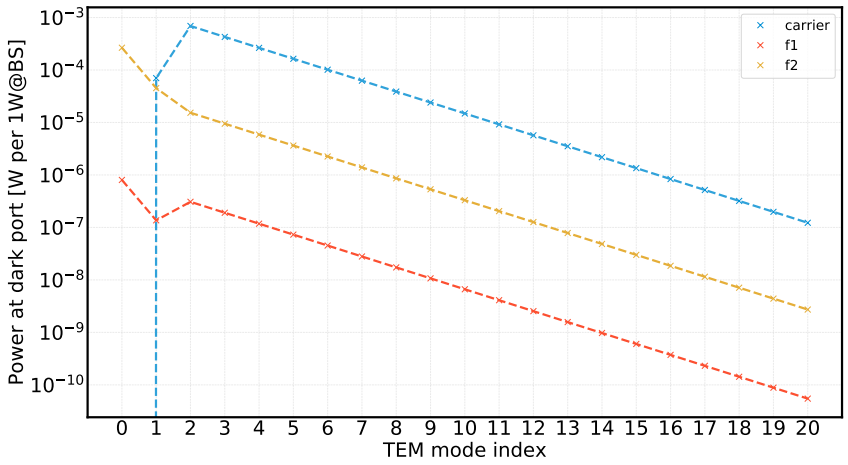


Figure 5.8: Assumed model spectrum of power in HOMs. It must be emphasized that this model is extracted from a mode-scan done on the eLIGO interferometer's output field. The 40m interferometer may have a different spectrum, in which case the transmission of the OMC for HOMs will have to be re-evaluated.

symmetric side of the interferometer. At first glance, this may suggest that the LO field will have strong $f_1$ content because the PRC is designed to be resonant for this field. However, assuming that the LO field is picked off from the transmission of a HR mirror (as is proposed), we estimate that the power of the $f_1$ content in the LO beam will be $\approx$ 1000$\times$ lower than the power of the $f_2$ field in the antisymmetric port beam, and hence, we did not change the spectral model assumed. The model assumed is shown in Figure 5.8.

### Cavity round-trip length

The cavity round-trip length should be chosen such that the RF sideband $\mathrm{TEM}_{00}$ modes are not resonant in the OMC when the carrier is resonant. For the 40m, the RF sideband frequencies are (i) $f_1 = 11.066209\,\mathrm{MHz}$ and (ii) $f_2 = 5 \times f_1$.

To convert frequency offset from the carrier to phase offset, we use the relation

$$\phi_{\mathrm{RT}}^{\mathrm{SB}} = \frac{2\pi f^{\mathrm{SB}} L_{\mathrm{RT}}}{c}. \tag{5.12}$$

The OMC *power* transmissivity is given by

$$T_{\mathrm{OMC}} = \left| \frac{t_{\mathrm{F}}^2}{1 - r_{\mathrm{C}}^2 r_{\mathrm{F}}^2 e^{-i\phi}} \right|^2, \tag{5.13}$$

so we can just examine what this looks like for the $\mathrm{TEM}_{00}$ mode of the RF sidebands as a function of the round-trip length of the cavity.

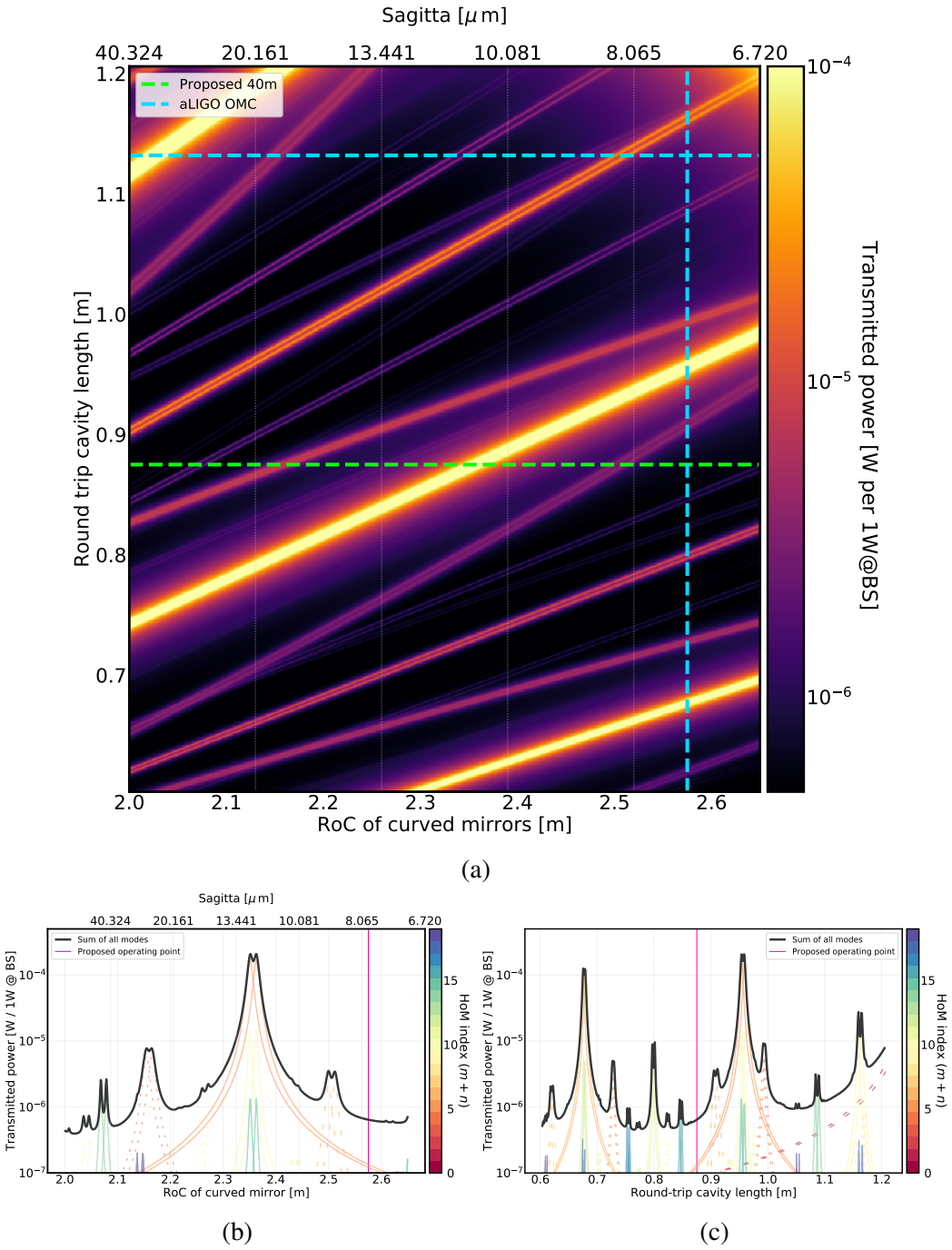


Figure 5.9: OMC design modeling results. Figure 5.9(a) Heatmap of the OMC transmission as a function of the parameters $L_1$ and ROC. For the 40m RF sideband frequencies, the appropriate choice of $L_1$ and ROC are 0.875 m and 2.575 m respectively, with $\theta_i = 4.042°$. Figures 5.9(b) and 5.9(c) show one-dimensional slices of the heatmap in Figure 5.9(a). The recommended design parameter choice is indicated by a vertical pink line. The various HOM resonances are shown by colored lines, with their sum shown in a thick grey line. The different linestyles are used to indicate different sideband frequencies.

### Higher-order modes

Equation 5.12 can be generalized for higher order HG modes by realizing that the $mn-$ th HOM experience an *additional* phase shift of $(m+n)\times\zeta$ relative to the $\mathrm{TEM}_{00}$ mode, with $\zeta_{\mathrm{RT}}$ being the round-trip cavity Gouy phase which can be calculated from an ABCD matrix (not to be confused with $\zeta$, the homodyne phase, used elsewhere in this thesis). This number is always additive, whereas the phase offset from the carrier due to the field being an RF sideband is a *signed* number, depending on whether we are considering the upper or lower sideband. So the $\phi$ that enters the cavity transmission equation may be broken up into the following components:

$$\phi_{\mathrm{RT}}^{mn}(f) = \phi_{\mathrm{RT}}^{00}(0) + \frac{2\pi f_{\mathrm{RF}}^{\mathrm{SB}} L_{\mathrm{RT}}}{c} + (m+n)\zeta_{\mathrm{RT}}. \tag{5.14}$$

Plugging this into Eq. 5.13 for $T_{\mathrm{OMC}}$, we get the power transmissivity of the OMC cavity.

The outcome of the modeling is shown in Figure 5.9, with the suggested operating point indicated. We chose to preserve the curvature specification for the mirrors to be identical to the aLIGO OMC [76], 2.575 m, and varied the cavity length to account for the different sideband frequencies at the 40m. **The cavity round-trip length is chosen to be 0.875 m**. For comparison, the aLIGO OMC design parameters are indicated by dashed cyan lines. The one-dimensional slices along the dashed green lines are shown in Figure 5.9(b) and Figure 5.9(c), with the vertical pink lines indicating the suggested design parameters.

## 5.6 Quadrature noise due to scattered light

The target sensitivity for the BHD readout at the 40m is $\approx 10^{-11}\mathrm{rad}/\sqrt{\mathrm{Hz}}$. In order to achieve such levels of precision, any stray light fields that manifest on the detection photodiodes must be carefully controlled (since these fields will generate a photocurrent, but carry no useful information about the DARM DoF). In the LIGO parlance, such stray light fields are referred to as "scattered light", and are known to limit the sensitivity of the LIGO interferometers if no mitigation strategies are implemented [9].

For BHD implementation, there are multiple possible pathways through which scattered light can manifest as noise in the readout. Three such examples are shown in Figure 5.10. For the purposes of this discussion, we may neglect the leftmost

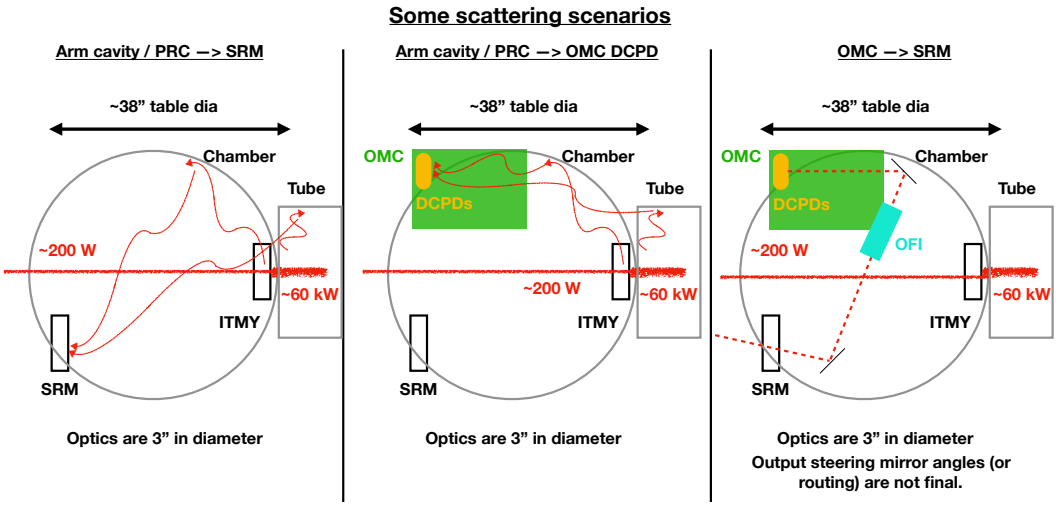


Figure 5.10: Pathways through which scattered light can degrade the interferometer sensitivity to DARM.

panel, as it does not directly set a requirement for the BHD system. The middle panel depicts the pathway where light is directly scattered out of the FP arm cavities and PRC onto the OMC DCPDs, and is henceforth referred to as direct backscatter. It is discussed in Section 5.6.1. The rightmost panel depicts a pathway whereby the *resonant* counter-propagating mode of the OMC contributes a field entering the antisymmetric port of the interferometer, in addition to the (unsqueezed or squeezed) vacuum field. This mechanism will be henceforth referred to as OMC backscatter, and is discussed in Section 5.6.2.

For the *rough* calculations presented in this section, we assume 8 W of optical power incident on the symmetric port of the interferometer, and a PRG of approximately 50. The requirements are largely set with the optomechanical squeezing experiment of Chapter 4 in mind (and so the readout quadrature is defined by $\zeta \approx 90°$), but a demonstration of the BHD measurement scheme without any squeezing will require similar levels of phase noise, and so this discussion remains relevant. The level at which unsqueezed vacuum noise manifests in the BHD readout is set by the interferometer's optomechanical gain, and the LO field power, which I assume to be 100 mW, split equally among two OMC cavities - the requirements on the scattered light are then referred to this unsqueezed vacuum level.

### 5.6.1 Direct backscatter

I assume that the scattered light contribution from the circulating field inside the FP arm cavity dominates any contribution from the circulating field inside the PRC,

which is reasonable since the arm cavity power gain is ≈ 300. The fraction of this field that makes it onto the OMC DCPDs is the product of three numbers (referred to as $\epsilon_{\text{scatter}}$):

1. Probability of light scattering out of the $\text{TEM}_{00}$ mode of the arm cavity. This is related to the BRDF of the ITM.

2. BRDF of the scattering surface - in this case, assumed to be the vacuum chamber walls, but additional contributions from the SOS towers, for example, could be present.

3. The solid angle subtended by the OMC DCPDs onto the scattering surface.

Figure 5.11 shows the calculated contribution of phase noise on the backscattered field to the readout in the quadrature defined by $\zeta = 90°$. Depending on the specific scattering mechanism, quadrature noises on the backscattered field can contribute differently to the readout quadrature (since the phase of the backscattered light relative to the LO field is not controlled). I make the simplistic assumption that any noise on the backscattered field may be divided equally among the two orthogonal quadratures.

### 5.6.2 OMC backscatter

Any light in the $\text{TEM}_{00}$ mode of the OMC cavity will be resonant in the cavity. Given that the OMC cavity is a ring cavity, there can be a *resonant* counter-propagating mode (generated by light scattering out of the forward propagating $\text{TEM}_{00}$ mode of the OMC at the HR mirror surfaces) which leaks out of the OMC's input coupler back to the antisymmetric port of the interferometer. While this field is attenuated by the OFI, any noise in either quadrature of the leakage light that makes it back to the interferometer's antisymmetric port will appear as noise additional to the squeezed/unsqueezed vacuum. It has been demonstrated that the total fraction of backscattered light from this path (after accounting for the OFI) is at the level of 10 ppm [77]. This analysis neglects the scatter of carrier HOM light back into the $\text{TEM}_{00}$ mode at the incident mirror of the OMC, which is assumed to be much less than the LO field level.

Fig. 5.12 shows the contribution of phase noise on the counterpropagating OMC field in the readout quadrature defined by $\zeta = 90°$. As described in the preceding section, the phase picked up by the scattered light can be random, and hence, may

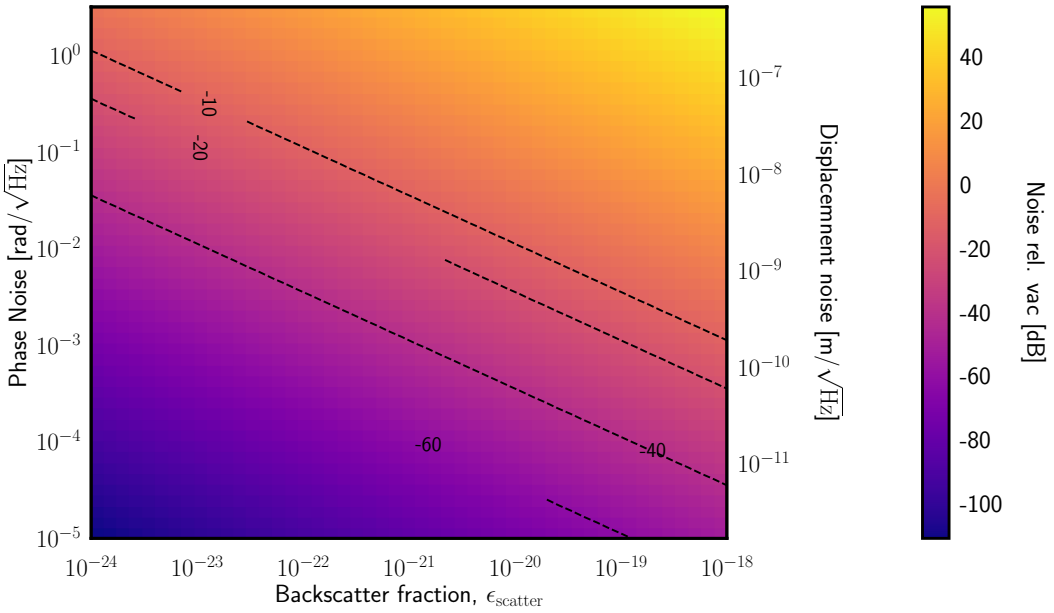


Figure 5.11: Contribution of phase noise on directly-backscattered light in the readout quadrature defined by $\zeta \approx 90°$. In this scenario (middle panel of Figure 5.10), a fraction $\epsilon_{\text{scatter}}$ of the assumed 60 kW of circulating power in the FP arm cavities is directly scattered onto the OMC DCPDs.

show up in any quadrature relative to the LO (i.e. RIN on this field may also manifest in the $\zeta = 90°$ quadrature). Nevertheless, using this simplistic picture, we can place some limit on the permissible motion of the OMC mirrors (which is assumed to dominate the motion due to the actual OMC suspension due to the amplification of phase noise by the resonant OMC cavity). Any length noise in the OMC will introduce a phase noise that is enhanced by the cavity. The thermally driven motion of the OMC mirrors is estimated to be $\sim 5 \times 10^{-17}\text{m}/\sqrt{\text{Hz}}$ [78]. The phase noise induced by the thermally driven OMC length noise is enhanced by a factor of $\sim 100$ to a level of $\sim 10^{-8}\text{rad}/\sqrt{\text{Hz}}$, which is at the lower end of the y-axis range in Fig. 5.12. This means that as long as we are able to keep the power of backscattered light from the OMC to $\lesssim 10$ ppm of the LO power, the induced noise is well below the level of unsqueezed vacuum noise.

## 5.7 In-air BHD experiment

Setting up the 40m for a *low-noise* BHD test is an invasive and labor-intensive process involving multiple vents of the vacuum system to install and re-arrange equipment (e.g. multiple additional suspended optics and two OMCs). We decided to try a much simplified version of the BHD readout scheme, which did not involve any

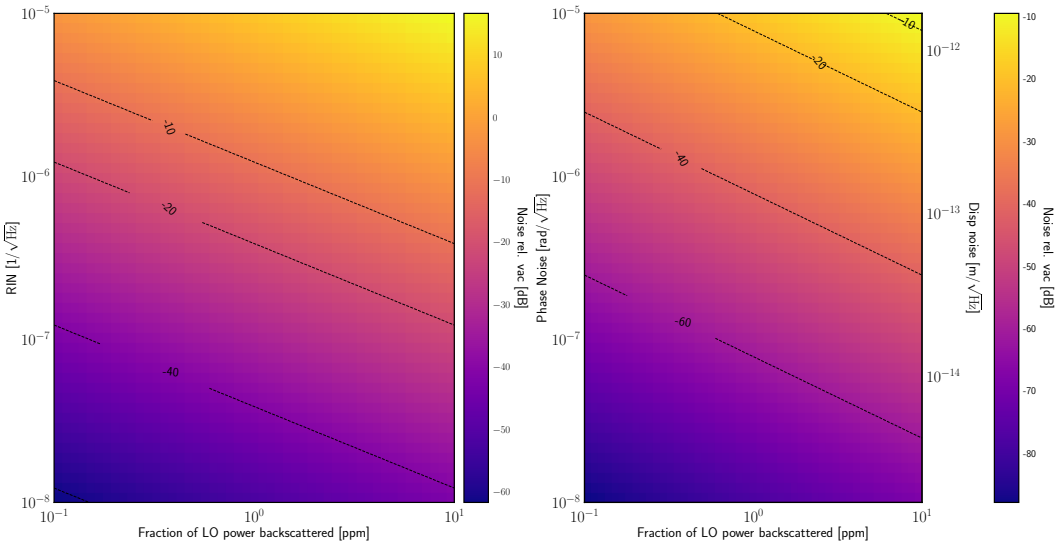


Figure 5.12: Contribution of quadrature noise as a function of the fraction of incident $TEM_{00}$ mode light backscattered towards the IFO's antisymmetric port. The LO field power dominates over other fields - these plots are generated assuming 50 mW of LO power incident on each OMC. The quoted fraction includes isolation by the OFI. This is primarily assumed to come from the LO field incident on the OMC cavity becoming resonant in the cavity's counter-propagating mode. The readout quadrature is assumed to be $\zeta \approx 90\,^{\circ}$.

significant modifications of the vacuum system (hence the moniker "in-air BHD"). The hope was that we could gain some experience, and possibly insights into some unanticipated noise couplings that were overlooked during the modeling phase. This section summarizes the setup and results from this experiment.

### 5.7.1 Optical setup, LO delivery, and homodyne phase actuation

The optical setup used is shown in Fig. 5.13. For the delivery of the LO field to the homodyne beamsplitter, we decided to use an optical fiber as it was logistically easiest, the alternative being routing either the LO beam or the IFO AS beam through free space over a distance of a few meters so that they could be optically interfered. For the first iteration of the setup, we decided to omit any OMC cavities to strip the RF sidebands on the fields before photodetection by a pair of DCPDs[2]. A custom [80] transimpedance amplifier ($Z \approx 300\,\Omega$ was chosen as the transimpedance) with integrated whitening is used to preamplify the photocurrent above the ADC noise level, before digitization into the digital control system.

A pickoff of the PSL beam before injection into the vacuum but after the two RF phase

[2] IG17X30001i [79], which use $\phi = 3$ mm diameter InGaAs as the photoelectric element.

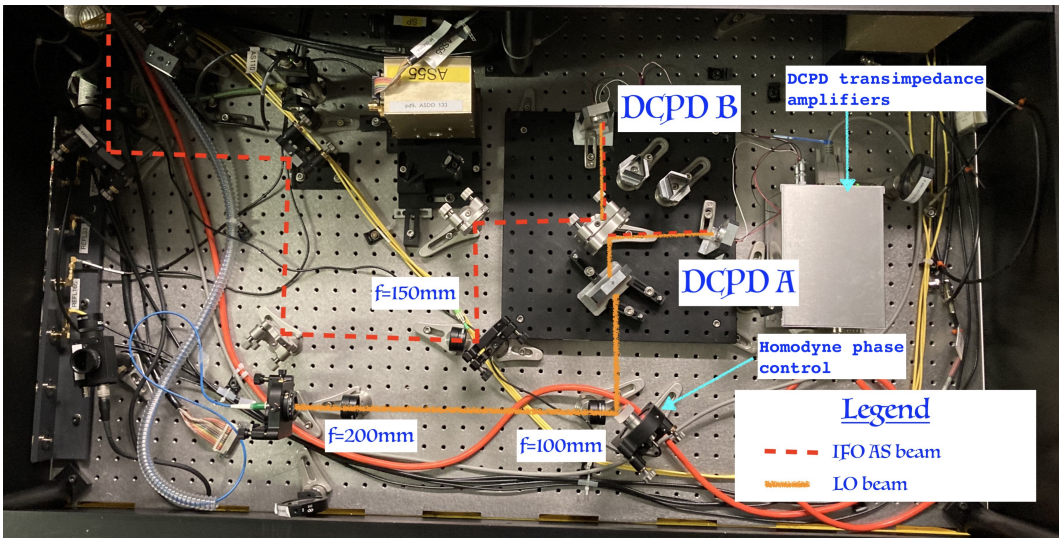


Figure 5.13: Optical setup for in-air BHD experiment. The coupling of light into the optical fiber to serve as an LO field happens on a separate optical table and is not shown in this photograph.

modulation sidebands were applied on it was coupled into a 10 m long polarization-maintaining fiber[3], aligned along the slow axis of the fiber. The coupling efficiency into the fiber was $\approx$ 70%, which was deemed sufficient for initial trials. The LO field was deliberately chosen to have RF sidebands imprinted, in order to test out a scheme for controlling the homodyne phase. Several lenses were placed in the beampaths of the IFO AS and LO beams, in order to maximize the spatial mode overlap between the two fields on the homodyne BS. After optimizing the lens positions and alignment, the measured overlap was $\approx$ 60%, which was deemed sufficient for initial trials.

For the homodyne phase ($\zeta$) control, a mirror glued onto a PZT transducer was used[4]. This part is actually designed for angular actuation and hence consists of 3 PZT stacks arranged along the circumference of a circle, but we adopted the part for longitudinal actuation (as is required for $\zeta$ control) by applying the same voltage to all 3 elements. A commercial high-voltage amplifier, Trek 603, was used amplify the output of the digital control system to drive this PZT, with the -10 V to 10 V range of the former mapped to 0 V to 250 V.

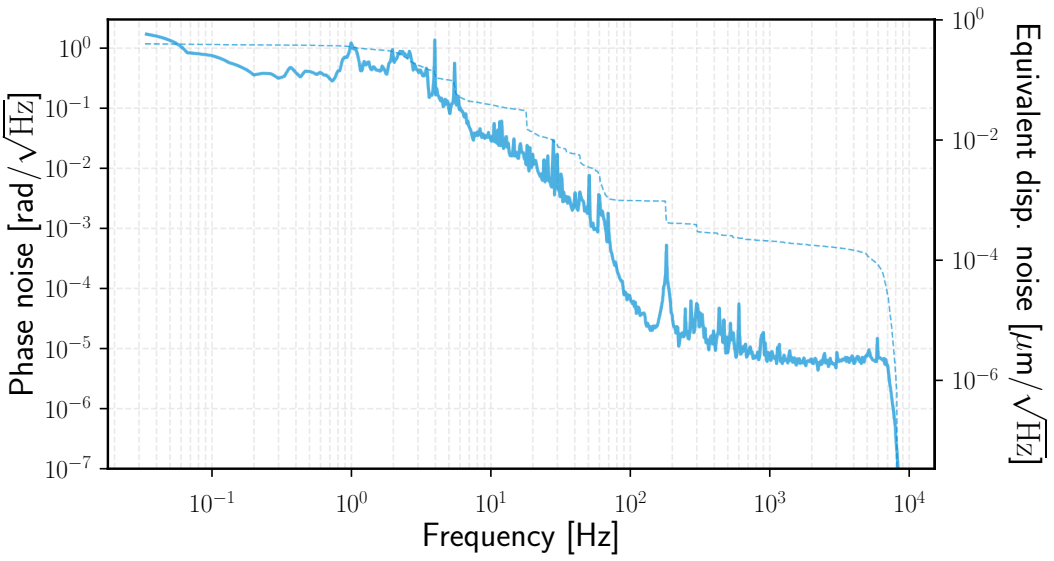


Figure 5.14: Estimate of the free-running phase noise between the LO and IFO AS fields, reconstructed using the demodulated quadratures of the RF44 photocurrent. The data was collected using the CDS system sampling at 16384 kHz, and so the sharp roll-off around 8 kHz are due to anti-aliasing filters.

### 5.7.2 Estimate of relative phase noise between IFO and LO fields

The first tests were done with a simple Michelson interferometer (i.e. PRM, SRM and ETMs misaligned), locked to the dark fringe using the AS55 photodiode as the error signal. In this configuration, the carrier field content in the IFO output beam is nearly 0 (because the Michelson length is controlled to make it so), and the transmission of the $f_2$ sideband due to the Schnupp asymmetry should make the dominant contribution. The LO field, meanwhile, has spectral components at the carrier, $f_1$, as well as $f_2$ frequencies. Without any control of $\zeta$, (i) length fluctuations in the LO delivery fiber, (ii) seismic length fluctuations in the positions of the various suspended optics routing the IFO AS field from inside the vacuum envelope to the in-air optical table, and (iii) phase noise due to the BHD setup being in air all cause relative phase fluctuations between the LO and IFO fields, and their spectral components. This is the idea behind one of the proposed schemes to sense and control $\zeta$, see Section 4.3.2 of [81]. Specifically, the $f_1$ spectral component beating with the $f_2$ component in the IFO AS beam will produce a photocurrent at $f_2 - f_1 \approx 44$ MHz. The transimpedance amplifiers for the DCPDs [80] were not

[3] Panda-style patch cable form Thorlabs (part number P3-1064PM-FC-10) was used.

[4] The PZT was S320.00 by Physik Instrumente - it is an obsolete part and so no in-date datasheet is available. A $\phi = 1$ inch high-reflective optic (coated for 1064 nm) from CVI was bonded to the PZT using EP30 epoxy from MasterBond.

designed to have sufficient bandwidth to measure photocurrent at this frequency - therefore, "DCPD B" in Fig. 5.13 was replaced with a broadband photodiode[5] for this part of the experiment. The absolute phase[6] of this 44 MHz photocurrent is a function of $\zeta$ as well as the digital demodulation phase - so by monitoring both demodulated quadratures, we can reconstruct the rotation of the 44 MHz phasor, which is in turn a proxy for fluctuations in the homodyne phase, $\zeta$. Explicitly,

$$\zeta = \arctan\left(\frac{\text{RF44 Q}}{\text{RF44 I}}\right). \tag{5.15}$$

The spectrum of phase fluctuations thus determined from a 10 minute stretch where the Michelson was maintained at the dark fringe is shown in Fig. 5.14. Between $1 - 200$ Hz, the measured structure of the spectral density suggests that the motion of the relay optics on the seismic isolation stacks routing the IFO AS beam to the homodyne BS are the dominant noise source. Above 200 Hz, the weak signal levels (since the RF44 signal is derived by the beating of a pair of PM sidebands) mean that the sensing electronics noise dominate, resulting in a flat spectral density profile. Over very long time scales $>$ 10 mins not shown in this plot, it is hypothesized that temperature-driven length fluctuations of the fiber used to pipe the LO field to the homodyne BS was the dominant noise source. *The conclusion from this measurement was that the PZT actuator, with a full stroke of* $\approx 10\,\mu$m *had sufficient range to attempt locking the homodyne phase, using the RF44 error signal, for at least periods of 10s of seconds.*

### 5.7.3 Single-bounce interferometer to lock the homodyne phase

For the first attempts of closing a feedback loop to control the homodyne angle, an even simpler configuration was adopted - all of the interferometer optics except a single ITM was misaligned, such that the IFO AS beam is simply the single-bounce reflection off this ITM. The DC power on each of the two DCPDs after the homodyne BS will then vary as

$$P^{\text{A}}_{\text{DCPD}} = \sqrt{P_{\text{LO}}}\sqrt{\text{P}_{\text{IFO}}}\cos^2\zeta, \quad P^{\text{B}}_{\text{DCPD}} = \sqrt{P_{\text{LO}}}\sqrt{\text{P}_{\text{IFO}}}\sin^2\zeta. \tag{5.16}$$

Since the modulation depths are small, we can neglect the RF sidebands for this analysis. At half-fringe (i.e. $\zeta = 45°$), each of these functions can be approximated

[5] Thorlabs PDA10CF was used.

[6] "Absolute" for our purposes can be defined relative to the phase of a noiseless electrical LO signal used to demodulate the 44 MHz signal.

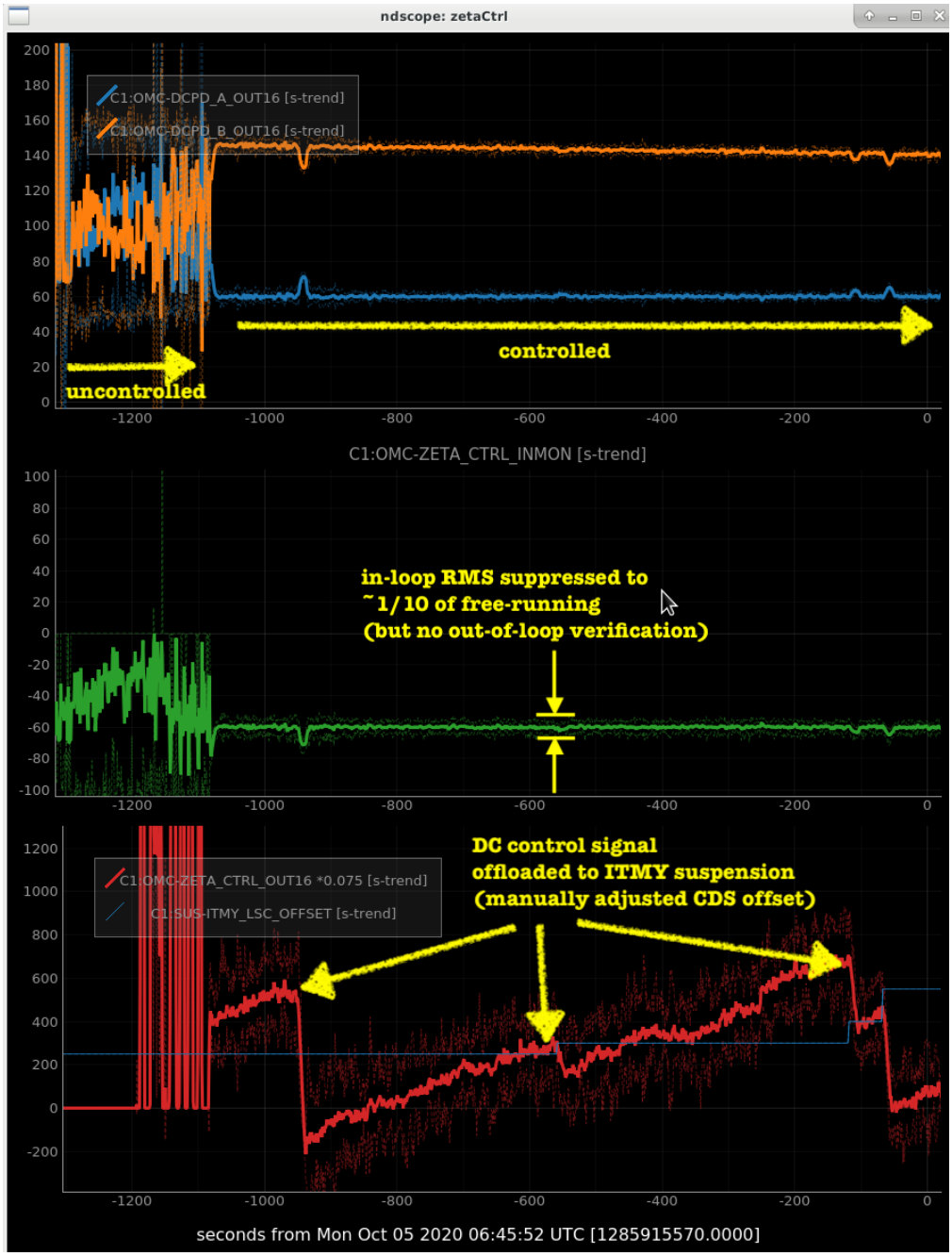


Figure 5.15: Time domain signals for a single-bounce interferometer to test locking the homodyne phase $\zeta$. The top panel shows that the DC light level on each DCPD is stabilized relative to when $\zeta$ is uncontrolled. The two lower panels show the error and control signals of the feedback loop respectively. Periodically, the DC actuation signal was offloaded to the suspended ITM, which had a wider range actuator compared to that used to control $\zeta$.

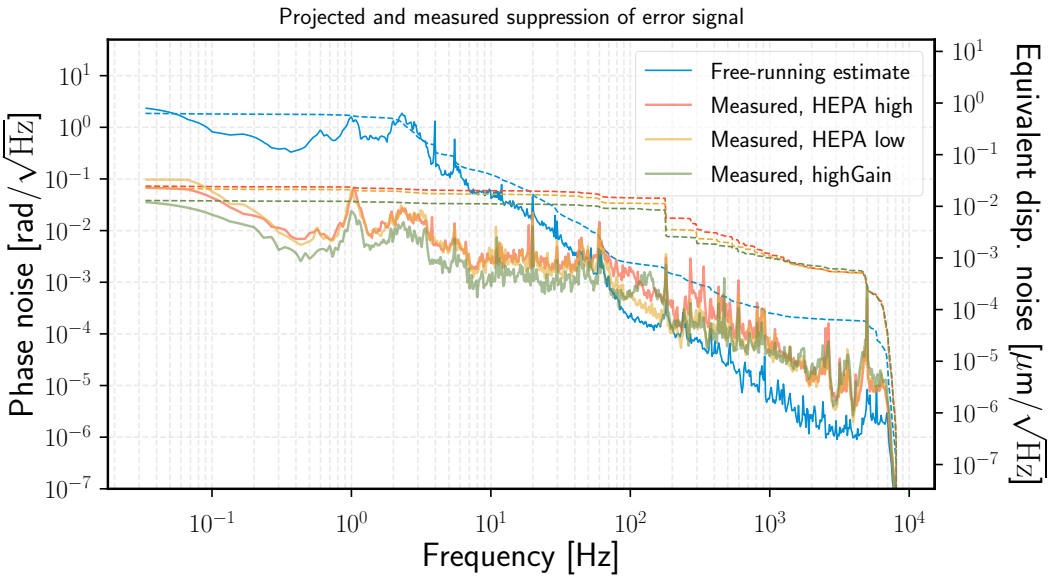


Figure 5.16: Free-running and suppressed signal spectra of the homodyne phase. The "HEPA high" trace was measured when the airflow in the area around the LO delivery fiber was unintentionally left at an elevated level - compared to the "HEPA low" trace made under nominal environmental conditions, there appears to be elevated noise in the 50 – 200 Hz range, possibly due to acoustic pickup in the LO delivery fiber. The "highGain" trace was measured with the digital feedback loop gain 3 dB higher than the other closed-loop traces - while this led to predictably better suppression of low-frequency noise, oscillations could be seen in the time-domain control signal. The bump in this trace around 150 Hz may be indicative of gain-peaking, and consequently, loop instability.

as a *linear* function of $\zeta$, with

$$P^{\mathrm{A}}_{\mathrm{DCPD}} \approx \zeta + \frac{1}{2} + \frac{\pi}{4}, \quad P^{\mathrm{B}}_{\mathrm{DCPD}} \approx \zeta + \frac{1}{2} - \frac{\pi}{4}, \tag{5.17}$$

and therefore, is a suitable error signal to close a linear feedback loop. For angles close to $\zeta = 45°$, the linear approximation remains valid, and therefore, we are not restricted to locking to this single point. The approximation does however fail for $\zeta$ close to 0° or 90°, and so arbitrary homodyne angles cannot be accessed using this scheme. Fig. 5.15 shows some important signals from when such a feedback loop was successfully closed. The primary purpose of this demonstration was to show that all parts of the system (photodiodes, PZT, High Voltage amplifier etc) were working. However, it reveals several difficulties, such as finite actuator bandwidth and sensitivity to environmental noises, in attempting to make any kind of low-noise measurement using the in-air BHD setup. Fig. 5.16 shows the same information as Fig. 5.15, but in the frequency domain. The loop bandwidth was ≈ 100 Hz - it

is difficult to realize much higher UGFs with the digital system. It is possible to suppress RMS fluctuations of $\zeta$ to the level of $\approx 50\,\mathrm{mHz}$, but this is several orders of magnitude larger than the eventual goal of stabilizing phase noise of the LO field to $< 3 \times 10^{-8}\,\mathrm{rad}/\sqrt{\mathrm{Hz}}$.

## 5.8 Conclusions and future work

In this chapter, I have briefly motivated using BHD as a technique to convert DARM phase fluctuations encoded in the IFO AS electric *field* to a measurable signal. A detailed modeling study was carried out to determine the requirements on such a system to be implemented at the 40m, some important aspects of which are discussed. A proof-of-concept experiment carried out with the BHD setup entirely in air and the LO field delivered using optical fiber confirmed the need for as many parts as possible to be well shielded and isolated in the vacuum envelope. Nevertheless, some experience was acquired in how the eventual, low-noise implementation would be characterized - starting with simple configurations such as the single bounce interferometer described in Section 5.7.3.

A scheme to sense and control the homodyne phase $\zeta$ using a beat signal generated by PM sidebands at the two RF modulation frequencies used at the 40m was also investigated. In the simplified air-BHD setup, we could not successfully implement this scheme - however, it is hoped that in the in-vacuum BHD implementation, the higher light levels and inherently lower phase noise on the LO field (because most of the optics delivering the LO field to the BHD BS will be suspended as pendulums) will yield a cleaner error signal that can be used to stabilize $\zeta$. An important area that needs to be explored is how arbitrary homodyne angles can be maintained. The aforementioned scheme relies on the extinction of the $f_2 - f_1$ spectral component at $\zeta = \phi_{\mathrm{SRC}}$. However, in order to measure an optomechanically squeezed field as discussed in Chapter 4, we need to read out the field at nearly the orthogonal quadrature. An alternative scheme which can stabilize $\zeta$ with sufficiently low noise around this quadrature will need to be conceptualized and commissioned.

*Chapter 6*

# PHASE-SENSITIVE OPTOMECHANICAL AMPLIFIER FOR QUANTUM NOISE REDUCTION IN LASER INTERFEROMETERS.

This work presented in this chapter was published as [82], in collaboration with Y. Bai and others - it is reproduced here with slight modifications.

## 6.1 Introduction and the need for an amplifier

Above $\approx 100\,\mathrm{Hz}$, the design sensitivity of current and future terrestrial gravitational wave detectors are limited by photon shot noise in the interferometers' readout. GW signals detected by these detectors are produced by some of the most violent events in the universe—the coalescence of compact objects such as black holes and neutron stars. They provide decisive tests of general relativity in the strong-gravity regime, may give clues about the rich nuclear physics within the ultra-dense cores of neutron stars, and most importantly have the potential to teach us many unexpected lessons about the universe. Some of the most interesting physics of these phenomena appear during and immediately after these merger events, but any signatures of new physics are expected to make only small signatures on the merger / post-merger signals, with frequency content in the $200\,\mathrm{Hz} - 3\,\mathrm{kHz}$ band. This band is also where shot noise is the dominant noise source.

Despite the limitations imposed by the quantum nature of light, shot noise is not a fundamental limit of nature, and therefore can be mitigated by clever optical techniques. In the 1980's, Carlton Caves showed that the sensitivity of shot noise-limited interferometers can be improved by injecting 'squeezed vacuum' [52]. This paved the way for 'quantum non-demolition' technologies for GW detection, such as those explored in [53]. Since then, squeezed vacuum injection has been implemented successfully both at GEO600 [83, 84] and at LIGO [85]. Indeed, both LIGO interferometers regularly operated with $\approx 3\,\mathrm{dB}$ of squeezed vacuum being injected into their AS ports [65] in LIGO's third observing run (O3), which was the richest to date in terms of number of astrophysical events observed. However, the extent to which sensitivity can be improved by this technique is limited by losses incurred within the interferometer optics, leading to decoherence of the squeezed field.

One way of overcoming losses in the final stage of photodetection, as proposed by Caves [52], is to pre-amplify the quadrature field containing the GW signal, using a quantum-limited phase-sensitive amplifier, before reading it out with a photodetector. This idea was more recently discussed by Knyazev et al. [86, 87]. In this work, we propose an optical layout that serves as an ultra-low noise, high gain, and phase-sensitive optomechanical amplifier for the GW signal, as shown in Fig. 6.1. We describe how this amplifier can mitigate the effect of optical losses in the readout chain and therefore let us listen to the universe in higher fidelity. Significant progress has been made toward demonstrating optomechanical parametric amplification in the gravitational-wave band, in order to generate squeezed vacuum [12, 47, 59]. The amplifier we propose and analyze here will be another application of such devices.

This rest of this chapter is organized as follows: we begin in Section 6.2 with a qualitative discussion of the role of quantum noise reduction and the potential need for an amplifier in the context of LIGO Voyager [68, 88], a next-generation upgrade to LIGO, for the purpose of loss mitigation. Then, in Section 6.3, we explain the physics of optomechanical amplification, and provide some simple formulae whose detailed derivations are postponed to Section 6.6. We then propose, in the same section, an optical layout for the amplifier. In Section 6.4, we discuss noise sources within the amplifier, which necessarily limit the amplifier's performance. The effectiveness of the amplifier is further limited by noise sources within the main interferometer (IFO), the most serious of which are discussed in Section 6.5. Finally, in Section 6.8 we discuss some parameter choices for the proposed design, and in Section 6.9 we discuss prospects for a more ambitious quantum amplifier.

## 6.2 Squeezed vacuum injection in LIGO Voyager

Voyager is a planned cryogenic upgrade to the terrestrial gravitational wave detectors [68]. The primary sensitivity improvement is realized by operating with silicon test masses and amorphous silicon optical coatings at 123 K. At this temperature, the coefficient of linear thermal expansion of silicon, $\alpha$, vanishes, which drives down phase noise imparted by thermally-driven fluctuations in the interferometer. Design studies and early R&D suggest that the sensitivity of Voyager will be limited throughout the detection band of 10 – 4000 Hz by quantum noise, provided that the Brownian noise of the optical coating is sufficiently mitigated (see Section 6.5 for more details). To reduce the quantum noise, squeezed vacuum is injected via the anti-symmetric/dark port (see Fig. 6.1) [52]. The rotation angle of the noise ellipse of the squeezed vacuum required for broadband sensitivity improvement is

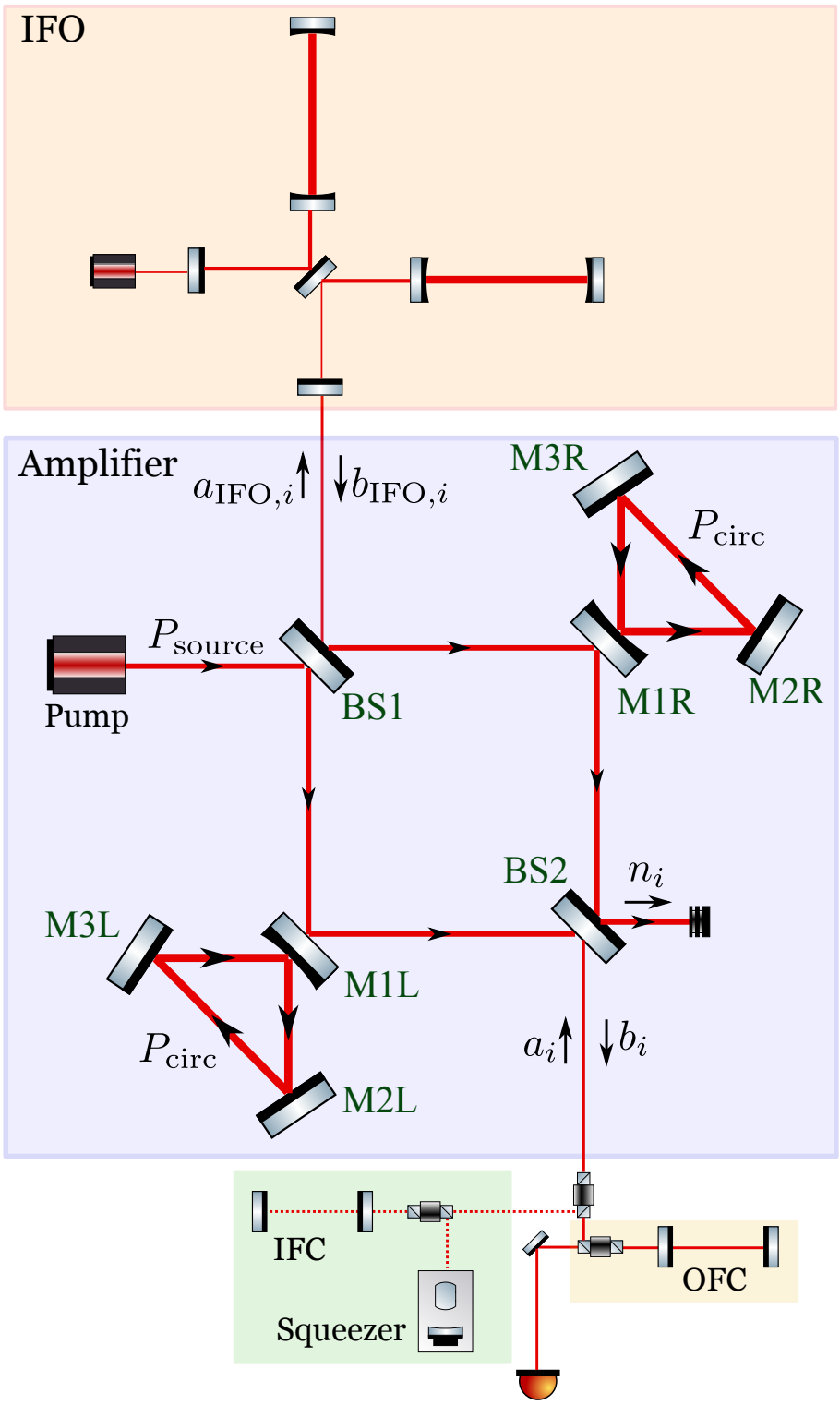


Figure 6.1: Optical layout for the Mach-Zehnder amplifier (shaded in light purple) installed between the anti-symmetric port of the IFO (shaded in light red) and the readout chain, with arrows indicating the direction of the amplifier pump. *The various subsystems are not drawn to scale*. IFC: input filter cavity; OFC: output filter cavity; BS1, BS2: 50/50 beam splitter; M1R, M1L: highly reflecting mirror; M2R, M2L, M3R, M3L: perfectly reflecting mirror

frequency-dependent. This frequency-dependence is realized by installing a filter cavity along the injection path [53]. We refer to this as the 'input filter cavity' (IFC), which is illustrated in Fig. 6.1. In principle, injecting more strongly squeezed vacuum improves the sensitivity monotonically. In practice, however, the improvement is limited by optical losses in various parts of the interferometer.

It is anticipated that optical losses in the Voyager arm cavities will be reduced to the tens of ppm level per round-trip, due to ultra high quality optical surfaces and coatings. However, the readout chain, consisting of an Output Faraday Isolator (OFI), Output Mode Cleaner (OMC), and balanced homodyne detection with photodetectors that have imperfect quantum efficiency, is expected to introduce significant loss; because many of these technologies have yet to be developed, a pessimistic prediction can be at the level of 10%. This is the value assumed in this chapter, c.f. the baseline estimate of 5% in Ref. [68]. Comparison to the performance achieved in the aLIGO interferometers, which are summarized in Table 6.1, gives an indication of the amount of improvement that needs to be realized before meeting even the target of 10% total loss, especially given the lack of photodiodes with $> 98\%$ quantum efficiency at $\lambda = 2\,\mu$m at the time of writing (although this is an area of active research).

Table 6.1: Estimates of readout chain losses in aLIGO, which may be reasonably considered the state-of-the-art at the time of writing.

| **Readout chain loss source** | **aLIGO performance** |
|---|---|
| OFI loss (single-pass) | 3.3% [89] |
| OMC optical loss | 4% [90] |
| Photodiode loss due to imperfect quantum efficiency | 2% at 1064 nm |
| Other losses (e.g. mode-matching) | 12% |
| **Total** | **20%** [91] |

Mitigating the readout loss directly would require substantial effort to improve multiple pieces of technology. However, requirements on these losses can be relaxed by pre-amplifying the GW signal, provided that the amplifier (a) has ultra-low noise, (b) has high gain in the frequency band of the GW signal, and (c) is phase-sensitive and therefore immune to the quantum mechanical limits of phase-insensitive amplifiers described in [92].

In the remainder of this chapter, we show how an optomechanical amplifier installed between the GW interferometer and the readout chain achieves all three properties, and discuss the resulting impact on detector sensitivity. We will focus on a "high-loss–high-squeeze" scenario, showing that the amplifier will allow us to take advantage of optimistically high levels of squeezing, in presence of pessimistic levels of readout chain losses.

## 6.3 Optomechanics for phase-sensitive amplification

In this section, we begin by reviewing the physics of optomechanical amplification in Section 6.3.1. Then we propose an optical layout and design parameters for the amplifier in Section 6.3.2, and explain how it should be incorporated in the main interferometer.

We analyze optomechanical interactions using the two-photon formalism developed by Caves and Schumaker [62, 63], and reviewed in Sec. II. A. of [53]. In particular, we use the notation and Fourier transform convention followed in the latter. We let $\omega_0/2\pi$ denote the carrier frequency of the laser beam in the main interferometer, and $\Omega/2\pi \lesssim 4\,\mathrm{kHz}$ denote the signal sideband frequency.

### 6.3.1 Optomechanical amplification

Optomechanical amplification [93] is a process by which a signal beam is amplified (i.e. anti-squeezed) via the radiation pressure coupling between the optical field and the mechanical modes of a suspended mirror. To enhance the coupling, the signal beam can be applied to the mirror together with a co-propagating pump beam. We decompose the signal into two quadratures in the usual way, referring to the quadrature in phase with the IFO pump amplitude as the 'amplitude quadrature', and the orthogonal quadrature as the 'phase quadrature'. Signal and pump fields interfere to produce amplitude and phase fluctuations in the light incident on the mirror. Incident amplitude fluctuations exert radiation pressure, which displaces the mirror, thus modulating the phase of the reflected light (eq. 6.6, 6.7). In the limit of a strong pump and low mirror mass, the induced phase fluctuations on reflection may be much larger than the amplitude fluctuations of the incident signal. Since this process only amplifies one quadrature, it is phase-sensitive and we reiterate that it is not subject to the quantum mechanical noise limits of phase-insensitive amplifiers [92].

Before discussing Voyager, let us provide a simple explanation why phase sensitive amplification, proposed by Caves, can improve robustness against losses in the

detection chain. Suppose the $b_1$ quadrature carries signal $h$ and squeezed noise, $e^{-r}a_1$,

$$b_1 = h + e^{-r}a_1. \tag{6.1}$$

This corresponds to a signal-referred noise spectrum of $S_h = e^{-2r}$ (see [53] for details of the two-photon formalism). If we were to detect this quadrature with losses, $\epsilon$, in the readout chain, we will be detecting

$$b_1^D = \sqrt{1-\epsilon}\,[h + e^{-r}a_1] + \sqrt{\epsilon}n_1 \tag{6.2}$$

which leads to

$$S_h^{\text{loss}} = e^{-2r} + \epsilon\,. \tag{6.3}$$

In Eq. (6.2), $n_1$ and $a_1$ denote unsqueezed vacuum. This simplified scenario highlights how losses in the detection chain, $\epsilon$, limit the sensitivity enhancement we are able to achieve by injecting squeezed vacuum. Now, suppose we feed $b_1$ into a phase-sensitive amplifier, which allows noise-free linear amplification by $G$, before feeding the amplified quadrature field into the *same* detection chain. Then, we will have

$$b_1^{D,\,\text{amp}} = \sqrt{1-\epsilon}\,G\,[h + e^{-r}a_1] + \sqrt{\epsilon}n_1\,, \tag{6.4}$$

with a signal-referred noise spectrum of

$$S_h^{\text{loss, amp}} = e^{-2r} + \frac{\epsilon}{G^2}. \tag{6.5}$$

In this way, the noise power due to losses in the detection process is suppressed by $G^2$. Note that in this process, the orthogonal quadrature $b_2$, which carries no signal, is suppressed by $G$.

### 6.3.2 The Mach-Zehnder Amplifier

For the optical layout of the amplifier, we propose a Mach-Zehnder (MZ) configuration to be installed between the anti-symmetric port of the main LIGO interferometer and the readout chain, as shown in Fig. 6.1. The topology consists of two input ports, with the output signal from the LIGO interferometer (labeled as $b_{\text{IFO},\,i}$) injected into one, and a pump (labeled as $P_{\text{source}}$) with the same carrier frequency injected into the other. The pump and signal are combined at a 50/50 beamsplitter (BS1) and

split into two beams, with each beam directed to a separate triangular ring cavity. In each ring, the beating between the pump and signal produces the optomechanical amplification discussed in Section 6.3.1. To enhance the gain, the mirrors of the ring are designed to weigh as little as possible, and the cavity length is locked to have the pump field be resonant, in order to achieve high circulating power. Finally, the output beams of the ring cavities are recombined at a second 50/50 beamsplitter (BS2), with the amplified signal (labeled as $b_i$) measured at one port and the strong pump field dumped at the other.

We now present the input-output relations for the MZ amplifier, where $b_{\mathrm{IFO},i}$ denote the field amplitudes for the input quadratures to the amplifier, and $b_i$ the field amplitudes for the output quadratures, as shown in Fig. 6.1. The normalization of the field amplitudes is defined in (6) of [53].

We let $R_{\mathrm{A}}, T_{\mathrm{A}}$ denote the power reflectivity and transmissivity respectively of the M1L & M1R mirrors, and $L_A$ denote the round-trip length of each ring. A more exact calculation in the lossless limit is given in Section 6.6, where additional assumptions are explained. Here we simply present the result in the limit $\Omega L_A/c \ll 1$ and $T_{\mathrm{A}} \ll 1$, giving

$$\begin{pmatrix} b_1 \\ b_2 \end{pmatrix} = e^{2i\eta} \begin{pmatrix} 1 & 0 \\ -\mathcal{K}_{\mathrm{A}} & 1 \end{pmatrix} \begin{pmatrix} b_{\mathrm{IFO},1} \\ b_{\mathrm{IFO},2} \end{pmatrix} + \sqrt{\frac{32\omega_0 P_{\mathrm{circ}}}{\hbar c^2}} \frac{1}{T_{\mathrm{A}}} \begin{pmatrix} 0 \\ 1 \end{pmatrix} \xi, \tag{6.6}$$

where

$$\begin{aligned} \mathcal{K}_{\mathrm{A}} &= \frac{4}{T_{\mathrm{A}}\left[1 + (\Omega/\gamma_{\mathrm{A}})^2\right]} \kappa_{\mathrm{A}}, \qquad \kappa_{\mathrm{A}} = -\frac{18\omega_0 P_{\mathrm{circ}}}{c^2} \chi_{\mathrm{A}}, \\ \eta &= \arctan\left(\Omega/\gamma_{\mathrm{A}}\right), \qquad \text{and} \quad \gamma_{\mathrm{A}} = \frac{cT_{\mathrm{A}}}{2L_{\mathrm{A}}}, \end{aligned} \tag{6.7}$$

with $\gamma_{\mathrm{A}}$ as the cavity pole frequency, $P_{\mathrm{circ}}$ as the power circulating in each ring, $\chi_{\mathrm{A}}$ as the mechanical susceptibility of the movable mirrors which for a mirror of mass $m_{\mathrm{A}}$ suspended as a lossless pendulum of natural frequency $\Omega_0/2\pi$ is given by

$$\chi_{\mathrm{A}} = \frac{1}{m_{\mathrm{A}}\left(-\Omega^2 + \Omega_0^2\right)}, \tag{6.8}$$

and $c$ as the speed of light. We have also included $\xi$, the motion of mirrors in the ring cavity, that are not due to quantum radiation-pressure noise (e.g. seismic or thermal noise).

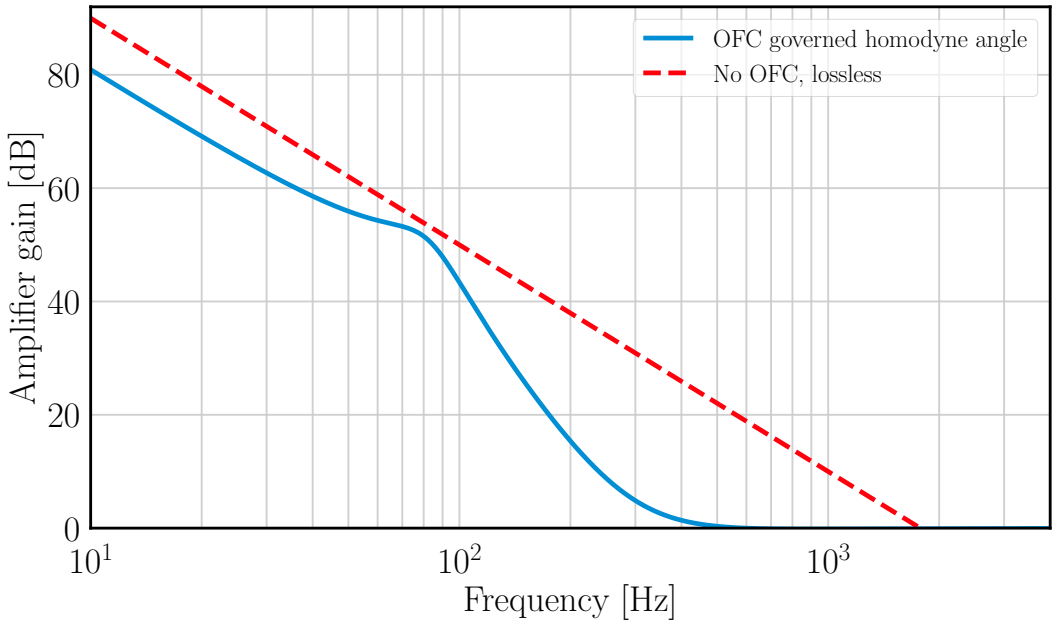


Figure 6.2: Optomechanical gain of the amplifier as a function of signal frequency, as seen in the frequency-dependent readout quadrature. For comparison, we have plotted the gain for both the simple case of a lossless amplifier with frequency independent readout quadrature (Eq. (6.9)), and a lossy amplifier with frequency dependent readout quadrature.

Moreover, for the beam propagating through the amplifier in the reverse direction (i.e., from $a_i$ to $a_{\mathrm{IFO},i}$), there is no amplification because the beam and pump counter-propagate. Hence, the input-output relation is a trivial phase shift Eq. (6.28). We defer a more complete discussion of the counter-propagating mode for Section 6.4.3.

The MZ topology overcomes several challenges associated with optomechanical amplification, such as pump noise rejection (see Section 6.4.2). One further advantage of the MZ configuration is that the pump and signal exit at separate ports. The signal can then be read out (e.g. using homodyne detection) without the strong amplifier pump field saturating the detection photodiodes.

We quantify the amplifier gain by considering the limit of a low-mass mirror and a strong pump, in which case the gain is simply the magnitude of the transfer function $\mathcal{K}_{\mathrm{A}}$ in (6.6). Furthermore, we take the limit where the signal frequency is high compared to natural frequencies associated with the suspended mirror (typically $\lesssim 10\,\mathrm{Hz}$) so that the mechanical susceptibility is of order $|\chi_{\mathrm{A}}| \simeq (m_{\mathrm{A}}\Omega^2)^{-1}$, and we assume a wide cavity bandwidth $\Omega/\gamma_{\mathrm{A}} \ll 1$ so that

$$|\mathcal{K}_{\mathrm{A}}| \simeq \left(\frac{0.01}{T_{\mathrm{A}}}\right)\left(\frac{30\,\mathrm{g}}{m_{\mathrm{A}}}\right)\left(\frac{P_{\mathrm{circ}}}{40\,\mathrm{kW}}\right)\left(\frac{1.5\,\mathrm{kHz}}{f}\right)^2, \tag{6.9}$$

where $f = \Omega/2\pi$ is the signal frequency, and we assume carrier wavelength $\lambda_0 = 2\pi c/\omega_0 = 2\,\mu$m. We find that the gain scales as $\propto 1/f^2$ with unity gain at $f \simeq 1.5\,$kHz for the characteristic $T_A$, $m_A$, and $P_{\rm source}$ given in (6.9). As expected, we achieve high gain at low frequencies $f \lesssim 500\,$Hz due to the high mechanical susceptibility of a low-mass mirror.

The power $P_{\rm circ}$ circulating in each ring is related to the source power $P_{\rm source}$ by

$$P_{\rm circ} = \frac{2}{T_A} P_{\rm source} = 40\,{\rm kW} \left(\frac{0.01}{T_A}\right) \left(\frac{P_{\rm source}}{200\,{\rm W}}\right), \tag{6.10}$$

which is derived in Section 6.6 at Eq. (6.29). Such a high source power can be achieved using a laser source of modest power by employing a power-recycling scheme (not shown in Fig. 6.1).

### 6.3.3 Synthesizing signal generation, amplification and detection

As *input* to the amplifier, we assume that the GW signal is contained in only one quadrature, $b_{\rm IFO,\,1}$, which is the case for the Resonant Sideband Extraction (RSE) configuration in which Voyager is planned to be operated in. More specifically, we can re-write Equation (2.20) of [54] to get (in absence of optical losses),

$$\begin{pmatrix} b_{\rm IFO,\,1} \\ b_{\rm IFO,\,2} \end{pmatrix} = e^{2i\Phi_{\rm IFO}} \begin{pmatrix} 1 & -\mathcal{K}_{\rm IFO} \\ 0 & 1 \end{pmatrix} \begin{pmatrix} a_{\rm IFO,\,1} \\ a_{\rm IFO,\,2} \end{pmatrix} + \sqrt{2\mathcal{K}_{\rm IFO}} e^{i\Phi_{\rm IFO}} \begin{pmatrix} 1 \\ 0 \end{pmatrix} \frac{h}{h_{\rm SQL}}. \tag{6.11}$$

Losses in the interferometer were treated in detail in [54], and will be further discussed in Section 6.5. Here, up to leading order in power loss $\mathcal{L}_{\rm IFO}$, we introduce additional fluctuations into the out-going field quadratures, in the same way as Eq. (101) in [53], yielding

$$b_{{\rm IFO},\,j} \to b_{{\rm IFO},\,j} + \sqrt{\mathcal{L}_{\rm IFO}}\, n_{{\rm IFO},\,j}, \tag{6.12}$$

where $n_{{\rm IFO},j}$ are vacuum fluctuations.

We further assume that frequency-dependent input squeezing of the $a_{{\rm IFO},\,i}$ quadratures is applied, with the help of an Input Filter Cavity (IFC), such that quantum fluctuations in the signal quadrature $b_{\rm IFO,\,1}$ is suppressed at all frequencies. Note that we do not alter the frequency dependence of the input squeezed vacuum relative

to the baseline Voyager design. Our amplifier is then designed to amplify $b_{\mathrm{IFO},1}$. More specifically, one can write

$$\begin{pmatrix} a_{\mathrm{IFO},1} \\ a_{\mathrm{IFO},2} \end{pmatrix} = e^{i\phi_{\mathrm{IFC}}} \mathcal{R}(\theta_{\mathrm{IFC}}) \begin{pmatrix} e^{-2r} a_{\mathrm{in},1} + \sqrt{\mathcal{L}_{\mathrm{inj}}} n_{\mathrm{in},1} \\ e^{+2r} a_{\mathrm{in},2} + \sqrt{\mathcal{L}_{\mathrm{inj}}} n_{\mathrm{in},2} \end{pmatrix} + \sqrt{\mathcal{L}_{\mathrm{IFC}}} \begin{pmatrix} n_{\mathrm{IFC},1} \\ n_{\mathrm{IFC},2} \end{pmatrix}. \quad (6.13)$$

Here $\mathcal{R}$ is a rotation matrix

$$\mathcal{R}(\theta) = \begin{pmatrix} \cos\theta & -\sin\theta \\ \sin\theta & \cos\theta \end{pmatrix}, \quad (6.14)$$

$e^{-2r}$ is the squeezing factor, $\mathcal{L}_{\mathrm{inj}}$ the injection loss of squeezing, and the rotation angle $\theta_{\mathrm{IFC}} = \arctan(\mathcal{K}_{\mathrm{IFO}})$ makes sure that the combined effect of $\mathcal{R}$ and the ponderomotive squeezing matrix in Eq. (6.11) is to squeeze the $b_{\mathrm{IFO},1}$ quadrature. The loss $\mathcal{L}_{\mathrm{IFC}}$ is the loss of the IFC, introducing vacuum fluctuations, $n_{\mathrm{IFC},j}$. The optical parameters for the IFC that achieve the desired 15 dB of squeezing for Voyager are given in Table 6.2.

One important difference between the MZ amplifier and the original Caves proposal is that the quadrature it amplifies is frequency dependent; in other words, the anti-squeezing angle in the $b_{1,2}$ quadrature basis is frequency-dependent. In fact, the angle varies by as much as 90° over the signal bandwidth. At lower frequencies, $\mathcal{K}_A \gg 1$, and the $b_{\mathrm{IFO},1}$ quadrature is highly amplified, making the dominant contribution to $b_2$ (the $b_{\mathrm{IFO},2}$ contribution is comparatively negligible). In this regime, the Caves proposal can be realized by detecting $b_2$.

However, by naively measuring the output quadrature $b_2$ at all frequencies, the signal is actually attenuated at high frequencies where $|\mathcal{K}_{\mathrm{A}}| \ll 1$, which is undesirable. Fortunately, this can be corrected by employing a frequency-dependent readout,

$$b_{\mathrm{out}} = b_\zeta = b_1 \cos\zeta + b_2 \sin\zeta \quad (6.15)$$

which measures the amplified $b_2$ quadrature ($\zeta = \pi/2$) at low frequencies and smoothly transitions to the unamplified $b_1$ quadrature ($\zeta = 0$) at high frequencies. This can be achieved by installing, between the amplifier and the readout chain, a filter cavity which we call the output filter cavity (OFC) (see Fig. 6.1). The frequency-dependent reflection coefficient of the filter cavity, as well as its effect in rotating quadratures, is given in Eq. (6.30); a more detailed treatment is given in

| | Parameter | Value |
|---|---|---|
| IFO | Arm cavity round-trip loss | 20 ppm |
| | SRC round-trip loss | 300 (100) ppm |
| | Readout chain loss | 10 % |
| | Carrier wavelength | 2 $\mu$m |
| SQZ | Squeeze injection | 15 (20) dB |
| | Injection loss | 1 (0.3) % |
| | IFC round-trip loss | 20 (10, 10) ppm |
| | IFC length | 500 (800, 800) m |
| | IFC detuning | -33.4 (-34.6, 4.96) Hz |
| | IFC input coupler transmission | 0.14 (0.22, 0.22) % |
| AMP | Ring cavity round-trip loss, $\mathscr{L}$ | 30 (15) ppm |
| | M1L/M1R transmissivity, $T_{\mathrm{A}}$ | 0.89 (0.90) % |
| | Round-trip cavity length, $L_{\mathrm{A}}$ | 30 m |
| | Pump source power, $P_{\mathrm{source}}$ | 220 (230) W |
| | Mirror mass, $m_{\mathrm{A}}$ | 30 (10) g |
| | Mirror substrate | Si |
| | Common mode rejection | 60 dB |
| | OFC round-trip loss | 20 (10) ppm |
| | OFC length | 40 (25) m |
| | OFC detuning | -80.4 (-77.8) Hz |
| | OFC input coupler transmission | 43 (22) ppm |
| COAT | Refractive index of aSi, $n_H$ | 3.65 [94] |
| | Reflactive index of SiN, $n_L$ | 2.17 [94] |
| | Number of layer pairs | 12 |
| | Mechanical loss of aSi (123 K) | $3 \times 10^{-5}$ [94] |
| | Mechanical loss of SiN (123 K) | $2 \times 10^{-5}$ [94] |
| | Beam radius, $w_{\mathrm{beam}}$ | 5 mm |
| SUS | Material | Silicon |
| | Width | 250 $\mu$m |
| | Thickness | 50 $\mu$m |
| | Number of fibers | 2 |
| | Length of pendulum | 60 cm |
| | Surface loss angle, $\phi_s$ (123 K) | $10^{-5}$ |
| | Bulk loss angle, $\phi_{\mathrm{bulk}}$ (123 K) | $2 \times 10^{-9}$ |
| | Surface depth, $h$ | 1 $\mu$m |
| | Young's modulus | 155.8 GPa |
| | Coefficient of thermal expansion | $10^{-10}\mathrm{K}^{-1}$ |
| | $d \log Y / dT$ | $-2 \times 10^{-5}\mathrm{K}^{-1}$ |
| | Heat capacity | 300 J kg$^{-1}$ K$^{-1}$ |
| | Thermal conductivity | 700 W m$^{-1}$ K$^{-1}$ |
| | Density | 2329 kg m$^{-3}$ |

Table 6.2: Summary of nominal design parameters (numbers in parentheses are for the optimistic case presented in Section 6.9) used in our simulations for the main interferometer (IFO), squeezed vacuum injection path (SQZ), amplifier optomechanics (AMP), amplifier HR coating (COAT) and amplifier suspension (SUS) subsystems.

Sec. IV C of Ref. [53]. We expect that a $\simeq 40\,\mathrm{m}$ scale OFC is needed, with more detailed design parameters given in Table 6.2. Losses in the OFC also introduces additional vacuum fluctuations, which can be combined with the effect of the loss of readout photodetectors, leading to

$$b_{\mathrm{out}} \to b_{\mathrm{out}} + \sqrt{\mathcal{L}_{\mathrm{OFC}} + \mathcal{L}_{\mathrm{det}}}\, n_{\mathrm{det},\zeta}. \tag{6.16}$$

Assuming that the noise that enters through this channel, $n_{\mathrm{det},\zeta}$, is unsqueezed vacuum, we plot the OFC-filtered amplifier gain in Fig. 6.2, showing no attenuation at high frequencies.

To summarize: putting together Eq. (6.11)–Eq. (6.16), and inserting the amplifier input-output relation Eq. (6.6), we can obtain the noise spectrum of the entire configuration, including losses from squeezing injection ($\mathcal{L}_{\mathrm{inj}}$), the IFC ($\mathcal{L}_{\mathrm{IFC}}$), the interferometer ($\mathcal{L}_{\mathrm{IFO}}$, see Ref. [54] and Section 6.5 for further details), the OFC ($\mathcal{L}_{\mathrm{OFC}}$), and the photodetectors ($\mathcal{L}_{\mathrm{PD}}$). We will devote the next section, Section 6.4, to noise in the amplifiers; there we will further introduce additional noise terms into Eq. (6.6).

Following the above steps, and incorporating discussions from the next two sections, we propose in Table 6.2 a set of design parameters for the amplifier, which were obtained by optimizing the total (amplifier & IFO) noise using a cost function emphasizing the mid-band region $50\,\mathrm{Hz} \lesssim f \lesssim 500\,\mathrm{Hz}$, where the amplifier is most effective. The impact on the overall detector sensitivity is plotted in Fig. 6.3, showing modest improvement in this range. *Given uncertainties in the parameters, our amplification strategy will be appropriate for application only if the interferometer's internal losses, test-mass coating thermal noise, achievable injected squeezed vacuum, and all other pre-amplification noises in Voyager turn out to be the same as or better than what we have chosen here, and if the readout photodetector inefficiency (and other losses from elements downstream of the amplifier, such as an Output Mode Cleaner) turn out to be the same as or worse than what we have chosen here.*

Finally, we point out that our calculations remain valid only in the limit where the *amplified* signal is much weaker than the pump, as expected since the pump is the source of the amplifier's energy. Since even for the strongest sources the signal *power* is expected to be much weaker than the amplifier pump, we are well within the range of validity.

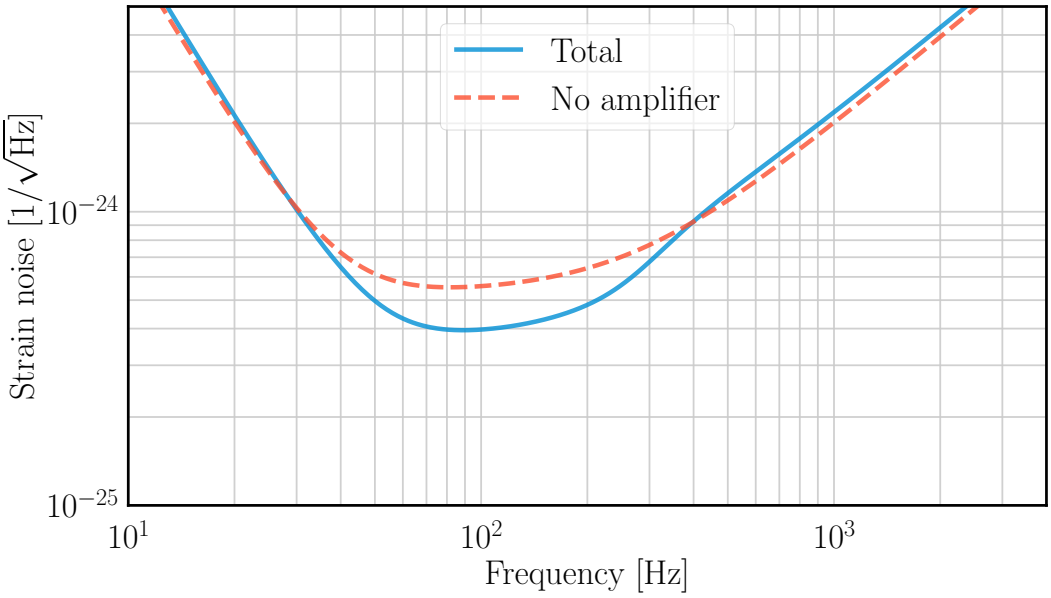


Figure 6.3: Comparison of baseline (no amplifier or OFC) Voyager sensitivity (dashed curve) and sensitivity with the amplifier and OFC added (solid curve). In both cases we assume 15 dB frequency-dependent squeezed vacuum injection. The design parameters are given in Table 6.2. Sub-budgets for noise contributions from the amplifier and IFO may be found in Fig. 6.4 and Fig. 6.5 respectively.

## 6.4 Amplifier noise sources

In order for the amplifier to be effective, it must not introduce significant noise sources of its own. In this section, we discuss some of the dominant amplifier noise sources, such as optical losses in the ring cavities, pump intensity fluctuations, backscattering of pump off amplifier optics, and finally the coating Brownian noise and suspension thermal noise of the amplifier optics. The associated noise curves are given in Fig. 6.4, assuming the parameters given in Table 6.2 for 15 dB squeezed vacuum injection. We find, under these assumptions, that the amplifier noise is dominated by optical loss in the ring cavities.

### 6.4.1 Optical losses in the ring cavities

As the signal beam circulates within the the ring cavities, dissipative and transmissive losses are accumulated at each optic. The small amount of unsqueezed vacuum that enters the signal mode in this process is amplified optomechanically, thus causing the squeezed vacuum to decohere. It is therefore crucial to keep the total loss as low as possible.

Transmissive loss through each high-reflective (HR) mirror, labelled M2R, M2L, M3R & M3L in Fig. 6.1, is limited to 5 ppm by a suitable dielectric bi-layer coating.

Dissipative losses arise due to a number of mechanisms, but may broadly be grouped into absorption or scatter. We assume absorption in the amplifier mirror substrate and dielectric coatings will be $\lesssim 1$ ppm per optic.

Modeling and characterizing loss due to scattering is an area of active research. An empirical scaling law has been found to describe the measured round-trip scatter loss in a variety of two-mirror optical cavities [95, 96], given by

$$\frac{\mathscr{L}}{\text{ppm}} = \left(\frac{4\pi}{\lambda/\text{nm}}\right)^2 \frac{A}{\text{nm}^2 \cdot \text{mm}} \frac{1}{\gamma - 1} \left(\frac{\text{mm}}{\sqrt{2}\alpha w}\right)^{1-\gamma}, \tag{6.17}$$

where $w$ denotes the Gaussian beam radius, while $A = 8 \times 10^{-3}\,\text{nm}^2 \cdot \text{mm}$ and $\gamma = 1.2$ are model parameters extracted from measurements. They parametrize the power spectral density (PSD) of micro-roughness on the mirror surface, which is assumed to obey $\text{PSD}(f_s) = A \left(\frac{f_s}{1/\text{mm}}\right)^{-\gamma}$ for spatial frequencies $f_s$ greater than some cutoff. This cutoff frequency is modelled as $f_s^{\text{min}} = \frac{1}{\alpha w}$, with $\alpha = 2$ corresponding to the Gaussian beam diameter. The contribution to scatter from spatial frequencies smaller than the cutoff are neglected. With $\lambda = 2\,\mu\text{m}$, $w = 5\,\text{mm}$ and $\alpha = 1$ in Eq. (6.17), we estimate $\simeq 3$ ppm of scatter loss per optic. Since understanding of the impact of scattered light is evolving [97], we choose for our analysis the round number 5 ppm of scatter loss per optic.

In summary, we assume a *total* of 30 ppm loss per round-trip in each ring cavity, accounting for the various mechanisms described in this section. This loss introduces additional vacuum fluctuations to $b_{1,2}$ in Eq. (6.6), in the same way as Eq. (6.12).

### 6.4.2 Pump intensity noise

Power fluctuations of the amplifier pump laser produce radiation pressure fluctuations on the ring cavity mirrors, and are thereby amplified by the optomechanical feedback explained in Section 6.3.1. With perfectly symmetric ring cavities, the MZ topology has the advantage of separating the pump noise, which couples only to the field labelled $n_i$ in Fig. 6.1, from the signal, which couples only to the field labelled $b_i$ in Fig. 6.1. In practice, however, slight differences between the two ring cavities lead to imperfect common-mode rejection. This noise can be estimated by first computing the spectrum of mirror of motion due to radiation-pressure fluctuations, propagating it through Eq. (6.6) (i.e., add this displacement noise contribution to the noise spectrum of $\xi$), and then suppressing it by a common mode rejection factor.

For our simulations, we crudely model the amplitude spectral density of the relative

intensity noise (RIN) of the amplifier pump according to

$$\mathrm{RIN}(f) = \left|\frac{f + f_0}{f}\right| \frac{1 \times 10^{-9}}{\sqrt{\mathrm{Hz}}}, \quad f_0 = 50\,\mathrm{Hz}. \tag{6.18}$$

Meeting this requirement on laser intensity noise is expected to be challenging. In order for the relative intensity noise due to shot noise on a sensing photodiode at 2 $\mu$m to be $\lesssim 1 \times 10^{-9}\,\mathrm{Hz}^{-1/2}$, we would need to detect $\simeq 300\,\mathrm{mW}$ of power on that photodiode, corresponding to a dynamic range of $\gtrsim 10^9$. Nevertheless, promising techniques have been demonstrated [98, 99], and we anticipate that sufficient progress will be made to achieve this level of stabilization.

Furthermore, we assume 60 dB common-mode rejection. In our simulations, the asymmetry is modeled as a difference in the ring cavity finesse. Realizing this level of common-mode noise rejection is challenging, but has been achieved in terrestrial gravitational wave detectors. Moreover, we expect to be able to tune the finesse of each cavity by $\simeq 1\,\%$, for instance by changing the spot positions on the cavity mirrors to sample regions of slightly different optical loss.

### 6.4.3 Noise from the counter-propagating mode

As discussed in Section 6.4.1, surface roughness and point defects on the amplifier optics can scatter the high power circulating pump field out of the resonant cavity mode. Some portion of this scattered light then becomes resonant in the *counter-propagating* mode of the ring cavities. Subsequently, this field leaves the amplifier and is injected directly back into the main interferometer via the anti-symmetric port, where it mixes with the squeezed vacuum quadratures $a_{\mathrm{IFO},i}$ (see Fig. 6.1). This gives rise to noise in the readout due to two effects: (1) displacement noise of the amplifier optics, and (2) amplifier pump noise. We expect that the amplifier optics are sufficiently well isolated from displacement noise, and focus instead on the latter with emphasis on the relative intensity noise discussed in Section 6.4.2 in the context of common-mode rejection.

Measurements on the Advanced LIGO output mode cleaner cavity, which has an angle of incidence of approximately 4 degrees, suggest that less than 1 ppm of the incident field is retro-reflected [27]. Since the ring cavities in our design have a 30 degree angle of incidence at each optic, the backscatter is expected to be smaller. For our calculations, we assume a fraction $\mathcal{E}_{\mathrm{bs}} = 10^{-7}$ of the pump power is back-scattered into the anti-symmetric port. This field then adds noise to the input quadratures $a_{\mathrm{IFO},i}$ which we can estimate by

$$\sqrt{S^{(\mathrm{bs})}_{a_{\mathrm{IFO},i}}} = \sqrt{\frac{1}{2}\mathcal{E}_{\mathrm{bs}}\left(\frac{P_{\mathrm{source}}}{2\hbar\omega_0}\right)}\mathrm{RIN}(f), \tag{6.19}$$

where the overall factor $1/\sqrt{2}$ splits the noise evenly into the two quadratures. With $P_{\mathrm{source}} = 200\,\mathrm{W}$ and $\mathrm{RIN} = 10^{-9}/\sqrt{\mathrm{Hz}}$, we find that (6.19) evaluates to $\simeq 7 \times 10^{-3}$ per quadrature, which is negligible even for the case of 20 dB ($= 10^{-1}$) squeezed vacuum injection. Hence, it is omitted from our analysis.

There are other possible mechanisms of scattered light degrading the interferometer sensitivity, particularly given the proximity of the high power amplifier pump field to the interferometer's anti-symmetric port. For instance, some of the scattered light could leave the ring cavity, scatter off the vacuum chamber walls, and recombine into the cavity's signal mode. Acoustic and seismic vibrations of the walls then lead to phase modulation of the back-scattered light. Problems of this nature may be addressed by installing baffles on the walls, as was done for the LIGO beam tubes. Another possible noise coupling mechanism is due to intensity fluctuations on the resonant counter-propagating mode displacing the amplifier mirrors via radiation-pressure. We find that the phase noise thus induced is below the level of the seismic noise for the amplifier systems considered in this paper, but this could become a significant noise source for amplifiers that use much lighter mirrors. We leave the detailed analysis of such noise coupling mechanisms to future work.

### 6.4.4 Coating Brownian noise

Thermal fluctuations of the dielectric coatings [41] on the amplifier optics produce phase fluctuations on the reflected beam, which manifests as noise in the amplifier readout. Mathematically, this contributes through $\xi$ in Eq. (6.6).

To mitigate this effect, we propose for the high reflectivity mirrors (i.e., M2L, M3L, M2R & M3R in Figure 6.1) a coating structure comprising of alternating layers of silicon nitride (SiN) and amorphous silicon (aSi). This choice was motivated by the promising mechanical loss of SiN at the proposed operating temperature of 123 K [94, 100]. Nevertheless, more work is needed to determine its feasibility and, in particular, to lower losses due to absorption in the SiN layers. Rather than using the canonical quarter wave stack to realize the HR coating, a numerical optimization algorithm was used to identify the thickness of each layer in a 12 bi-layer pair stack in order to optimize the resulting noise [101]. For the assumed mechanical properties of aSi/SiN (see Table 6.2), and meeting the coating power transmissivity requirement

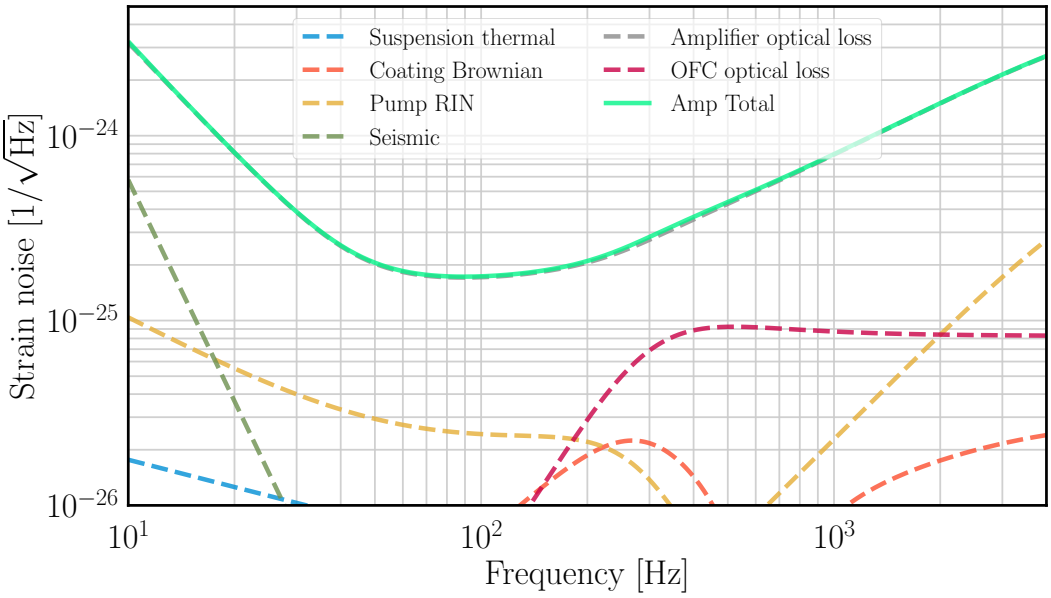


Figure 6.4: Breakdown of the dominant noise sources in the amplifier, including the OFC, based on parameters given in Table 6.2 for 15 dB frequency-dependent squeezed vacuum injection. The noise spectra plotted are projections onto the GW strain sensitivity of the main interferometer. See Section 6.4 for a detailed discussion of the various noise curves. The noise is dominated by optical loss in the ring cavities.

of $\lesssim 5$ ppm, we estimate a Brownian noise contribution per optic that is $\simeq 3.5$ dB below that of an $\alpha$-Si/$SiO_2$ coating with the same power transmissivity. Note that we neglect the Brownian noise contribution from the M1R & M1L optics in Fig. 6.6, since they have higher transmissivity and therefore require fewer dielectric layers.

While coating Brownian noise in the amplifier ring cavities is not the dominant noise source, we find that in order to take full advantage of the sensitivity improvement offered by the amplifier, the coating Brownian noise of the test masses will have to be improved by a factor of $\simeq 4-5$ from the current design. This is further discussed in Section 6.5.2.

### 6.4.5 Suspension thermal noise

Similar to coating Brownian noise, any fluctuations of the position of the mirrors in the amplifier, also enter the output of the amplifier through $\xi$ in Eq. (6.6).

To isolate the amplifier mirrors from seismic vibrations, we propose a double pendulum suspension for each optic in the ring cavities. Internal friction in the fibers couple environmental thermal fluctuations to mirror displacement. For this analysis,

we consider only the thermal noise due to the lower (of the double-stage) suspension fiber. The key parameter characterizing internal friction in the fibers is the frequency-dependent loss angle $\phi(\omega)$ which has contributions from (a) the surface, (b) the bulk and (c) thermoelastic effects [102]. For high-purity silicon fibers at 123 K, the thermoelastic and bulk loss contributions are negligible. The loss angle is then dominated by surface imperfections and defects, which can be modeled by a characteristic depth $h$ and a surface loss angle $\phi_s$. We assume $h = 1\,\mu$m and $\phi_s = 10^{-5}$, and follow the formalism described in [102] to evaluate the loss angle. Finally, the amplitude spectral density of this displacement noise can be obtained by applying the fluctuation-dissipation theorem [103], as

$$x(\omega) = \sqrt{\frac{4k_BT}{\omega m_{\rm A}}\left(\frac{\omega_0^2\phi(\omega)}{\omega_0^4\phi^2(\omega) + [\omega_0^2 - \omega^2]^2}\right)}, \tag{6.20}$$

where $T$ is the equilibrium temperature of the system, and $f_0 = \omega_0/2\pi$ is the resonant frequency of the suspension. A more thorough analysis requires Finite Element Analysis (FEA) calculations to validate the analytic approximations. In our present modeling, we have a large safety factor for this noise contribution, and so are immune to it being higher by a factor of a few (the analytic calculation is expected to be accurate to within this factor).

At the time of writing, work is underway to build a table-top version of this amplifier, to assess overall feasibility and get more experience with the practical difficulties and noise sources associated with the idea. A choice has to be made for the type of suspension to be used. In this chapter, all the noise models assume a conventional, pendulum type suspension in which the mirrors are attached to a suspension point by means of fibers. However, alternative geometries have been used in similar experiments[58, 59, 104], such as attaching the mirror to a cantilever with an extremely high mechanical quality factor. A possible advantage offered by the cantilever approach is that it allows using much lighter mirrors than would be possible with the pendulum type suspensions. Lighter mirrors are desirable, because the optomechanical gain is in general a function of the ratio $P_{\rm circ}/m_{\rm A}$, as in Eq. (6.9). However, the increased susceptibility of lighter mirrors to suspension thermal noise may nullify any advantage due to larger amplifier gain. In effect, the requirement on the cantilevers having mechanical $Q > 10^4$ places requirements on the manufacturing and optic-bonding quality. For a rough estimate, we can consider the results of Fig. 11.19 in [104]. The suspension thermal noise is estimated to be $\approx 10^{-15}\,\mathrm{m}/\sqrt{\mathrm{Hz}}$ at 100 Hz, falling off as $f^{-2}$ at higher frequencies - this level of

displacement noise is $\approx 10^5$ times larger than the levels assumed in Fig. 6.4. The mirrors bonded to the cantilevers weighed $\approx 360\,\mathrm{mg}$. Assuming the other optical parameters remain the same, this will increase $\mathcal{K}_\mathrm{A}$ by approximately $10^2$. So, the $\xi$ contribution in Eq. (6.6) increases by $10^5$ while the signal amplification only increases by $10^2$, which completely negates the effect of using lighter mirrors.

Suspension thermal noise has been the bane of many previous attempts to measure room-temperature optomechanical squeezing at audio frequencies using gram-scale suspended optics, such as [57]. So, a detailed analysis of the exact cantilever geometry is required to assess merits of different suspension options - for example, it must be ensured that there aren't too many resonant modes of the cantilever in the frequency band the amplifier is supposed to improve Voyager's astrophysical sensitivity. Such an analysis is beyond the scope of this thesis, and is left for future work.

## 6.5 Noise in the main interferometer

In order for the amplifier to be effective, the detector sensitivity must be limited by optical losses in the readout chain. In this section, we discuss some noise sources in the IFO, including a variety of other optical losses and coating Brownian noise of the test masses, which in the current Voyager design are at a level comparable to readout losses. A plot of these noise curves is given in Figure 6.5, assuming the parameters in Table 6.2 for 15 dB squeezed injection.

### 6.5.1 Optical losses

In addition to readout loss, we consider a variety of optical losses within the main interferometer optics, consisting of four independent contributions: (a) 'injection losses' to be explained below, (b) input filter cavity (IFC) losses, (c) signal recycling cavity (SRC) losses, and (d) arm cavity losses.

The 'injection loss' lumps together the insertion loss of (i) two Faraday isolators (one double-pass and one single-pass) between the squeezed vacuum source and the interferometer, and (ii) mismatch between the SRC and IFC spatial modes. We assume a total injection loss of 1 %, anticipating that the insertion loss of the Faraday Isolators can be improved to 0.2 % per pass.

The SRC loss can be broken down further into (i) the spatial mode mismatch between the SRC and the interferometer's differential mode, (ii) absorption in the IFO beamsplitter (BS) and corner mirror (ITM) substrates, and (iii) reflection from

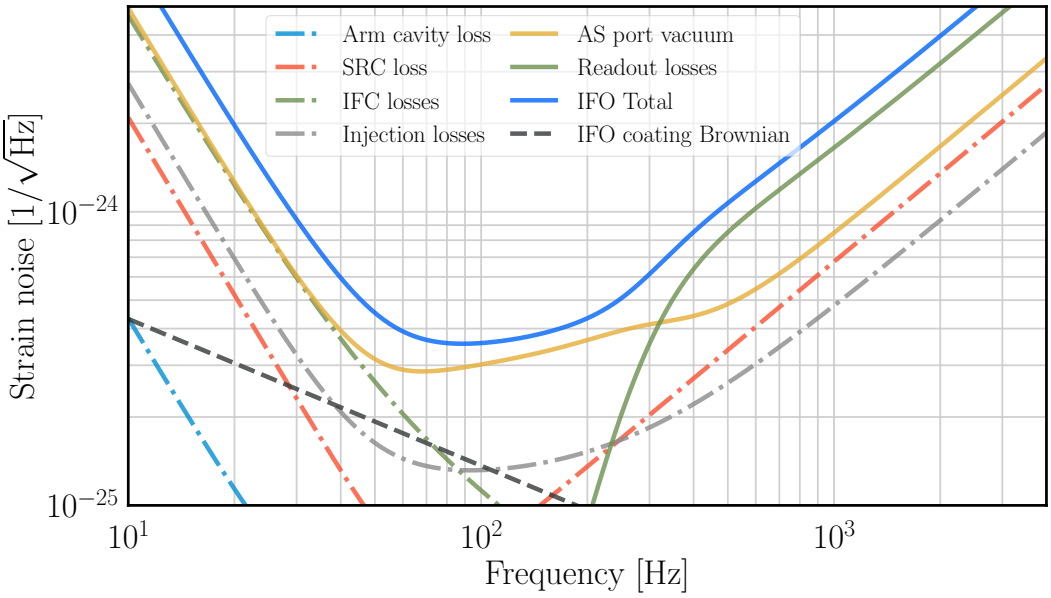


Figure 6.5: Breakdown of the dominant noise sources in the IFO, assuming the parameters given in Table 6.2 for 15 dB frequency-dependent squeezed vacuum injection. The noise levels are signal-referred assuming the amplifier is installed. See Section 6.5 for a detailed discussion of the various noise sources.

the anti-reflective (AR) coatings on the BS and ITMs. In particular, we require less than 300 ppm total round-trip loss for the SRC. Assuming that substrate absorption in, and reflection from the AR coatings for the ITMs and BS add up to a total loss of 50 ppm, the requirement on the mode mismatch to the interferometer's differential mode is 250 ppm, which is expected to be challenging considering that the lowest achieved mode mismatch in the current generation of interferometers is $\simeq 1\%$.

Our choices for the losses represent an optimistic estimate of the progress in loss reduction over the next 10 years. In particular, we are emphasizing the situation in which a high level of squeezing is injected, but the readout losses are high. In the case where injection losses are high and readout losses are low, the efficacy of the amplifier is substantially reduced (or even non-existent). A summary of our design requirements for the losses is given in Table 6.2, with the corresponding noise curves given in Fig. 6.5.

### 6.5.2 Coating Brownian noise in Voyager test masses

According to the current Voyager design, which only assumes 10 dB of squeezed vacuum injection [68], it is anticipated that coating Brownian noise of the interferometer's arm cavity optics will be the dominant noise contribution from 40 – 100 Hz.

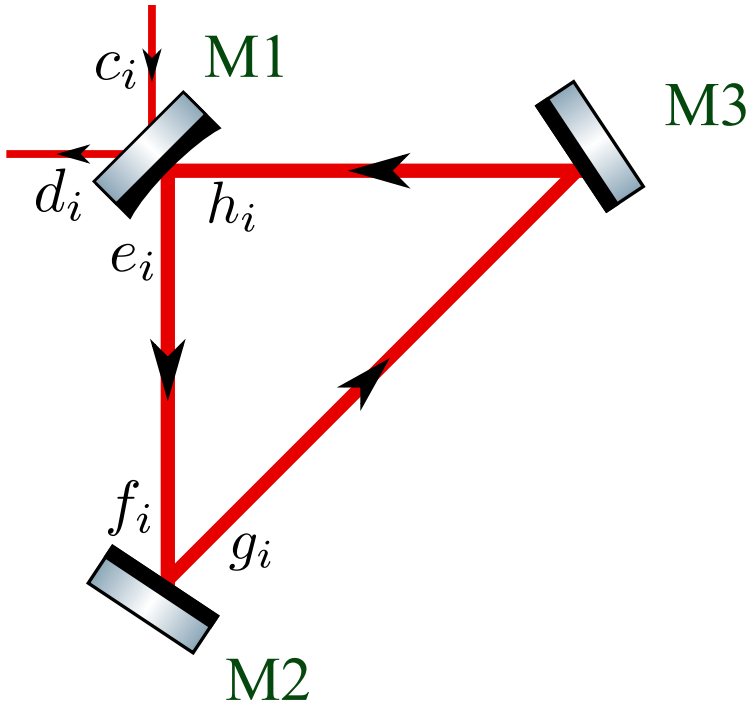


Figure 6.6: A three-mirror triangular ring cavity with pump and signal co-circulating counterclockwise (not drawn to scale). We assume all three mirrors have the same mass $m_{\mathrm{A}}$. Two of these ring cavities are combined to form the MZ amplifier in Fig. 6.1

.

This would impose a serious limit on the performance of all quantum non-demolition schemes, not just the amplifier proposed in this work. Furthermore, in our analysis, we have considered even higher levels of squeezed vacuum injection, and so we expect an even broader band over which coating Brownian noise will be dominant. This is especially problematic since the amplifier is designed to be most effective in the same frequency band (see Figure 6.3). To fully take advantage of the sensitivity improvement offered by the amplifier, we have assumed that the coating Brownian noise can be reduced by a further factor of $4-5$ at all frequencies. This more speculative coating Brownian noise is plotted in Fig. 6.5 (and Fig. 6.8 for 20 dB, as discussed in Section 6.9). While achieving this reduction is a challenging prospect, several promising leads are being explored [105].

## 6.6 Derivation for the input-output relations of the Mach-Zehnder amplifier

In this section, we provide a detailed derivation of the input-output relation for the MZ amplifier introduced in Section 6.3.2. While the effect of optical losses, mirror displacement noise, and other technical noise sources are neglected in the

calculations presented in this section, they are included in our numerical simulations.

We begin by computing the input-output relation for one of the two triangular ring cavities whose field amplitudes are labeled in Fig. 6.6. We consider the case where the pump and signal co-propagate counterclockwise. We let $c_{1,2}$ and $d_{1,2}$ denote the incident and reflected signal field amplitudes, respectively, and we assume the incident pump (electric) field has the form $E(t) = E_0 \cos(\omega_0 t)$ for some constant amplitude $E_0$. We let $r_\mathrm{A} = \sqrt{1 - T_\mathrm{A}}$, $t_\mathrm{A} = \sqrt{T_\mathrm{A}}$ denote the amplitude reflection and transmission coefficients of mirror M1, respectively, as seen from the cavity interior. The amplitude reflection coefficient of M2 and M3 is set to +1 (again as seen from the interior of the cavity). We let $l_1$ denote the distance that the beam travels from M1 to M2, and $l_2$ the distance that the beam travels from M2 to M3 and then to M1. Furthermore, we assume no cavity detuning. Under these conditions, the pump resonates in the cavity, thus enhancing the radiation pressure effect we are exploiting.

The beating between the pump and signal as they co-propagate along the ring produces the optomechanical amplification discussed in Section 6.3. The total amplification is equivalent to that produced by a cavity where M1 and M3 are fixed and where the boundary condition at the free mirror M2 is

$$g_1 = f_1, \quad g_2 = -\kappa_\mathrm{A} f_1 + f_2, \tag{6.21}$$

with

$$\kappa_\mathrm{A} = -\frac{8\omega_0 P_\mathrm{circ}}{c^2} \sum_{i=1}^{3} \cos^2\left(\theta_{\mathrm{inc},i}\right) \chi_i, \tag{6.22}$$

where $P_\mathrm{circ}$ is the power circulating in the ring, and for each optic $\mathrm{M}_i$ ($i = 1, 2, 3$) we have $\theta_{\mathrm{inc},i}$ as the angle of incidence and $\chi_i$ as the mechanical susceptibility. For a detailed derivation of Eq. (6.21) in the limit where the mirrors are free masses, see Sec. IV. A. of [61]. In our simulations, we assume that all three mirrors have the same mechanical susceptibility, $\chi_\mathrm{A}$, and that the ring is arranged as an equilateral triangle configuration (i.e., $\theta_{\mathrm{inc},i} = \pi/6$), in which case $\kappa_\mathrm{A}$ reduces to Eq. (6.7). Furthermore, the boundary conditions at M1 are given by

$$\begin{aligned} d_1 &= t_\mathrm{A} h_1 - r_\mathrm{A} c_1, \quad & d_2 &= t_\mathrm{A} h_2 - r_\mathrm{A} c_2, \\ e_1 &= t_\mathrm{A} c_1 + r_\mathrm{A} h_1, \quad & e_2 &= t_\mathrm{A} c_2 + r_\mathrm{A} h_2, \end{aligned} \tag{6.23}$$

and the field amplitudes propagate along the ring as

$$\begin{aligned} f_1 &= e_1 e^{i\Omega l_1/c}, \quad f_2 = e_2 e^{i\Omega l_1/c}, \\ h_1 &= g_1 e^{i\Omega l_2/c}, \quad h_2 = g_2 e^{i\Omega l_2/c}. \end{aligned} \tag{6.24}$$

Solving this system gives us the input-output relation for the ring as

$$\begin{pmatrix} d_1 \\ d_2 \end{pmatrix} = e^{i2\eta} \begin{pmatrix} 1 & 0 \\ -\mathcal{K}_\mathrm{A} & 1 \end{pmatrix} \begin{pmatrix} c_1 \\ c_2 \end{pmatrix}, \tag{6.25}$$

where

$$e^{i2\eta} = \frac{e^{i\Omega L_\mathrm{A}/c} - r_\mathrm{A}}{1 - e^{i\Omega L_\mathrm{A}/c} r_\mathrm{A}}, \quad \mathcal{K}_\mathrm{A} = \left( \frac{t_\mathrm{A}^2}{1 - 2\cos(\Omega L_\mathrm{A}/c) r_\mathrm{A} + r_\mathrm{A}^2} \right) \kappa_\mathrm{A}, \tag{6.26}$$

with $L_A = l_1 + l_2$ as the round-trip length of the ring.

For the full MZ configuration of Fig. 6.1, we need to analyze the input-output relations for both the 'forward' direction (i.e., from $b_{\mathrm{IFO},i}$ to $b_i$) and the 'backward' direction (i.e., from $a_i$ to $a_{\mathrm{IFO},i}$). The relations for the forward direction can be trivially derived from Eq. (6.25) to be

$$\begin{pmatrix} b_1 \\ b_2 \end{pmatrix} = e^{i2\eta} \begin{pmatrix} 1 & 0 \\ -\mathcal{K}_\mathrm{A} & 1 \end{pmatrix} \begin{pmatrix} b_{\mathrm{IFO},1} \\ b_{\mathrm{IFO},2} \end{pmatrix}. \tag{6.27}$$

In the limit $\Omega L_A/c \ll 1$ where the cavity is short compared to a signal wavelength, and in the limit $t_\mathrm{A}^2 \ll 1$ where M1 is highly reflecting, the forward relation reduces to Eq. (6.6), whereby the results are expressed in terms of the power reflectivity $R_\mathrm{A} = r_\mathrm{A}^2$ and power transmissivity $T_\mathrm{A} = t_\mathrm{A}^2$. For the backward direction, the beam is immune to the optomechanical effect since it counter-propagates against the pump, and so the relations are like Eq. (6.27) but with the pump 'turned off', giving

$$\begin{pmatrix} a_{\mathrm{IFO},1} \\ a_{\mathrm{IFO},2} \end{pmatrix} = e^{i2\eta} \begin{pmatrix} a_1 \\ a_2 \end{pmatrix}. \tag{6.28}$$

While amplitude fluctuations of the pump induce mirror displacement fluctuations that couple to the phase of the counter-propagating mode, these fluctuations can be ignored since the counter-propagating mode is weak to begin with, and the mirror's displacement is small compared to a carrier wavelength. Finally, we must also

deduce the relation between the power $P_{\rm circ}$ circulating in each ring and the source power $P_{\rm source}$ of the amplifier, as labeled in Fig. 6.1. A simplified version of the above calculation gives

$$P_{\rm circ} = \frac{1}{2}\left(\frac{t_{\rm A}}{1-r_{\rm A}}\right)^2 P_{\rm source}, \tag{6.29}$$

where the overall factor $1/2$ takes into account the beam-splitting at BS1. In the limit $T_{\rm A} \ll 1$ this reduces to Eq. (6.10).

## 6.7 Output filter cavity reflectivity

The reflectivity of a filter cavity has been derived in Appendix A of [49], while a more general treatment of its quadrature rotation effects were given in Appendix A of [106]. We have adopted the equations derived there, but due to a difference in Fourier transform convention, have used the complex conjugate of Equation A6 from [49]. Explicitly, in our calculations, the amplitude reflectivity $r_{\rm fc}(\Omega)$ of a two mirror filter cavity, for an *audio sideband frequency* $\Omega$ is given by

$$r_{\rm fc}(\Omega) = r_{\rm in} - \frac{t_{\rm in}^2}{r_{\rm in}}\frac{r_{\rm rt}e^{i\phi(\Omega)}}{1-r_{\rm rt}e^{i\phi(\Omega)}}, \tag{6.30}$$

where the symbols $r_{\rm rt}$, $r_{\rm in}$ and $\phi(\Omega)$ are defined in Eqs. A7–A8 of [49].

Using the relation between quadrature fields $a_{1,2}(\Omega)$ and sideband fields $a(\omega_0 \pm \Omega)$, Eq. (6.30) allows us to calculate the phase rotation a quadrature field experiences upon reflection from the OFC, as

$$b_{\rm out}(\omega_0+\Omega) = r_{\rm fc}(\Omega) b_{\rm in}(\omega_0+\Omega). \tag{6.31}$$

## 6.8 Effect of amplifier mirror mass on sensitivity

An important design consideration is the choice of mass of the amplifier mirrors. In Fig. 6.7, we show the sensitivity for three different mass choices (all for the case of 15 dB frequency-dependent squeezed vacuum injection). The amplifier and OFC parameters for the 30 g case are those given in Table 6.2. However, for 3 g and 300 g, the amplifier properties (except for optical loss and displacement noise) and OFC properties (except for optical loss and cavity length) were re-adjusted to achieve optimal sensitivity. Lighter mirrors offer more sensitivity improvement, mainly due to the higher amplifier optomechanical gain. We therefore propose to make the mirror as light as possible.

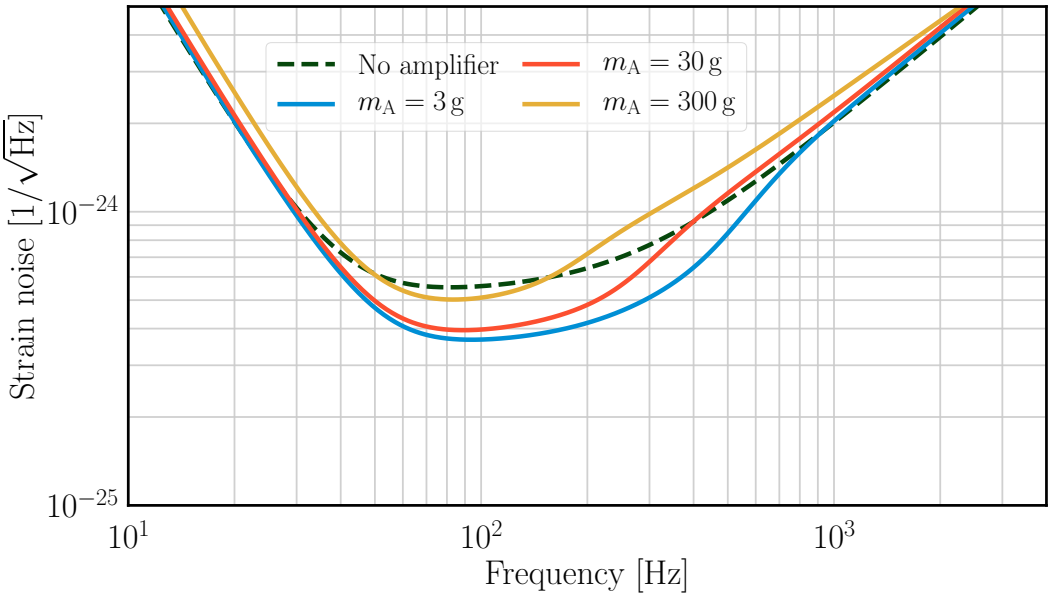


Figure 6.7: Voyager sensitivity improvement as a function of the mass of the amplifier mirrors. In all cases, 15 dB of frequency-dependent squeezed vacuum is assumed to be injected into the anti-symmetric port of main interferometer.

However, there are several practical difficulties involved in working with very light mirrors. Firstly, with extremely light mirrors, it is difficult to sustain large circulating power in the amplifier ring cavities. Another concern is related to suspension thermal noise, which scales as $\propto m_A^{-1/2}$. The difficulty in realizing low $\phi(f)$ for suspension fibers with a large surface-area-to-volume ratio motivates the choice of $m_A = 30\,g$. This allows for a wide margin of safety since the suspension noise is $\simeq 1/10$ of the limiting noises in our noise budget.

## 6.9 Prospects for 20 dB squeeze injection

In addition to the nominal case considered thus far in this chapter, in this section, we consider prospects for 20 dB of frequency dependent squeezed vacuum injection, for which the amplifier makes a much bigger impact on the detector sensitivity. To achieve the correct rotation of the vacuum noise ellipse as a function of frequency, we find that two input filter cavities in series are needed, unlike the 15 dB case, where only one is needed. Furthermore, all of the noise sources within the main interferometer must be maintained well below the squeezed vacuum noise, which would be extremely challenging at this level. Finally, to fully take advantage of the sensitivity improvement, we propose using even lighter mirrors for the amplifier ($m_A = 10\,g$), which results in higher optomechanical gain. The detailed design

parameters for all the optics and associated losses are given in Table 6.2, and the corresponding noise curves are shown in Fig. 6.8.

## 6.10 Conclusion

In this work, we have presented a novel approach to amplify the GW signal to protect the signal to noise ratio against quantum decoherence. We emphasize that this work is only meant to be an exploratory study of the idea of using an optomechanical device as a phase sensitive amplifier for terrestrial GW detectors. In order for this to be incorporated into the design of a detector such as Voyager, significant work will have to be done, starting with table-top scale experiments, to get a deeper understanding of the many technical noise sources we have not addressed in this paper (e.g. feedback control of the amplifier, losses due to the mode matching between the interferometer and the amplifier, fluctuations of the relative alignment of the cavities, imperfections in the amplifier optics, etc.).

It has been previously been proposed to use nonlinear crystals to amplify the interferometer output [107], and to use atomic systems to generate "negative inertia" that leads to back-action evasion [108]. These are promising approaches, but requires mitigating (i) backscatter noise due to the lower optical quality of crystals relative to super-mirrors, (ii) high scatter loss induced decoherence due to the poor optical quality, and (iii) pump noise coupling due to a non-vacuum seed.

Promising future directions to consider include:

1. lighter masses in the amplifier (where the optomechanical gain would extend to higher frequencies),

2. interferometers (with higher masses) which are limited by shot noise rather than radiation pressure at lower frequencies (where there is already significant optomechanical gain),

3. a hybrid diplexed crystal-optomechanical approach where a crystal amplifier is used to extend the optomechanical amplifier gain to higher frequencies.

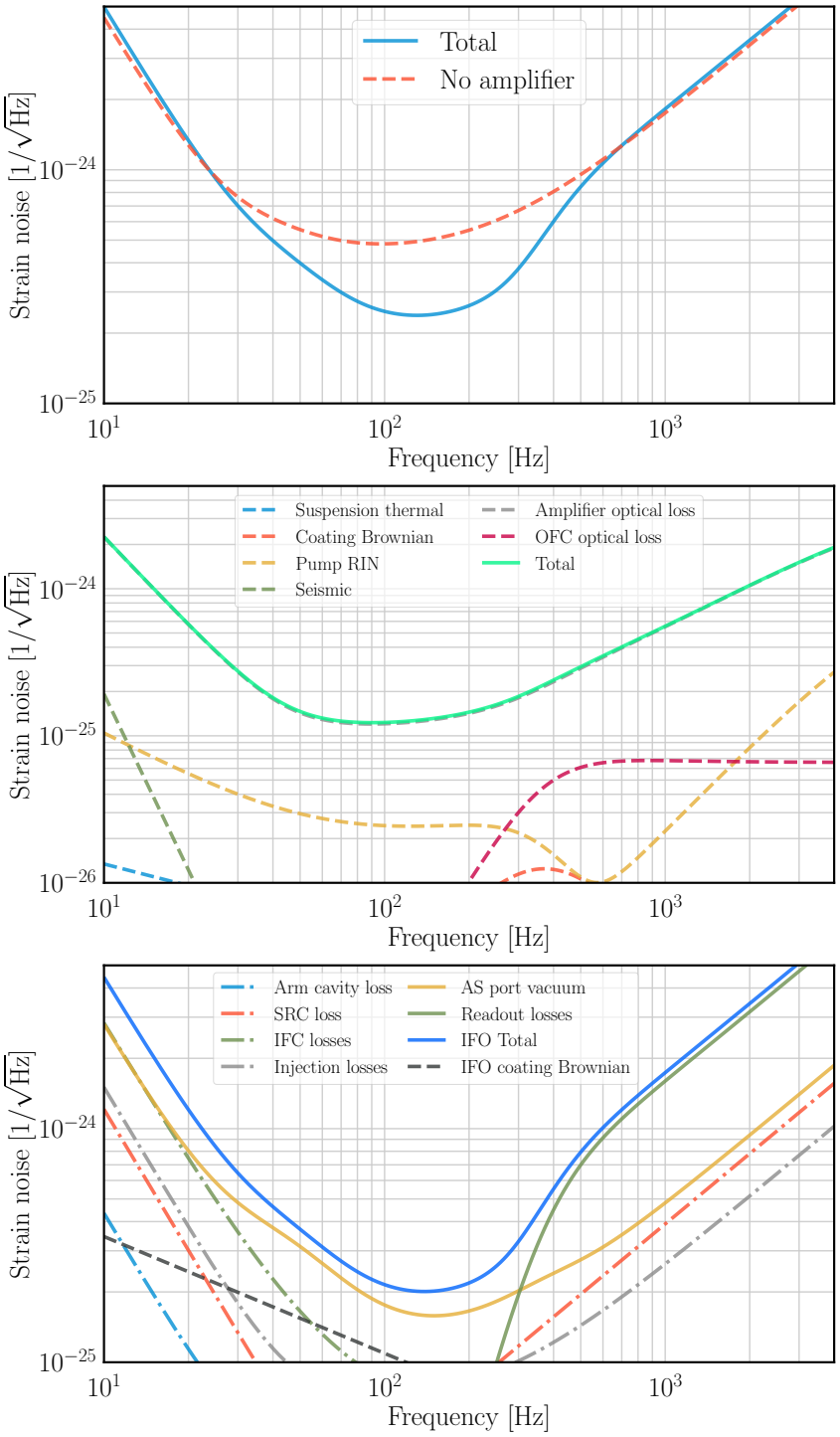


Figure 6.8: Sensitivity of LIGO Voyager for a more ambitious design that incorporates 20 dB frequency-dependent squeezed vacuum injection, and an amplifier with 10 g mirrors. The detailed parameter assumptions are given in Table 6.2. The interpretation of the top, middle, and bottom subplots are the same as the 15 dB plots Fig. 6.3, Fig. 6.4, and Fig. 6.5, respectively. The coating Brownian noise shown in the lower plot is a factor of 5 lower than the nominal Voyager design.

*Chapter 7*

# GLOBAL OPTIMIZATION OF MULTILAYER DIELECTRIC COATINGS FOR PRECISION MEASUREMENTS

The work presented in this chapter was motivated by the need to get replacement folding mirrors for the PRC and SRC at the 40m, see Appendix D.2 for a discussion on problems with the existing configuration. The replacement mirrors had to satisfy spectral reflectivity requirements at multiple wavelengths. Given past experience with difficulty in obtaining such custom designs from commercial manufacturers, we decided to specify the design at the level of the thickness of individual layers of dielectrics to be deposited on a substrate. Building on some early work, this investigation led to an entirely open-source software package that allows for designing dielectric coatings that have to meet multiple performance targets. The text is largely adapted from [101].

## 7.1 Introduction

Interferometric gravitational wave detectors such as Advanced LIGO require mirrors with dielectric coatings that satisfy multiple requirements on reflectivity at multiple wavelengths, surface electric field, absorption within the coating, and thermal noise [9]. For the next generation of detectors, it is anticipated that there will be tighter requirements on these specifications. Furthermore, it is desirable that the coating design chosen will have minimal sensitivity to manufacturing tolerances.

In this chapter, I describe the construction of a cost function that quantifies how closely a given coating design satisfies the multiple requirements on it. Once this cost function has been constructed, it can be used with a numerical optimization algorithm, such as Particle Swarm Optimization [109] or Differential Evolution [110, 111], to compute the coating design (i.e. the set of thicknesses of various layers in a dielectric stack of alternating high- and low-index materials) that gives the (global) minimum value of the cost function in the allowed parameter space. Since most numerical optimization algorithms are designed to handle a scalar cost function, I convert the vector (multi-objective) cost function to a scalar number by taking the scalar product of it with a weight vector. The latter allows us to quantify which design objectives are more important than others.

Once an optimal solution has been arrived at, we verify its sensitivity to small perturbations in layer thicknesses as well as various assumed model parameters using Monte-Carlo (MC) analysis. This approach allows us to evaluate the relative performance of coating designs that vary along 'hyper-parameter' axes, such as the choice of number of layer pairs that make up the coating.

This approach of mapping a complex design problem into a scalar objective function minimization problem can be readily generalized to several other problems in the field of Gravitational Wave Astronomy. It is also of interest to the broader category of experiments that use optical cavities for precision measurements, such as the atomic and molecular optics community.

## 7.2 Requirements on multilayer dielectric coatings

In this section, the requirements on dielectric coatings of the type considered in this paper are described. Although the method is easily generalized to a multilayer stack with arbitrary refractive index profile, I only consider cases in which the stack is comprised of alternating layers of two dielectrics, with refractive indices $n_1$ (low-index) and $n_2$ (high-index). The coating is deposited on a fused silica substrate, with refractive index $n_{\text{sub}}$. These considerations are typical in the field of laser interferometry, but are also of relevance in various other fields such as nanoscale optomechanics. Strategies to increase the numerical efficiency of computing these properties are also briefly discussed.

### 7.2.1 Spectral reflectivity

The primary requirement on a dielectric coating design is the *power* reflectivity at wavelengths of interest, $R$. For a given dielectric coating stack with $M$ interfaces, this may be calculated in several ways. We opt to do the computation of the *amplitude* reflectivity, $\Gamma$ recursively, using the relation [112]

$$\Gamma_i = \frac{\rho_i + \Gamma_{i+1} e^{-2ik_i l_i}}{1 + \rho_i \Gamma_{i+1} e^{-2ik_i l_i}}, \tag{7.1}$$

where the index $i = M, M-1, ..., 1$, with $i = 1$ corresponding to the interface of the coating with the incident electromagnetic field. In Equation (7.1),

$$k_i = \frac{2\pi n_i^T \cos\theta}{\lambda}, \tag{7.2a}$$

$$\rho_i = \frac{n_{i-1}^T - n_i^T}{n_{i-1}^T + n_i^T}, \tag{7.2b}$$

$$n_i^T = \begin{cases} \frac{n_i}{\cos\theta_i}, & \text{p-polarization,} \\ n_i \cos\theta_i, & \text{s-polarization,} \end{cases} \tag{7.2c}$$

where $l_i$ is the *physical* thickness of, $n_i$ is the refractive index of, and $\theta_i$ is the angle of incidence into the $i-$th layer. The recursion relation Equation (7.1) is initialized with $\Gamma_{M+1} = \rho_{M+1} = \frac{n_M^T - n_{\text{sub}}^T}{n_M^T + n_{\text{sub}}^T}$, where $n_{\text{sub}}^T$ is defined by Equation (7.2b) for the substrate onto which the dielectric stack is deposited. The power reflectivity of the stack may then be computed as $R = |\Gamma_1|^2$. A typical coating design requirement will specify $R(\lambda, \theta, \text{polarization})$.

### 7.2.2 Surface electric field and absorption

In optical cavities in which the circulating power is high, absorption in the dielectric layers becomes important for a number of reasons. The coatings have to be able to withstand the absorption-induced thermal heating for the highest expected incident electromagnetic field intensity. In applications, where the cavity mirrors have to be maintained at cryogenic temperatures, the requirement becomes even more stringent as the rate at which heat can be extracted from the optic will set the maximum permissible absorption in the coating [88].

Absorption is quoted as a dimensionless fraction of the incident power which is converted to thermal energy in the coating. We evaluate absorption by first determining the square of the electric field as a function of penetration depth, z, normalized by the incident electric field, $N = \frac{|\vec{E}(\text{z})|^2}{|\vec{E}_o^+|^2}$ [113]. The total absorption, $\alpha_{\text{T}}$ in a coating of thickness $L$ is

$$\alpha_{\text{T}} = \int_0^{\text{L}} d\text{z}\, N\alpha(\text{z}), \tag{7.3}$$

with $\alpha(\text{z})$ describing the bulk absorption of the materials used in the coating, for which measured values are available. In practise, the integral in Equation (7.3) can be evaluated numerically. However, this is a computationally expensive operation. A good proxy for use in an optimizer is the value of the electric field transmitted into the first layer of coating, given by [114]

$$|\vec{E}_{\text{surface}}| = |\vec{E_o^+}||1 + \Gamma_1|. \tag{7.4}$$

$\vec{E_o^+}$ is set by the incident power density, which varies in different applications. Since $\Gamma_1$ has to be computed for evaluating the power reflectivity, the additional

computational overhead is minimized. In order to minimize $\vec{E}_{\text{surface}}$, and hence the absorption, it is conventional to add a nearly half-wavelength optical thickness 'cap' of dielectric material to a high-reflectivity (HR) coating.

### 7.2.3 Thermo-optic and Brownian noise

Sensitivity of the current generation of laser interferometric gravitaitonal wave detectors is expected to be limited by the Brownian thermal noise of the coatings used. These consist of up to 20 pairs of alternating layers of $SiO_2$ (low-index material) and $Ta_2O_5$ (high-index material). In order to improve the sensitivity of future generation of detectors, an active area of research pursued in the last decade is the development of alternative dielectrics with which coatings that can meet the power reflectivity requirements can be developed.

Another application in which the Brownian noise of dielectric coatings can be a limiting noise source is the development of ultrastable frequency reference cavities [115]. The frequency stability of lasers used in precision metrology experiments are often referred to such reference cavities, and efforts are underway to identify alternative dielectrics so that even more stable reference cavities can be constructed.

One promising option is the pair of crystalline materials AlGaAs/GaAs [116]. However, there is a second effect which has to be simultaneously considered, the 'Thermo-optic' noise, which arises as a result of the temperature dependence of the refractive index of the dielectrics, and their thermally driven length fluctuations. With clever design, it is possible to suppress this noise contribution by coherent cancellation of the two effects [117].

### 7.2.4 Immunity to small perturbations in assumed model parameters

In evaluating the coating properties, assumptions are made about the layer thicknesses, refractive indices, dispersion, bulk absorption, and mechanical loss angle of the dielectrics. Additionally, uncertainties may exist, for example, in the assumed value of the angle of incidence. Since parameters of interest such as the power reflectivity of the coating are functions of these parameters, any uncertainty in them (due to manufacturing process limitations, measurement errors etc.) propagate through to the performance of the manufactured coating. In order to meet the tight tolerances on these parameters, it is desirable to choose (for fabrication) the coating design whose sensitivity to small errors in these model parameters is low.

We address this using a two step approach. First, during the optimization stage, the

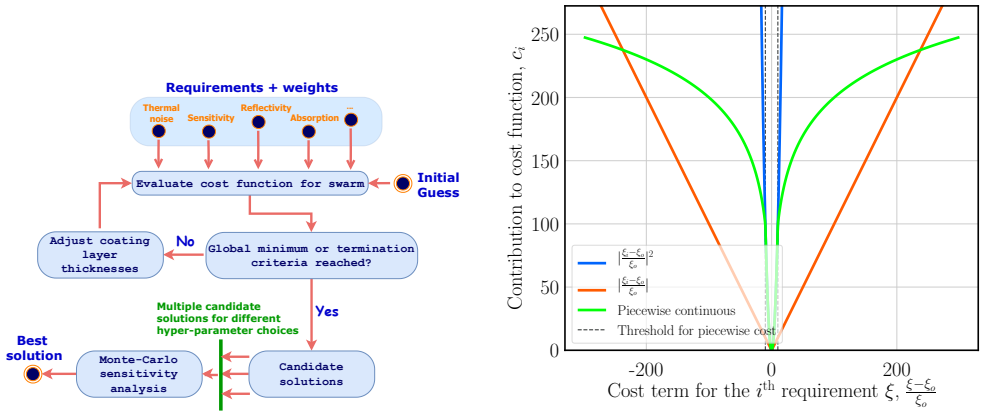


(a) (b)

Figure 7.1: Overview of the workflow adopted. As shown in Figure 7.1(a), the process starts by identifying the requirements, and encoding these in a cost function. The cost function is then minimized using a global optimizer, such as `MATLAB`'s particle swarm optimization toolbox [109] or `SciPy`'s Differential Evolution [110, 111]. In order to choose between multiple candidate solutions, Monte-Carlo sensitivity analysis is used to choose the solution with the least sensitivity to model parameters. Figure 7.1(b) shows the advantage of defining the cost function in a piecewise manner, see text for more discussion.

(numerical) derivative of coating properties with respect to model parameters are used in constructing the cost-function to be minimized. Secondly, the sensitivity of a given design to small ($\approx 1\%$) perturbations to the assumed model parameters is evaluated explicitly. The errors themselves are assumed to be i.i.d., and are drawn from an uncorrelated multivariate zero-mean Gaussian distribution whose standard deviation is chosen to be 0.5% of the optimized value of the parameter. For example, errors in the thickness of the $i$-th layer, $l_i$, is sampled from the distribution $p(l_i) = \frac{1}{\sqrt{2\pi\sigma^2}} e^{-l_i^2/2\sigma^2}$, with $\sigma = 0.005 l_i^{\text{opt}}$ and $l_i^{\text{opt}}$ being the value of the thickness of the $i$-th layer that best achieves the design objectives. The `emcee` package [118] or `MATLAB` is used to generate $\approx 1 \times 10^5$ samples, and the `corner` package [119] provides a convenient way to visualize the results. A confidence interval on meeting specifications within tolerance can thus be stated.

## 7.3 Numerical optimization techniques for coating design

The methodology adopted for optimizing the dielectric coating design is schematically illustrated in Figure 7.1.

### 7.3.1 Cost function construction and minimization

The parameter space over which the optimization is done is the set of coating layer thicknesses, $\{l_i\}$, and in the problems we consider, can be $O(100)$-dimensional. Furthermore, the values $l_i$ can take are constrained to not be too small (for practical manufacturing reasons) and not larger than the longest optical wavelength of interest, $\lambda$. Once a set of requirements, $c_i$, and weights that reflect their relative importance, $w_i$ have been arrived at, these are encoded into a cost function, $C(c_i, w_i, l_i)$. The weights are necessary to convert the *multiple* objectives of the optimization problem into a *scalar* which can be minimized using a numerical optimzation algorithm. The mathematical statement of the optimization problem amounts to

$$\begin{aligned} \min_{\{l_i\}} \quad & C(c_i, w_i, l_i), \\ \text{subject to} \quad & l_{\min} \leq l_i \leq l_{\max} \; \forall \; i. \end{aligned} \tag{7.5}$$

We chose `MATLAB`'s Particle Swarm Optimization (PSO) toolbox for implementing Equation (7.5). Typical runtimes on a machine that can perform 45 GFlops is $O(10)$ minutes. Subsequently, we also found similar performance could be realized using `SciPy`'s Differential Evolution optimizer [110], which has the added advantage of being an open-source utility. The functional form of the individual terms contributing to the cost function, $c_i$, was deliberately constructed in a normalized, piecewise manner. Normalization was necessary in order to compare costs from different requirements. Furthermore, since PSO looks for a globally optimal solution, it is likely that individual particles will traverse regions of high cost in the multi-dimensional parameter space. Defining the cost in a piecewise manner preserves a derivative term that allows the PSO functions to converge to a global minimum, but varied quadratically near the desired values and only logarithmically above some threshold value. As illustrated in Figure 7.1(b), this prevents the cost function from blowing up to large values for poor candidate solutions, as compared to other ways of specifying the error such as the L2− and L1− norms. More exotic functional forms, such as $\sinh^{-1}\left(|\frac{\xi-\xi_o}{\xi_o}|\right)$ can also be used to achieve the same goal.

### 7.3.2 Monte-Carlo sensitivity analysis

As there are "hyper-parameters" that do not directly enter the cost function, such as the number of layers in a coating, it is possible to have the optimization algorithm yield multiple candidate solutions. We wish to choose the simplest solution (from a fabrication standpoint) that is least sensitive to small perturbations in model

parameters, and meets the coating requirements within specified tolerances. For the cases considered in this paper, the perturbations used are summarized in Table 7.1.

Table 7.1: Summary of perturbations (assumed to be uncorrelated, and hence, sampled from a multi-dimensional Gaussian probability distribution with diagonal covariance matrix). These were motivated with input from manufacturers.

| **Model parameter** | **Uncertainty [%]** |
|---|---|
| Physical thickness of layers, $\Delta l_i$ † | 0.5 |
| Refractive indices of layers, $\Delta n_1$ and $\Delta n_2$ | 0.5 |
| Angle of incidence, $\Delta\theta_1$ ‡ | 1 |

† Due to the nature of the manufacturing process, all layers are expected to have identical *fractional* uncertainties in *physical* thickness.

‡ Applicable only for non-normal incidence cases.

**Application to the inverse problem**

An interesting application of the Monte-Carlo approach is to apply it to the inverse problem of inferring the optical thicknesses of a dielectric coating, given a *noisy measurement* of its spectral reflectivity as a function of the wavelength, $\lambda$. The problem becomes computationally expensive to evaluate if the dimensionality is unrestricted - that is, if we allow the physical thicknesses and refractive indices of all layers to be arbitrary. However, in practise, the dimensionality of the problem can be reduced. For concreteness, consider an optical coating composed of two dielectrics, $SiO_2$ and $Ta_2O_5$. Assume the coating is built up with 19 repeated identical bilayer pairs, with the top bilayer pair having a different thickness for reducing the surface electric field amplitude. Furthermore, the dispersion of the dielectrics composing the coating are well characterized, and so may be taken as fixed. In this example, the task then amounts to the following - given the power transmissivity $T(\lambda)$, can we infer 4 numbers: $l_1$, the thickness of the top layer of $SiO_2$, $l_2$, the thickness of the next layer of $Ta_2O_5$, and $[l_3, l_4]$, the thicknesses of the repeated bilayer pair. Applying this approach to the harmonic separator described in Section 7.4.1, we infer thicknesses for the constructed coating that are within manufacturing tolerances. The modelled spectral reflectivity curve for the inferred coating is in good agreement with the measurement, as shown in Figure 7.2(a). The algorithm was also applied to the problem of inferring the coating structure of the aLIGO ETMs, for which spectral

reflectivity data was available for a much wider range of wavelengths than the harmonic separator. Results are shown in Figure 7.2(b). The approach worked reasonably well at the wavelengths of interest - however, there was considerable divergence between the inferred model and measurement at short wavelengths. It is hypothesized that this disagreement is because we do not have access to the (proprietary) dispersion data for the dielectrics used to coat the aLIGO ETM - rather, we just know their refractive indices at the two wavelengths of interest, 1064 nm and 532 nm.

Table 7.2: Summary of the requirements on various parameters for three different coating designs that were optimized using the methodology outlined in this paper.

| | **Case Studies** | | |
|---|---|---|---|
| **Parameter** | Harmonic separator | aLIGO ETM | AlGaAs ETM * |
| Power reflectivity [%] / transmissivity [ppm] † | $T_{\lambda_1} \leq 50$, $R_{\lambda_2} \geq 99.9$ | $T_{\lambda_1} \leq 5$, $R_{\lambda_2} \geq 99$ | $T_{\lambda_1} \leq 5$ |
| Thermo-optic noise [m/$\sqrt{\text{Hz}}$] ‡ | — | $1.2 \times 10^{-21}$ | $1 \times 10^{-21}$ |
| Brownian noise [m/$\sqrt{\text{Hz}}$]‡ | — | $7.5 \times 10^{-21}$ | $2.5 \times 10^{-21}$ |
| Surface electric field [V/m] | — | $\leq 1$ | $\leq 2$ |
| Absorption [ppm] | — | $\leq 1$ | $\leq 1$ |
| Angle of incidence [deg] | 41.1 | 0 | 0 |
| Polarization ^ | p-pol for $\lambda_1$, s- and p-pol for $\lambda_2$ | — | — |

* AlGaAs is used to collectively refer to alternating layers of $Al_{0.92}Ga_{0.08}As$ (low-index material) and GaAs (high-index material).

† $\lambda_1$ = 1064nm, $\lambda_2$ = 532nm.

‡ For noise requirements, numbers quoted are *amplitude* spectral densities at 100 Hz.

^ Both polarizations are degenerate for normal incidence, as is the case for the ETMs.

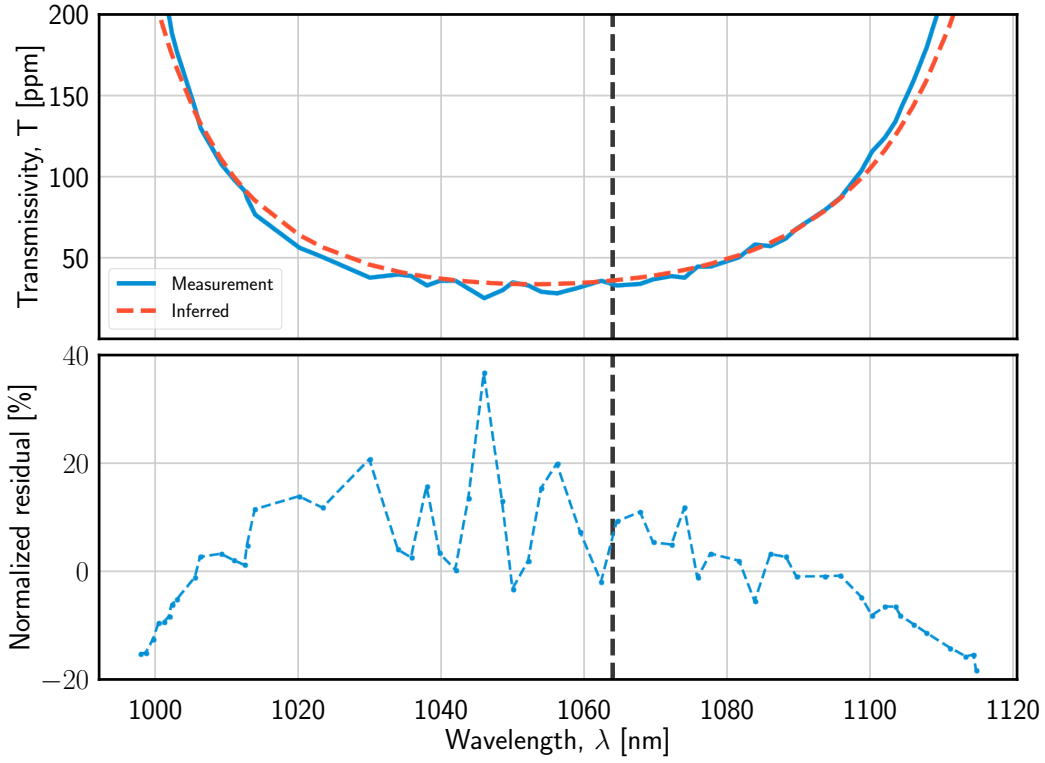


(a)

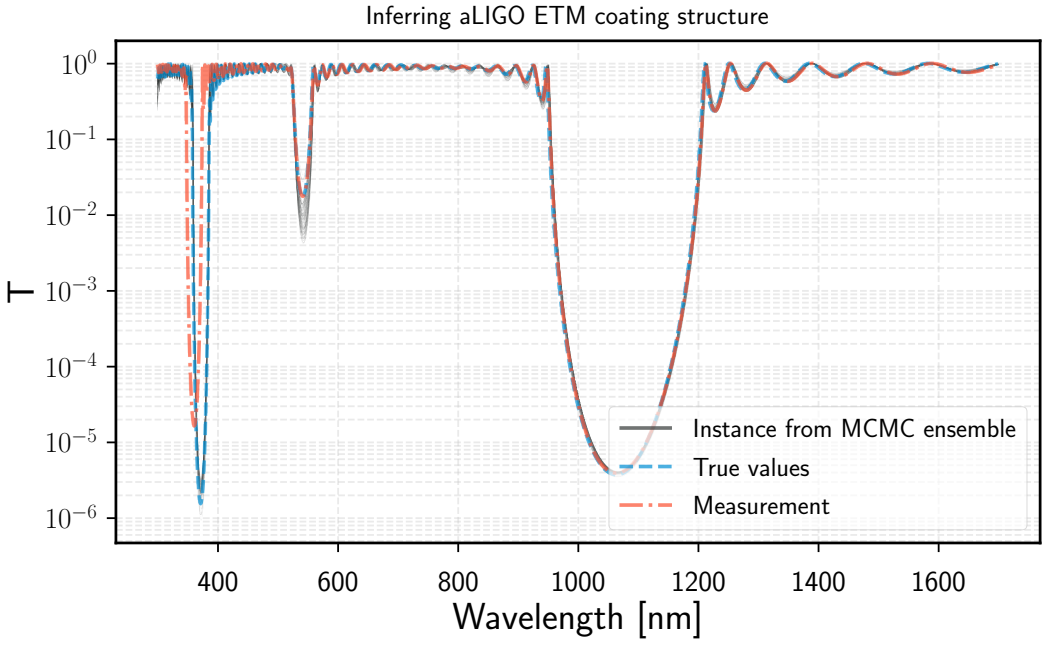


(b)

Figure 7.2: Inferring the coating structure from a spectral reflectivity measurement. Figure 7.2(a) is for a harmonic separator procured for the 40m interferometer, while Figure 7.2(b) is for the aLIGO ETM.

## 7.4 Case studies and results

Table 7.2 summarizes the requirements for a few case studies to which this methodology was applied. More details about the individual design requirements and results from the optimization runs are presented in the following subsections.

### 7.4.1 Harmonic separator

The aLIGO interferometers use multiple wavelengths of laser light to sense and control interferometric degrees of freedom of the suspended optical cavities [15, 120]. In this case, the objective was to design a harmonic separator that allowed extraction of light at the second harmonic, $\lambda_2 = 532$nm, from a folded optical cavity, while preserving high reflectivity for the fundamental light field at $\lambda_1 = 1064$nm. Furthermore, since the expected angle of incidence on this optic was $\approx 41.1^\circ$, the design had to meet the $R$ and $T$ specifications for both s- and p-polarizaitons at 532nm, while only p-polarization was of interest at 1064nm.

Figure 7.3(a) shows the spectral reflectivity of the optimized coating design. Figure 7.3(b) compares the *measured* performance of a harmonic separator fabricated with layer thicknesses generated using this optimization routine. The measured spectra appear blue-shifted relative to the design - this is consistent with systematic errors in either the layer thicknesses or the dielectric dispersions between the model and the manufactured optic. Nevertheless, the design requirement of $T < 50$ ppm at 1064 nm for $\approx 41^\circ$ angle of incidence was met. Based on the tolerance analysis done during the design phase, presented in Figure 7.3(c), we had high confidence that the design was robust to manufacturing errors, and indeed, this turned out to be the case.

### 7.4.2 HR cavity mirror coating for a gravitational wave detector

The aLIGO interferometers are designed to have Fabry-Pérot arm cavities with finesse $\approx 450$, for which the output coupling mirrors of the Fabry-Pérot arm cavities (referred to as the End Test Mass, ETM) is required to have $T \leq 5$ppm at $\lambda_1 = 1064$nm [121]. It also has to have $R \geq 99\%$ for $\lambda_2 = 532$nm to facilitate sensing and control of the arm cavity length using an auxiliary laser wavelength during the lock-acquisiton process [15, 120].

Additionally, since thermally driven microscopic fluctuations in the coating's optical and physical thickness is expected to limit the sensitivity of the instrument in the 100Hz-1kHz frequency band, the chosen coating design's Thermo-Optic (TO) and Brownian noise spectral densities should not exceed specified thresholds in this

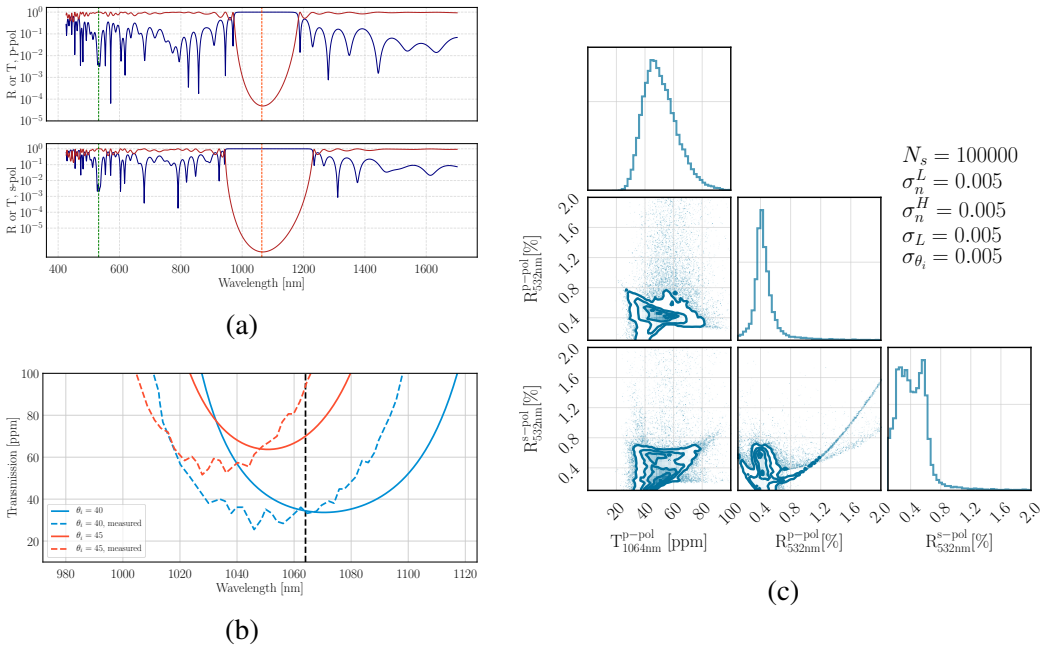


Figure 7.3: Performance of an optimized harmonic separator coating design. Figure 7.3(a) indicates the wavelengths of interest, $\lambda_1$ (orange) and $\lambda_2$ (green), with dashed vertical lines. Figure 7.3(b) shows the measured performance of a harmonic separator fabricated with layer thicknesses generated using the optimization routine described in the text. Figure 7.3(c) shows the robustness of the design choice of 20 layer pairs in the dielectric stack to small variations in assumed model parameters.

frequency range. For $SiO_2/Ta_2O_5$ coatings of the type used on the aLIGO optics, the mechanical loss angle, $\phi_{\text{dielectric}}$ is $\approx 4\times$ larger for $Ta_2O_5$ than for $SiO_2$ [122], and so the total thickness of the latter in a given coating design dominates the thermal noise contribution. Hence, the design should be optimized for minimum thermal noise, while still meeting other requirements.

Finally, the circulating power in these Fabry-Pérot cavities is expected to be $O(1\,\text{MW})$ during high power operation. The coating should be designed with a safety factor such that it is not damaged under these conditions. One possible damage mechanism is that residual particulate matter on the optic's surface gets burnt into the coating. In order to protect against this, the coating has to be optimized to have minimum surface electric field.

With these requirements as inputs to the optimization problem, we ran the particle swarm and sensitivity analysis and obtained a set of layer thicknesses. Figure 7.4 show the performance of the optimized coating, and compares it to the commonly used "quarter-wave stack" HR coating design.

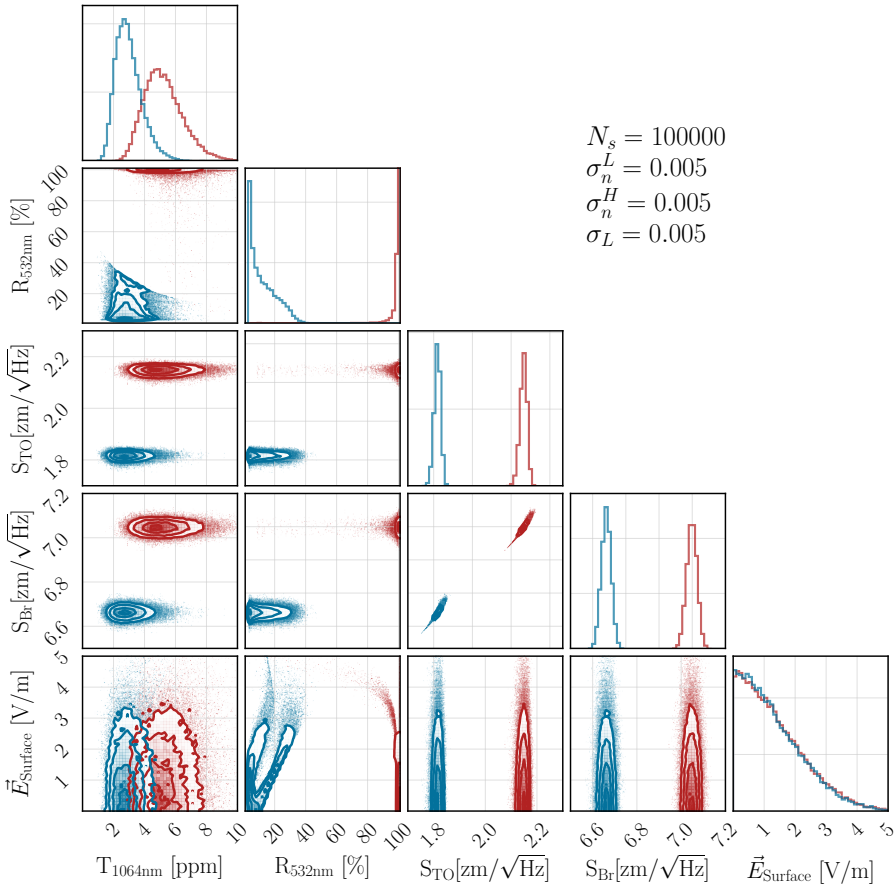


Figure 7.4: Performance of an optimized aLIGO ETM coating design. Here, we compare the robustness of the optimized design (red) and the naive quarter-wave design (blue) to small variations in assumed model parameters. The superior performance of the optimized coating, with respect to the design goals at both wavelengths, is evident.

### 7.4.3 Crystalline HR coatings

As mentioned in Section 7.2.3, alternative dielectric materials are being considered in an effort to reduce the coating Brownian noise, and hence, improve the sensitivity of laser interferometric GW detectors. One promising alternative is to use crystalline dielectrics consisting of alternating layers of $Al_{0.92}Ga_{0.08}As$ (low-index material) and GaAs (high-index material), which has been shown to yield up to tenfold reduction in Brownian noise, relative to $SiO_2/Ta_2O_5$ coatings with comparable reflectivity. However, the overall thermal noise has to take into account both the Brownian noise contribution, as well as the Thermo-Optic noise contribution. The latter can be minimized by coherent cancellation of thermorefractive and thermoelastic effects. The optimizer is encouraged to favor solutions that have this cancellation effect by including a penalty for the TO noise at a representative

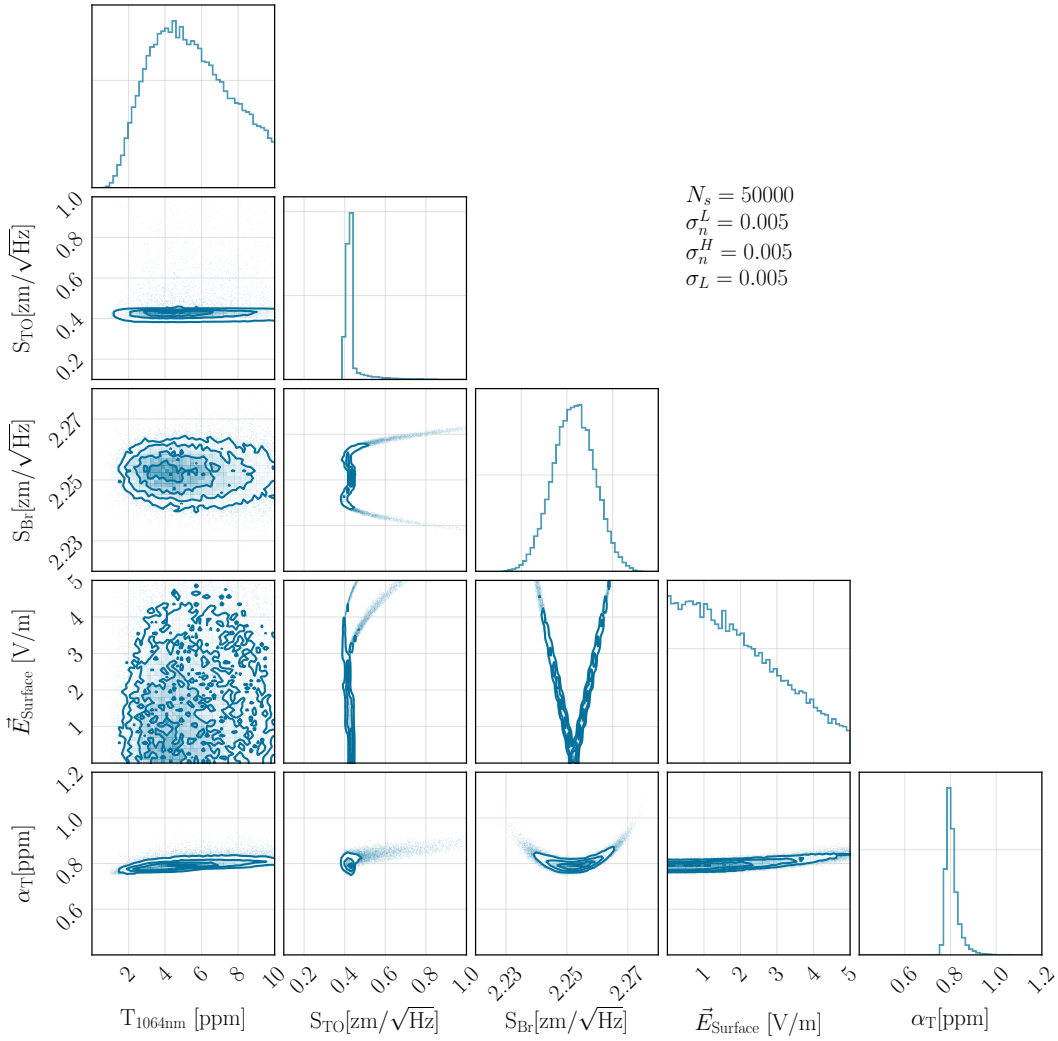


Figure 7.5: Sensitivity analysis of the optimized coating's performance.

frequency (we choose 100 Hz) in the cost function.

An additional consideration for future laser interferometric GW detectors, which are expected to be operated at cryogenic temperatures for thermal noise improvements [123], is that absorption in the mirror coating must be sufficiently small as to allow efficient radiative heat extraction and maintain the temperature of the optic at 123 K. While the absorption is not explicitly included in the cost function that is minimized by PSO, we include it in the MC sensitivity analysis, and confirm that the likelihood of it lying within the acceptable range of $\leq$ 1ppm is high, even if there are small deviations in assumed model parameters. The overall performance of the optimized coating is shown in Figure 7.5. Figure 7.6 shows the variation of the electric field inside the coating, and also the layer thickness profile.

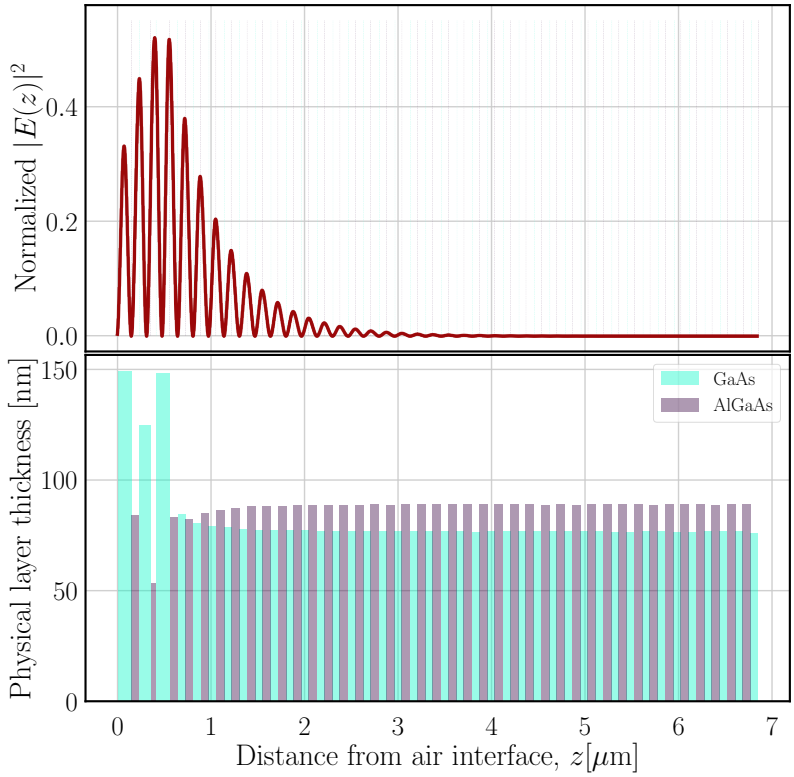


Figure 7.6: **Right top panel:** Square of electric field inside coating, normalized to the incident electric field, $|\frac{E(z)}{E_o^+}|^2$. The dashed vertical lines indicate boundaries between low- and high-index materials. **Right bottom panel:** Physical thickness profile of the individual dielectric layers.

### 7.4.4 Corner plots

In this chapter, corner plots are used extensively to visualize the ensemble of samples from MCMC sampling. So I will briefly remark on why they are a powerful visualization tool. The plot is made by arranging 2D histograms of samples, marginalizing over the other dimensions of the parameter space. The set of such 2D histograms are then arranged in a matrix - but of course, such a matrix would be symmetric, with the upper triangular plots contributing no new information (the correlations between parameters $\theta_1$ and $\theta_2$ are independent of the order in which they are considered). Finally, the topmost row in each column marginalizes over *all* other dimensions, to make a 1D histogram of the *posterior* distribution of a particular parameter in the MCMC ensemble. In the case of the inverse problem described in Section 7.3.2, it is useful to overlay the *prior* distributions of parameters used to draw samples. The difference between these two histograms would indicate how *informative* the measurement is - if they are nearly identical, then the measurement with which the inference is being made adds very little information to our prior assumptions, sig-

nalling the need for more data to make any meaningful conclusions. As can be seen in Figure 7.5, the 2D histogramscan reveal correlations between the variables being studied. When strong correlations exist between a pair of parameters, the density of points will be high along flattened ellipses (e.g. bottom left plot). Conversely, when the correlation is weaker, the density will tend to be more randomly (and evenly) distributed (e.g. the 2D histogram between $T_{1064\,\mathrm{nm}}$ and $\vec{E}_{\mathrm{surface}}$). The inset in thee upper right part of the corner plots presented in this chapter indicate the number of samples drawn in the MCMC sampling phase, as well as the assumed fractional uncertainties in various model parameters.

## 7.5 Survey of past work and conclusions

We have presented a method to find a globally optimum solution to multilayer dielectric coating design problems such that multiple competing objectives are satisfied. While initial development of the software implementation of this algorithm relied on `MATLAB`'s PSO toolbox, the current incarnation depends only on standard libraries available in the `Python` ecosystem. The performance of our optimized coatings are superior to conventional designs such as the "quarter-wave stack", and are robust to small perturbations in assumed model parameters. We have demonstrated the successful application of this technique to multiple design problems with varying requirements - the ultimate validation being the manufacture of an optic designed using this algorithm that met strict design requirements (Section 7.4.1).

There have been many proposed optimization algorithms for realizing dielectric coating thicknesses [124–127]. The general algorithm is to define a cost function based on the design objectives, and then use some algorithm to find the global minimum value of this cost function in the allowed parameter space. Popular choices for global cost function minimization are the genetic algorithm, needle optimization, and swarm optimization algorithms [128]. Compared to these past works, our approach can easily handle these multiple design goals in a weighted manner. Moreover, our algorithm preferentially selects coating designs that are minimally sensitive to manufacturing tolerances, thereby decreasing the probability of fabricating a coating that does not meet the design specifications. Our optimization code has yielded comparable or superior coating designs relative to commercial coating design software, and since it is built using `Python`, does not incur expensive licensing fees. Development of a GUI will make the experience even smoother for a casual user, while more advanced problems of interest in the coating community can be set up easily given the modular nature of the algorithm.

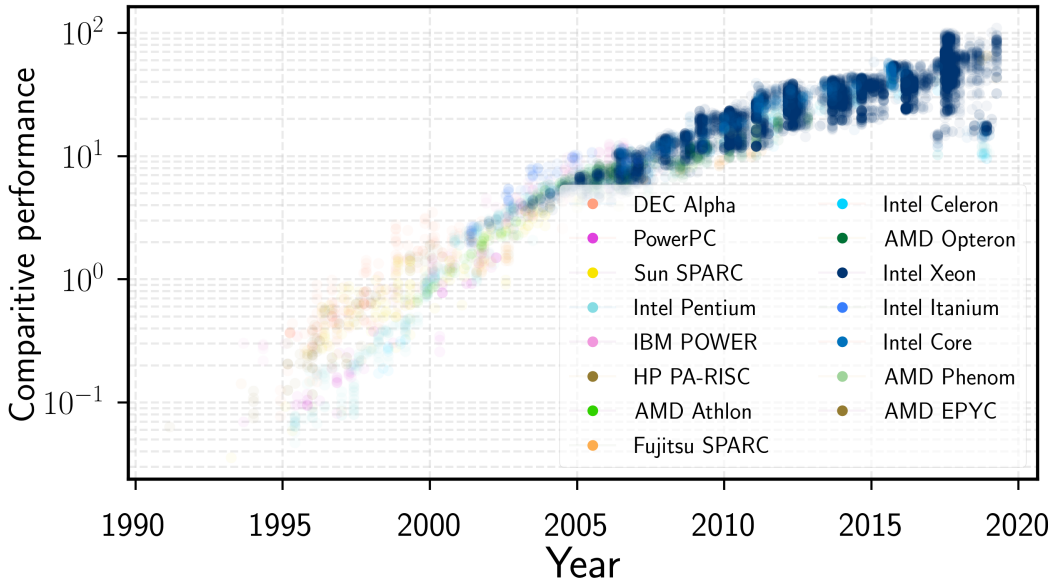


Figure 7.7: Evolution of the computational power available in popular commercial processors. The score is normalized such that the average processor in the year 2000 has a score of 1. The data used to generate this plot was obtained from benchmark tests done by SPEC [129].

It must be emphasized that rapid development of the computing power available in modern personal computers (see Figure 7.7) is what has made it possible to implement the simple idea of minimizing a cost function for the design of non-trivial dielectric coatings. Therefore, while the software implementation of the algorithm described in this chapter can be improved for better efficiency, it is not expected to be the bottleneck in using this algorithm over a wider class of coating design problems not specific to the field of GW interferometers.

# GLOSSARY

**BHD** Balanced Homodyne Detection

**OMC** Output Mode Cleaner

**PDH** Pound-Drever-Hall (laser frequency stabilization technique)

**A+** A proposed upgrade to the aLIGO interferometers

**IMC** Input Mode Cleaner

**IFO** Interferometer

**AS port** Anti-symmetric port, a.k.a. 'Dark' port

**HOM** Higher order mode

**BRDF** Bi-directional reflectance function

**DARM** Differential arm length

**HR** High reflectivity

**LO** Local oscillator

**EOM** Electro-optic modulator

**RF** Radio-frequency

**NPRO** Non-planar ring oscillator

**PZT** Piezoelectric

**UGF** Unity gain frequency

**AM** Amplitude modulation

**PM** Phase modulation

**FPGA** Field programmable gate array

**FSR** Free spectral range

**CARM** Common arm length

**PRCL** Power recycling cavity length

**SRCL** Signal recycling cavity length

**MICH** Michelson (differential) length

**DoF** Degree of freedom

**RMS** Root-mean-square

**LTI** Linear, time-invariant

**RoC** Radius of Curvature

**PRM** Power Recycling Mirror

**SRM** Signal Recycling Mirror

**PRFPMI** Power-Recycled Fabry-Pérot Michelson Interferometer

**DRFPMI** Dual-Recycled Fabry-Pérot Michelson Interferometer

**ASC** Angular Sensing and Control

**LSC** Length Sensing and Control

**QPD** Quadrant photodiode

**TTs** Tip-Tilt suspensions

**SOSs** Small Optic Suspensions

**MISO** Multiple Input Single Output, feedback topology

**SISO** Single Input Single Output, feedback topology

**MIMO** Multiple Input Multiple Output, feedback topology

**FIR** Finite Impulse Response

**IIR** Infinite Impulse Response

**ADC** Analog to digital converter

**DAC** Digital to analog converter

**A2L** Angle to length coupling, cross-coupling from force applied to change position along the beam axis to angular motion of a suspended optic.

**AR** Anti-reflective, commonly used coating type on interferometer optics.

**RAM** Residual amplitude modulation, unwanted side-effect of phase modulation using an EOM.

**WFS** Wavefront sensors (WFS), type of angular motion sensor.

**PRG** Power recycling gain.

**OFI** Output faraday isolator.

**RIN** Relative intensity noise.

**RSE** Resonant sideband extraction, tuning of the signal recycling cavity.

# BIBLIOGRAPHY

[1] Benjamin P Abbott, Richard Abbott, TD Abbott, MR Abernathy, Fausto Acernese, Kendall Ackley, Carl Adams, Thomas Adams, Paolo Addesso, RX Adhikari, et al. Observation of gravitational waves from a binary black hole merger. *Physical review letters*, 116(6):061102, 2016. [Cited on page 1.]

[2] B. P. Abbott, R. Abbott, T. D. Abbott, F. Acernese, K. Ackley, C. Adams, T. Adams, P. Addesso, R. X. Adhikari, V. B. Adya, C. Affeldt, M. Afrough, B. Agarwal, M. Agathos, K. Agatsuma, N. Aggarwal, O. D. Aguiar, L. Aiello, A. Ain, P. Ajith, B. Allen, G. Allen, A. Allocca, P. A. Altin, A. Amato, A. Ananyeva, S. B. Anderson, W. G. Anderson, S. V. Angelova, S. Antier, S. Appert, K. Arai, M. C. Araya, J. S. Areeda, N. Arnaud, K. G. Arun, S. Ascenzi, G. Ashton, M. Ast, S. M. Aston, P. Astone, D. V. Atallah, P. Aufmuth, C. Aulbert, K. AultONeal, C. Austin, A. Avila-Alvarez, S. Babak, P. Bacon, M. K. M. Bader, S. Bae, M. Bailes, P. T. Baker, F. Baldaccini, G. Ballardin, S. W. Ballmer, S. Banagiri, J. C. Barayoga, S. E. Barclay, B. C. Barish, D. Barker, K. Barkett, F. Barone, B. Barr, L. Barsotti, M. Barsuglia, D. Barta, S. D. Barthelmy, J. Bartlett, I. Bartos, R. Bassiri, A. Basti, J. C. Batch, M. Bawaj, J. C. Bayley, M. Bazzan, B. Bécsy, C. Beer, M. Bejger, I. Belahcene, A. S. Bell, B. K. Berger, G. Bergmann, S. Bernuzzi, J. J. Bero, C. P. L. Berry, D. Bersanetti, A. Bertolini, J. Betzwieser, S. Bhagwat, R. Bhandare, I. A. Bilenko, G. Billingsley, C. R. Billman, J. Birch, R. Birney, O. Birnholtz, S. Biscans, S. Biscoveanu, A. Bisht, M. Bitossi, C. Biwer, M. A. Bizouard, J. K. Blackburn, J. Blackman, C. D. Blair, D. G. Blair, R. M. Blair, S. Bloemen, O. Bock, N. Bode, M. Boer, G. Bogaert, A. Bohe, F. Bondu, E. Bonilla, R. Bonnand, B. A. Boom, R. Bork, V. Boschi, S. Bose, K. Bossie, Y. Bouffanais, A. Bozzi, C. Bradaschia, P. R. Brady, M. Branchesi, J. E. Brau, T. Briant, A. Brillet, M. Brinkmann, V. Brisson, P. Brockill, J. E. Broida, A. F. Brooks, D. A. Brown, D. D. Brown, S. Brunett, C. C. Buchanan, A. Buikema, T. Bulik, H. J. Bulten, A. Buonanno, D. Buskulic, C. Buy, R. L. Byer, M. Cabero, L. Cadonati, G. Cagnoli, C. Cahillane, J. Calderón Bustillo, T. A. Callister, E. Calloni, J. B. Camp, M. Canepa, P. Canizares, K. C. Cannon, H. Cao, J. Cao, C. D. Capano, E. Capocasa, F. Carbognani, S. Caride, M. F. Carney, G. Carullo, J. Casanueva Diaz, C. Casentini, S. Caudill, M. Cavaglià, F. Cavalier, R. Cavalieri, G. Cella, C. B. Cepeda, P. Cerdá-Durán, G. Cerretani, E. Cesarini, S. J. Chamberlin, M. Chan, S. Chao, P. Charlton, E. Chase, E. Chassande-Mottin, D. Chatterjee, K. Chatziioannou, B. D. Cheeseboro, H. Y. Chen, X. Chen, Y. Chen, H.-P. Cheng, H. Chia, A. Chincarini, A. Chiummo, T. Chmiel, H. S. Cho, M. Cho, J. H. Chow, N. Christensen, Q. Chu, A. J. K. Chua, S. Chua, A. K. W. Chung, S. Chung, G. Ciani, R. Ciolfi, C. E. Cirelli, A. Cirone, F. Clara, J. A. Clark, P. Clearwater, F. Cleva, C. Cocchieri, E. Coccia, P.-F. Cohadon, D. Cohen, A. Colla, C. G. Collette, L. R. Cominsky,

M. Constancio, L. Conti, S. J. Cooper, P. Corban, T. R. Corbitt, I. Cordero-Carrión, K. R. Corley, N. Cornish, A. Corsi, S. Cortese, C. A. Costa, M. W. Coughlin, S. B. Coughlin, J.-P. Coulon, S. T. Countryman, P. Couvares, P. B. Covas, E. E. Cowan, D. M. Coward, M. J. Cowart, D. C. Coyne, R. Coyne, J. D. E. Creighton, T. D. Creighton, J. Cripe, S. G. Crowder, T. J. Cullen, A. Cumming, L. Cunningham, E. Cuoco, T. Dal Canton, G. Dálya, S. L. Danilishin, S. D'Antonio, K. Danzmann, A. Dasgupta, C. F. Da Silva Costa, V. Dattilo, I. Dave, M. Davier, D. Davis, E. J. Daw, B. Day, S. De, D. DeBra, J. Degallaix, M. De Laurentis, S. Deléglise, W. Del Pozzo, N. Demos, T. Denker, T. Dent, R. De Pietri, V. Dergachev, R. De Rosa, R. T. DeRosa, C. De Rossi, R. DeSalvo, O. de Varona, J. Devenson, S. Dhurandhar, M. C. Díaz, T. Dietrich, L. Di Fiore, M. Di Giovanni, T. Di Girolamo, A. Di Lieto, S. Di Pace, I. Di Palma, F. Di Renzo, Z. Doctor, V. Dolique, F. Donovan, K. L. Dooley, S. Doravari, I. Dorrington, R. Douglas, M. Dovale Álvarez, T. P. Downes, M. Drago, C. Dreissigacker, J. C. Driggers, Z. Du, M. Ducrot, R. Dudi, P. Dupej, S. E. Dwyer, T. B. Edo, M. C. Edwards, A. Effler, H.-B. Eggenstein, P. Ehrens, J. Eichholz, S. S. Eikenberry, R. A. Eisenstein, R. C. Essick, D. Estevez, Z. B. Etienne, T. Etzel, M. Evans, T. M. Evans, M. Factourovich, V. Fafone, H. Fair, S. Fairhurst, X. Fan, S. Farinon, B. Farr, W. M. Farr, E. J. Fauchon-Jones, M. Favata, M. Fays, C. Fee, H. Fehrmann, J. Feicht, M. M. Fejer, A. Fernandez-Galiana, I. Ferrante, E. C. Ferreira, F. Ferrini, F. Fidecaro, D. Finstad, I. Fiori, D. Fiorucci, M. Fishbach, R. P. Fisher, M. Fitz-Axen, R. Flaminio, M. Fletcher, H. Fong, J. A. Font, P. W. F. Forsyth, S. S. Forsyth, J.-D. Fournier, S. Frasca, F. Frasconi, Z. Frei, A. Freise, R. Frey, V. Frey, E. M. Fries, P. Fritschel, V. V. Frolov, P. Fulda, M. Fyffe, H. Gabbard, B. U. Gadre, S. M. Gaebel, J. R. Gair, L. Gammaitoni, M. R. Ganija, S. G. Gaonkar, C. Garcia-Quiros, F. Garufi, B. Gateley, S. Gaudio, G. Gaur, V. Gayathri, N. Gehrels, G. Gemme, E. Genin, A. Gennai, D. George, J. George, L. Gergely, V. Germain, S. Ghonge, Abhirup Ghosh, Archisman Ghosh, S. Ghosh, J. A. Giaime, K. D. Giardina, A. Giazotto, K. Gill, L. Glover, E. Goetz, R. Goetz, S. Gomes, B. Goncharov, G. González, J. M. Gonzalez Castro, A. Gopakumar, M. L. Gorodetsky, S. E. Gossan, M. Gosselin, R. Gouaty, A. Grado, C. Graef, M. Granata, A. Grant, S. Gras, C. Gray, G. Greco, A. C. Green, E. M. Gretarsson, P. Groot, H. Grote, S. Grunewald, P. Gruning, G. M. Guidi, X. Guo, A. Gupta, M. K. Gupta, K. E. Gushwa, E. K. Gustafson, R. Gustafson, O. Halim, B. R. Hall, E. D. Hall, E. Z. Hamilton, G. Hammond, M. Haney, M. M. Hanke, J. Hanks, C. Hanna, M. D. Hannam, O. A. Hannuksela, J. Hanson, T. Hardwick, J. Harms, G. M. Harry, I. W. Harry, M. J. Hart, C.-J. Haster, K. Haughian, J. Healy, A. Heidmann, M. C. Heintze, H. Heitmann, P. Hello, G. Hemming, M. Hendry, I. S. Heng, J. Hennig, A. W. Heptonstall, M. Heurs, S. Hild, T. Hinderer, W. C. G. Ho, D. Hoak, D. Hofman, K. Holt, D. E. Holz, P. Hopkins, C. Horst, J. Hough, E. A. Houston, E. J. Howell, A. Hreibi, Y. M. Hu, E. A. Huerta, D. Huet, B. Hughey, S. Husa, S. H. Huttner, T. Huynh-Dinh, N. Indik, R. Inta, G. Intini, H. N. Isa, J.-M. Isac, M. Isi, B. R. Iyer, K. Izumi, T. Jacqmin, K. Jani, P. Jaranowski,

S. Jawahar, F. Jiménez-Forteza, W. W. Johnson, N. K. Johnson-McDaniel, D. I. Jones, R. Jones, R. J. G. Jonker, L. Ju, J. Junker, C. V. Kalaghatgi, V. Kalogera, B. Kamai, S. Kandhasamy, G. Kang, J. B. Kanner, S. J. Kapadia, S. Karki, K. S. Karvinen, M. Kasprzack, W. Kastaun, M. Katolik, E. Katsavounidis, W. Katzman, S. Kaufer, K. Kawabe, F. Kéfélian, D. Keitel, A. J. Kemball, R. Kennedy, C. Kent, J. S. Key, F. Y. Khalili, I. Khan, S. Khan, Z. Khan, E. A. Khazanov, N. Kijbunchoo, Chunglee Kim, J. C. Kim, K. Kim, W. Kim, W. S. Kim, Y.-M. Kim, S. J. Kimbrell, E. J. King, P. J. King, M. Kinley-Hanlon, R. Kirchhoff, J. S. Kissel, L. Kleybolte, S. Klimenko, T. D. Knowles, P. Koch, S. M. Koehlenbeck, S. Koley, V. Kondrashov, A. Kontos, M. Korobko, W. Z. Korth, I. Kowalska, D. B. Kozak, C. Krämer, V. Kringel, B. Krishnan, A. Królak, G. Kuehn, P. Kumar, R. Kumar, S. Kumar, L. Kuo, A. Kutynia, S. Kwang, B. D. Lackey, K. H. Lai, M. Landry, R. N. Lang, J. Lange, B. Lantz, R. K. Lanza, S. L. Larson, A. Lartaux-Vollard, P. D. Lasky, M. Laxen, A. Lazzarini, C. Lazzaro, P. Leaci, S. Leavey, C. H. Lee, H. K. Lee, H. M. Lee, H. W. Lee, K. Lee, J. Lehmann, A. Lenon, E. Leon, M. Leonardi, N. Leroy, N. Letendre, Y. Levin, T. G. F. Li, S. D. Linker, T. B. Littenberg, J. Liu, X. Liu, R. K. L. Lo, N. A. Lockerbie, L. T. London, J. E. Lord, M. Lorenzini, V. Loriette, M. Lormand, G. Losurdo, J. D. Lough, C. O. Lousto, G. Lovelace, H. Lück, D. Lumaca, A. P. Lundgren, R. Lynch, Y. Ma, R. Macas, S. Macfoy, B. Machenschalk, M. MacInnis, D. M. Macleod, I. Magaña Hernandez, F. Magaña Sandoval, L. Magaña Zertuche, R. M. Magee, E. Majorana, I. Maksimovic, N. Man, V. Mandic, V. Mangano, G. L. Mansell, M. Manske, M. Mantovani, F. Marchesoni, F. Marion, S. Márka, Z. Márka, C. Markakis, A. S. Markosyan, A. Markowitz, E. Maros, A. Marquina, P. Marsh, F. Martelli, L. Martellini, I. W. Martin, R. M. Martin, D. V. Martynov, J. N. Marx, K. Mason, E. Massera, A. Masserot, T. J. Massinger, M. Masso-Reid, S. Mastrogiovanni, A. Matas, F. Matichard, L. Matone, N. Mavalvala, N. Mazumder, R. McCarthy, D. E. McClelland, S. McCormick, L. McCuller, S. C. McGuire, G. McIntyre, J. McIver, D. J. McManus, L. McNeill, T. McRae, S. T. McWilliams, D. Meacher, G. D. Meadors, M. Mehmet, J. Meidam, E. Mejuto-Villa, A. Melatos, G. Mendell, R. A. Mercer, E. L. Merilh, M. Merzougui, S. Meshkov, C. Messenger, C. Messick, R. Metzdorff, P. M. Meyers, H. Miao, C. Michel, H. Middleton, E. E. Mikhailov, L. Milano, A. L. Miller, B. B. Miller, J. Miller, M. Millhouse, M. C. Milovich-Goff, O. Minazzoli, Y. Minenkov, J. Ming, C. Mishra, S. Mitra, V. P. Mitrofanov, G. Mitselmakher, R. Mittleman, D. Moffa, A. Moggi, K. Mogushi, M. Mohan, S. R. P. Mohapatra, I. Molina, M. Montani, C. J. Moore, D. Moraru, G. Moreno, S. Morisaki, S. R. Morriss, B. Mours, C. M. Mow-Lowry, G. Mueller, A. W. Muir, Arunava Mukherjee, D. Mukherjee, S. Mukherjee, N. Mukund, A. Mullavey, J. Munch, E. A. Muñiz, M. Muratore, P. G. Murray, A. Nagar, K. Napier, I. Nardecchia, L. Naticchioni, R. K. Nayak, J. Neilson, G. Nelemans, T. J. N. Nelson, M. Nery, A. Neunzert, L. Nevin, J. M. Newport, G. Newton, K. K. Y. Ng, P. Nguyen, T. T. Nguyen, D. Nichols, A. B. Nielsen, S. Nissanke, A. Nitz, A. Noack, F. Nocera, D. Nolt-

ing, C. North, L. K. Nuttall, J. Oberling, G. D. O'Dea, G. H. Ogin, J. J. Oh, S. H. Oh, F. Ohme, M. A. Okada, M. Oliver, P. Oppermann, Richard J. Oram, B. O'Reilly, R. Ormiston, L. F. Ortega, R. O'Shaughnessy, S. Ossokine, D. J. Ottaway, H. Overmier, B. J. Owen, A. E. Pace, J. Page, M. A. Page, A. Pai, S. A. Pai, J. R. Palamos, O. Palashov, C. Palomba, A. Pal-Singh, Howard Pan, Huang-Wei Pan, B. Pang, P. T. H. Pang, C. Pankow, F. Pannarale, B. C. Pant, F. Paoletti, A. Paoli, M. A. Papa, A. Parida, W. Parker, D. Pascucci, A. Pasqualetti, R. Passaquieti, D. Passuello, M. Patil, B. Patricelli, B. L. Pearlstone, M. Pedraza, R. Pedurand, L. Pekowsky, A. Pele, S. Penn, C. J. Perez, A. Perreca, L. M. Perri, H. P. Pfeiffer, M. Phelps, O. J. Piccinni, M. Pichot, F. Piergiovanni, V. Pierro, G. Pillant, L. Pinard, I. M. Pinto, M. Pirello, M. Pitkin, M. Poe, R. Poggiani, P. Popolizio, E. K. Porter, A. Post, J. Powell, J. Prasad, J. W. W. Pratt, G. Pratten, V. Predoi, T. Prestegard, M. Prijatelj, M. Principe, S. Privitera, R. Prix, G. A. Prodi, L. G. Prokhorov, O. Puncken, M. Punturo, P. Puppo, M. Pürrer, H. Qi, V. Quetschke, E. A. Quintero, R. Quitzow-James, F. J. Raab, D. S. Rabeling, H. Radkins, P. Raffai, S. Raja, C. Rajan, B. Rajbhandari, M. Rakhmanov, K. E. Ramirez, A. Ramos-Buades, P. Rapagnani, V. Raymond, M. Razzano, J. Read, T. Regimbau, L. Rei, S. Reid, D. H. Reitze, W. Ren, S. D. Reyes, F. Ricci, P. M. Ricker, S. Rieger, K. Riles, M. Rizzo, N. A. Robertson, R. Robie, F. Robinet, A. Rocchi, L. Rolland, J. G. Rollins, V. J. Roma, J. D. Romano, R. Romano, C. L. Romel, J. H. Romie, D. Rosińska, M. P. Ross, S. Rowan, A. Rüdiger, P. Ruggi, G. Rutins, K. Ryan, S. Sachdev, T. Sadecki, L. Sadeghian, M. Sakellariadou, L. Salconi, M. Saleem, F. Salemi, A. Samajdar, L. Sammut, L. M. Sampson, E. J. Sanchez, L. E. Sanchez, N. Sanchis-Gual, V. Sandberg, J. R. Sanders, B. Sassolas, B. S. Sathyaprakash, P. R. Saulson, O. Sauter, R. L. Savage, A. Sawadsky, P. Schale, M. Scheel, J. Scheuer, J. Schmidt, P. Schmidt, R. Schnabel, R. M. S. Schofield, A. Schönbeck, E. Schreiber, D. Schuette, B. W. Schulte, B. F. Schutz, S. G. Schwalbe, J. Scott, S. M. Scott, E. Seidel, D. Sellers, A. S. Sengupta, D. Sentenac, V. Sequino, A. Sergeev, D. A. Shaddock, T. J. Shaffer, A. A. Shah, M. S. Shahriar, M. B. Shaner, L. Shao, B. Shapiro, P. Shawhan, A. Sheperd, D. H. Shoemaker, D. M. Shoemaker, K. Siellez, X. Siemens, M. Sieniawska, D. Sigg, A. D. Silva, L. P. Singer, A. Singh, A. Singhal, A. M. Sintes, B. J. J. Slagmolen, B. Smith, J. R. Smith, R. J. E. Smith, S. Somala, E. J. Son, J. A. Sonnenberg, B. Sorazu, F. Sorrentino, T. Souradeep, A. P. Spencer, A. K. Srivastava, K. Staats, A. Staley, M. Steinke, J. Steinlechner, S. Steinlechner, D. Steinmeyer, S. P. Stevenson, R. Stone, D. J. Stops, K. A. Strain, G. Stratta, S. E. Strigin, A. Strunk, R. Sturani, A. L. Stuver, T. Z. Summerscales, L. Sun, S. Sunil, J. Suresh, P. J. Sutton, B. L. Swinkels, M. J. Szczepańczyk, M. Tacca, S. C. Tait, C. Talbot, D. Talukder, D. B. Tanner, M. Tápai, A. Taracchini, J. D. Tasson, J. A. Taylor, R. Taylor, S. V. Tewari, T. Theeg, F. Thies, E. G. Thomas, M. Thomas, P. Thomas, K. A. Thorne, K. S. Thorne, E. Thrane, S. Tiwari, V. Tiwari, K. V. Tokmakov, K. Toland, M. Tonelli, Z. Tornasi, A. Torres-Forné, C. I. Torrie, D. Töyrä, F. Travasso, G. Traylor, J. Trinastic, M. C. Tringali, L. Trozzo,

K. W. Tsang, M. Tse, R. Tso, L. Tsukada, D. Tsuna, D. Tuyenbayev, K. Ueno, D. Ugolini, C. S. Unnikrishnan, A. L. Urban, S. A. Usman, H. Vahlbruch, G. Vajente, G. Valdes, M. Vallisneri, N. van Bakel, M. van Beuzekom, J. F. J. van den Brand, C. Van Den Broeck, D. C. Vander-Hyde, L. van der Schaaf, J. V. van Heijningen, A. A. van Veggel, M. Vardaro, V. Varma, S. Vass, M. Vasúth, A. Vecchio, G. Vedovato, J. Veitch, P. J. Veitch, K. Venkateswara, G. Venugopalan, D. Verkindt, F. Vetrano, A. Viceré, A. D. Viets, S. Vinciguerra, D. J. Vine, J.-Y. Vinet, S. Vitale, T. Vo, H. Vocca, C. Vorvick, S. P. Vyatchanin, A. R. Wade, L. E. Wade, M. Wade, R. Walet, M. Walker, L. Wallace, S. Walsh, G. Wang, H. Wang, J. Z. Wang, W. H. Wang, Y. F. Wang, R. L. Ward, J. Warner, M. Was, J. Watchi, B. Weaver, L.-W. Wei, M. Weinert, A. J. Weinstein, R. Weiss, L. Wen, E. K. Wessel, P. Weßels, J. Westerweck, T. Westphal, K. Wette, J. T. Whelan, S. E. Whitcomb, B. F. Whiting, C. Whittle, D. Wilken, D. Williams, R. D. Williams, A. R. Williamson, J. L. Willis, B. Willke, M. H. Wimmer, W. Winkler, C. C. Wipf, H. Wittel, G. Woan, J. Woehler, J. Wofford, K. W. K. Wong, J. Worden, J. L. Wright, D. S. Wu, D. M. Wysocki, S. Xiao, H. Yamamoto, C. C. Yancey, L. Yang, M. J. Yap, M. Yazback, Hang Yu, Haocun Yu, M. Yvert, A. Zadrożny, M. Zanolin, T. Zelenova, J.-P. Zendri, M. Zevin, L. Zhang, M. Zhang, T. Zhang, Y.-H. Zhang, C. Zhao, M. Zhou, Z. Zhou, S. J. Zhu, X. J. Zhu, A. B. Zimmerman, M. E. Zucker, and J. Zweizig. Gw170817: Observation of gravitational waves from a binary neutron star inspiral. *Phys. Rev. Lett.*, 119:161101, Oct 2017. [Cited on page 1.]

[3] B. P. Abbott, R. Abbott, T. D. Abbott, S. Abraham, F. Acernese, K. Ackley, C. Adams, R. X. Adhikari, V. B. Adya, C. Affeldt, M. Agathos, K. Agatsuma, N. Aggarwal, O. D. Aguiar, L. Aiello, A. Ain, P. Ajith, G. Allen, A. Allocca, M. A. Aloy, P. A. Altin, A. Amato, A. Ananyeva, S. B. Anderson, W. G. Anderson, S. V. Angelova, S. Antier, S. Appert, K. Arai, M. C. Araya, J. S. Areeda, M. Arène, N. Arnaud, K. G. Arun, S. Ascenzi, G. Ashton, S. M. Aston, P. Astone, F. Aubin, P. Aufmuth, K. AultONeal, C. Austin, V. Avendano, A. Avila-Alvarez, S. Babak, P. Bacon, F. Badaracco, M. K. M. Bader, S. Bae, P. T. Baker, F. Baldaccini, G. Ballardin, S. W. Ballmer, S. Banagiri, J. C. Barayoga, S. E. Barclay, B. C. Barish, D. Barker, K. Barkett, S. Barnum, F. Barone, B. Barr, L. Barsotti, M. Barsuglia, D. Barta, J. Bartlett, I. Bartos, R. Bassiri, A. Basti, M. Bawaj, J. C. Bayley, M. Bazzan, B. Bécsy, M. Bejger, I. Belahcene, A. S. Bell, D. Beniwal, B. K. Berger, G. Bergmann, S. Bernuzzi, J. J. Bero, C. P. L. Berry, D. Bersanetti, A. Bertolini, J. Betzwieser, R. Bhandare, J. Bidler, I. A. Bilenko, S. A. Bilgili, G. Billingsley, J. Birch, R. Birney, O. Birnholtz, S. Biscans, S. Biscoveanu, A. Bisht, M. Bitossi, M. A. Bizouard, J. K. Blackburn, C. D. Blair, D. G. Blair, R. M. Blair, S. Bloemen, N. Bode, M. Boer, Y. Boetzel, G. Bogaert, F. Bondu, E. Bonilla, R. Bonnand, P. Booker, B. A. Boom, C. D. Booth, R. Bork, V. Boschi, S. Bose, K. Bossie, V. Bossilkov, J. Bosveld, Y. Bouffanais, A. Bozzi, C. Bradaschia, P. R. Brady, A. Bramley, M. Branchesi, J. E. Brau, M. Breschi, T. Briant, J. H. Briggs,

F. Brighenti, A. Brillet, M. Brinkmann, V. Brisson, R. Brito, P. Brockill, A. F. Brooks, D. D. Brown, S. Brunett, A. Buikema, T. Bulik, H. J. Bulten, A. Buonanno, D. Buskulic, M. J. Bustamante Rosell, C. Buy, R. L. Byer, M. Cabero, L. Cadonati, G. Cagnoli, C. Cahillane, J. Calderón Bustillo, T. A. Callister, E. Calloni, J. B. Camp, W. A. Campbell, M. Canepa, K. C. Cannon, H. Cao, J. Cao, C. D. Capano, E. Capocasa, F. Carbognani, S. Caride, M. F. Carney, G. Carullo, J. Casanueva Diaz, C. Casentini, S. Caudill, M. Cavaglià, F. Cavalier, R. Cavalieri, G. Cella, P. Cerdá-Durán, G. Cerretani, E. Cesarini, O. Chaibi, K. Chakravarti, S. J. Chamberlin, M. Chan, S. Chao, P. Charlton, E. A. Chase, E. Chassande-Mottin, D. Chatterjee, M. Chaturvedi, K. Chatziioannou, B. D. Cheeseboro, H. Y. Chen, X. Chen, Y. Chen, H.-P. Cheng, C. K. Cheong, H. Y. Chia, A. Chincarini, A. Chiummo, G. Cho, H. S. Cho, M. Cho, N. Christensen, Q. Chu, S. Chua, K. W. Chung, S. Chung, G. Ciani, A. A. Ciobanu, R. Ciolfi, F. Cipriano, A. Cirone, F. Clara, J. A. Clark, P. Clearwater, F. Cleva, C. Cocchieri, E. Coccia, P.-F. Cohadon, D. Cohen, R. Colgan, M. Colleoni, C. G. Collette, C. Collins, L. R. Cominsky, M. Constancio, L. Conti, S. J. Cooper, P. Corban, T. R. Corbitt, I. Cordero-Carrión, K. R. Corley, N. Cornish, A. Corsi, S. Cortese, C. A. Costa, R. Cotesta, M. W. Coughlin, S. B. Coughlin, J.-P. Coulon, S. T. Countryman, P. Couvares, P. B. Covas, E. E. Cowan, D. M. Coward, M. J. Cowart, D. C. Coyne, R. Coyne, J. D. E. Creighton, T. D. Creighton, J. Cripe, M. Croquette, S. G. Crowder, T. J. Cullen, A. Cumming, L. Cunningham, E. Cuoco, T. Dal Canton, G. Dálya, S. L. Danilishin, S. D'Antonio, K. Danzmann, A. Dasgupta, C. F. Da Silva Costa, L. E. H. Datrier, V. Dattilo, I. Dave, M. Davier, D. Davis, E. J. Daw, D. DeBra, M. Deenadayalan, J. Degallaix, M. De Laurentis, S. Deléglise, W. Del Pozzo, L. M. DeMarchi, N. Demos, T. Dent, R. De Pietri, J. Derby, R. De Rosa, C. De Rossi, R. DeSalvo, O. de Varona, S. Dhurandhar, M. C. Díaz, T. Dietrich, L. Di Fiore, M. Di Giovanni, T. Di Girolamo, A. Di Lieto, B. Ding, S. Di Pace, I. Di Palma, F. Di Renzo, A. Dmitriev, Z. Doctor, F. Donovan, K. L. Dooley, S. Doravari, I. Dorrington, T. P. Downes, M. Drago, J. C. Driggers, Z. Du, J.-G. Ducoin, P. Dupej, S. E. Dwyer, P. J. Easter, T. B. Edo, M. C. Edwards, A. Effler, P. Ehrens, J. Eichholz, S. S. Eikenberry, M. Eisenmann, R. A. Eisenstein, R. C. Essick, H. Estelles, D. Estevez, Z. B. Etienne, T. Etzel, M. Evans, T. M. Evans, V. Fafone, H. Fair, S. Fairhurst, X. Fan, S. Farinon, B. Farr, W. M. Farr, E. J. Fauchon-Jones, M. Favata, M. Fays, M. Fazio, C. Fee, J. Feicht, M. M. Fejer, F. Feng, A. Fernandez-Galiana, I. Ferrante, E. C. Ferreira, T. A. Ferreira, F. Ferrini, F. Fidecaro, I. Fiori, D. Fiorucci, M. Fishbach, R. P. Fisher, J. M. Fishner, M. Fitz-Axen, R. Flaminio, M. Fletcher, E. Flynn, H. Fong, J. A. Font, P. W. F. Forsyth, J.-D. Fournier, S. Frasca, F. Frasconi, Z. Frei, A. Freise, R. Frey, V. Frey, P. Fritschel, V. V. Frolov, P. Fulda, M. Fyffe, H. A. Gabbard, B. U. Gadre, S. M. Gaebel, J. R. Gair, L. Gammaitoni, M. R. Ganija, S. G. Gaonkar, A. Garcia, C. García-Quirós, F. Garufi, B. Gateley, S. Gaudio, G. Gaur, V. Gayathri, G. Gemme, E. Genin, A. Gennai, D. George, J. George, L. Gergely, V. Germain, S. Ghonge, Abhirup Ghosh, Archisman

Ghosh, S. Ghosh, B. Giacomazzo, J. A. Giaime, K. D. Giardina, A. Giazotto, K. Gill, G. Giordano, L. Glover, P. Godwin, E. Goetz, R. Goetz, B. Goncharov, G. González, J. M. Gonzalez Castro, A. Gopakumar, M. L. Gorodetsky, S. E. Gossan, M. Gosselin, R. Gouaty, A. Grado, C. Graef, M. Granata, A. Grant, S. Gras, P. Grassia, C. Gray, R. Gray, G. Greco, A. C. Green, R. Green, E. M. Gretarsson, P. Groot, H. Grote, S. Grunewald, P. Gruning, G. M. Guidi, H. K. Gulati, Y. Guo, A. Gupta, M. K. Gupta, E. K. Gustafson, R. Gustafson, L. Haegel, O. Halim, B. R. Hall, E. D. Hall, E. Z. Hamilton, G. Hammond, M. Haney, M. M. Hanke, J. Hanks, C. Hanna, M. D. Hannam, O. A. Hannuksela, J. Hanson, T. Hardwick, K. Haris, J. Harms, G. M. Harry, I. W. Harry, C.-J. Haster, K. Haughian, F. J. Hayes, J. Healy, A. Heidmann, M. C. Heintze, H. Heitmann, P. Hello, G. Hemming, M. Hendry, I. S. Heng, J. Hennig, A. W. Heptonstall, Francisco Hernandez Vivanco, M. Heurs, S. Hild, T. Hinderer, D. Hoak, S. Hochheim, D. Hofman, A. M. Holgado, N. A. Holland, K. Holt, D. E. Holz, P. Hopkins, C. Horst, J. Hough, E. J. Howell, C. G. Hoy, A. Hreibi, E. A. Huerta, D. Huet, B. Hughey, M. Hulko, S. Husa, S. H. Huttner, T. Huynh-Dinh, B. Idzkowski, A. Iess, C. Ingram, R. Inta, G. Intini, B. Irwin, H. N. Isa, J.-M. Isac, M. Isi, B. R. Iyer, K. Izumi, T. Jacqmin, S. J. Jadhav, K. Jani, N. N. Janthalur, P. Jaranowski, A. C. Jenkins, J. Jiang, D. S. Johnson, N. K. Johnson-McDaniel, A. W. Jones, D. I. Jones, R. Jones, R. J. G. Jonker, L. Ju, J. Junker, C. V. Kalaghatgi, V. Kalogera, B. Kamai, S. Kandhasamy, G. Kang, J. B. Kanner, S. J. Kapadia, S. Karki, K. S. Karvinen, R. Kashyap, M. Kasprzack, S. Katsanevas, E. Katsavounidis, W. Katzman, S. Kaufer, K. Kawabe, N. V. Keerthana, F. Kéfélian, D. Keitel, R. Kennedy, J. S. Key, F. Y. Khalili, H. Khan, I. Khan, S. Khan, Z. Khan, E. A. Khazanov, M. Khursheed, N. Kijbunchoo, Chunglee Kim, J. C. Kim, K. Kim, W. Kim, W. S. Kim, Y.-M. Kim, C. Kimball, E. J. King, P. J. King, M. Kinley-Hanlon, R. Kirchhoff, J. S. Kissel, L. Kleybolte, J. H. Klika, S. Klimenko, T. D. Knowles, P. Koch, S. M. Koehlenbeck, G. Koekoek, S. Koley, V. Kondrashov, A. Kontos, N. Koper, M. Korobko, W. Z. Korth, I. Kowalska, D. B. Kozak, V. Kringel, N. Krishnendu, A. Królak, G. Kuehn, A. Kumar, P. Kumar, R. Kumar, S. Kumar, L. Kuo, A. Kutynia, S. Kwang, B. D. Lackey, K. H. Lai, T. L. Lam, M. Landry, B. B. Lane, R. N. Lang, J. Lange, B. Lantz, R. K. Lanza, A. Lartaux-Vollard, P. D. Lasky, M. Laxen, A. Lazzarini, C. Lazzaro, P. Leaci, S. Leavey, Y. K. Lecoeuche, C. H. Lee, H. K. Lee, H. M. Lee, H. W. Lee, J. Lee, K. Lee, J. Lehmann, A. Lenon, N. Leroy, N. Letendre, Y. Levin, J. Li, K. J. L. Li, T. G. F. Li, X. Li, F. Lin, F. Linde, S. D. Linker, T. B. Littenberg, J. Liu, X. Liu, R. K. L. Lo, N. A. Lockerbie, L. T. London, A. Longo, M. Lorenzini, V. Loriette, M. Lormand, G. Losurdo, J. D. Lough, C. O. Lousto, G. Lovelace, M. E. Lower, H. Lück, D. Lumaca, A. P. Lundgren, R. Lynch, Y. Ma, R. Macas, S. Macfoy, M. MacInnis, D. M. Macleod, A. Macquet, F. Magaña Sandoval, L. Magaña Zertuche, R. M. Magee, E. Majorana, I. Maksimovic, A. Malik, N. Man, V. Mandic, V. Mangano, G. L. Mansell, M. Manske, M. Mantovani, F. Marchesoni, F. Marion, S. Márka, Z. Márka, C. Markakis, A. S. Markosyan,

A. Markowitz, E. Maros, A. Marquina, S. Marsat, F. Martelli, I. W. Martin, R. M. Martin, D. V. Martynov, K. Mason, E. Massera, A. Masserot, T. J. Massinger, M. Masso-Reid, S. Mastrogiovanni, A. Matas, F. Matichard, L. Matone, N. Mavalvala, N. Mazumder, J. J. McCann, R. McCarthy, D. E. McClelland, S. McCormick, L. McCuller, S. C. McGuire, J. McIver, D. J. McManus, T. McRae, S. T. McWilliams, D. Meacher, G. D. Meadors, M. Mehmet, A. K. Mehta, J. Meidam, A. Melatos, G. Mendell, R. A. Mercer, L. Mereni, E. L. Merilh, M. Merzougui, S. Meshkov, C. Messenger, C. Messick, R. Metzdorff, P. M. Meyers, H. Miao, C. Michel, H. Middleton, E. E. Mikhailov, L. Milano, A. L. Miller, A. Miller, M. Millhouse, J. C. Mills, M. C. Milovich-Goff, O. Minazzoli, Y. Minenkov, A. Mishkin, C. Mishra, T. Mistry, S. Mitra, V. P. Mitrofanov, G. Mitselmakher, R. Mittleman, G. Mo, D. Moffa, K. Mogushi, S. R. P. Mohapatra, M. Montani, C. J. Moore, D. Moraru, G. Moreno, S. Morisaki, B. Mours, C. M. Mow-Lowry, Arunava Mukherjee, D. Mukherjee, S. Mukherjee, N. Mukund, A. Mullavey, J. Munch, E. A. Muñiz, M. Muratore, P. G. Murray, A. Nagar, I. Nardecchia, L. Naticchioni, R. K. Nayak, J. Neilson, G. Nelemans, T. J. N. Nelson, M. Nery, A. Neunzert, K. Y. Ng, S. Ng, P. Nguyen, D. Nichols, A. B. Nielsen, S. Nissanke, A. Nitz, F. Nocera, C. North, L. K. Nuttall, M. Obergaulinger, J. Oberling, B. D. O'Brien, G. D. O'Dea, G. H. Ogin, J. J. Oh, S. H. Oh, F. Ohme, H. Ohta, M. A. Okada, M. Oliver, P. Oppermann, Richard J. Oram, B. O'Reilly, R. G. Ormiston, L. F. Ortega, R. O'Shaughnessy, S. Ossokine, D. J. Ottaway, H. Overmier, B. J. Owen, A. E. Pace, G. Pagano, M. A. Page, A. Pai, S. A. Pai, J. R. Palamos, O. Palashov, C. Palomba, A. Pal-Singh, Huang-Wei Pan, B. Pang, P. T. H. Pang, C. Pankow, F. Pannarale, B. C. Pant, F. Paoletti, A. Paoli, A. Parida, W. Parker, D. Pascucci, A. Pasqualetti, R. Passaquieti, D. Passuello, M. Patil, B. Patricelli, B. L. Pearlstone, C. Pedersen, M. Pedraza, R. Pedurand, A. Pele, S. Penn, C. J. Perez, A. Perreca, H. P. Pfeiffer, M. Phelps, K. S. Phukon, O. J. Piccinni, M. Pichot, F. Piergiovanni, G. Pillant, L. Pinard, M. Pirello, M. Pitkin, R. Poggiani, D. Y. T. Pong, S. Ponrathnam, P. Popolizio, E. K. Porter, J. Powell, A. K. Prajapati, J. Prasad, K. Prasai, R. Prasanna, G. Pratten, T. Prestegard, S. Privitera, G. A. Prodi, L. G. Prokhorov, O. Puncken, M. Punturo, P. Puppo, M. Pürrer, H. Qi, V. Quetschke, P. J. Quinonez, E. A. Quintero, R. Quitzow-James, F. J. Raab, H. Radkins, N. Radulescu, P. Raffai, S. Raja, C. Rajan, B. Rajbhandari, M. Rakhmanov, K. E. Ramirez, A. Ramos-Buades, Javed Rana, K. Rao, P. Rapagnani, V. Raymond, M. Razzano, J. Read, T. Regimbau, L. Rei, S. Reid, D. H. Reitze, W. Ren, F. Ricci, C. J. Richardson, J. W. Richardson, P. M. Ricker, K. Riles, M. Rizzo, N. A. Robertson, R. Robie, F. Robinet, A. Rocchi, L. Rolland, J. G. Rollins, V. J. Roma, M. Romanelli, R. Romano, C. L. Romel, J. H. Romie, K. Rose, D. Rosińska, S. G. Rosofsky, M. P. Ross, S. Rowan, A. Rüdiger, P. Ruggi, G. Rutins, K. Ryan, S. Sachdev, T. Sadecki, M. Sakellariadou, L. Salconi, M. Saleem, A. Samajdar, L. Sammut, E. J. Sanchez, L. E. Sanchez, N. Sanchis-Gual, V. Sandberg, J. R. Sanders, K. A. Santiago, N. Sarin, B. Sassolas, B. S. Sathyaprakash, P. R. Saulson, O. Sauter, R. L.

Savage, P. Schale, M. Scheel, J. Scheuer, P. Schmidt, R. Schnabel, R. M. S. Schofield, A. Schönbeck, E. Schreiber, B. W. Schulte, B. F. Schutz, S. G. Schwalbe, J. Scott, S. M. Scott, E. Seidel, D. Sellers, A. S. Sengupta, N. Sennett, D. Sentenac, V. Sequino, A. Sergeev, Y. Setyawati, D. A. Shaddock, T. Shaffer, M. S. Shahriar, M. B. Shaner, L. Shao, P. Sharma, P. Shawhan, H. Shen, R. Shink, D. H. Shoemaker, D. M. Shoemaker, S. ShyamSundar, K. Siellez, M. Sieniawska, D. Sigg, A. D. Silva, L. P. Singer, N. Singh, A. Singhal, A. M. Sintes, S. Sitmukhambetov, V. Skliris, B. J. J. Slagmolen, T. J. Slaven-Blair, J. R. Smith, R. J. E. Smith, S. Somala, E. J. Son, B. Sorazu, F. Sorrentino, T. Souradeep, E. Sowell, A. P. Spencer, A. K. Srivastava, V. Srivastava, K. Staats, C. Stachie, M. Standke, D. A. Steer, M. Steinke, J. Steinlechner, S. Steinlechner, D. Steinmeyer, S. P. Stevenson, D. Stocks, R. Stone, D. J. Stops, K. A. Strain, G. Stratta, S. E. Strigin, A. Strunk, R. Sturani, A. L. Stuver, V. Sudhir, T. Z. Summerscales, L. Sun, S. Sunil, J. Suresh, P. J. Sutton, B. L. Swinkels, M. J. Szczepańczyk, M. Tacca, S. C. Tait, C. Talbot, D. Talukder, D. B. Tanner, M. Tápai, A. Taracchini, J. D. Tasson, R. Taylor, F. Thies, M. Thomas, P. Thomas, S. R. Thondapu, K. A. Thorne, E. Thrane, Shubhanshu Tiwari, Srishti Tiwari, V. Tiwari, K. Toland, M. Tonelli, Z. Tornasi, A. Torres-Forné, C. I. Torrie, D. Töyrä, F. Travasso, G. Traylor, M. C. Tringali, A. Trovato, L. Trozzo, R. Trudeau, K. W. Tsang, M. Tse, R. Tso, L. Tsukada, D. Tsuna, D. Tuyenbayev, K. Ueno, D. Ugolini, C. S. Unnikrishnan, A. L. Urban, S. A. Usman, H. Vahlbruch, G. Vajente, G. Valdes, N. van Bakel, M. van Beuzekom, J. F. J. van den Brand, C. Van Den Broeck, D. C. Vander-Hyde, J. V. van Heijningen, L. van der Schaaf, A. A. van Veggel, M. Vardaro, V. Varma, S. Vass, M. Vasúth, A. Vecchio, G. Vedovato, J. Veitch, P. J. Veitch, K. Venkateswara, G. Venugopalan, D. Verkindt, F. Vetrano, A. Viceré, A. D. Viets, D. J. Vine, J.-Y. Vinet, S. Vitale, T. Vo, H. Vocca, C. Vorvick, S. P. Vyatchanin, A. R. Wade, L. E. Wade, M. Wade, R. M. Wald, R. Walet, M. Walker, L. Wallace, S. Walsh, G. Wang, H. Wang, J. Z. Wang, W. H. Wang, Y. F. Wang, R. L. Ward, Z. A. Warden, J. Warner, M. Was, J. Watchi, B. Weaver, L.-W. Wei, M. Weinert, A. J. Weinstein, R. Weiss, F. Wellmann, L. Wen, E. K. Wessel, P. Weßels, J. W. Westhouse, K. Wette, J. T. Whelan, B. F. Whiting, C. Whittle, D. M. Wilken, D. Williams, A. R. Williamson, J. L. Willis, B. Willke, M. H. Wimmer, W. Winkler, C. C. Wipf, H. Wittel, G. Woan, J. Woehler, J. K. Wofford, J. Worden, J. L. Wright, D. S. Wu, D. M. Wysocki, L. Xiao, H. Yamamoto, C. C. Yancey, L. Yang, M. J. Yap, M. Yazback, D. W. Yeeles, Hang Yu, Haocun Yu, S. H. R. Yuen, M. Yvert, A. K. Zadrożny, M. Zanolin, T. Zelenova, J.-P. Zendri, M. Zevin, J. Zhang, L. Zhang, T. Zhang, C. Zhao, M. Zhou, Z. Zhou, X. J. Zhu, A. B. Zimmerman, M. E. Zucker, and J. Zweizig. Tests of general relativity with the binary black hole signals from the ligo-virgo catalog gwtc-1. *Phys. Rev. D*, 100:104036, Nov 2019. [Cited on page 1.]

[4] B. P. Abbott, R. Abbott, T. D. Abbott, S. Abraham, F. Acernese, K. Ackley, C. Adams, R. X. Adhikari, V. B. Adya, C. Affeldt, M. Agathos, K. Agatsuma,

N. Aggarwal, O. D. Aguiar, L. Aiello, A. Ain, P. Ajith, G. Allen, A. Allocca, M. A. Aloy, P. A. Altin, A. Amato, S. Anand, A. Ananyeva, S. B. Anderson, W. G. Anderson, S. V. Angelova, S. Antier, S. Appert, K. Arai, M. C. Araya, J. S. Areeda, M. Arène, N. Arnaud, S. M. Aronson, K. G. Arun, S. Ascenzi, G. Ashton, S. M. Aston, P. Astone, F. Aubin, P. Aufmuth, K. AultONeal, C. Austin, V. Avendano, A. Avila-Alvarez, S. Babak, P. Bacon, F. Badaracco, M. K. M. Bader, S. Bae, J. Baird, P. T. Baker, F. Baldaccini, G. Ballardin, S. W. Ballmer, A. Bals, S. Banagiri, J. C. Barayoga, C. Barbieri, S. E. Barclay, B. C. Barish, D. Barker, K. Barkett, S. Barnum, F. Barone, B. Barr, L. Barsotti, M. Barsuglia, D. Barta, J. Bartlett, I. Bartos, R. Bassiri, A. Basti, M. Bawaj, J. C. Bayley, M. Bazzan, B. Bécsy, M. Bejger, I. Belahcene, A. S. Bell, D. Beniwal, M. G. Benjamin, B. K. Berger, G. Bergmann, S. Bernuzzi, C. P. L. Berry, D. Bersanetti, A. Bertolini, J. Betzwieser, R. Bhandare, J. Bidler, E. Biggs, I. A. Bilenko, S. A. Bilgili, G. Billingsley, R. Birney, O. Birnholtz, S. Biscans, M. Bischi, S. Biscoveanu, A. Bisht, M. Bitossi, M. A. Bizouard, J. K. Blackburn, J. Blackman, C. D. Blair, D. G. Blair, R. M. Blair, S. Bloemen, F. Bobba, N. Bode, M. Boer, Y. Boetzel, G. Bogaert, F. Bondu, R. Bonnand, P. Booker, B. A. Boom, R. Bork, V. Boschi, S. Bose, V. Bossilkov, J. Bosveld, Y. Bouffanais, A. Bozzi, C. Bradaschia, P. R. Brady, A. Bramley, M. Branchesi, J. E. Brau, M. Breschi, T. Briant, J. H. Briggs, F. Brighenti, A. Brillet, M. Brinkmann, P. Brockill, A. F. Brooks, J. Brooks, D. D. Brown, S. Brunett, A. Buikema, T. Bulik, H. J. Bulten, A. Buonanno, D. Buskulic, C. Buy, R. L. Byer, M. Cabero, L. Cadonati, G. Cagnoli, C. Cahillane, J. Calderón Bustillo, T. A. Callister, E. Calloni, J. B. Camp, W. A. Campbell, M. Canepa, K. C. Cannon, H. Cao, J. Cao, G. Carapella, F. Carbognani, S. Caride, M. F. Carney, G. Carullo, J. Casanueva Diaz, C. Casentini, S. Caudill, M. Cavaglià, F. Cavalier, R. Cavalieri, G. Cella, P. Cerdá-Durán, E. Cesarini, O. Chaibi, K. Chakravarti, S. J. Chamberlin, M. Chan, S. Chao, P. Charlton, E. A. Chase, E. Chassande-Mottin, D. Chatterjee, M. Chaturvedi, B. D. Cheeseboro, H. Y. Chen, X. Chen, Y. Chen, H.-P. Cheng, C. K. Cheong, H. Y. Chia, F. Chiadini, A. Chincarini, A. Chiummo, G. Cho, H. S. Cho, M. Cho, N. Christensen, Q. Chu, S. Chua, K. W. Chung, S. Chung, G. Ciani, M. Cieślar, A. A. Ciobanu, R. Ciolfi, F. Cipriano, A. Cirone, F. Clara, J. A. Clark, P. Clearwater, F. Cleva, E. Coccia, P.-F. Cohadon, D. Cohen, M. Colleoni, C. G. Collette, C. Collins, M. Colpi, L. R. Cominsky, M. Constancio, L. Conti, S. J. Cooper, P. Corban, T. R. Corbitt, I. Cordero-Carrión, S. Corezzi, K. R. Corley, N. Cornish, D. Corre, A. Corsi, S. Cortese, C. A. Costa, R. Cotesta, M. W. Coughlin, S. B. Coughlin, J.-P. Coulon, S. T. Countryman, P. Couvares, P. B. Covas, E. E. Cowan, D. M. Coward, M. J. Cowart, D. C. Coyne, R. Coyne, J. D. E. Creighton, T. D. Creighton, J. Cripe, M. Croquette, S. G. Crowder, T. J. Cullen, A. Cumming, L. Cunningham, E. Cuoco, T. Dal Canton, G. Dálya, B. D'Angelo, S. L. Danilishin, S. D'Antonio, K. Danzmann, A. Dasgupta, C. F. Da Silva Costa, L. E. H. Datrier, V. Dattilo, I. Dave, M. Davier, D. Davis, E. J. Daw, D. DeBra, M. Deenadayalan, J. Degallaix, M. De Laurentis, S. Deléglise, W. Del Pozzo,

L. M. DeMarchi, N. Demos, T. Dent, R. De Pietri, R. De Rosa, C. De Rossi, R. DeSalvo, O. de Varona, S. Dhurandhar, M. C. Díaz, T. Dietrich, L. Di Fiore, C. DiFronzo, C. Di Giorgio, F. Di Giovanni, M. Di Giovanni, T. Di Girolamo, A. Di Lieto, B. Ding, S. Di Pace, I. Di Palma, F. Di Renzo, A. K. Divakarla, A. Dmitriev, Z. Doctor, F. Donovan, K. L. Dooley, S. Doravari, I. Dorrington, T. P. Downes, M. Drago, J. C. Driggers, Z. Du, J.-G. Ducoin, P. Dupej, O. Durante, S. E. Dwyer, P. J. Easter, G. Eddolls, T. B. Edo, A. Effler, P. Ehrens, J. Eichholz, S. S. Eikenberry, M. Eisenmann, R. A. Eisenstein, L. Errico, R. C. Essick, H. Estelles, D. Estevez, Z. B. Etienne, T. Etzel, M. Evans, T. M. Evans, V. Fafone, S. Fairhurst, X. Fan, S. Farinon, B. Farr, W. M. Farr, E. J. Fauchon-Jones, M. Favata, M. Fays, M. Fazio, C. Fee, J. Feicht, M. M. Fejer, F. Feng, A. Fernandez-Galiana, I. Ferrante, E. C. Ferreira, T. A. Ferreira, F. Fidecaro, I. Fiori, D. Fiorucci, M. Fishbach, R. P. Fisher, J. M. Fishner, R. Fittipaldi, M. Fitz-Axen, V. Fiumara, R. Flaminio, M. Fletcher, E. Floden, E. Flynn, H. Fong, J. A. Font, P. W. F. Forsyth, J.-D. Fournier, Francisco Hernandez Vivanco, S. Frasca, F. Frasconi, Z. Frei, A. Freise, R. Frey, V. Frey, P. Fritschel, V. V. Frolov, G. Fronzè, P. Fulda, M. Fyffe, H. A. Gabbard, B. U. Gadre, S. M. Gaebel, J. R. Gair, L. Gammaitoni, S. G. Gaonkar, C. García-Quirós, F. Garufi, B. Gateley, S. Gaudio, G. Gaur, V. Gayathri, G. Gemme, E. Genin, A. Gennai, D. George, J. George, L. Gergely, S. Ghonge, Abhirup Ghosh, Archisman Ghosh, S. Ghosh, B. Giacomazzo, J. A. Giaime, K. D. Giardina, D. R. Gibson, K. Gill, L. Glover, J. Gniesmer, P. Godwin, E. Goetz, R. Goetz, B. Goncharov, G. González, J. M. Gonzalez Castro, A. Gopakumar, S. E. Gossan, M. Gosselin, R. Gouaty, B. Grace, A. Grado, M. Granata, A. Grant, S. Gras, P. Grassia, C. Gray, R. Gray, G. Greco, A. C. Green, R. Green, E. M. Gretarsson, A. Grimaldi, S. J. Grimm, P. Groot, H. Grote, S. Grunewald, P. Gruning, G. M. Guidi, H. K. Gulati, Y. Guo, A. Gupta, Anchal Gupta, P. Gupta, E. K. Gustafson, R. Gustafson, L. Haegel, O. Halim, B. R. Hall, E. D. Hall, E. Z. Hamilton, G. Hammond, M. Haney, M. M. Hanke, J. Hanks, C. Hanna, M. D. Hannam, O. A. Hannuksela, T. J. Hansen, J. Hanson, T. Harder, T. Hardwick, K. Haris, J. Harms, G. M. Harry, I. W. Harry, R. K. Hasskew, C. J. Haster, K. Haughian, F. J. Hayes, J. Healy, A. Heidmann, M. C. Heintze, H. Heitmann, F. Hellman, P. Hello, G. Hemming, M. Hendry, I. S. Heng, J. Hennig, M. Heurs, S. Hild, T. Hinderer, S. Hochheim, D. Hofman, A. M. Holgado, N. A. Holland, K. Holt, D. E. Holz, P. Hopkins, C. Horst, J. Hough, E. J. Howell, C. G. Hoy, Y. Huang, M. T. Hübner, E. A. Huerta, D. Huet, B. Hughey, V. Hui, S. Husa, S. H. Huttner, T. Huynh-Dinh, B. Idzkowski, A. Iess, H. Inchauspe, C. Ingram, R. Inta, G. Intini, B. Irwin, H. N. Isa, J.-M. Isac, M. Isi, B. R. Iyer, T. Jacqmin, S. J. Jadhav, K. Jani, N. N. Janthalur, P. Jaranowski, D. Jariwala, A. C. Jenkins, J. Jiang, D. S. Johnson, A. W. Jones, D. I. Jones, J. D. Jones, R. Jones, R. J. G. Jonker, L. Ju, J. Junker, C. V. Kalaghatgi, V. Kalogera, B. Kamai, S. Kandhasamy, G. Kang, J. B. Kanner, S. J. Kapadia, C. Karathanasis, S. Karki, R. Kashyap, M. Kasprzack, S. Katsanevas, E. Katsavounidis, W. Katzman, S. Kaufer, K. Kawabe, N. V. Keerthana, F. Kéfélian, D. Keitel, R. Kennedy, J. S. Key,

F. Y. Khalili, I. Khan, S. Khan, E. A. Khazanov, N. Khetan, M. Khursheed, N. Kijbunchoo, Chunglee Kim, J. C. Kim, K. Kim, W. Kim, W. S. Kim, Y.-M. Kim, C. Kimball, P. J. King, M. Kinley-Hanlon, R. Kirchhoff, J. S. Kissel, L. Kleybolte, J. H. Klika, S. Klimenko, T. D. Knowles, P. Koch, S. M. Koehlenbeck, G. Koekoek, S. Koley, V. Kondrashov, A. Kontos, N. Koper, M. Korobko, W. Z. Korth, M. Kovalam, D. B. Kozak, C. Krämer, V. Kringel, N. Krishnendu, A. Królak, N. Krupinski, G. Kuehn, A. Kumar, P. Kumar, Rahul Kumar, Rakesh Kumar, L. Kuo, A. Kutynia, S. Kwang, B. D. Lackey, D. Laghi, K. H. Lai, T. L. Lam, M. Landry, B. B. Lane, R. N. Lang, J. Lange, B. Lantz, R. K. Lanza, A. Lartaux-Vollard, P. D. Lasky, M. Laxen, A. Lazzarini, C. Lazzaro, P. Leaci, S. Leavey, Y. K. Lecoeuche, C. H. Lee, H. K. Lee, H. M. Lee, H. W. Lee, J. Lee, K. Lee, J. Lehmann, A. K. Lenon, N. Leroy, N. Letendre, Y. Levin, A. Li, J. Li, K. J. L. Li, T. G. F. Li, X. Li, F. Lin, F. Linde, S. D. Linker, T. B. Littenberg, J. Liu, X. Liu, M. Llorens-Monteagudo, R. K. L. Lo, L. T. London, A. Longo, M. Lorenzini, V. Loriette, M. Lormand, G. Losurdo, J. D. Lough, C. O. Lousto, G. Lovelace, M. E. Lower, H. Lück, D. Lumaca, A. P. Lundgren, R. Lynch, Y. Ma, R. Macas, S. Macfoy, M. MacInnis, D. M. Macleod, A. Macquet, I. Magaña Hernandez, F. Magaña-Sandoval, R. M. Magee, E. Majorana, I. Maksimovic, A. Malik, N. Man, V. Mandic, V. Mangano, G. L. Mansell, M. Manske, M. Mantovani, M. Mapelli, F. Marchesoni, F. Marion, S. Márka, Z. Márka, C. Markakis, A. S. Markosyan, A. Markowitz, E. Maros, A. Marquina, S. Marsat, F. Martelli, I. W. Martin, R. M. Martin, V. Martinez, D. V. Martynov, H. Masalehdan, K. Mason, E. Massera, A. Masserot, T. J. Massinger, M. Masso-Reid, S. Mastrogiovanni, A. Matas, F. Matichard, L. Matone, N. Mavalvala, J. J. McCann, R. McCarthy, D. E. McClelland, S. McCormick, L. McCuller, S. C. McGuire, C. McIsaac, J. McIver, D. J. McManus, T. McRae, S. T. McWilliams, D. Meacher, G. D. Meadors, M. Mehmet, A. K. Mehta, J. Meidam, E. Mejuto Villa, A. Melatos, G. Mendell, R. A. Mercer, L. Mereni, K. Merfeld, E. L. Merilh, M. Merzougui, S. Meshkov, C. Messenger, C. Messick, F. Messina, R. Metzdorff, P. M. Meyers, F. Meylahn, A. Miani, H. Miao, C. Michel, H. Middleton, L. Milano, A. L. Miller, M. Millhouse, J. C. Mills, M. C. Milovich-Goff, O. Minazzoli, Y. Minenkov, A. Mishkin, C. Mishra, T. Mistry, S. Mitra, V. P. Mitrofanov, G. Mitselmakher, R. Mittleman, G. Mo, D. Moffa, K. Mogushi, S. R. P. Mohapatra, M. Molina-Ruiz, M. Mondin, M. Montani, C. J. Moore, D. Moraru, F. Morawski, G. Moreno, S. Morisaki, B. Mours, C. M. Mow-Lowry, F. Muciaccia, Arunava Mukherjee, D. Mukherjee, S. Mukherjee, Subroto Mukherjee, N. Mukund, A. Mullavey, J. Munch, E. A. Muñiz, M. Muratore, P. G. Murray, A. Nagar, I. Nardecchia, L. Naticchioni, R. K. Nayak, B. F. Neil, J. Neilson, G. Nelemans, T. J. N. Nelson, M. Nery, A. Neunzert, L. Nevin, K. Y. Ng, S. Ng, C. Nguyen, P. Nguyen, D. Nichols, S. A. Nichols, S. Nissanke, F. Nocera, C. North, L. K. Nuttall, M. Obergaulinger, J. Oberling, B. D. O'Brien, G. Oganesyan, G. H. Ogin, J. J. Oh, S. H. Oh, F. Ohme, H. Ohta, M. A. Okada, M. Oliver, P. Oppermann, Richard J. Oram, B. O'Reilly, R. G. Ormiston, L. F. Or-

tega, R. O'Shaughnessy, S. Ossokine, D. J. Ottaway, H. Overmier, B. J. Owen, A. E. Pace, G. Pagano, M. A. Page, G. Pagliaroli, A. Pai, S. A. Pai, J. R. Palamos, O. Palashov, C. Palomba, H. Pan, P. K. Panda, P. T. H. Pang, C. Pankow, F. Pannarale, B. C. Pant, F. Paoletti, A. Paoli, A. Parida, W. Parker, D. Pascucci, A. Pasqualetti, R. Passaquieti, D. Passuello, M. Patil, B. Patricelli, E. Payne, B. L. Pearlstone, T. C. Pechsiri, A. J. Pedersen, M. Pedraza, R. Pedurand, A. Pele, S. Penn, A. Perego, C. J. Perez, C. Périgois, A. Perreca, J. Petermann, H. P. Pfeiffer, M. Phelps, K. S. Phukon, O. J. Piccinni, M. Pichot, F. Piergiovanni, V. Pierro, G. Pillant, L. Pinard, I. M. Pinto, M. Pirello, M. Pitkin, W. Plastino, R. Poggiani, D. Y. T. Pong, S. Ponrathnam, P. Popolizio, E. K. Porter, J. Powell, A. K. Prajapati, J. Prasad, K. Prasai, R. Prasanna, G. Pratten, T. Prestegard, M. Principe, G. A. Prodi, L. Prokhorov, M. Punturo, P. Puppo, M. Pürrer, H. Qi, V. Quetschke, P. J. Quinonez, F. J. Raab, G. Raaijmakers, H. Radkins, N. Radulesco, P. Raffai, S. Raja, C. Rajan, B. Rajbhandari, M. Rakhmanov, K. E. Ramirez, A. Ramos-Buades, Javed Rana, K. Rao, P. Rapagnani, V. Raymond, M. Razzano, J. Read, T. Regimbau, L. Rei, S. Reid, D. H. Reitze, P. Rettegno, F. Ricci, C. J. Richardson, J. W. Richardson, P. M. Ricker, G. Riemenschneider, K. Riles, M. Rizzo, N. A. Robertson, F. Robinet, A. Rocchi, L. Rolland, J. G. Rollins, V. J. Roma, M. Romanelli, J. Romano, R. Romano, C. L. Romel, J. H. Romie, C. A. Rose, D. Rose, K. Rose, D. Rosińska, S. G. Rosofsky, M. P. Ross, S. Rowan, A. Rüdiger, P. Ruggi, G. Rutins, K. Ryan, S. Sachdev, T. Sadecki, M. Sakellariadou, O. S. Salafia, L. Salconi, M. Saleem, A. Samajdar, L. Sammut, E. J. Sanchez, L. E. Sanchez, N. Sanchis-Gual, J. R. Sanders, K. A. Santiago, E. Santos, N. Sarin, B. Sassolas, B. S. Sathyaprakash, O. Sauter, R. L. Savage, P. Schale, M. Scheel, J. Scheuer, P. Schmidt, R. Schnabel, R. M. S. Schofield, A. Schönbeck, E. Schreiber, B. W. Schulte, B. F. Schutz, J. Scott, S. M. Scott, E. Seidel, D. Sellers, A. S. Sengupta, N. Sennett, D. Sentenac, V. Sequino, A. Sergeev, Y. Setyawati, D. A. Shaddock, T. Shaffer, M. S. Shahriar, M. B. Shaner, A. Sharma, P. Sharma, P. Shawhan, H. Shen, R. Shink, D. H. Shoemaker, D. M. Shoemaker, K. Shukla, S. ShyamSundar, K. Siellez, M. Sieniawska, D. Sigg, L. P. Singer, D. Singh, N. Singh, A. Singhal, A. M. Sintes, S. Sitmukhambetov, V. Skliris, B. J. J. Slagmolen, T. J. Slaven-Blair, J. R. Smith, R. J. E. Smith, S. Somala, E. J. Son, S. Soni, B. Sorazu, F. Sorrentino, T. Souradeep, E. Sowell, A. P. Spencer, M. Spera, A. K. Srivastava, V. Srivastava, K. Staats, C. Stachie, M. Standke, D. A. Steer, M. Steinke, J. Steinlechner, S. Steinlechner, D. Steinmeyer, S. P. Stevenson, D. Stocks, R. Stone, D. J. Stops, K. A. Strain, G. Stratta, S. E. Strigin, A. Strunk, R. Sturani, A. L. Stuver, V. Sudhir, T. Z. Summerscales, L. Sun, S. Sunil, A. Sur, J. Suresh, P. J. Sutton, B. L. Swinkels, M. J. Szczepańczyk, M. Tacca, S. C. Tait, C. Talbot, D. B. Tanner, D. Tao, M. Tápai, A. Tapia, J. D. Tasson, R. Taylor, R. Tenorio, L. Terkowski, M. Thomas, P. Thomas, S. R. Thondapu, K. A. Thorne, E. Thrane, Shubhanshu Tiwari, Srishti Tiwari, V. Tiwari, K. Toland, M. Tonelli, Z. Tornasi, A. Torres-Forné, C. I. Torrie, D. Töyrä, F. Travasso, G. Traylor, M. C. Tringali, A. Tripathee, A. Trovato, L. Trozzo, K. W. Tsang,

M. Tse, R. Tso, L. Tsukada, D. Tsuna, T. Tsutsui, D. Tuyenbayev, K. Ueno, D. Ugolini, C. S. Unnikrishnan, A. L. Urban, S. A. Usman, H. Vahlbruch, G. Vajente, G. Valdes, M. Valentini, N. van Bakel, M. van Beuzekom, J. F. J. van den Brand, C. Van Den Broeck, D. C. Vander-Hyde, L. van der Schaaf, J. V. VanHeijningen, A. A. van Veggel, M. Vardaro, V. Varma, S. Vass, M. Vasúth, A. Vecchio, G. Vedovato, J. Veitch, P. J. Veitch, K. Venkateswara, G. Venugopalan, D. Verkindt, F. Vetrano, A. Viceré, A. D. Viets, S. Vinciguerra, D. J. Vine, J.-Y. Vinet, S. Vitale, T. Vo, H. Vocca, C. Vorvick, S. P. Vyatchanin, A. R. Wade, L. E. Wade, M. Wade, R. Walet, M. Walker, L. Wallace, S. Walsh, H. Wang, J. Z. Wang, S. Wang, W. H. Wang, Y. F. Wang, R. L. Ward, Z. A. Warden, J. Warner, M. Was, J. Watchi, B. Weaver, L.-W. Wei, M. Weinert, A. J. Weinstein, R. Weiss, F. Wellmann, L. Wen, E. K. Wessel, P. Weßels, J. W. Westhouse, K. Wette, J. T. Whelan, B. F. Whiting, C. Whittle, D. M. Wilken, D. Williams, A. R. Williamson, J. L. Willis, B. Willke, W. Winkler, C. C. Wipf, H. Wittel, G. Woan, J. Woehler, J. K. Wofford, J. L. Wright, D. S. Wu, D. M. Wysocki, S. Xiao, R. Xu, H. Yamamoto, C. C. Yancey, L. Yang, Y. Yang, Z. Yang, M. J. Yap, M. Yazback, D. W. Yeeles, Hang Yu, Haocun Yu, S. H. R. Yuen, A. K. Zadrożny, A. Zadrożny, M. Zanolin, T. Zelenova, J.-P. Zendri, M. Zevin, J. Zhang, L. Zhang, T. Zhang, C. Zhao, G. Zhao, M. Zhou, Z. Zhou, X. J. Zhu, A. B. Zimmerman, M. E. Zucker, and J. Zweizig. A gravitational-wave measurement of the hubble constant following the second observing run of advanced LIGO and virgo. *The Astrophysical Journal*, 909(2):218, mar 2021. [Cited on page 1.]

[5] B. P. Abbott, R. Abbott, T. D. Abbott, F. Acernese, K. Ackley, C. Adams, T. Adams, P. Addesso, R. X. Adhikari, V. B. Adya, C. Affeldt, B. Agarwal, M. Agathos, K. Agatsuma, N. Aggarwal, O. D. Aguiar, L. Aiello, A. Ain, P. Ajith, B. Allen, G. Allen, A. Allocca, M. A. Aloy, P. A. Altin, A. Amato, A. Ananyeva, S. B. Anderson, W. G. Anderson, S. V. Angelova, S. Antier, S. Appert, K. Arai, M. C. Araya, J. S. Areeda, M. Arène, N. Arnaud, K. G. Arun, S. Ascenzi, G. Ashton, M. Ast, S. M. Aston, P. Astone, D. V. Atallah, F. Aubin, P. Aufmuth, C. Aulbert, K. AultONeal, C. Austin, A. Avila-Alvarez, S. Babak, P. Bacon, F. Badaracco, M. K. M. Bader, S. Bae, P. T. Baker, F. Baldaccini, G. Ballardin, S. W. Ballmer, S. Banagiri, J. C. Barayoga, S. E. Barclay, B. C. Barish, D. Barker, K. Barkett, S. Barnum, F. Barone, B. Barr, L. Barsotti, M. Barsuglia, D. Barta, J. Bartlett, I. Bartos, R. Bassiri, A. Basti, J. C. Batch, M. Bawaj, J. C. Bayley, M. Bazzan, B. Bécsy, C. Beer, M. Bejger, I. Belahcene, A. S. Bell, D. Beniwal, M. Bensch, B. K. Berger, G. Bergmann, S. Bernuzzi, J. J. Bero, C. P. L. Berry, D. Bersanetti, A. Bertolini, J. Betzwieser, R. Bhandare, I. A. Bilenko, S. A. Bilgili, G. Billingsley, C. R. Billman, J. Birch, R. Birney, O. Birnholtz, S. Biscans, S. Biscoveanu, A. Bisht, M. Bitossi, M. A. Bizouard, J. K. Blackburn, J. Blackman, C. D. Blair, D. G. Blair, R. M. Blair, S. Bloemen, O. Bock, N. Bode, M. Boer, Y. Boetzel, G. Bogaert, A. Bohe, F. Bondu, E. Bonilla, R. Bonnand, P. Booker, B. A. Boom, C. D. Booth, R. Bork, V. Boschi, S. Bose,

K. Bossie, V. Bossilkov, J. Bosveld, Y. Bouffanais, A. Bozzi, C. Bradaschia, P. R. Brady, A. Bramley, M. Branchesi, J. E. Brau, T. Briant, F. Brighenti, A. Brillet, M. Brinkmann, V. Brisson, P. Brockill, A. F. Brooks, D. D. Brown, S. Brunett, C. C. Buchanan, A. Buikema, T. Bulik, H. J. Bulten, A. Buonanno, D. Buskulic, C. Buy, R. L. Byer, M. Cabero, L. Cadonati, G. Cagnoli, C. Cahillane, J. Calderón Bustillo, T. A. Callister, E. Calloni, J. B. Camp, M. Canepa, P. Canizares, K. C. Cannon, H. Cao, J. Cao, C. D. Capano, E. Capocasa, F. Carbognani, S. Caride, M. F. Carney, G. Carullo, J. Casanueva Diaz, C. Casentini, S. Caudill, M. Cavaglià, F. Cavalier, R. Cavalieri, G. Cella, C. B. Cepeda, P. Cerdá-Durán, G. Cerretani, E. Cesarini, O. Chaibi, S. J. Chamberlin, M. Chan, S. Chao, P. Charlton, E. Chase, E. Chassande-Mottin, D. Chatterjee, K. Chatziioannou, B. D. Cheeseboro, H. Y. Chen, X. Chen, Y. Chen, H.-P. Cheng, H. Y. Chia, A. Chincarini, A. Chiummo, T. Chmiel, H. S. Cho, M. Cho, J. H. Chow, N. Christensen, Q. Chu, A. J. K. Chua, S. Chua, K. W. Chung, S. Chung, G. Ciani, A. A. Ciobanu, R. Ciolfi, F. Cipriano, C. E. Cirelli, A. Cirone, F. Clara, J. A. Clark, P. Clearwater, F. Cleva, C. Cocchieri, E. Coccia, P.-F. Cohadon, D. Cohen, A. Colla, C. G. Collette, C. Collins, L. R. Cominsky, M. Constancio, L. Conti, S. J. Cooper, P. Corban, T. R. Corbitt, I. Cordero-Carrión, K. R. Corley, N. Cornish, A. Corsi, S. Cortese, C. A. Costa, R. Cotesta, M. W. Coughlin, S. B. Coughlin, J.-P. Coulon, S. T. Countryman, P. Couvares, P. B. Covas, E. E. Cowan, D. M. Coward, M. J. Cowart, D. C. Coyne, R. Coyne, J. D. E. Creighton, T. D. Creighton, J. Cripe, S. G. Crowder, T. J. Cullen, A. Cumming, L. Cunningham, E. Cuoco, T. Dal Canton, G. Dálya, S. L. Danilishin, S. D'Antonio, K. Danzmann, A. Dasgupta, C. F. Da Silva Costa, V. Dattilo, I. Dave, M. Davier, D. Davis, E. J. Daw, B. Day, D. DeBra, M. Deenadayalan, J. Degallaix, M. De Laurentis, S. Deléglise, W. Del Pozzo, N. Demos, T. Denker, T. Dent, R. De Pietri, J. Derby, V. Dergachev, R. De Rosa, C. De Rossi, R. DeSalvo, O. de Varona, S. Dhurandhar, M. C. Díaz, T. Dietrich, L. Di Fiore, M. Di Giovanni, T. Di Girolamo, A. Di Lieto, B. Ding, S. Di Pace, I. Di Palma, F. Di Renzo, A. Dmitriev, Z. Doctor, V. Dolique, F. Donovan, K. L. Dooley, S. Doravari, I. Dorrington, M. Dovale Álvarez, T. P. Downes, M. Drago, C. Dreissigacker, J. C. Driggers, Z. Du, P. Dupej, S. E. Dwyer, P. J. Easter, T. B. Edo, M. C. Edwards, A. Effler, H.-B. Eggenstein, P. Ehrens, J. Eichholz, S. S. Eikenberry, M. Eisenmann, R. A. Eisenstein, R. C. Essick, H. Estelles, D. Estevez, Z. B. Etienne, T. Etzel, M. Evans, T. M. Evans, V. Fafone, H. Fair, S. Fairhurst, X. Fan, S. Farinon, B. Farr, W. M. Farr, E. J. Fauchon-Jones, M. Favata, M. Fays, C. Fee, H. Fehrmann, J. Feicht, M. M. Fejer, F. Feng, A. Fernandez-Galiana, I. Ferrante, E. C. Ferreira, F. Ferrini, F. Fidecaro, I. Fiori, D. Fiorucci, M. Fishbach, R. P. Fisher, J. M. Fishner, M. Fitz-Axen, R. Flaminio, M. Fletcher, H. Fong, J. A. Font, P. W. F. Forsyth, S. S. Forsyth, J.-D. Fournier, S. Frasca, F. Frasconi, Z. Frei, A. Freise, R. Frey, V. Frey, P. Fritschel, V. V. Frolov, P. Fulda, M. Fyffe, H. A. Gabbard, B. U. Gadre, S. M. Gaebel, J. R. Gair, L. Gammaitoni, M. R. Ganija, S. G. Gaonkar, A. Garcia, C. García-Quirós, F. Garufi, B. Gateley,

S. Gaudio, G. Gaur, V. Gayathri, G. Gemme, E. Genin, A. Gennai, D. George, J. George, L. Gergely, V. Germain, S. Ghonge, Abhirup Ghosh, Archisman Ghosh, S. Ghosh, B. Giacomazzo, J. A. Giaime, K. D. Giardina, A. Giazotto, K. Gill, G. Giordano, L. Glover, E. Goetz, R. Goetz, B. Goncharov, G. González, J. M. Gonzalez Castro, A. Gopakumar, M. L. Gorodetsky, S. E. Gossan, M. Gosselin, R. Gouaty, A. Grado, C. Graef, M. Granata, A. Grant, S. Gras, C. Gray, G. Greco, A. C. Green, R. Green, E. M. Gretarsson, P. Groot, H. Grote, S. Grunewald, P. Gruning, G. M. Guidi, H. K. Gulati, X. Guo, A. Gupta, M. K. Gupta, K. E. Gushwa, E. K. Gustafson, R. Gustafson, O. Halim, B. R. Hall, E. D. Hall, E. Z. Hamilton, H. F. Hamilton, G. Hammond, M. Haney, M. M. Hanke, J. Hanks, C. Hanna, M. D. Hannam, O. A. Hannuksela, J. Hanson, T. Hardwick, J. Harms, G. M. Harry, I. W. Harry, M. J. Hart, C.-J. Haster, K. Haughian, J. Healy, A. Heidmann, M. C. Heintze, H. Heitmann, P. Hello, G. Hemming, M. Hendry, I. S. Heng, J. Hennig, A. W. Heptonstall, F. J. Hernandez, M. Heurs, S. Hild, T. Hinderer, W. C. G. Ho, D. Hoak, S. Hochheim, D. Hofman, N. A. Holland, K. Holt, D. E. Holz, P. Hopkins, C. Horst, J. Hough, E. A. Houston, E. J. Howell, A. Hreibi, E. A. Huerta, D. Huet, B. Hughey, M. Hulko, S. Husa, S. H. Huttner, T. Huynh-Dinh, A. Iess, N. Indik, C. Ingram, R. Inta, G. Intini, B. S. Irwin, H. N. Isa, J.-M. Isac, M. Isi, B. R. Iyer, K. Izumi, T. Jacqmin, K. Jani, P. Jaranowski, D. S. Johnson, W. W. Johnson, D. I. Jones, R. Jones, R. J. G. Jonker, L. Ju, J. Junker, C. V. Kalaghatgi, V. Kalogera, B. Kamai, S. Kandhasamy, G. Kang, J. B. Kanner, S. J. Kapadia, S. Karki, K. S. Karvinen, M. Kasprzack, M. Katolik, S. Katsanevas, E. Katsavounidis, W. Katzman, S. Kaufer, K. Kawabe, N. V. Keerthana, F. Kéfélian, D. Keitel, A. J. Kemball, R. Kennedy, J. S. Key, F. Y. Khalili, B. Khamesra, H. Khan, I. Khan, S. Khan, Z. Khan, E. A. Khazanov, N. Kijbunchoo, Chunglee Kim, J. C. Kim, K. Kim, W. Kim, W. S. Kim, Y.-M. Kim, E. J. King, P. J. King, M. Kinley-Hanlon, R. Kirchhoff, J. S. Kissel, L. Kleybolte, S. Klimenko, T. D. Knowles, P. Koch, S. M. Koehlenbeck, S. Koley, V. Kondrashov, A. Kontos, M. Korobko, W. Z. Korth, I. Kowalska, D. B. Kozak, C. Krämer, V. Kringel, B. Krishnan, A. Królak, G. Kuehn, P. Kumar, R. Kumar, S. Kumar, L. Kuo, A. Kutynia, S. Kwang, B. D. Lackey, K. H. Lai, M. Landry, P. Landry, R. N. Lang, J. Lange, B. Lantz, R. K. Lanza, A. Lartaux-Vollard, P. D. Lasky, M. Laxen, A. Lazzarini, C. Lazzaro, P. Leaci, S. Leavey, C. H. Lee, H. K. Lee, H. M. Lee, H. W. Lee, K. Lee, J. Lehmann, A. Lenon, M. Leonardi, N. Leroy, N. Letendre, Y. Levin, J. Li, T. G. F. Li, X. Li, S. D. Linker, T. B. Littenberg, J. Liu, X. Liu, R. K. L. Lo, N. A. Lockerbie, L. T. London, A. Longo, M. Lorenzini, V. Loriette, M. Lormand, G. Losurdo, J. D. Lough, C. O. Lousto, G. Lovelace, H. Lück, D. Lumaca, A. P. Lundgren, R. Lynch, Y. Ma, R. Macas, S. Macfoy, B. Machenschalk, M. MacInnis, D. M. Macleod, I. Magaña Hernandez, F. Magaña Sandoval, L. Magaña Zertuche, R. M. Magee, E. Majorana, I. Maksimovic, N. Man, V. Mandic, V. Mangano, G. L. Mansell, M. Manske, M. Mantovani, F. Marchesoni, F. Marion, S. Márka, Z. Márka, C. Markakis, A. S. Markosyan, A. Markowitz,

E. Maros, A. Marquina, F. Martelli, L. Martellini, I. W. Martin, R. M. Martin, D. V. Martynov, K. Mason, E. Massera, A. Masserot, T. J. Massinger, M. Masso-Reid, S. Mastrogiovanni, A. Matas, F. Matichard, L. Matone, N. Mavalvala, N. Mazumder, J. J. McCann, R. McCarthy, D. E. McClelland, S. McCormick, L. McCuller, S. C. McGuire, J. McIver, D. J. McManus, T. McRae, S. T. McWilliams, D. Meacher, G. D. Meadors, M. Mehmet, J. Meidam, E. Mejuto-Villa, A. Melatos, G. Mendell, D. Mendoza-Gandara, R. A. Mercer, L. Mereni, E. L. Merilh, M. Merzougui, S. Meshkov, C. Messenger, C. Messick, R. Metzdorff, P. M. Meyers, H. Miao, C. Michel, H. Middleton, E. E. Mikhailov, L. Milano, A. L. Miller, A. Miller, B. B. Miller, J. Miller, M. Millhouse, J. Mills, M. C. Milovich-Goff, O. Minazzoli, Y. Minenkov, J. Ming, C. Mishra, S. Mitra, V. P. Mitrofanov, G. Mitselmakher, R. Mittleman, D. Moffa, K. Mogushi, M. Mohan, S. R. P. Mohapatra, M. Montani, C. J. Moore, D. Moraru, G. Moreno, S. Morisaki, B. Mours, C. M. Mow-Lowry, G. Mueller, A. W. Muir, Arunava Mukherjee, D. Mukherjee, S. Mukherjee, N. Mukund, A. Mullavey, J. Munch, E. A. Muñiz, M. Muratore, P. G. Murray, A. Nagar, K. Napier, I. Nardecchia, L. Naticchioni, R. K. Nayak, J. Neilson, G. Nelemans, T. J. N. Nelson, M. Nery, A. Neunzert, L. Nevin, J. M. Newport, K. Y. Ng, S. Ng, P. Nguyen, T. T. Nguyen, D. Nichols, A. B. Nielsen, S. Nissanke, A. Nitz, F. Nocera, D. Nolting, C. North, L. K. Nuttall, M. Obergaulinger, J. Oberling, B. D. O'Brien, G. D. O'Dea, G. H. Ogin, J. J. Oh, S. H. Oh, F. Ohme, H. Ohta, M. A. Okada, M. Oliver, P. Oppermann, Richard J. Oram, B. O'Reilly, R. Ormiston, L. F. Ortega, R. O'Shaughnessy, S. Ossokine, D. J. Ottaway, H. Overmier, B. J. Owen, A. E. Pace, G. Pagano, J. Page, M. A. Page, A. Pai, S. A. Pai, J. R. Palamos, O. Palashov, C. Palomba, A. Pal-Singh, Howard Pan, Huang-Wei Pan, B. Pang, P. T. H. Pang, C. Pankow, F. Pannarale, B. C. Pant, F. Paoletti, A. Paoli, M. A. Papa, A. Parida, W. Parker, D. Pascucci, A. Pasqualetti, R. Passaquieti, D. Passuello, M. Patil, B. Patricelli, B. L. Pearlstone, C. Pedersen, M. Pedraza, R. Pedurand, L. Pekowsky, A. Pele, S. Penn, A. Perego, C. J. Perez, A. Perreca, L. M. Perri, H. P. Pfeiffer, M. Phelps, K. S. Phukon, O. J. Piccinni, M. Pichot, F. Piergiovanni, V. Pierro, G. Pillant, L. Pinard, I. M. Pinto, M. Pirello, M. Pitkin, R. Poggiani, P. Popolizio, E. K. Porter, L. Possenti, A. Post, J. Powell, J. Prasad, J. W. W. Pratt, G. Pratten, V. Predoi, T. Prestegard, M. Principe, S. Privitera, G. A. Prodi, L. G. Prokhorov, O. Puncken, M. Punturo, P. Puppo, M. Pürrer, H. Qi, V. Quetschke, E. A. Quintero, R. Quitzow-James, F. J. Raab, D. S. Rabeling, H. Radkins, P. Raffai, S. Raja, C. Rajan, B. Rajbhandari, M. Rakhmanov, K. E. Ramirez, A. Ramos-Buades, Javed Rana, P. Rapagnani, V. Raymond, M. Razzano, J. Read, T. Regimbau, L. Rei, S. Reid, D. H. Reitze, W. Ren, F. Ricci, P. M. Ricker, G. M. Riemenschneider, K. Riles, M. Rizzo, N. A. Robertson, R. Robie, F. Robinet, T. Robson, A. Rocchi, L. Rolland, J. G. Rollins, V. J. Roma, R. Romano, C. L. Romel, J. H. Romie, D. Rosińska, M. P. Ross, S. Rowan, A. Rüdiger, P. Ruggi, G. Rutins, K. Ryan, S. Sachdev, T. Sadecki, M. Sakellariadou, L. Salconi, M. Saleem, F. Salemi, A. Samajdar, L. Sammut, L. M. Sampson, E. J. Sanchez, L. E. Sanchez, N. Sanchis-Gual,

V. Sandberg, J. R. Sanders, N. Sarin, B. Sassolas, B. S. Sathyaprakash, P. R. Saulson, O. Sauter, R. L. Savage, A. Sawadsky, P. Schale, M. Scheel, J. Scheuer, P. Schmidt, R. Schnabel, R. M. S. Schofield, A. Schönbeck, E. Schreiber, D. Schuette, B. W. Schulte, B. F. Schutz, S. G. Schwalbe, J. Scott, S. M. Scott, E. Seidel, D. Sellers, A. S. Sengupta, D. Sentenac, V. Sequino, A. Sergeev, Y. Setyawati, D. A. Shaddock, T. J. Shaffer, A. A. Shah, M. S. Shahriar, M. B. Shaner, L. Shao, B. Shapiro, P. Shawhan, H. Shen, D. H. Shoemaker, D. M. Shoemaker, K. Siellez, X. Siemens, M. Sieniawska, D. Sigg, A. D. Silva, L. P. Singer, A. Singh, A. Singhal, A. M. Sintes, B. J. J. Slagmolen, T. J. Slaven-Blair, B. Smith, J. R. Smith, R. J. E. Smith, S. Somala, E. J. Son, B. Sorazu, F. Sorrentino, T. Souradeep, A. P. Spencer, A. K. Srivastava, K. Staats, M. Steinke, J. Steinlechner, S. Steinlechner, D. Steinmeyer, B. Steltner, S. P. Stevenson, D. Stocks, R. Stone, D. J. Stops, K. A. Strain, G. Stratta, S. E. Strigin, A. Strunk, R. Sturani, A. L. Stuver, T. Z. Summerscales, L. Sun, S. Sunil, J. Suresh, P. J. Sutton, B. L. Swinkels, M. J. Szczepańczyk, M. Tacca, S. C. Tait, C. Talbot, D. Talukder, D. B. Tanner, M. Tápai, A. Taracchini, J. D. Tasson, J. A. Taylor, R. Taylor, S. V. Tewari, T. Theeg, F. Thies, E. G. Thomas, M. Thomas, P. Thomas, K. A. Thorne, E. Thrane, S. Tiwari, V. Tiwari, K. V. Tokmakov, K. Toland, M. Tonelli, Z. Tornasi, A. Torres-Forné, C. I. Torrie, D. Töyrä, F. Travasso, G. Traylor, J. Trinastic, M. C. Tringali, A. Trovato, L. Trozzo, K. W. Tsang, M. Tse, R. Tso, D. Tsuna, L. Tsukada, D. Tuyenbayev, K. Ueno, D. Ugolini, A. L. Urban, S. A. Usman, H. Vahlbruch, G. Vajente, G. Valdes, N. van Bakel, M. van Beuzekom, J. F. J. van den Brand, C. Van Den Broeck, D. C. Vander-Hyde, L. van der Schaaf, J. V. van Heijningen, A. A. van Veggel, M. Vardaro, V. Varma, S. Vass, M. Vasúth, A. Vecchio, G. Vedovato, J. Veitch, P. J. Veitch, K. Venkateswara, G. Venugopalan, D. Verkindt, F. Vetrano, A. Viceré, A. D. Viets, S. Vinciguerra, D. J. Vine, J.-Y. Vinet, S. Vitale, T. Vo, H. Vocca, C. Vorvick, S. P. Vyatchanin, A. R. Wade, L. E. Wade, M. Wade, R. Walet, M. Walker, L. Wallace, S. Walsh, G. Wang, H. Wang, J. Z. Wang, W. H. Wang, Y. F. Wang, R. L. Ward, J. Warner, M. Was, J. Watchi, B. Weaver, L.-W. Wei, M. Weinert, A. J. Weinstein, R. Weiss, F. Wellmann, L. Wen, E. K. Wessel, P. Weßels, J. Westerweck, K. Wette, J. T. Whelan, B. F. Whiting, C. Whittle, D. Wilken, D. Williams, R. D. Williams, A. R. Williamson, J. L. Willis, B. Willke, M. H. Wimmer, W. Winkler, C. C. Wipf, H. Wittel, G. Woan, J. Woehler, J. K. Wofford, W. K. Wong, J. Worden, J. L. Wright, D. S. Wu, D. M. Wysocki, S. Xiao, W. Yam, H. Yamamoto, C. C. Yancey, L. Yang, M. J. Yap, M. Yazback, Hang Yu, Haocun Yu, M. Yvert, A. Zadrożny, M. Zanolin, T. Zelenova, J.-P. Zendri, M. Zevin, J. Zhang, L. Zhang, M. Zhang, T. Zhang, Y.-H. Zhang, C. Zhao, M. Zhou, Z. Zhou, S. J. Zhu, X. J. Zhu, A. B. Zimmerman, Y. Zlochower, M. E. Zucker, and J. Zweizig. Gw170817: Measurements of neutron star radii and equation of state. *Phys. Rev. Lett.*, 121:161101, Oct 2018. [Cited on page 1.]

[6] Robert Lawrence Ward. *Length Sensing and Control of a Prototype Advanced*

*Interferometric Gravitational Wave Detector*. PhD thesis, California Institute of Technology, 2010. [Cited on pages 1, 27, 192, and 205.]

[7] Jennifer Clair Driggers. *Noise Cancellation for Gravitational Wave Detectors*. PhD thesis, California Institute of Technology, 2015. [Not cited.]

[8] Eric Antonio Quintero. *Improving the Performance and Sensitivity of Gravitational Wave Detectors*. PhD thesis, California Institute of Technology, 2018. [Cited on pages 1, 14, and 19.]

[9] D. V. Martynov, E. D. Hall, B. P. Abbott, R. Abbott, T. D. Abbott, C. Adams, R. X. Adhikari, R. A. Anderson, S. B. Anderson, K. Arai, M. A. Arain, S. M. Aston, L. Austin, S. W. Ballmer, M. Barbet, D. Barker, B. Barr, L. Barsotti, J. Bartlett, M. A. Barton, I. Bartos, J. C. Batch, A. S. Bell, I. Belopolski, J. Bergman, J. Betzwieser, G. Billingsley, J. Birch, S. Biscans, C. Biwer, E. Black, C. D. Blair, C. Bogan, C. Bond, R. Bork, D. O. Bridges, A. F. Brooks, D. D. Brown, L. Carbone, C. Celerier, G. Ciani, F. Clara, D. Cook, S. T. Countryman, M. J. Cowart, D. C. Coyne, A. Cumming, L. Cunningham, M. Damjanic, R. Dannenberg, K. Danzmann, C. F. Da Silva Costa, E. J. Daw, D. DeBra, R. T. DeRosa, R. DeSalvo, K. L. Dooley, S. Doravari, J. C. Driggers, S. E. Dwyer, A. Effler, T. Etzel, M. Evans, T. M. Evans, M. Factourovich, H. Fair, D. Feldbaum, R. P. Fisher, S. Foley, M. Frede, A. Freise, P. Fritschel, V. V. Frolov, P. Fulda, M. Fyffe, V. Galdi, J. A. Giaime, K. D. Giardina, J. R. Gleason, R. Goetz, S. Gras, C. Gray, R. J. S. Greenhalgh, H. Grote, C. J. Guido, K. E. Gushwa, E. K. Gustafson, R. Gustafson, G. Hammond, J. Hanks, J. Hanson, T. Hardwick, G. M. Harry, K. Haughian, J. Heefner, M. C. Heintze, A. W. Heptonstall, D. Hoak, J. Hough, A. Ivanov, K. Izumi, M. Jacobson, E. James, R. Jones, S. Kandhasamy, S. Karki, M. Kasprzack, S. Kaufer, K. Kawabe, W. Kells, N. Kijbunchoo, E. J. King, P. J. King, D. L. Kinzel, J. S. Kissel, K. Kokeyama, W. Z. Korth, G. Kuehn, P. Kwee, M. Landry, B. Lantz, A. Le Roux, B. M. Levine, J. B. Lewis, V. Lhuillier, N. A. Lockerbie, M. Lormand, M. J. Lubinski, A. P. Lundgren, T. MacDonald, M. MacInnis, D. M. Macleod, M. Mageswaran, K. Mailand, S. Márka, Z. Márka, A. S. Markosyan, E. Maros, I. W. Martin, R. M. Martin, J. N. Marx, K. Mason, T. J. Massinger, F. Matichard, N. Mavalvala, R. McCarthy, D. E. McClelland, S. McCormick, G. McIntyre, J. McIver, E. L. Merilh, M. S. Meyer, P. M. Meyers, J. Miller, R. Mittleman, G. Moreno, C. L. Mueller, G. Mueller, A. Mullavey, J. Munch, P. G. Murray, L. K. Nuttall, J. Oberling, J. O'Dell, P. Oppermann, Richard J. Oram, B. O'Reilly, C. Osthelder, D. J. Ottaway, H. Overmier, J. R. Palamos, H. R. Paris, W. Parker, Z. Patrick, A. Pele, S. Penn, M. Phelps, M. Pickenpack, V. Pierro, I. Pinto, J. Poeld, M. Principe, L. Prokhorov, O. Puncken, V. Quetschke, E. A. Quintero, F. J. Raab, H. Radkins, P. Raffai, C. R. Ramet, C. M. Reed, S. Reid, D. H. Reitze, N. A. Robertson, J. G. Rollins, V. J. Roma, J. H. Romie, S. Rowan, K. Ryan, T. Sadecki, E. J. Sanchez, V. Sandberg, V. Sannibale, R. L. Savage, R. M. S. Schofield, B. Schultz, P. Schwinberg, D. Sellers, A. Sevigny, D. A. Shaddock,

Z. Shao, B. Shapiro, P. Shawhan, D. H. Shoemaker, D. Sigg, B. J. J. Slagmolen, J. R. Smith, M. R. Smith, N. D. Smith-Lefebvre, B. Sorazu, A. Staley, A. J. Stein, A. Stochino, K. A. Strain, R. Taylor, M. Thomas, P. Thomas, K. A. Thorne, E. Thrane, K. V. Tokmakov, C. I. Torrie, G. Traylor, G. Vajente, G. Valdes, A. A. van Veggel, M. Vargas, A. Vecchio, P. J. Veitch, K. Venkateswara, T. Vo, C. Vorvick, S. J. Waldman, M. Walker, R. L. Ward, J. Warner, B. Weaver, R. Weiss, T. Welborn, P. Weßels, C. Wilkinson, P. A. Willems, L. Williams, B. Willke, I. Wilmut, L. Winkelmann, C. C. Wipf, J. Worden, G. Wu, H. Yamamoto, C. C. Yancey, H. Yu, L. Zhang, M. E. Zucker, and J. Zweizig. Sensitivity of the Advanced LIGO detectors at the beginning of gravitational wave astronomy. *Phys. Rev. D*, 93:112004, Jun 2016. [Cited on pages 3, 99, and 137.]

[10] A. Buikema, C. Cahillane, G. L. Mansell, C. D. Blair, R. Abbott, C. Adams, R. X. Adhikari, A. Ananyeva, S. Appert, K. Arai, J. S. Areeda, Y. Asali, S. M. Aston, C. Austin, A. M. Baer, M. Ball, S. W. Ballmer, S. Banagiri, D. Barker, L. Barsotti, J. Bartlett, B. K. Berger, J. Betzwieser, D. Bhattacharjee, G. Billingsley, S. Biscans, R. M. Blair, N. Bode, P. Booker, R. Bork, A. Bramley, A. F. Brooks, D. D. Brown, K. C. Cannon, X. Chen, A. A. Ciobanu, F. Clara, S. J. Cooper, K. R. Corley, S. T. Countryman, P. B. Covas, D. C. Coyne, L. E. H. Datrier, D. Davis, C. Di Fronzo, K. L. Dooley, J. C. Driggers, P. Dupej, S. E. Dwyer, A. Effler, T. Etzel, M. Evans, T. M. Evans, J. Feicht, A. Fernandez-Galiana, P. Fritschel, V. V. Frolov, P. Fulda, M. Fyffe, J. A. Giaime, K. D. Giardina, P. Godwin, E. Goetz, S. Gras, C. Gray, R. Gray, A. C. Green, E. K. Gustafson, R. Gustafson, J. Hanks, J. Hanson, T. Hardwick, R. K. Hasskew, M. C. Heintze, A. F. Helmling-Cornell, N. A. Holland, J. D. Jones, S. Kandhasamy, S. Karki, M. Kasprzack, K. Kawabe, N. Kijbunchoo, P. J. King, J. S. Kissel, Rahul Kumar, M. Landry, B. B. Lane, B. Lantz, M. Laxen, Y. K. Lecoeuche, J. Leviton, J. Liu, M. Lormand, A. P. Lundgren, R. Macas, M. MacInnis, D. M. Macleod, S. Márka, Z. Márka, D. V. Martynov, K. Mason, T. J. Massinger, F. Matichard, N. Mavalvala, R. McCarthy, D. E. McClelland, S. McCormick, L. McCuller, J. McIver, T. McRae, G. Mendell, K. Merfeld, E. L. Merilh, F. Meylahn, T. Mistry, R. Mittleman, G. Moreno, C. M. Mow-Lowry, S. Mozzon, A. Mullavey, T. J. N. Nelson, P. Nguyen, L. K. Nuttall, J. Oberling, Richard J. Oram, B. O'Reilly, C. Osthelder, D. J. Ottaway, H. Overmier, J. R. Palamos, W. Parker, E. Payne, A. Pele, R. Penhorwood, C. J. Perez, M. Pirello, H. Radkins, K. E. Ramirez, J. W. Richardson, K. Riles, N. A. Robertson, J. G. Rollins, C. L. Romel, J. H. Romie, M. P. Ross, K. Ryan, T. Sadecki, E. J. Sanchez, L. E. Sanchez, T. R. Saravanan, R. L. Savage, D. Schaetzl, R. Schnabel, R. M. S. Schofield, E. Schwartz, D. Sellers, T. Shaffer, D. Sigg, B. J. J. Slagmolen, J. R. Smith, S. Soni, B. Sorazu, A. P. Spencer, K. A. Strain, L. Sun, M. J. Szczepańczyk, M. Thomas, P. Thomas, K. A. Thorne, K. Toland, C. I. Torrie, G. Traylor, M. Tse, A. L. Urban, G. Vajente, G. Valdes, D. C. Vander-Hyde, P. J. Veitch, K. Venkateswara, G. Venugopalan, A. D. Viets, T. Vo, C. Vorvick, M. Wade,

R. L. Ward, J. Warner, B. Weaver, R. Weiss, C. Whittle, B. Willke, C. C. Wipf, L. Xiao, H. Yamamoto, Hang Yu, Haocun Yu, L. Zhang, M. E. Zucker, and J. Zweizig. Sensitivity and performance of the advanced ligo detectors in the third observing run. *Phys. Rev. D*, 102:062003, Sep 2020. [Cited on page 3.]

[11] Markus Aspelmeyer, Pierre Meystre, and Keith Schwab. Quantum optomechanics. *Physics Today*, 65(7):29–35, 2021/05/02 2012. [Cited on pages 3 and 67.]

[12] Nancy Aggarwal, Torrey J. Cullen, Jonathan Cripe, Garrett D. Cole, Robert Lanza, Adam Libson, David Follman, Paula Heu, Thomas Corbitt, and Nergis Mavalvala. Room-temperature optomechanical squeezing. *Nature Physics*, 16(7):784–788, 2020. [Cited on pages 4 and 111.]

[13] T Akutsu, M Ando, K Arai, K Arai, Y Arai, S Araki, A Araya, N Aritomi, Y Aso, S Bae, Y Bae, L Baiotti, R Bajpai, M A Barton, K Cannon, E Capocasa, M Chan, C S Chen, K Chen, Y Chen, H Chu, Y-K Chu, K Doi, S Eguchi, Y Enomoto, R Flaminio, Y Fujii, M Fukunaga, M Fukushima, G-G Ge, A Hagiwara, S Haino, K Hasegawa, H Hayakawa, K Hayama, Y Himemoto, Y Hiranuma, N Hirata, E Hirose, Z Hong, B H Hsieh, G-Z Huang, P-W Huang, Y Huang, B Ikenoue, S Imam, K Inayoshi, Y Inoue, K Ioka, Y Itoh, K Izumi, K Jung, P Jung, T Kajita, M Kamiizumi, S Kanbara, N Kanda, G Kang, K Kawaguchi, N Kawai, T Kawasaki, C Kim, J C Kim, W S Kim, Y-M Kim, N Kimura, N Kita, H Kitazawa, Y Kojima, K Kokeyama, K Komori, A K H Kong, K Kotake, C Kozakai, R Kozu, R Kumar, J Kume, C Kuo, H-S Kuo, S Kuroyanagi, K Kusayanagi, K Kwak, H K Lee, H W Lee, R Lee, M Leonardi, L C-C Lin, C-Y Lin, F-L Lin, G C Liu, L-W Luo, M Marchio, Y Michimura, N Mio, O Miyakawa, A Miyamoto, Y Miyazaki, K Miyo, S Miyoki, S Morisaki, Y Moriwaki, M Musha, K Nagano, S Nagano, K Nakamura, H Nakano, M Nakano, R Nakashima, T Narikawa, R Negishi, W-T Ni, A Nishizawa, Y Obuchi, W Ogaki, J J Oh, S H Oh, M Ohashi, N Ohishi, M Ohkawa, N Ohmae, K Okutomi, K Oohara, C P Ooi, S Oshino, K-C Pan, H Pang, J Park, F E Peña Arellano, I Pinto, N Sago, S Saito, Y Saito, K Sakai, Y Sakai, Y Sakuno, S Sato, T Sato, T Sawada, T Sekiguchi, Y Sekiguchi, S Shibagaki, R Shimizu, T Shimoda, K Shimode, H Shinkai, T Shishido, A Shoda, K Somiya, E J Son, H Sotani, R Sugimoto, T Suzuki, T Suzuki, H Tagoshi, H Takahashi, R Takahashi, A Takamori, S Takano, H Takeda, M Takeda, H Tanaka, K Tanaka, K Tanaka, T Tanaka, T Tanaka, S Tanioka, E N Tapia San Martin, D Tatsumi, S Telada, T Tomaru, Y Tomigami, T Tomura, F Travasso, L Trozzo, T Tsang, K Tsubono, S Tsuchida, T Tsuzuki, D Tuyenbayev, N Uchikata, T Uchiyama, A Ueda, T Uehara, K Ueno, G Ueshima, F Uraguchi, T Ushiba, M H P M van Putten, H Vocca, J Wang, C Wu, H Wu, S Wu, W-R Xu, T Yamada, K Yamamoto, K Yamamoto, T Yamamoto, K Yokogawa, J Yokoyama, T Yokozawa, T Yoshioka, H Yuzurihara, S Zeidler, Y Zhao, and Z-H Zhu. An arm length stabilization system for

KAGRA and future gravitational-wave detectors. *Classical and Quantum Gravity*, 37(3):035004, jan 2020. [Cited on pages 6 and 8.]

[14] A Staley, D Martynov, R Abbott, R X Adhikari, K Arai, S Ballmer, L Barsotti, A F Brooks, R T DeRosa, S Dwyer, A Effler, M Evans, P Fritschel, V V Frolov, C Gray, C J Guido, R Gustafson, M Heintze, D Hoak, K Izumi, K Kawabe, E J King, J S Kissel, K Kokeyama, M Landry, D E McClelland, J Miller, A Mullavey, B O'Reilly, J G Rollins, J R Sanders, R M S Schofield, D Sigg, B J J Slagmolen, N D Smith-Lefebvre, G Vajente, R L Ward, and C Wipf. Achieving resonance in the advanced LIGO gravitational-wave interferometer. *Classical and Quantum Gravity*, 31(24):245010, nov 2014. [Not cited.]

[15] Kiwamu Izumi, Koji Arai, Bryan Barr, Joseph Betzwieser, Aidan Brooks, Katrin Dahl, Suresh Doravari, Jennifer C. Driggers, W. Zach Korth, Haixing Miao, Jameson Rollins, Stephen Vass, David Yeaton-Massey, and Rana X. Adhikari. Multicolor cavity metrology. *J. Opt. Soc. Am. A*, 29(10):2092–2103, Oct 2012. [Cited on pages 6, 7, 14, 17, 19, and 146.]

[16] E. Quintero. New AUX laser measurements. "https://nodus.ligo.caltech.edu:8081/40m/12077", 2016. [Cited on pages 9 and 10.]

[17] G. Venugopalan. Laser swap + optical layout. "https://nodus.ligo.caltech.edu:8081/40m/12083", 2016. [Cited on page 10.]

[18] Masanori Okada, Takahiro Serikawa, James Dannatt, Masaya Kobayashi, Atsushi Sakaguchi, Ian Petersen, and Akira Furusawa. Extending the piezoelectric transducer bandwidth of an optical interferometer by suppressing resonance using a high dimensional iir filter implemented on an fpga. *Review of Scientific Instruments*, 91(5):055102, 2020. [Cited on page 10.]

[19] Hewlett Packard. Phase noise characterization of microwave oscillators. "https://www.keysight.com/upload/cmc_upload/All/5952-8286E.pdf", 1985. [Cited on page 14.]

[20] Times Microwave Systems. LMR 195 series datasheet. LIGO Technical Document T1000276, Available at https://dcc.ligo.org/T1000276/public (2010). [Cited on page 14.]

[21] Wanser K. H. Fundamental phase noise limit in optical fibres due to temperature fluctuations. *Electron. Lett.*, 28:53, 1992. [Cited on pages 17 and 88.]

[22] Jing Dong, Junchao Huang, Tang Li, and Liang Liu. Observation of fundamental thermal noise in optical fibers down to infrasonic frequencies. *Applied Physics Letters*, 108(2):021108, 2016. [Cited on pages 17 and 88.]

[23] Dick Gustafson, Ewan Douglas, Peter Fritschel, and Sam Waldman. Fiber Phase Noise Measurements at LHO. [Cited on page 17.]

[24] G. Venugopalan. DFD electronics checkout. "https://nodus.ligo.caltech.edu:8081/40m/14981", 2019. [Cited on page 21.]

[25] Alexa N Staley. *Locking the Advanced LIGO Gravitational Wave Detector: with a focus on the Arm Length Stabilization Technique*. PhD thesis, Columbia University, 2015. [Cited on pages 22 and 23.]

[26] D. Sigg. Out of loop als comm frequency measurement - take two. [Cited on pages 22 and 23.]

[27] Denis Martynov. *Lock Acquisition and Sensitivity Analysis of Advanced LIGO Interferometers*. PhD thesis, California Institute of Technology, California Institute of Technology, May 2015. See section 8.3.4, in which the OMC reflectivity is measured. [Cited on pages 22 and 124.]

[28] Dana Z. Anderson. Alignment of resonant optical cavities. *Appl. Opt.*, 23(17):2944–2949, Sep 1984. [Cited on pages 26 and 92.]

[29] Adrian Ottewill Bruce Allen, Wensheng Hua. Automatic cross-talk removal from multi-channel data. *arXiv:gr-qc/9909083*, 1999. [Cited on page 31.]

[30] Rana Adhikari. Barry controls 'air puck' instead of 'vopo style' breadboard. [Cited on page 31.]

[31] P. King R. Abbott. (infrared) pre-stabilized laser (PSL) final design. Technical report, LIGO Laboratory, 1999. [Cited on pages 33 and 194.]

[32] Betsy Weaver Janeen Romie. Small optics suspension (sos) assembly. [Cited on page 33.]

[33] Jennifer C. Driggers, Matthew Evans, Keenan Pepper, and Rana Adhikari. Active noise cancellation in a suspended interferometer. *Review of Scientific Instruments*, 83(2):024501, 2012. [Cited on page 34.]

[34] Tobin Thomas Fricke. *Homodyne Detection for Laser-Interferometric Gravitational Wave Detectors*. PhD thesis, Louisiana State University and Agricultural and Mechanical College, 2011. Section 3.2. [Cited on pages 37, 83, and 88.]

[35] Kaitlin Gushwa. Ni-plated smco magnet procurement (internal ligo document). [Cited on page 39.]

[36] Gautam Venugopalan. Dac noise estimate. [Cited on page 39.]

[37] Gautam Venugopalan. Seismic noise, dac noise, and coil driver electronics noise. [Not cited.]

[38] Gautam Venugopalan. De-whitening. [Cited on page 39.]

[39] Joseph Giaime, Partha Saha, David Shoemaker, and Lisa Sievers. A passive vibration isolation stack for ligo: Design, modeling, and testing. *Review of Scientific Instruments*, 67(1):208–214, 1996. [Cited on page 41.]

[40] M. Evans, S. Ballmer, M. Fejer, P. Fritschel, G. Harry, and G. Ogin. Thermo-optic noise in coated mirrors for high-precision optical measurements. *Phys. Rev. D*, 78:102003, Nov 2008. [Cited on page 41.]

[41] Ting Hong, Huan Yang, Eric K. Gustafson, Rana X. Adhikari, and Yanbei Chen. Brownian thermal noise in multilayer coated mirrors. *Phys. Rev. D*, 87:082001, Apr 2013. [Cited on pages 41 and 125.]

[42] Stanley E. Whitcomb Michael E. Zucker. Measurement of optical path fluctuations due to residual gas in the ligo 40m interferometer. In *Proceedings of the Seventh Marcel Grossman Meeting on General Relativity*. LIGO Laboratory, World Scientific Publishing Co., Singapore, 1434-1436 (1996), 1994. [Cited on page 42.]

[43] Koji Arai. *Robust extraction of control signals for power-recycled interferometric gravitational-wave detectors*. PhD thesis, University of Tokyo, 2001. [Cited on pages 44 and 214.]

[44] Jennifer C. Driggers. Length feedforward calculations (ligo internal document). [Cited on page 56.]

[45] Rana Adhikari, Gabriela Gonz lez, Michael Landry, and Brian O Reilly (for the LIGO Scient Collaboration). Calibration of the LIGO detectors for the first LIGO science run. *Classical and Quantum Gravity*, 20(17):S903–S914, aug 2003. [Cited on page 56.]

[46] Katherine Laird Dooley. *Design and performance of high laser power interferometers for gravitational-wave detection*. PhD thesis, University of Florida, 2011. [Cited on page 58.]

[47] Haocun Yu, L. McCuller, M. Tse, N. Kijbunchoo, L. Barsotti, N. Mavalvala, J. Betzwieser, C. D. Blair, S. E. Dwyer, A. Effler, M. Evans, A. Fernandez-Galiana, P. Fritschel, V. V. Frolov, F. Matichard, D. E. McClelland, T. McRae, A. Mullavey, D. Sigg, B. J. J. Slagmolen, C. Whittle, A. Buikema, Y. Chen, T. R. Corbitt, R. Schnabel, R. Abbott, C. Adams, R. X. Adhikari, A. Ananyeva, S. Appert, K. Arai, J. S. Areeda, Y. Asali, S. M. Aston, C. Austin, A. M. Baer, M. Ball, S. W. Ballmer, S. Banagiri, D. Barker, J. Bartlett, B. K. Berger, D. Bhattacharjee, G. Billingsley, S. Biscans, R. M. Blair, N. Bode, P. Booker, R. Bork, A. Bramley, A. F. Brooks, D. D. Brown, C. Cahillane, K. C. Cannon, X. Chen, A. A. Ciobanu, F. Clara, S. J. Cooper, K. R. Corley, S. T. Countryman, P. B. Covas, D. C. Coyne, L. E. H. Datrier, D. Davis, C. Di Fronzo, K. L. Dooley, J. C. Driggers, P. Dupej, T. Etzel, T. M. Evans, J. Feicht, P. Fulda, M. Fyffe, J. A. Giaime, K. D. Giardina, P. Godwin, E. Goetz, S. Gras, C. Gray, R. Gray, A. C. Green, Anchal Gupta, E. K. Gustafson, R. Gustafson, J. Hanks,

J. Hanson, T. Hardwick, R. K. Hasskew, M. C. Heintze, A. F. Helmling-Cornell, N. A. Holland, J. D. Jones, S. Kandhasamy, S. Karki, M. Kasprzack, K. Kawabe, P. J. King, J. S. Kissel, Rahul Kumar, M. Landry, B. B. Lane, B. Lantz, M. Laxen, Y. K. Lecoeuche, J. Leviton, J. Liu, M. Lormand, A. P. Lundgren, R. Macas, M. MacInnis, D. M. Macleod, G. L. Mansell, S. Márka, Z. Márka, D. V. Martynov, K. Mason, T. J. Massinger, R. McCarthy, S. McCormick, J. McIver, G. Mendell, K. Merfeld, E. L. Merilh, F. Meylahn, T. Mistry, R. Mittleman, G. Moreno, C. M. Mow-Lowry, S. Mozzon, T. J. N. Nelson, P. Nguyen, L. K. Nuttall, J. Oberling, Richard J. Oram, C. Osthelder, D. J. Ottaway, H. Overmier, J. R. Palamos, W. Parker, E. Payne, A. Pele, C. J. Perez, M. Pirello, H. Radkins, K. E. Ramirez, J. W. Richardson, K. Riles, N. A. Robertson, J. G. Rollins, C. L. Romel, J. H. Romie, M. P. Ross, K. Ryan, T. Sadecki, E. J. Sanchez, L. E. Sanchez, T. R. Saravanan, R. L. Savage, D. Schaetzl, R. M. S. Schofield, E. Schwartz, D. Sellers, T. Shaffer, J. R. Smith, S. Soni, B. Sorazu, A. P. Spencer, K. A. Strain, L. Sun, M. J. Szczepańczyk, M. Thomas, P. Thomas, K. A. Thorne, K. Toland, C. I. Torrie, G. Traylor, A. L. Urban, G. Vajente, G. Valdes, D. C. Vander-Hyde, P. J. Veitch, K. Venkateswara, G. Venugopalan, A. D. Viets, T. Vo, C. Vorvick, M. Wade, R. L. Ward, J. Warner, B. Weaver, R. Weiss, B. Willke, C. C. Wipf, L. Xiao, H. Yamamoto, Hang Yu, L. Zhang, M. E. Zucker, J. Zweizig, and members of the LIGO Scientific Collaboration. Quantum correlations between light and the kilogram-mass mirrors of ligo. *Nature*, 583(7814):43–47, 2020. [Cited on pages 59, 67, 70, 77, 79, and 111.]

[48] Koji Arai. ASC singularity. [Cited on page 61.]

[49] Matthew J. Evans, Lisa Barsotti, Jan Harms, Patrick Kwee, and H Miao. Realistic filter cavities for advanced gravitational wave detectors. *Physical Review D*, 88, 05 2013. [Cited on pages 63, 81, and 133.]

[50] Kaitlin E. Gushwa and Calum I. Torrie. Coming clean: understanding and mitigating optical contamination and laser induced damage in advanced LIGO. In *Proc. SPIE*, volume 9237, 10 2014. [Cited on pages 62 and 222.]

[51] Kiwamu Izumi and Daniel Sigg. Advanced LIGO: length sensing and control in a dual recycled interferometric gravitational wave antenna. *Classical and Quantum Gravity*, 34(1):015001, dec 2016. [Cited on pages 63 and 208.]

[52] Carlton M. Caves. Quantum-mechanical noise in an interferometer. *Phys. Rev. D*, 23:1693–1708, Apr 1981. [Cited on pages 67, 110, and 111.]

[53] H. J. Kimble, Yuri Levin, Andrey B. Matsko, Kip S. Thorne, and Sergey P. Vyatchanin. Conversion of conventional gravitational-wave interferometers into quantum nondemolition interferometers by modifying their input and/or output optics. *Phys. Rev. D*, 65:022002, Dec 2001. [Cited on pages 68, 110, 113, 114, 115, 116, 118, and 121.]

[54] Alessandra Buonanno and Yanbei Chen. Quantum noise in second generation, signal-recycled laser interferometric gravitational-wave detectors. *Phys. Rev. D*, 64:042006, Jul 2001. [Cited on pages 67, 68, 70, 71, 73, 85, 118, and 121.]

[55] Thomas Corbitt, Yanbei Chen, Farid Khalili, David Ottaway, Sergey Vyatchanin, Stan Whitcomb, and Nergis Mavalvala. Squeezed-state source using radiation-pressure-induced rigidity. *Phys. Rev. A*, 73:023801, Feb 2006. [Cited on page 67.]

[56] Thomas Randall Corbitt. *Quantum noise and radiation pressure effects in high power optical interferometers*. PhD thesis, Massachusetts Institute of Technology, 2008. [Not cited.]

[57] Christopher Wipf. *Toward Quantum Opto-Mechanics in a Gram-Scale Suspended Mirror Interferometer*. PhD thesis, Massachusetts Institute of Technology, February 2013. [Cited on pages 67 and 128.]

[58] Nancy Aggarwal. *A room temperature optomechanical squeezer*. PhD thesis, Massachusetts Institute of Technology, February 2019. [Cited on pages 67 and 127.]

[59] Jonathan Cripe, Nancy Aggarwal, Robert Lanza, Adam Libson, Robinjeet Singh, Paula Heu, David Follman, Garrett D Cole, Nergis Mavalvala, and Thomas Corbitt. Measurement of quantum back action in the audio band at room temperature. *Nature*, 568(7752):364–367, 2019. [Cited on pages 67, 111, and 127.]

[60] Kevin Kuns. *Future Networks of Gravitational Wave Detectors: Quantum Noise and Space Detectors*. PhD thesis, University of California, Santa Barbara, March 2019. [Cited on pages 67, 70, and 77.]

[61] Thomas Corbitt, Yanbei Chen, and Nergis Mavalvala. Mathematical framework for simulation of quantum fields in complex interferometers using the two-photon formalism. *Phys. Rev. A*, 72:013818, Jul 2005. [Cited on pages 68, 131, and 207.]

[62] Carlton M. Caves and Bonny L. Schumaker. New formalism for two-photon quantum optics. i. quadrature phases and squeezed states. *Phys. Rev. A*, 31:3068–3092, May 1985. [Cited on pages 68, 84, 114, and 207.]

[63] Bonny L. Schumaker and Carlton M. Caves. New formalism for two-photon quantum optics. ii. mathematical foundation and compact notation. *Phys. Rev. A*, 31:3093–3111, May 1985. [Cited on pages 68, 84, 114, and 207.]

[64] P. Kwee, J. Miller, T. Isogai, L. Barsotti, and M. Evans. Decoherence and degradation of squeezed states in quantum filter cavities. *Phys. Rev. D*, 90:062006, Sep 2014. [Cited on page 69.]

[65] M. Tse, Haocun Yu, N. Kijbunchoo, A. Fernandez-Galiana, P. Dupej, L. Barsotti, C. D. Blair, D. D. Brown, S. E. Dwyer, A. Effler, M. Evans, P. Fritschel, V. V. Frolov, A. C. Green, G. L. Mansell, F. Matichard, N. Mavalvala, D. E. McClelland, L. McCuller, T. McRae, J. Miller, A. Mullavey, E. Oelker, I. Y. Phinney, D. Sigg, B. J. J. Slagmolen, T. Vo, R. L. Ward, C. Whittle, R. Abbott, C. Adams, R. X. Adhikari, A. Ananyeva, S. Appert, K. Arai, J. S. Areeda, Y. Asali, S. M. Aston, C. Austin, A. M. Baer, M. Ball, S. W. Ballmer, S. Banagiri, D. Barker, J. Bartlett, B. K. Berger, J. Betzwieser, D. Bhattacharjee, G. Billingsley, S. Biscans, R. M. Blair, N. Bode, P. Booker, R. Bork, A. Bramley, A. F. Brooks, A. Buikema, C. Cahillane, K. C. Cannon, X. Chen, A. A. Ciobanu, F. Clara, S. J. Cooper, K. R. Corley, S. T. Countryman, P. B. Covas, D. C. Coyne, L. E. H. Datrier, D. Davis, C. Di Fronzo, J. C. Driggers, T. Etzel, T. M. Evans, J. Feicht, P. Fulda, M. Fyffe, J. A. Giaime, K. D. Giardina, P. Godwin, E. Goetz, S. Gras, C. Gray, R. Gray, Anchal Gupta, E. K. Gustafson, R. Gustafson, J. Hanks, J. Hanson, T. Hardwick, R. K. Hasskew, M. C. Heintze, A. F. Helmling-Cornell, N. A. Holland, J. D. Jones, S. Kandhasamy, S. Karki, M. Kasprzack, K. Kawabe, P. J. King, J. S. Kissel, Rahul Kumar, M. Landry, B. B. Lane, B. Lantz, M. Laxen, Y. K. Lecoeuche, J. Leviton, J. Liu, M. Lormand, A. P. Lundgren, R. Macas, M. MacInnis, D. M. Macleod, S. Márka, Z. Márka, D. V. Martynov, K. Mason, T. J. Massinger, R. McCarthy, S. McCormick, J. McIver, G. Mendell, K. Merfeld, E. L. Merilh, F. Meylahn, T. Mistry, R. Mittleman, G. Moreno, C. M. Mow-Lowry, S. Mozzon, T. J. N. Nelson, P. Nguyen, L. K. Nuttall, J. Oberling, R. J. Oram, B. O'Reilly, C. Osthelder, D. J. Ottaway, H. Overmier, J. R. Palamos, W. Parker, E. Payne, A. Pele, C. J. Perez, M. Pirello, H. Radkins, K. E. Ramirez, J. W. Richardson, K. Riles, N. A. Robertson, J. G. Rollins, C. L. Romel, J. H. Romie, M. P. Ross, K. Ryan, T. Sadecki, E. J. Sanchez, L. E. Sanchez, T. R. Saravanan, R. L. Savage, D. Schaetzl, R. Schnabel, R. M. S. Schofield, E. Schwartz, D. Sellers, T. J. Shaffer, J. R. Smith, S. Soni, B. Sorazu, A. P. Spencer, K. A. Strain, L. Sun, M. J. Szczepańczyk, M. Thomas, P. Thomas, K. A. Thorne, K. Toland, C. I. Torrie, G. Traylor, A. L. Urban, G. Vajente, G. Valdes, D. C. Vander-Hyde, P. J. Veitch, K. Venkateswara, G. Venugopalan, A. D. Viets, C. Vorvick, M. Wade, J. Warner, B. Weaver, R. Weiss, B. Willke, C. C. Wipf, L. Xiao, H. Yamamoto, M. J. Yap, Hang Yu, L. Zhang, M. E. Zucker, and J. Zweizig. Quantum-enhanced advanced ligo detectors in the era of gravitational-wave astronomy. *Phys. Rev. Lett.*, 123:231107, Dec 2019. [Cited on pages 69 and 110.]

[66] Fabian Thies, Nina Bode, Patrick Oppermann, Maik Frede, Bastian Schulz, and Benno Willke. Nd:yvo4 high-power master oscillator power amplifier laser system for second-generation gravitational wave detectors. *Opt. Lett.*, 44(3):719–722, Feb 2019. [Cited on page 71.]

[67] Matthew Evans, Slawek Gras, Peter Fritschel, John Miller, Lisa Barsotti, Denis Martynov, Aidan Brooks, Dennis Coyne, Rich Abbott, Rana X. Ad-

hikari, Koji Arai, Rolf Bork, Bill Kells, Jameson Rollins, Nicolas Smith-Lefebvre, Gabriele Vajente, Hiroaki Yamamoto, Carl Adams, Stuart Aston, Joseph Betzweiser, Valera Frolov, Adam Mullavey, Arnaud Pele, Janeen Romie, Michael Thomas, Keith Thorne, Sheila Dwyer, Kiwamu Izumi, Keita Kawabe, Daniel Sigg, Ryan Derosa, Anamaria Effler, Keiko Kokeyama, Stefan Ballmer, Thomas J. Massinger, Alexa Staley, Matthew Heinze, Chris Mueller, Hartmut Grote, Robert Ward, Eleanor King, David Blair, Li Ju, and Chunnong Zhao. Observation of parametric instability in advanced ligo. *Phys. Rev. Lett.*, 114:161102, Apr 2015. [Cited on page 75.]

[68] Rana X Adhikari, Odylio Aguiar, Koji Arai, Bryan Barr, Riccardo Bassiri, Garilynn Billingsley, Ross Birney, David Blair, Joseph Briggs, Aidan F Brooks, et al. A cryogenic silicon interferometer for gravitational-wave detection. *arXiv preprint arXiv:2001.11173*, 2020. [Cited on pages 81, 111, 113, and 129.]

[69] Gautam Venugopalan, Jonathan Richardson, Yehonathan Drori, Hang Yu, Shruti Maliakal, Aaron Markowitz, Koji Arai, and Rana Adhikari. Design requirement document for the balanced homodyne readout of the 40m prototype interferometer, 2019. [Cited on pages 82 and 87.]

[70] Alessandra Buonanno, Yanbei Chen, and Nergis Mavalvala. Quantum noise in laser-interferometer gravitational-wave detectors with a heterodyne readout scheme. *Phys. Rev. D*, 67:122005, Jun 2003. [Cited on page 84.]

[71] Lee McCuller. Lsc final design review revisit, srcl noise projections into darm. [Cited on page 84.]

[72] Peter Fritschel, Matthew Evans, and Valery Frolov. Balanced homodyne readout for quantum limited gravitational wave detectors. *Opt. Express*, 22(4):4224–4234, Feb 2014. [Cited on page 84.]

[73] Stefan L. Danilishin and Farid Ya. Khalili. Quantum measurement theory in gravitational-wave detectors. *Living Reviews in Relativity*, 15(1):5, 2012. [Cited on pages 84 and 207.]

[74] Sebastian Steinlechner, Bryan W. Barr, Angus S. Bell, Stefan L. Danilishin, Andreas Gläfke, Christian Gräf, Jan-Simon Hennig, E. Alasdair Houston, Sabina H. Huttner, Sean S. Leavey, Daniela Pascucci, Borja Sorazu, Andrew Spencer, Kenneth A. Strain, Jennifer Wright, and Stefan Hild. Local-oscillator noise coupling in balanced homodyne readout for advanced gravitational wave detectors. *Phys. Rev. D*, 92:072009, Oct 2015. [Cited on page 85.]

[75] Koji Arai. Effect of the end mirror curvature error to contrast defect of a fabry-pérot based michelson interferometer. [Cited on pages 92 and 93.]

[76] Koji Arai, Sam Barnum, Peter Fritschel, Jeffrey Lewis, and Sam Waldman. Output mode cleaner (OMC) design. LIGO Technical Document T1000276,

Available at https://dcc.ligo.org/T1000276/public (2010). [Cited on pages 95 and 99.]

[77] LIGO Livingston Observatory logbook, OMC backscatter. https://alog.ligo-la.caltech.edu/aLOG/index.php?callRep=13607. Accessed: 2019-04-25. [Cited on page 101.]

[78] Koji Arai. OMC thermal noise calculation. [Cited on page 102.]

[79] Laser Components. Infrared components catalog. [Cited on page 103.]

[80] Gautam Venugopalan. 40m in-air BHD DCPD satellite amplifier. [Cited on pages 103 and 105.]

[81] Teng Zhang. *Advanced techniques for future generation gravitational wave detectors*. PhD thesis, University of Glasgow, July 2019. [Cited on page 105.]

[82] Yuntao Bai, Gautam Venugopalan, Kevin Kuns, Christopher Wipf, Aaron Markowitz, Andrew R. Wade, Yanbei Chen, and Rana X. Adhikari. Phase-sensitive optomechanical amplifier for quantum noise reduction in laser interferometers. *Phys. Rev. A*, 102:023507, Aug 2020. [Cited on page 110.]

[83] Henning Vahlbruch, Alexander Khalaidovski, Nico Lastzka, Christian Gräf, Karsten Danzmann, and Roman Schnabel. The GEO 600 squeezed light source. *Classical and Quantum Gravity*, 27(8):084027, 2010. [Cited on page 110.]

[84] J. Abadie, B. P. Abbott, R. Abbott, T. D. Abbott, M. Abernathy, C. Adams, R. Adhikari, et al. A gravitational wave observatory operating beyond the quantum shot-noise limit. *Nature Physics*, 7(12):962–965, 2011. [Cited on page 110.]

[85] Junaid Aasi, J Abadie, BP Abbott, Richard Abbott, TD Abbott, MR Abernathy, Carl Adams, Thomas Adams, Paolo Addesso, RX Adhikari, et al. Enhanced sensitivity of the ligo gravitational wave detector by using squeezed states of light. *Nature Photonics*, 7(8):613, 2013. [Cited on page 110.]

[86] E Knyazev, K Yu Spasibko, Maria V Chekhova, and F Ya Khalili. Quantum tomography enhanced through parametric amplification. *New Journal of Physics*, 20(1):013005, 2018. [Cited on page 111.]

[87] Eugene Knyazev, Farid Ya Khalili, and Maria V Chekhova. Overcoming inefficient detection in sub-shot-noise absorption measurement and imaging. *Optics express*, 27(6):7868–7885, 2019. [Cited on page 111.]

[88] R. X. Adhikari, P. Ajith, Y. Chen, J. A. Clark, V. Dergachev, N. V. Fotopoulos, S. E. Gossan, I. Mand el, M. Okounkova, V. Raymond, and J. S. Read. Astrophysical science metrics for next-generation gravitational-wave detectors. *Classical and Quantum Gravity*, 36(24):245010, December 2019. [Cited on pages 111 and 139.]

[89] Koji Arai. Ofi pre-/post adjustment performance test. [Cited on page 113.]

[90] Koji Arai. Advanced ligo output mode cleaner: Design, fabrication and testing. [Cited on page 113.]

[91] Valery Frolov. Darm optical gain and losses. [Cited on page 113.]

[92] Carlton M. Caves. Quantum limits on noise in linear amplifiers. *Phys. Rev. D*, 26:1817–1839, Oct 1982. [Cited on pages 113 and 114.]

[93] Thierry Botter, Daniel W. C. Brooks, Nathan Brahms, Sydney Schreppler, and Dan M. Stamper-Kurn. Linear amplifier model for optomechanical systems. *Phys. Rev. A*, 85:013812, Jan 2012. [Cited on page 114.]

[94] J. Steinlechner, I. W. Martin, A. S. Bell, J. Hough, M. Fletcher, P. G. Murray, R. Robie, S. Rowan, and R. Schnabel. Silicon-based optical mirror coatings for ultrahigh precision metrology and sensing. *Phys. Rev. Lett.*, 120:263602, Jun 2018. [Cited on pages 120 and 125.]

[95] T. Isogai, J. Miller, P. Kwee, L. Barsotti, and M. Evans. Loss in long-storage-time optical cavities. *Opt. Express*, 21(24):30114–30125, Dec 2013. [Cited on page 123.]

[96] Tomoki Isogai. *Applications of long storage time optical cavities*. PhD thesis, Massachusetts Institute of Technology, Massachusetts Institute of Technology, February 2016. See section 2.3.1. [Cited on page 123.]

[97] Simon Zeidler, Tomotada Akutsu, Yasuo Torii, Eiichi Hirose, Yoichi Aso, and Raffaele Flaminio. Calculation method for light scattering caused by multilayer coated mirrors in gravitational wave detectors. *Opt. Express*, 25(5):4741–4760, Mar 2017. [Cited on page 123.]

[98] Henning Vahlbruch, Dennis Wilken, Moritz Mehmet, and Benno Willke. Laser power stabilization beyond the shot noise limit using squeezed light. *Phys. Rev. Lett.*, 121:173601, Oct 2018. [Cited on page 124.]

[99] Patrick Kwee, Benno Willke, and Karsten Danzmann. Laser power stabilization using optical ac coupling and its quantum and technical limits. *Appl. Opt.*, 48(28):5423–5431, Oct 2009. [Cited on page 124.]

[100] D. R. Southworth, R. A. Barton, S. S. Verbridge, B. Ilic, A. D. Fefferman, H. G. Craighead, and J. M. Parpia. Stress and silicon nitride: A crack in the universal dissipation of glasses. *Phys. Rev. Lett.*, 102:225503, Jun 2009. [Cited on page 125.]

[101] Gautam Venugopalan, Koji Arai, and Rana X Adhikari. Global optimization of multilayer dielectric coatings for precision measurements. In preparation. [Cited on pages 125 and 137.]

[102] A V Cumming, L Cunningham, G D Hammond, K Haughian, J Hough, S Kroker, I W Martin, R Nawrodt, S Rowan, C Schwarz, and A A van Veggel. Silicon mirror suspensions for gravitational wave detectors. *Classical and Quantum Gravity*, 31(2):025017, Dec 2013. See Eq. 1. [Cited on page 127.]

[103] Herbert B. Callen and Theodore A. Welton. Irreversibility and generalized noise. *Phys. Rev.*, 83:34–40, Jul 1951. [Cited on page 127.]

[104] William Zachary Korth. *Mitigating Noise in Interferometric Gravitational Wave Detectors*. PhD thesis, California Institute of Technology, February 2019. [Cited on page 127.]

[105] Stuart Reid and Iain Martin. Development of mirror coatings for gravitational wave detectors. *Coatings*, 6(4):61, 2016. [Cited on page 130.]

[106] Patricia Purdue and Yanbei Chen. Practical speed meter designs for quantum nondemolition gravitational-wave interferometers. *Physical Review D*, 66(12):122004, 2002. [Cited on page 133.]

[107] Mikhail Korobko, F Ya Khalili, and Roman Schnabel. Engineering the optical spring via intra-cavity optical-parametric amplification. *Physics Letters A*, 382(33):2238–2244, 2018. [Cited on page 135.]

[108] F Ya Khalili and Eugene S Polzik. Overcoming the standard quantum limit in gravitational wave detectors using spin systems with a negative effective mass. *Physical review letters*, 121(3):031101, 2018. [Cited on page 135.]

[109] Particle Swarm, MATLAB Global Optimization Toolbox, R2016b. The MathWorks, Natick, MA, USA. [Cited on pages 137 and 141.]

[110] Pauli Virtanen, Ralf Gommers, Travis E. Oliphant, Matt Haberland, Tyler Reddy, David Cournapeau, Evgeni Burovski, Pearu Peterson, Warren Weckesser, Jonathan Bright, Stéfan J. van der Walt, Matthew Brett, Joshua Wilson, K. Jarrod Millman, Nikolay Mayorov, Andrew R. J. Nelson, Eric Jones, Robert Kern, Eric Larson, C J Carey, İlhan Polat, Yu Feng, Eric W. Moore, Jake VanderPlas, Denis Laxalde, Josef Perktold, Robert Cimrman, Ian Henriksen, E. A. Quintero, Charles R. Harris, Anne M. Archibald, Antônio H. Ribeiro, Fabian Pedregosa, Paul van Mulbregt, and SciPy 1.0 Contributors. SciPy 1.0: Fundamental Algorithms for Scientific Computing in Python. *Nature Methods*, 17:261–272, 2020. [Cited on pages 137, 141, and 142.]

[111] Rainer Storn and Kenneth Price. Differential evolution - a simple and efficient heuristic for global optimization over continuous spaces. *Journal of Global Optimization*, 11:341–359, 01 1997. [Cited on pages 137 and 141.]

[112] S.J. Orfanidis. *Electromagnetic Waves and Antennas*. S.J. Orfanidis, 2016. [Cited on page 138.]

[113] O. Arnon and P. Baumeister. Electric field distribution and the reduction of laser damage in multilayers. *Appl. Opt.*, 19(11):1853–1855, Jun 1980. [Cited on page 139.]

[114] R. Dannenberg. LMA computation of surface E-field acheivable for Advanced LIGO ITM, Dec. 2009. [Cited on page 139.]

[115] John M. Robinson, Eric Oelker, William R. Milner, Wei Zhang, Thomas Legero, Dan G. Matei, Fritz Riehle, Uwe Sterr, and Jun Ye. Crystalline optical cavity at 4 K with thermal-noise-limited instability and ultralow drift. *Optica*, 6(2):240, February 2019. [Cited on page 140.]

[116] Garrett D. Cole, Wei Zhang, Michael J. Martin, Jun Ye, and Markus Aspelmeyer. Tenfold reduction of brownian noise in high-reflectivity optical coatings. *Nature Photonics*, 7:644 EP –, Jul 2013. Article. [Cited on page 140.]

[117] Tara Chalermsongsak, Evan D Hall, Garrett D Cole, David Follman, Frank Seifert, Koji Arai, Eric K Gustafson, Joshua R Smith, Markus Aspelmeyer, and Rana X Adhikari. Coherent cancellation of photothermal noise in GaAs/al0.92ga0.08as bragg mirrors. *Metrologia*, 53(2):860–868, mar 2016. [Cited on page 140.]

[118] D. Foreman-Mackey, D. W. Hogg, D. Lang, and J. Goodman. emcee: The mcmc hammer. *PASP*, 125:306–312, 2013. [Cited on pages 141 and 221.]

[119] Daniel Foreman-Mackey. corner.py: Scatterplot matrices in python. *The Journal of Open Source Software*, 1(2):24, jun 2016. [Cited on pages 141 and 221.]

[120] Adam J. Mullavey, Bram J. J. Slagmolen, John Miller, Matthew Evans, Peter Fritschel, Daniel Sigg, Sam J. Waldman, Daniel A. Shaddock, and David E. McClelland. Arm-length stabilisation for interferometric gravitational-wave detectors using frequency-doubled auxiliary lasers. *Opt. Express*, 20(1):81–89, Jan 2012. [Cited on page 146.]

[121] R. Dannenberg. Advanced LIGO End Test Mass (ETM) Coating Specification. Technical Report E0900068, LIGO Laboratory, California Institute of Technology, Mar. 2009. [Cited on page 146.]

[122] S. Gras, H. Yu, W. Yam, D. Martynov, and M. Evans. Audio-band coating thermal noise measurement for Advanced LIGO with a multimode optical resonator. *Phys. Rev. D*, 95:022001, Jan 2017. [Cited on page 147.]

[123] LIGO Scientific Collaboration. Instrument Science White Paper. Technical report, LIGO Laboratory, California Institute of Technology, Feb. 2015. [Cited on page 149.]

[124] H. Angus Macleod. *Thin-Film Optical Filters*. Series in optics and optoelectronics. CRC Press, Taylor & Francis Group, fourth edition, 2010. [Cited on page 151.]

[125] Fabien Lemarchand. Application of clustering global optimization to thin film design problems. *Opt. Express*, 22(5):5166–5176, Mar 2014. [Not cited.]

[126] Jonathan R. Birge, Franz X. Kärtner, and Omid Nohadani. Improving thin-film manufacturing yield with robust optimization. *Appl. Opt.*, 50(9):C36–C40, Mar 2011. [Not cited.]

[127] Alexander Tikhonravov, Michael Trubetskov, and G W DeBell. Optical coating design approaches based on the needle optimization technique. *Applied optics*, 46:704–10, 03 2007. [Cited on page 151.]

[128] Sawyer D. Campbell, David Sell, Ronald P. Jenkins, Eric B. Whiting, Jonathan A. Fan, and Douglas H. Werner. Review of numerical optimization techniques for meta-device design. *Opt. Mater. Express*, 9(4):1842–1863, Apr 2019. [Cited on page 151.]

[129] Standard Performance Evaluation Corporation. [Cited on page 152.]

[130] G. Venugopalan. PSL NPRO PZT calibration. "https://nodus.ligo.caltech.edu:8081/40m/12925", 2017. [Cited on page 194.]

[131] K. Arai. PMC servo calibration. "https://nodus.ligo.caltech.edu:8081/40m/11780", 2015. [Cited on page 194.]

[132] G. Venugopalan. Modulation depth measurement. "https://nodus.ligo.caltech.edu:8081/40m/15769", 2021. [Cited on page 194.]

[133] G. Venugopalan. Setting modulation frequency and checking IMC offset. "https://nodus.ligo.caltech.edu:8081/40m/15845", 2021. [Cited on page 194.]

[134] G. Venugopalan. IMC ringdown fitting. "https://nodus.ligo.caltech.edu:8081/40m/14328", 2018. [Cited on page 194.]

[135] G. Venugopalan. IMC input beam mode matching. "https://nodus.ligo.caltech.edu:8081/40m/12898", 2017. [Cited on page 194.]

[136] Gautam Venugopalan, Koji Arai, and Rana Adhikari. Specification : 40m dichroic rc folding mirrors. [Cited on page 195.]

[137] Richard. M. Murray Karl Johan Åström. *Feedback Systems - An Introduction for Scientists and Engineers*. Princeton University Press, 2012. [Cited on pages 196, 197, 200, and 203.]

[138] Johan Schoukens Rik Pintelon. *System Identification - A Frequency Domain Approach*. IEEE Press, 2001. [Cited on page 198.]

[139] Jonathan J Carter, Samuel J Cooper, Edward Thrift, Joseph Briggs, Jim Warner, Michael P Ross, and Conor M Mow-Lowry. Particle swarming of sensor correction filters. *Classical and Quantum Gravity*, 37(20):205009, sep 2020. [Cited on page 204.]

[140] Rolf Bork, Jonathan Hanks, David Barker, Joseph Betzwieser, Jameson Rollins, Keith Thorne, and Erik von Reis. advligorts: The advanced ligo real-time digital control and data acquisition system. *SoftwareX*, 13:100619, 2021. [Cited on page 204.]

[141] Martin W. Regehr. *Signal Extraction and Control for an Interferometric Gravitational Wave Detector*. PhD thesis, California Institute of Technology, 1995. [Cited on page 208.]

[142] Daniel David Brown and Andreas Freise. Finesse, May 2014. The software and source code is available at http://www.gwoptics.org/finesse. [Cited on pages 211 and 219.]

[143] Brian J. Meers. Recycling in laser-interferometric gravitational-wave detectors. *Phys. Rev. D*, 38:2317–2326, Oct 1988. [Cited on page 213.]

[144] Jun Mizuno. *Comparison of optical configurations for laser-interferometric gravitational-wave detectors*. PhD thesis, Universität Hannover, 1995. [Cited on page 213.]

[145] L. Schnupp. Talk at a european collaboration meeting on interferometric detection of gravitational waves. Sorrento, 1988. [Cited on page 216.]

[146] K. Arai. Tip-tilt phase maps. "https://nodus.ligo.caltech.edu:8081/40m/8060", 2019. [Cited on page 216.]

[147] Muzammil A. Arain and Guido Mueller. Design of the advanced ligo recycling cavities. *Opt. Express*, 16(14):10018–10032, Jul 2008. [Cited on page 216.]

[148] Koji Arai. On the accumulated round-trip gouy phase shift for a general optical cavity. LIGO Technical Document T1000276, Available at https://dcc.ligo.org/T1300189/public (2013). [Cited on page 218.]

[149] Andri M. Gretarsson, Erika D'Ambrosio, Valery Frolov, Brian O'Reilly, and Peter K. Fritschel. Effects of mode degeneracy in the ligo livingston observatory recycling cavity. *J. Opt. Soc. Am. B*, 24(11):2821–2828, Nov 2007. [Cited on page 218.]

[150] Daniel D. Brown, Philip Jones, Samuel Rowlinson, Sean Leavey, Anna C. Green, Daniel Toyra, and Andreas Freise. Pykat: Python package for modelling precision optical interferometers. *SoftwareX*, 12:100613, 2020. [Cited on page 219.]

[151] Margot Hennig, GariLynn Billingsley, and Liyuan Zhang. First Contact Brush and Pour Application Procedure. [Cited on pages 222 and 224.]

*Appendix A*

# INTERFEROMETER LAYOUT AND PARAMETERS

## A.1 C1 interferometer layout and signal extraction ports

Fig. A.1 shows the optical layout of the C1 interferometer. Several ports at which signals carrying interferometer length and alignment information can be extracted are indicated. The photodetectors used may be grouped into three categories:

### Length sensing

To extract the signals using the PDH technique, the raw photocurrent must be demodulated at some integer multiple of one of the RF frequencies used to apply phase modulation on the input beam to the IFO. For C1, $f_1 \approx 11\,\mathrm{MHz}$ and $f_2 = 5 \times f_1 \approx 55\,\mathrm{MHz}$. In order to maximize SNR, most ports use photodetectors with a custom resonant transimpedance amplifier[1] in favor of broadband designs. These are tuned to read out photocurrent at a specific frequency while notching out other components at which optical signals are present (to avoid saturating the transimpedance electronics, reserving its range for the signal of interest). For example, the "REFL11" photodiode will have a transimpedance amplifier with frequency response tuned to have high gain at 11 MHz, with notches at 22 MHz and 55 MHz. The ratio between the resonant gain and the notch is usually $> 40\,\mathrm{dB}$. At other frequencies like 33 MHz, the expected signal levels are small and the gain at that frequency is already low enough to justify not having the additional complexity of implementing a dedicated notch.

### Angular sensing

Quadrant photodiodes (QPDs) split the beam incident on them onto 4 segmented photoelectric elements (hence the name), allowing resolution of the spatial position of the beam on the detector. These allow reading out signals encoding information about the angular position of various optics in the IFO. Signals may be read out at DC or at RF frequencies, with the former having a simpler sensing chain with fewer

[1] The photocurrent is converted to a voltage by a $Q \approx 5 - 10$ LC network with resonant frequency tuned to the frequency of interest. Separate LC networks implement notches at other frequencies.

pieces of electronics (since no demodulation is necessary), and the latter technique, called wavefront sensing, typically having better noise performance.

#### Power buildup monitors

Photodiodes are also used to monitor the DC (TRX, TRY and POPDC) and RF sideband power buildups (POP22, POP110, AS110) in various optical cavities. These signals are used to infer when the cavity length is such that the PDH signal sensed by one of the length sensing photodiodes is in its linear regime, a technique known as triggering. When trigger signals cross pre-defined thresholds set in the digital control system, servo loops are engaged to keep the cavity length under feedback control. In addition to dedicated power buildup monitoring photodiodes, the length and angle sensing photodiodes also provide a readback of the DC light level incident on them. These are used to normalize the PDH error signals, so that the feedback loop gains can remain unchanged for a range of laser power levels injected into the IFO. In some cases, such normalization can also be used to extend the linear range of the PDH error signal (e.g. Fig 8.1 of [6]).

## A.2 Interferometer parameters

Various optical and mechanical parameters of the C1 interferometer are collected here for easy reference.

### A.2.1 PSL and IOO

These systems are responsible for injecting a stabilized, spatially filtered, laser field with phase-modulation sidebands imprinted[2] to the core IFO. At the time of writing, there is no dedicated Intensity Stabilization Servo (ISS), laser amplifier, or remote power control, all of which are planned for the ongoing upgrade and would come under the PSL subsystem. Table A.1 lists some key parameters.

### A.2.2 Core IFO

Table A.2 lists important parameters for the core interferometer. The polarization used in the entire core IFO is p-pol.

[2]The EOM used is a broadband, free-space, Pockel-Cell, part number NewFocus 4004. A custom, resonant circuit tuned for high gain at the modulation frequencies is used for impedance matching and to realize the desired modulation depths.

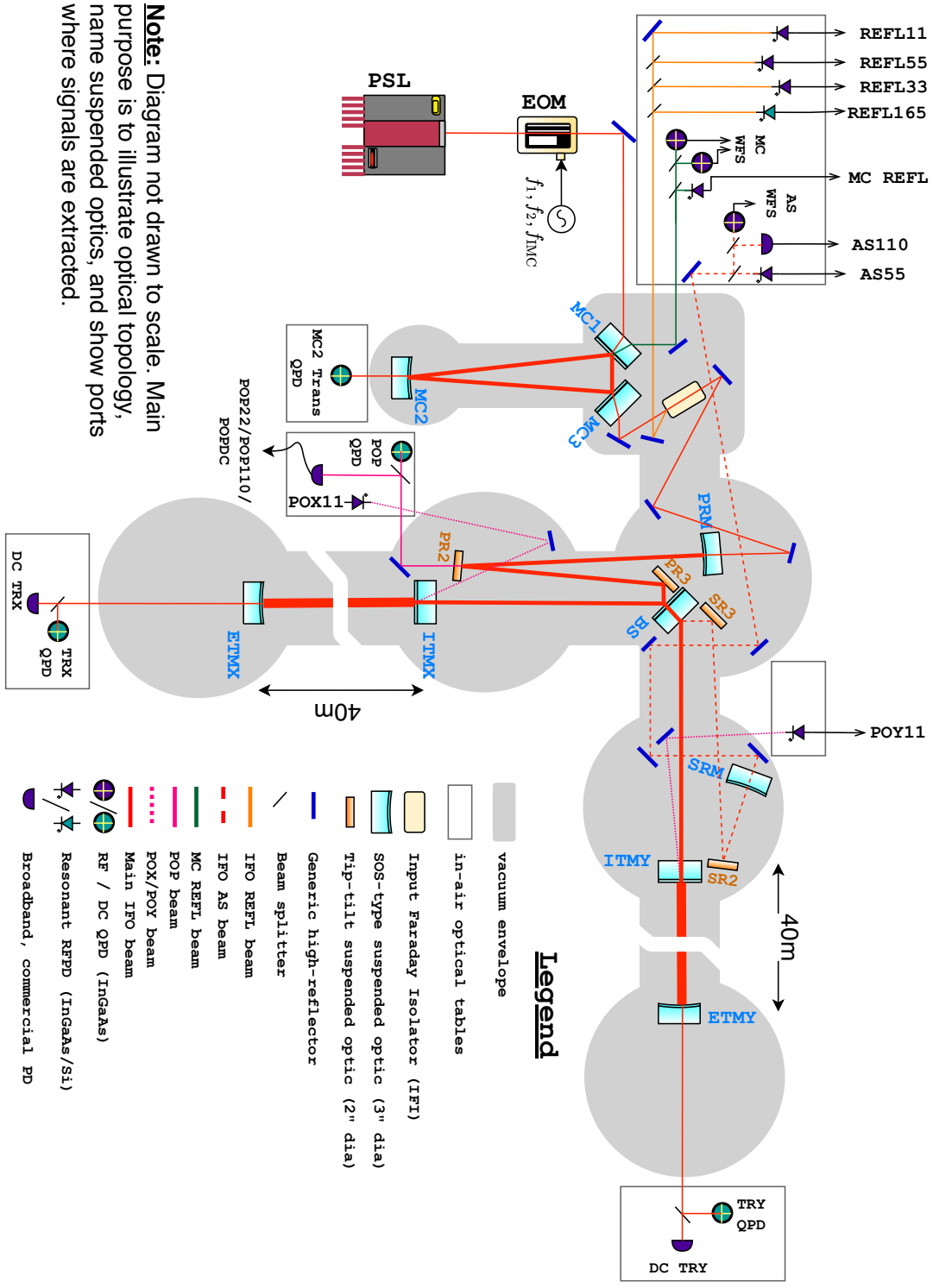


Figure A.1: Schematic layout of the C1 interferometer. This diagram emphasizes the main laser wavelength, and the ALS system is excluded. A schematic diagram of the latter is Fig. 2.1.

| | Parameter | Value (RF readout) | Value (BHD) |
|---|---|---|---|
| PSL | Laser power (into PMC) | 1.3 W | 25 W |
| | Laser wavelength | 1064 nm | 1064 nm |
| | PZT actuator coefficient | 1.47 ± 0.04 MHz [130] | 1.47 ± 0.04 MHz |
| PMC [31] | PZT actuator coefficient | 10.8 ± 0.3 nm/V [131] | 10.8 ± 0.3 nm/V |
| | Linewidth | 975 kHz (spec) | 975 kHz |
| | PDH Modulation frequency | 35.5 MHz | 35.5 MHz |
| | Modulation depth | 60 mrad [132] | 60 mrad |
| | Polarization | p-pol | p-pol |
| | Transmission | 85% | >85% |
| EOM | Half-wave voltage $V_\pi$ | 210 V | 210 V |
| | $\Gamma_1$ @ 11 MHz | 0.18 rad [132] | 0.19 rad |
| | $\Gamma_2$ @ 55 MHz | 0.22 rad [132] | 0.25 rad |
| | $\Gamma_{\mathrm{IMC}}$ @ 29.5 MHz | 0.1 rad [132] | 0.1 rad |
| | Damage threshold | 4 W/mm$^2$ | 4 W/mm$^2$ |
| IMC + IFI | Input coupler transmissivity | 2000 ppm (45°, s-pol) | 2000 ppm (45°, s-pol) |
| | End mirror power transmissivity | 10 ppm (0°, s-pol) | 10 ppm (0°, s-pol) |
| | Input coupler RoC | > 8000 m | > 8000 m |
| | End mirror RoC | 17.87 m | 17.87 m |
| | Round-trip length | 27.091 m [133] | 27.091 m |
| | Round-trip loss | 300 ± 20 ppm [134] | 100 ppm |
| | Linewidth | 7.56 ± 0.02 kHz [134] | 7.2 kHz |
| | Finesse | ≈ 1450 | ≈ 1525 |
| | Transverse mode spacing | 4.675 MHz (spec) | 4.675 MHz |
| | Mode-matching to input beam | 96% [135] | >96 % (target) |
| | IMC Transmission | ≈ 85% | > 95% (target) |
| | IFI loss (single-pass) | 15% (guess) | < 5% (target) |

Table A.1: Summary of parameters for the input laser system, grouped by subsystem. For the eventual detection of optomechanical squeezing and BHD readout, various upgrades are in the process of being implemented (at the time of writing). I have grouped these two sets of parameters under the blanket terms "RF readout" (before upgrade) and "BHD" (after upgrade). Where available, measurements of these parameters are referenced - other numbers are from old specification documents or design targets.

| | Parameter | Value (RF readout) | Value (BHD) |
|---|---|---|---|
| PRC | PRM transmissivity | 5.637% | 5.637% |
| | PR2 transmissivity @ $\theta_i \approx 1°$ | 25 ppm | 25 ppm |
| | PR3 transmissivity @ $\theta_i \approx 41°$ | ≈1000 ppm | 50 ppm [136] |
| | PRM curvature | 122.1 m | 122.1 m |
| | PR2 curvature | 600 m | −600 m |
| | PR3 curvature | 700 m | 1000 ± 150 m [136] |
| | Transverse mode spacing | ≈ 2.44 MHz (calculated) | 1.4-1.8 MHz [136] |
| | Mode matching to arm cavities | ≈ 97% (calculated) | > 99% (target) |
| | Cavity length, $L_{\mathrm{PRC}}$ | 6.753 m | 6.753 m |
| | Cavity finesse, $\mathcal{F}_{\mathrm{PRC}}$ | ≈ 80 | > 105 |
| | Round-trip loss, $\mathcal{L}_{\mathrm{PRC}}$ | ≈ 2% | < 1000 ppm |
| | Power recycling gain (for carrier) | ≈ 22 | > 40 |
| SRC | SRM transmissivity | 9.903% | 9.903% |
| | SR2 transmissivity | 25 ppm @ $\theta_i \approx 1°$ | 75 ppm @ $\theta_i \approx 45°$ |
| | SR3 transmissivity @ $\theta_i \approx 41°$ | ≈1000 ppm | — |
| | SRM curvature | 148.1 m | 148.1 m |
| | SR2 curvature | 600 m | −600 m |
| | SR3 curvature | 700 m | — |
| | Transverse mode spacing | ≈ 3.56 MHz (calculated) | 1.3-1.8 MHz [136] |
| | Mode matching to arm cavities | ≈ 96% (calculated) | > 99% (target) |
| | Cavity length, $L_{\mathrm{SRC}}$ | 5.399 m | 4.044 m |
| | Cavity finesse, $\mathcal{F}_{\mathrm{SRC}}$ | ≈ 50 | ≈ 60 |
| | Round-trip loss, $\mathcal{L}_{\mathrm{SRC}}$ | ≈ 2% | < 1000 ppm |
| Arm cavities + Michelson | ITM transmissivity @ 1064 (532) nm | 1.384 (1.094) % | 1.384 (1.094 )% |
| | ETM transmissivity @ 1064 (532) nm | 13 ppm (4.579%) | 13 ppm (4.579%) |
| | BS transmissivity | 0.50 ± 0.01 | 0.50 ± 0.01 |
| | ITMX (ITMY) curvature | 83 (-883) km | 83 (-883) km |
| | ETMX (ETMY) curvature | 60.2 (57.6) m | 60.2 (57.6) m |
| | Transverse mode spacing | 1.145 MHz | 1.145 MHz |
| | Contrast defect due to mode-mismatch | ≈ 0.1% (calculated) | ≤ 0.1% (target) |
| | Cavity length, $L_{\mathrm{arm}}$ | 37.79 m | 37.79 m |
| | Schnupp asymmetry | ≈ 3.5 cm | 2.319 cm |
| | Cavity finesse, $\mathcal{F}_{\mathrm{arm}}$ @ 1064 (532) nm | ≈ 450(100) | ≈ 450(100) |
| | Round-trip loss, $\mathcal{L}_{\mathrm{arm}}$ | ≈ 30 ppm | < 30 ppm |

Table A.2: Summary of the C1 core interferometer parameters. As in Table A.1, a second column is used to indicate design/target values for the planned upgrade. Unless otherwise specified, the angle of incidence is 0°, polarization is p-pol, and wavelength is 1064 nm.

*Appendix B*

# FEEDBACK SYSTEMS - MODELING AND MEASUREMENT

The concepts of modeling systems using Transfer Functions is ubiquitous in the field of GW interferometry. Here, I review some useful concepts. Much of the content in this Appendix is adapted from the excellent resource [137].

## B.1 Block diagram algebra

The advantages of using transfer functions to model complex systems is that input/output relations can be evaluated algebraically rather than by solving differential equations. The limitation, however, is that solving the system in this way only captures the "steady-state" behavior. Ironically, it is easiest to understand what is meant by "steady-state" in the time-domain. Suppose the time evolution of a system with initial state x(0) is described by

$$y(t) = Ce^{At}x(0) + De^{st}, s \equiv i\omega, \quad \text{and } A, C, D, \omega, t \in \mathbb{R}. \tag{B.1}$$

If $A < 0$, then the first term in the above equation will exponentially decay to zero for sufficiently large values of $t$, and hence, this term is often called the transient response. Of course, if $A \geq 0$, then the output $y(t)$ grows exponentially with time and the system is unstable. For a stable system, the second term is called the "steady-state response", and transfer function analysis is largely only useful when dealing with this part of the response. This limitation must be kept in mind when assessing the performance of a system on the basis of its transfer function - while a transfer function evaluated using block diagram algebra can tell us if a system is stable or not, the algebraic relations are only valid for the steady-state. In a practical implementation of a system such as a feedback loop stabilizing the angular pointing of a suspended mirror in the LIGO interferometers, the transient response may render a particular design unsuitable even though the transfer function analysis doesn't throw up any red flags. With this caveat in mind, block diagram algebra is sufficient to assess the performance of most feedback loops used in the LIGO interferometers. The typical topology of such a feedback system is shown in Figure B.1. While this is in some sense the simplest system imaginable, more complex systems like that described in Chapter 3 can be decomposed into simpler subsystems that have this topology.

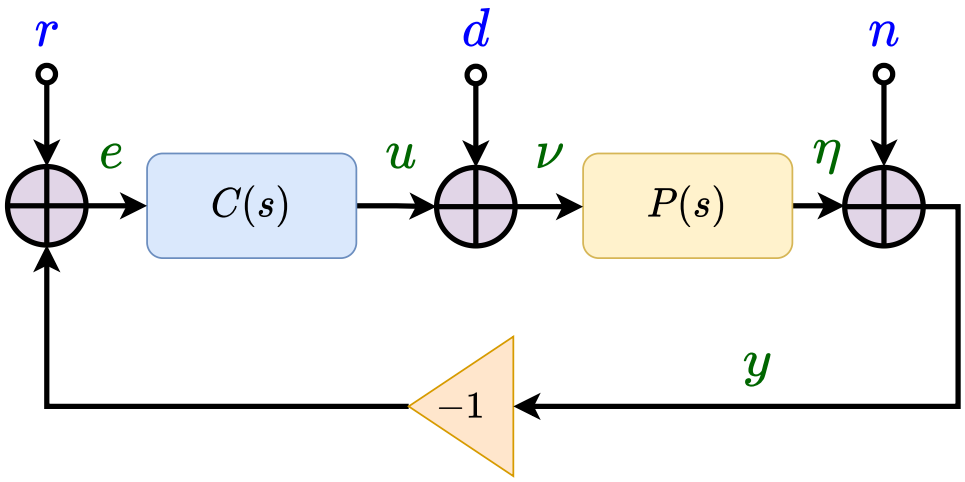


Figure B.1: Topology of a typical feedback system used in controlling the LIGO interferometers. $P(s)$ denotes the "Plant" (i.e. the system to be controlled, like a suspended mirror forming an optical cavity) while $C(s)$ denotes the feedback controller used. Inputs to the system are denoted in blue. $r$ is the desired reference you want the output, $y$, to track (usually 0). $d$ denotes disturbances to the plant (e.g. seismic perturbations) and $n$ denotes sensing noise (e.g. photon shot noise).

We are usually interested in evaluating the transfer function from some input (colored blue) to some output (colored green). The power of the block diagram technique is evident - in the Laplace domain, the *steady state* values at various points in the loop can be related to other points using simple algebra[1] - for example, $\eta = P\nu$, and $y = \eta + n$. Going around the loop once, we get a system of equations, from which we can extract the transfer functions of interest by eliminating all variables except those of interest. There are four special transfer functions that are frequently used, which [137] call the "Gang-of-Four". These are:

$$\begin{aligned} H_{yn} &= \frac{1}{1+PC}, & H_{yd} &= \frac{P}{1+PC}, \\ H_{ur} &= \frac{C}{1+PC}, & H_{yr} &= \frac{PC}{1+PC}. \end{aligned} \tag{B.2}$$

In the above, $H_{ji}$ is the transfer function from the input "$i$" to the point "$j$" in the loop. Knowing these transfer functions, and the spectral densities of the inputs to the system (i.e, $r$, $d$ and $n$), relative contributions of each input to the system output

[1] Interestingly, this technique is also used for deriving the field reflectivity/transmissivity equations for optical cavities, subject to the same limitations that the transient effects must really be unimportant in the system reaching the steady state.

of interest, usually $y$, can be computed. In particular, note that the sensing noise, $n$, couples to the system with unity gain when $PC \ll 1$, as a result of closing the feedback loop. This highlights the need for low noise sensors in order to realize low-noise feedback loops. The product $PC$ is sometimes assigned the symbol $L$ and denotes the *Open-Loop* Transfer Function (OLTF) of the system. All of these transfer functions are, in general, frequency-dependent complex numbers, and are usually visualized in Bode plots, from which various performance metrics like the loop gain and some stability margins can be read off. However, in some cases, other methods of visualization, such as the Nyquist plot, better indicate the system's stability.

## B.2 Measuring transfer functions

An instrument like an FFT analyzer or a network analyzer[2] can be used to measure the transfer function of a system. We are usually interested in measuring $L$ while the feedback loop is closed - particularly when the plant is an optical cavity, there isn't any other good way to access the optical gain of the plant, since the cavity length (or equivalently laser frequency) has to be precisely controlled for the field resonant conditions to be satisfied. A commonly used technique[3] is to inject a single frequency excitation at the servo's error point "$r$" in Figure B.1, and then evaluate the response just before and just after the excitation is summed into the loop. Mathematically,

$$\begin{aligned} L &= \frac{H_{yr}}{H_{er}} \\ &= \frac{L/\cancel{(1+L)}}{1/\cancel{(1+L)}}. \end{aligned} \tag{B.3}$$

In fact, the ratios $\frac{H_{ud}}{H_{vd}}$ and $\frac{H_{\eta n}}{H_{yn}}$ simplify to $L$ as well, and so the specific point in the loop at which an excitation is injected depends on several practical considerations, some of which are:

1. The excitation must not be so large that the feedback loop is pushed out of its linear range of operation. In particular, there shouldn't be any saturation (due

[2] The workhorses in LIGO labs at the time of writing are the SR785 by Stanford Research Systems and the Agilent AG4395A, although alternatives like the HF2LI by Zurich Instruments and the Moku Lab by Liquid Instruments are being adopted as alternatives.

[3] [138] describes more "optimal" methods of system identification by transfer function measurement, which are being studied to improve the characterization of feedback loops in the LIGO interferometers

to finite ranges of servo electronics for example) at any point in the loop due to the injected excitation.

2. The excitation must not be so small that it gets suppressed to below the steady-state noise level of the system at either of the points being measured, or below the measurement noise of the measuring instrument.

3. The SNR (i.e. the part of the signal at the measurement points coherent with the injected signal) must be high enough that a measurement with low statistical uncertainty can be made in a "reasonable" amount of time. Seconds to minutes are usually considered "reasonable", although depending on the frequency range over which the measurement must be made, measurements that take hours are sometimes unavoidable due to the reciprocal relationship between frequency $f$ and time $T$, $f = \frac{1}{T}$.

4. A convenient mechanism must exist for the excitation to be injected (e.g. a circuit that sums in an excitation and blends it into the feedback loop with the option to enable or disable these paths).

Feedback loops with a large dynamic range that are commonly encountered in interferometers are difficult to characterize over a large range of frequencies, given the finite dynamic range of the measurement instruments themselves. For example, when $L \gg 1$, any excitation that is injected tends to get squished to a levels comparable to the steady-state levels at various points in the loop, making it impossible to make a coherent measurement. For example, consider the measurement in Figure 2.4 - around 40 kHz, $L \approx 10^4$, and so a 1 V electrical signal injected at the servo's error point "$r$" will be suppressed to 100 $\mu$V at "$e$", which is comparable to the signal levels normally present at the point $e$ (due to ambient levels of "$d$" and "$n$"). Making the coherent measurement required would, therefore, take a long time - in fact, the poor coherence is what is responsible for the deviation between the modelled and measured OLTFs around 40 kHz in Figure 2.4. The excitation amplitude cannot be arbitrarily increased to circumvent this limitation because doing so would lead to saturations at other points in the servo - in the specific case of the IMC OLTF, $C(s) \approx 10^4$, and so $H_{ur} \approx 1$, while the servo electronics usually has a range of ±10 V, and consuming a larger fraction of this finite range to null our injected excitation and keep the system in the linear range could lead to the cavity losing lock (at which point the measurement becomes meaningless). Similar constraints are imposed in the regime $L \ll 1$. Therefore, the usual practice adopted

is to make a measurement in a frequency range at which the SNR is high and the statistical uncertainty of the measurement is low. Then, a model of the loop which extends to frequencies outside the measured range can be fit to the measurement. Once the model has some performance indicators like the loop UGF consistent with a measurement, that model can be used for subsequent calculations with greater confidence.

### B.3 Stability margins

The disturbances which a feedback loop has to null might be changing with time - for example, seismic noise levels at the 40m are elevated during the daytime when there is considerable anthropogenic activity on Caltech's campus. Furthermore, the system to be controlled, $P(s)$, may itself be changing. We would like for the feedback loops that we use to be able to handle such varying conditions, at least for *small* variations from the assumed parameters.

But when does a system become "unstable"? As mentioned earlier in this Appendix, frequency domain modeling has the drawback of not capturing possible subtle effects due to *transient* responses to external stimuli. Nevertheless, for the system to be stable, at the very least, the steady-state solution must remain finite. Going back to Figure B.1, let us "break" the feedback loop by disconnecting the output of the negative feedback block (labelled with $-1$) to the node at which it is summed with the reference input "$r$". Then, let us ask what would happen if we inject a single frequency signal to $r$ (let us set $d = n = 0$ for this thought experiment) - following the signal through the loop, we would expect the injected signal to return to the summing node as $-L \times r$. So, if $L = -1$, the injected signal returns to the injection point with equal amplitude as, and in phase with, the original injection. If we re-connect the negative feedback to once again close the feedback loop, this input would reinforce the original injection. With repeated round trips around the feedback loop, the injected signal grows unbounded, which is equivalent to saying that the system becomes unstable. The point $-1$ on the complex plane is special for this reason, and is called a "critical-point" in control systems literature like [137]. For all other values of $L$, this kind of run-away buildup of an injected excitation does not happen, and therefore, the system passes a preliminary stability test.

From a Bode plot, two stability metrics that can just be "read-off" are the Gain-Margin (GM) and Phase Margin (PM), as shown in Figure B.2. Keeping the discussion in the preceding paragraph in mind, we are looking for points where

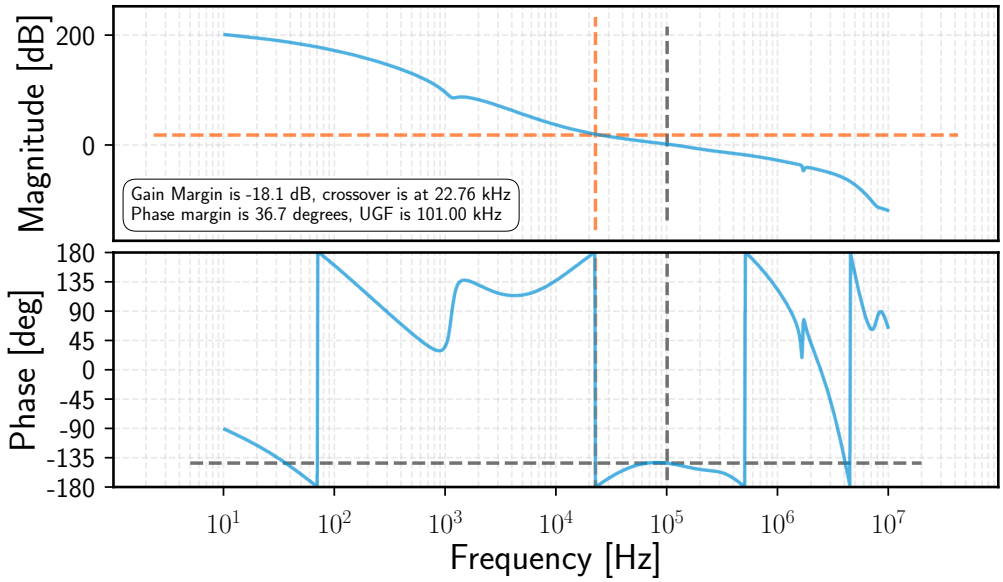


Figure B.2: Determining Gain and Phase Margins from a Bode plot. This Bode plot is for a *model* of the IMC cavity at the 40m interferometer. A phase margin of 36.7° indicates that this particular loop design can tolerate a total additional phase lag of that amount at the UGF (for instance, due to erroneous modeling of the plant). Similarly, the gain margin of −18.1 dB means that the overall gain of the loop can be lowered by that amount before it becomes unstable (due to $\arg(L) = -180°$ at the UGF with the lowered loop gain).

$|L(\omega)| = 1$ and $\arg(L(\omega)) = \pm 180°$. However, what we would really like to know is how close $L(\omega)$ approaches the point $-1$, as then, even a small perturbation to $L(\omega)$ (due to a changing plant for example) can push the system into the unstable regime.

A Nyquist plot presents the same information as a Bode plot, but rather than plotting the magnitude and phase of the complex valued transfer function $L(\omega)$ on two separate plots as a function of frequency $f = \omega/2\pi$, it presents the same information by tracing the trajectory of $L(\omega)$ on the complex plane, for $-\infty \leq \omega \leq \infty$. Such a plot offers a third diagnostic of the loop's stability - namely, the distance of closest approach[4] to the point $-1$ on the complex plane, called the *stability margin*. Nyquist plots for $L(\omega)$ that spans several orders of magnitude are not very informative to look at over the full range of frequencies, because the point $-1$ is very close to the origin but the Nyquist contour will have very large real or imaginary components (or both) when $|L(\omega)| \gg 1$. A zoomed-in Nyquist plot for the IMC servo is shown

[4] A more general requirement is that the Nyquist contour encircle the $-1$ point *counterclockwise* as many times as the number of poles of $L(\omega)$ in the right-half complex plane. The stability margin remains a suitable metric to evaluate stability, as with a sufficiently large stability margin, small perturbations to the Nyquist contour cannot change the *net* number of encirclements of the $-1$ point.

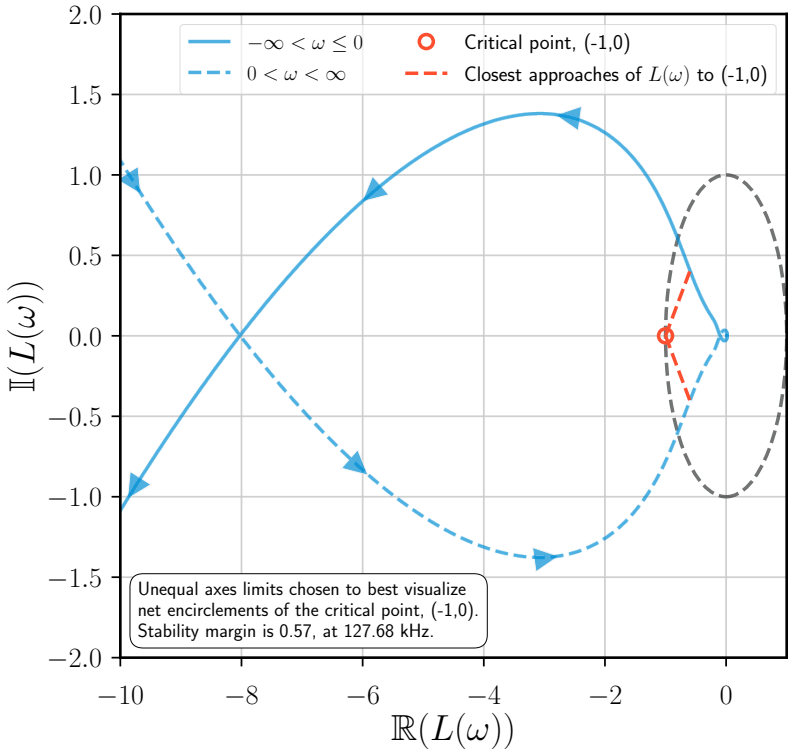


Figure B.3: Nyquist plot for the 40m IMC OLTF model. The information in this plot is the same as that available in Figure B.2, except that $L(\omega)$ is plotted as a parametric curve with $-\infty < \omega < \infty$. I have heavily zoomed in on the area near the origin to focus on the critical point $(-1, 0)$, and the shortest distance between $L(\omega)$ and this critical point. Note that the $\mathbb{R}$ and $\mathbb{I}$ axes have unequal scales, which is why the shortest distance between $L(\omega)$ and the critial point does not *appear* to intersect $L(\omega)$ at a right angle. Also plotted (in grey) is the unit circle. Other stability margins like the phase margin can also be read off a Nyquist plot (the angle between the real axis and the point where the Nyquist contour intersects the unit circle).

in Figure B.3, focusing on the distance of closest approach between $L(\omega)$ and the point $(-1, 0)$. Note that the Nyquist contours have a direction associated with them. For $|\omega| \to \infty$, the loop gain approaches 0, and so the contours in Figure B.3 start out at the origin as $\omega$ runs from $-\infty \to 0$ , and then again return to the origin as $\omega$ runs from $0 \to \infty$. For frequencies $< 80$ kHz, the loop gain is large and the Nyquist contours lie outside the axes limits of Figure B.3.

*The important takeaway from* Figures B.2 and B.3 *is that the stability margins that can be easily read off a Bode plot are not always the ones that ultimately determine a system's stability*. For the IMC loop, the Nyquist plot tells us that the point most likely to introduce an instability is located at $\approx 130$ kHz, and not at 100 kHz or 22.76 kHz, the frequencies associated with the Phase and Gain Margins respectively.

## B.4 Loop design - the present and the future

I close this appendix with a brief discussion on how the feedback loops in LIGO interferometers are designed, and how the process may be made more systematic. The typical set of requirements on a feedback loop may consist of the following:

1. The closed loop must sufficiently stabilize the system against the influence of external disturbances, within some desired control bandwidth. From Equation (B.2), we can see that the suppression is $\propto 1/|L(\omega)|$, and this requirement amounts to setting a lower bound on the loop gain at frequencies within the control bandwidth.

2. Closing the feedback loop must not degrade the system's performance by injecting sensing noise at frequencies outside the control bandwidth (within the control bandwidth, the loop suppression applies and therefore, the performance is not degraded).

3. The loop must be stable, in the sense described in Appendix B.3.

4. A more advanced requirement stems from the fact that LIGO is a Multiple-Input-Multiple-Output (MIMO) system. Therefore, a given feedback loop must not degrade the performance of other loops in the larger MIMO system inside which it may be nested. Practically, this means that the preceding three requirements have to be considered with the global MIMO system in mind.

At the time of writing, the usual procedure in feedback loop design is that an experienced scientist iteratively tweaks an initial design, based on measurements like that described in Appendix B.2, until the requirements are deemed to have been satisfied.

As far as precision measurement experiments go, the individual subsystems that must be controlled in LIGO interferometers have dynamics that can be easily modelled, and are amenable to techniques in feedback control design techniques like $H_\infty$[137] and $\mu-$synthesis (indeed, these techniques have been successfully applied to some LIGO feedback design problems). However, the MIMO nature of the system and the large number of feedback loops, $O(100)$, make the problem challenging. One promising approach that is being explored is to attack the problem numerically, using a global optimization algorithm (analogously to the approach described in Chapter 7). If the list of requirements can be formulated as a cost-function, then it

is reasonable to think that a global optimizer would be able to reliably generate an "optimal" controller, provided the assumptions and model parameters that go into the cost function formulation are close to reality. Some early success in using such an approach is described in [139].

Since the majority of feedback controllers are digital filters implemented in realtime [140], another approach that is being explored is to use Neural Networks as the feedback controller, rather than the simple, linear controller $C(s)$ depicted in Figure B.1. These are easily compatible with the MIMO nature of the LIGO interferometers, and may be able to extend the useful range of the feedback loops they are used in by virtue of their inherent non-linearity. However, these explorations are very much in their infancy. A technical difficulty that has to be kept in mind when considering Neural Networks for *realtime* control is that the computational cost of the network must be compatible with the clock rate of the realtime system. However, progress in this realm is being driven so quickly that this is unlikely to be a real bottleneck.

*Appendix C*

# OPTICAL CAVITIES - STATICS AND DYNAMICS

Nearly every LIGO thesis has a chapter, or at least an Appendix, on this subject, so my objective here is to simply collect some concepts / results that are particularly relevant to the topics discussed in this thesis. Perhaps the way it is presented here offers some alternative insights compared to the mountain of literature available.

## C.1 Adjacency matrix and steady-state field relations

To analyze the optomechanical response of an interferometer, we have to know how it responds to being pumped with electromagnetic fields at various ports (including the vacuum fields that couple in at each port where there is some optical loss). In the LIGO parlance, these are frequently referred to as Input-Output (IO) relations. A common technique to calculate these is to start with an abstracted sketch of the interferometer, as shown in Figure C.1. In fact, this is one of the more complicated configurations one would encounter, but the *same* technique can be applied to simpler configurations like a two mirror Fabry-Pérot cavity, leading to Equation (D.1).

The algorithm is to write equations relating the various fields, in terms of propagation phases, and the *field* reflectivities and transmissivities of various mirrors (which may compound mirrors like the FPMI in Figure C.1). For example, $E_2 = -r_P E_1 + t_P E_6$[1], where $r_P$ ($t_P$) is the field reflectivity (transmissivity) of the PRM[2]. The *set* of such equations for $E_i, i = 1 \ldots 11$ can then be written down in a matrix, $\mathcal{A}$[3]. We can then calculate the matrix $\mathcal{M} \equiv (\mathbb{I} - \mathcal{A})^{-1}$[4]. $\mathcal{M}$ encodes the *steady-state* relations between fields at various nodes indexed by $i = 1 \ldots 11$ in Figure C.1. For example,

[1] For the field reflectivity of a simple mirror, I follow a commonly used convention, see for example, Eq. 3.8 of [6].

[2] These are related to the more easily measured *power* transmissivity ($T_P$) as $t_P = \sqrt{T_P}$, $r_P = \sqrt{1 - T_P - \mathcal{L}_P}$, with $\mathcal{L}_P$ denoting the fraction of power lost due to processes like scattering and absorption. When specifying the requirement on a dielectric coating for an optic like the PRM, $T_P$ is typically the principal specification a manufacturer has to meet.

[3] In graph theory parlance, this is called an adjacency matrix, hence the section title. The systems analyzed in this thesis are not so complex/high dimensional that I could leverage any techniques from graph theory to simplify or speed up solving this set of equations, but future applications may be able to exploit this connection.

[4] $\mathcal{A}$ has to be padded with rows of zeros appropriately to make it a square matrix that can be inverted. For the system shown in Figure C.1, the elements of the first row of $\mathcal{A}$ would be all zeros. Physically, this can be interpreted as $E_1$ being a source term that is independent of the interferometer configuration.

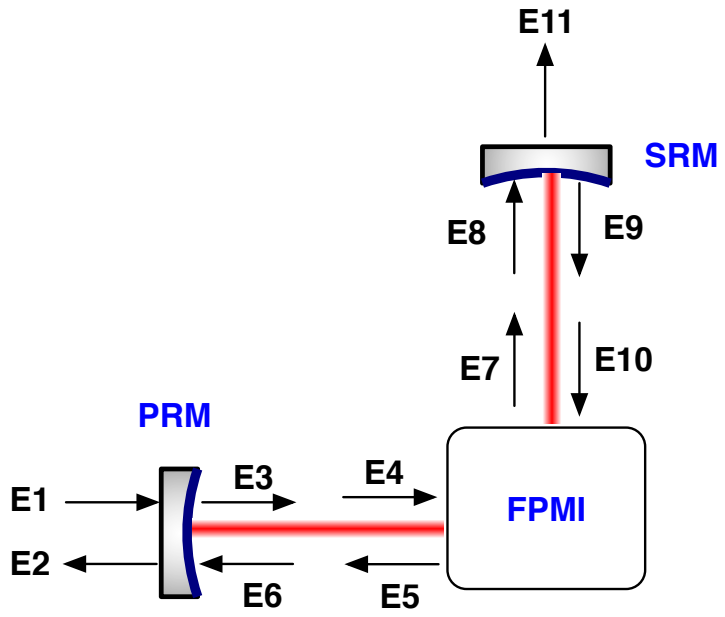


Figure C.1: Electric fields at various points in an abstracted Dual-Recycled interferometer. The interferometer formed by the two arm cavities and the beamsplitter are abstracted as "FPMI" (Fabry-Pérot Michelson Interferometer), to emphasize the role of the two recycling mirrors.

the relationship between the pump field $E_1$ and the dark port field $E_{11}$ is the element in the $11^{\text{th}}$ row and $1^{\text{st}}$ column of $\mathcal{M}$, which is typically functions of the tunings of the various cavities and mirror reflectivities/transmissivities. The power of the technique is that once this matrix is calculated, it remains valid for fields that are offset from the carrier frequency as well (with appropriate modifications for propagation phases), as long as we are interested in the steady-state solution. We can then calculate several quantities of interest, such as the PDH error signal generated at a given node in response to one or more cavity length changes, and the coupling of noise sources such as laser frequency noise to the DARM readout channel. The length ($\leq 50\,\text{m}$) and finesse ($\leq 100$) of most of the optical cavities in LIGO interferometers are such that the steady-state assumption is surprisingly good at all frequencies ($\lesssim 10\,\text{kHz}$) of relevance. An exception is the 4 km long arm cavity, and care has to be taken when using $\mathcal{M}$ to calculate signals that may be used to control the arm cavity length (for example)[5].

[5] Corrections due to the finite time it takes for the optical fields to build up to their steady state value will be even more important for $3^{\text{rd}}$ generation detectors which are expected to have arm cavities that are $\approx 10\times$ longer. Very high finesse optical cavities are the other class of systems for which the time for field buildup to reach the steady state may be comparable to the signal frequencies of interest.

The notation presented in this section is the so-called one-photon formalism, where the electromagnetic fields of the interferometer are treated as completely classical plane waves. This approach is sufficient in many cases, such as the recycling cavity design study presented in Appendix D.1. However, when the quantum-mechanical nature of the fields in the interferometer have to be taken into account, such as when calculating the instrument noise level due to quantum vacuum fluctuations entering the interferometer's AS port, or correctly modeling radiation pressure effects, it is more appropriate to use the formalism of two-photon quantum optics from [62, 63]. Fortunately, the adjacency matrix generalizes easily to the two-photon formalism, as described in [61]. Each scalar field quantity is promoted to a two-element vector, representing the two quadrature fields, and the matrices representing optical elements like mirrors and beamsplitters, as well as the propagation of the field, are appropriately modified to capture the interaction between the two quadrature fields.

## C.2 Modulation, demodulation, and optical beats

Photodetectors available at the time of writing are not capable of directly responding to the oscillating laser field used, with $\lambda \approx 1.064\,\mu$m, $f \approx 282\,$THz. The quantity being measured, therefore, is a time-averaged optical power incident on the photodetector, which is $\propto E^*E$, where $E$ is the electric field. The fact that $E$ may have multiple spectral components is central to deriving signals that are sensitive to changes in the length (and indeed, angular) DoFs of the interferometer.

### C.2.1 Amplitude and phase modulation

There are several equivalent ways of representing an electric field, see for example Section 2.2.1, Equation 13 of [73]. Since an electric field has an amplitude and a phase, we may in principle modulate each of them independently. When analyzed in terms of the spectral content of the field, the effect of applying a modulation to a monochromatic field is that sideband(s)[6] are created, with the offset frequency of the sideband from the unmodulated carrier being equal to the modulation frequency. For sensing and controlling the interferometer, the technique used in all the large-scale suspended GW detectors is known as "frontal-modulation". Explicitly, the *phase-modulated* electric field injected into the interferometer may be represented

[6] Depending on the specific modulation mechanism, either a single sideband or a pair of symmetric sidebands about the unmodulated carrier ($f = f_0$ )may be created. For example, there are heterodyne schemes that use the first order diffracted beam from an *travelling-wave* Acousto-Optic Modulator (AOM), with a single sideband (at $f = f_0 + f_{\mathrm{mod}}$). The traditional PDH scheme uses a Pockel Cell type Electro-Optic Modulator (EOM), that creates a pair of symmetric sidebands ($f = f_0 \pm f_{\mathrm{mod}}$).

using the Jacobi-Anger expansion as

$$\begin{aligned} E_{\text{in}} &= E_0 e^{i\Gamma \cos 2\pi f_{\text{mod}} t} \\ &= E_0 \sum_{n=-\infty}^{\infty} i^{|n|} J_{|n|}(\Gamma) e^{in2\pi f_{\text{mod}} t}, \end{aligned} \tag{C.1}$$

where $E_0 \equiv |E_0| e^{i2\pi f_0 t}$ is the unmodulated laser field, $\Gamma$ is the modulation depth (also known as modulation index), $f_{\text{mod}}$ is the modulation frequency, $J_n$ are Bessel functions of the first kind, and $n$ indexes the *order* of a sideband. If the field in Equation (C.1) were incident on a photodiode, there would *not* be any component in the detected power, $E_{\text{in}}^* E_{\text{E}}$, varying at $f_{\text{mod}}$ - terms indexed by $+n$ and $-n$ in the expansion would cancel each other out. In order to measure such a modulation profile, $E_{in}$ has to be optically interfered with some other stabilized field (i.e. the frequency of this second field has to maintain a fixed relation with $E_{in}$ over the measurement time). A heterodyne measurement of the modulation profile for the beam injected into the 40m, using a Phase Locked Loop (PLL), is shown in Figure C.2.

The details of how PM sidebands can be used to sense the difference between laser frequency and the resonant frequency of the coupled optical cavities in an interferometer are detailed in [51, 141], and are not rehashed here. The central idea is worth restating - in general, we are looking for an error signal on a photodiode at a particular port of the interferometer that has the functional form

$$S \propto \left( \frac{\partial E^{(\text{c})}}{\partial L_i} \otimes E^{(\text{sb})} + \frac{\partial E^{(\text{sb})}}{\partial L_i} \otimes E^{(\text{c})} \right) \Delta L_i \left( \cos 2\pi f_{\text{mod}} t + \sin 2\pi f_{\text{mod}} t \right). \tag{C.2}$$

In Equation (C.2), $E^{(\text{c})}$ and $E^{(\text{sb})}$ denote the carrier and sideband spectral components of the field respectively, $L_i$ is a length degree of freedom of the interferometer, and $\otimes$ denotes a "beat operator". The partial derivatives $\frac{\partial E^{(\text{c})}}{\partial L_i}$ and $\frac{\partial E^{(\text{sb})}}{\partial L_i}$ represent sidebands imprinted on a field due to fluctuations in the quantity $L_i$ - for example, a mirror moving back and forth will imprint PM sidebands, offset from the carrier frequency by the frequency at which the mirror is moving, on any light that is reflected off it. These sidebands then beat with a static LO field, such as $E^{(\text{c})}$ or $E^{(\text{sb})}$, to produce a signal in either one or both quadratures (i.e. $\propto \sin 2\pi f_{\text{mod}} t$ or $\propto \cos 2\pi f_{\text{mod}} t$). Note that in order to determine the relation between fields like $E^{(\text{c})}$, $\frac{\partial E^{(\text{c})}}{\partial L_i}$ at the photodiode and the field injected into the interferometer, e.g. Equation (C.1), we can use the methods of Appendix C.1 to evaluate the relevant transfer functions *at DC*. In

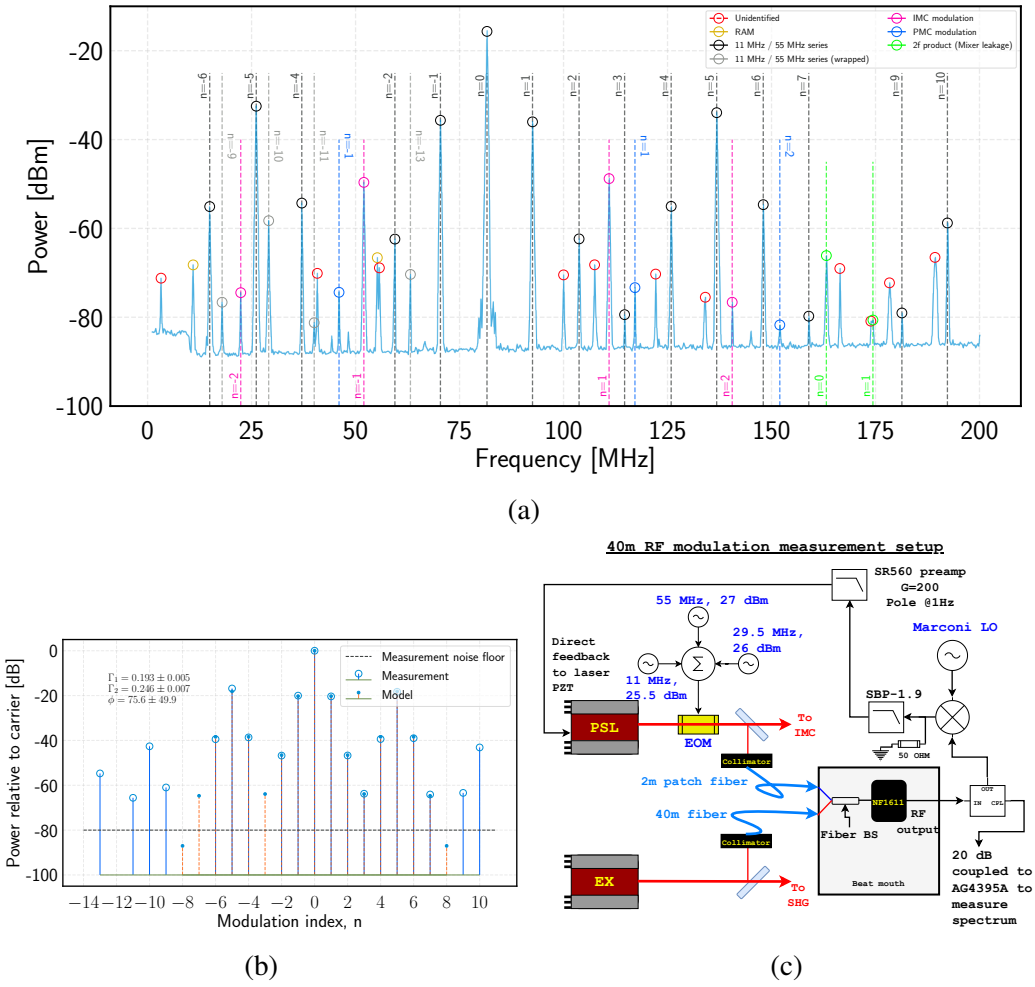


Figure C.2: Characterization of the modulation profile of the input beam to the 40m interferometer. Figure C.2(c) shows the measurement setup - such a heterodyne scheme using a Phase-Locked Loop (PLL) is necessary as a purely phase-modulated field like that in Equation (C.1) doesn't produce any power variations at the modulation frequency, and hence, cannot be directly characterized by a photodiode. Figure C.2(a) shows the measured spectrum of the heterodyne beat from the PLL, while Figure C.2(b) shows how we can extract the parameters of the phase modulation from the peak heights. The spectrum in Figure C.2(a) is more complicated than one would naively expect from Equation (C.1) as there are multiple modulation frequencies used. Furthermore, there are practical imperfections, such as Residual Amplitude Modulation (RAM) that create *amplitude* modulation sidebands at the modulation frequencies of 11 MHz and 55 MHz.

general, these transfer functions have a frequency dependence - i.e. depending on the frequency at which the aforementioned mirror is moving, the transmission of the PM sidebands thus generated to the detection photodiode might vary in amplitude. Fortunately, the single pole approximation works well in modeling this frequency dependence. To set up this approximation, I reproduce Equation (D.1), the reflectivity of a simple, two-mirror Fabry-Pérot cavity of length $L$, here for easy reference:

$$r_{\mathrm{cav}}(\phi,\Omega) = \frac{-r_i + r_e \mathrm{e}^{-2i\phi}}{1 - r_i r_e \mathrm{e}^{-2i\phi}}, \quad \phi \equiv \frac{\omega L}{c}, \tag{C.3}$$

where $\omega$ denotes the frequency offset of the field being considered from the carrier frequency. Note that

$$\begin{aligned} r_{\mathrm{cav}}(\phi,\Omega) &\propto \frac{1}{1 - r e^{\frac{2i\omega L}{c}}}, \quad r \equiv r_i r_e \\ &= \frac{1}{1 - r e^{i\frac{\omega}{\omega_1}\ln r}}, \ \omega_1 \equiv \frac{c}{2L}|\ln(r)| \\ &= \frac{1}{1 - r e^{\ln(r^{i\frac{\omega}{\omega_1}})}} \quad \because i\frac{\omega}{\omega_1}\ln(r) = \ln(r^{i\frac{\omega}{\omega_1}}) \\ &= \frac{1}{1 - r^{1+i\frac{\omega}{\omega_1}}}. \end{aligned} \tag{C.4}$$

Up till this point, the manipulation is exact, and no approximations have been invoked yet. Now in the limit $r \to 1$ as is usually the case,

$$\begin{aligned} r_{\mathrm{cav}}(\phi,\Omega) &\propto \frac{1}{1 - (1-\delta r)^{1+i\frac{\omega}{\omega_1}}}, \ \delta r \ll 1 \\ &\approx \frac{1}{1 - 1 + (1 + i\frac{\omega}{\omega_1})\delta r} \quad \because (1-\delta r)^n \approx 1 - n\delta r, \delta r \ll 1 \\ &\propto \frac{1}{1-r}\frac{1}{1 + i\frac{\omega}{\omega_1}}. \end{aligned} \tag{C.5}$$

Equation (C.5) represents the transfer function of a system that has a single pole at angular frequency $\omega_1$, for which reason this quantity is often referred to as a "cavity-pole". While Equation (C.2) isn't mathematically rigorous in the form it is presented, it is very useful conceptually. For instance, it tells us that if the static field $E^{(\mathrm{c})} = 0$, as it is when a Michelson interferometer is tuned to operate at a perfect dark fringe, then we only need consider the term $\frac{\partial E^{(\mathrm{c})}}{\partial L_i} \otimes E^{(\mathrm{sb})}$, considerably simplifying analytic calculations. If a more exact calculation is desired, then careful accounting of all

the spectral components, i.e. terms in Equation (C.1), is required. However, for complex interferometer configurations with multiple modulation frequencies, such a calculation is better done by a numerical tool such as `finesse`[142]. Analytic models remain, nevertheless, useful tools in validating numerical calculations.

### C.3 Sensing matrix, signal separation, and noise

The tools of the previous two sections are useful when choosing the optical configuration of an interferometer. Design parameters such as the macroscopic lengths of the various cavities (where "macroscopic" is used to distinguish from the *microscopic tuning* of the cavity, which is usually at the scale of the laser wavelength, i.e. $\approx 1\ \mu$m), power transmissivities of the mirrors, and modulation frequencies, have to be chosen such that at least in this simple, plane-wave analysis, it will be possible to sense *all* of the DoFs of interest with sufficient fidelity. An example of such a design study is presented in Appendix D.1. There, the objective was to ensure *existence* of the desired signals - for instance, the length of the arm cavity was chosen such that the $2f_{1,2}$ modulation sidebands did not become resonant at the operating point, to ensure that the amplitude of this field component at the interferometer's reflection port, which serves as the LO field for the $3f$ recycling cavity locking scheme, had relatively low sensitivity to small perturbations in the design parameters (e.g. due to errors in positioning the optics in the vacuum envelope).

A more sophisticated analysis can be done, for example, by setting requirements on the shot-noise limited sensitivity of the PDH error signals. Another important consideration is *separation* between the error signals sensing individual DoFs. In general, perturbing any DoF will produce a signal at all ports of the interferometer. The design problem amounts to ensuring that there exists at least one quadrature signal (either the sin or the cos term in Equation (C.2)) to which the *dominant* contribution comes from one DoF only. The transfer functions from DoFs $\rightarrow$ quadrature signals can be collected together in a matrix, which is known as a sensing matrix. A convenient way to visualize the sensing matrix is in a set of radar plots - the lengths of the stems indicate the strength of the sensing response, while the angles between the stems are representative of the relative magnitudes of the response in each quadrature. An example of such a sensing matrix is shown in Figure C.3. In characterizing the interferometer, one would compare such a simulated sensing matrix to a *measured* one.

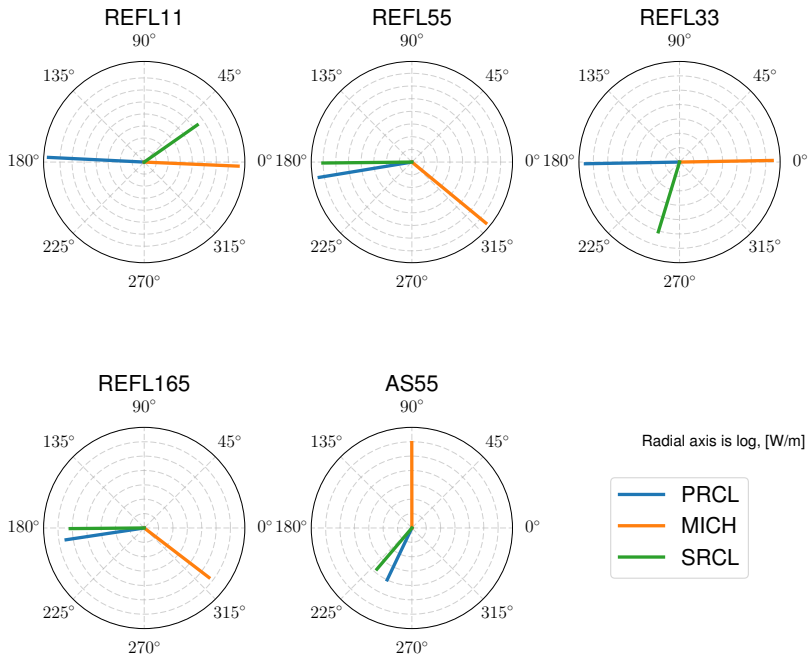


Figure C.3: Example of a (simulated) sensing matrix, generated using `finesse`. The interferometer configuration simulated here is a Dual-Recycled Michelson Interferometer (DRMI). The DoFs of interest in this configuration are PRCL, SRCL and MICH, and this simulation is made for five photodiodes, each of which is measuring a field at some RF frequency offset from the carrier frequency (e.g. the REFL11 photodiode is located at the "REFL" port of the interferometer, and measures photocurrents at a 11 MHz offset from the PSL carrier frequency). From such a simulation, one could conclude that the "Q" quadrature (i.e. 90° phase on the radar plot) of the AS55 photodiode is a suitable sensor for sensing the MICH DoF, while the I quadrature (i.e. 0° phase on the radar plot) of the REFL11 photodiode is a goos sensor for the PRCL DoF. The `finesse` model takes into account geometric cross-couplings between DoFs (e.g. moving the beamsplitter changes *both* MICH and PRCL), which explains why the 3 DoFs in these plots are not orthogonal as one would expect, for example, MICH and PRCL to be.

*Appendix D*

# RECYCLING CAVITIES

There are numerous detailed analyses of different interferometric configurations, e.g. [143, 144] which I don't reproduce here. Briefly, skating over several practical concerns, the motivation behind adding a Power Recycling Mirror (PRM) is to boost the effective laser power injected into the interferometer, while the Signal Recycling Mirror (SRM) allows the shaping of the detector bandwidth (sensitivity to differential arm cavity motion) without changing the bandwidth of the Fabry-Pérot arm cavities. Adding these optics, however, means that two additional length degrees of freedom (in addition to several additional angular degrees of freedom) have to be sensed and controlled. This section describes the design and control topology of the recycling cavities at the 40m.

## D.1 Recycling cavity lengths

The PDH technique is used to sense and control the PRC and SRC lengths (the DoFs themselves are denoted as PRCL and SRCL). In order to allow sensing of both of these DoFs, phase-modulation of the incident laser field at *two* RF frequencies is employed. The PM sidebands thus generated have to be transmitted through the IMC, and so do not have arbitrary frequency offsets from the carrier - rather, they are chosen to be $f_1$ and $f_2 = 5 \times f_1$, where $f_1 = 11.066209\,\mathrm{MHz}$ is the FSR of the IMC. This choice ensures that both the upper and lower PM sidebands are symmetrically and critically coupled through the IMC.

With the RF sideband frequencies thus set, the lengths of the recycling cavities also have to be carefully matched to these frequencies to allow robust PDH sensing with high SNR. Most of the PDH signals used to control the 40m interferometer are generated in reflection from an optical cavity. Therefore, it is useful to review the field reflectivity, $r(\phi, \Omega)$ for a two mirror cavity,

$$r(\phi, \Omega) = \frac{-r_i + r_e \mathrm{e}^{-2i\phi}}{1 - r_i r_e \mathrm{e}^{-2i\phi}}, \tag{D.1}$$

where $\phi = \Omega L/c$ is the phase accumulated by the field (at a frequency offset $\Omega$ relative to the carrier) in traversing the cavity of length $L$ one-way, and $r_i$ and $r_e$ are the field reflectivites for the input and end mirror of the cavity respectively. $\phi$ can, in

general, include any Gouy phase shifts in addition to the propagation phase, though the former can be set to 0 for the fundamental $\mathrm{TEM}_{00}$ mode. Equation (D.1) remains valid if either or both mirrors are "compound mirrors" composed of multiple simple mirrors themselves - the difference being that the field reflectivity, $r_i, r_e$, become a complex numbers (as opposed to a real number for a simple mirror). The possible explicit dependence of $r_i$ and $r_e$ on $\Omega$ is suppressed in Equation (D.1). The terms "resonant" and "anti-resonant" will be used frequently in this section, and are defined as

$$\text{resonant} : \arg(r_i r_e e^{-2i\phi}) = 2n\pi, \text{ and} \tag{D.2a}$$

$$\text{anti} - \text{resonant} : \arg(r_i r_e e^{-2i\phi}) = 2(n+1)\pi, \tag{D.2b}$$

where $n \in \mathbb{Z}_{\geq 0}$.

With these definitions in mind, it is instructive to review the resonance conditions that must be satisfied in various parts of the interferometer, and suitable macroscopic[1] cavity length choices:

1. The $f_1$ and $f_2$ sidebands must not be resonant in the arm cavities when the carrier field is resonant, since generating a PDH error signal relies on the sidebands being reflected from the cavity. They must also not be *exactly* anti-resonant - the reason being that a technique known as $3f-$ locking[43], which is essential for lock acquisition, relies on the $2\times f_1$ and $2\times f_2$ PM sidebands being reflected from the arm cavities. If the $f_1$ and $f_2$ sidebands were exactly anti-resonant, then the $2\times f_1$ and $2\times f_2$ sidebands would necessarily become resonant in the arm cavities, eliminating the field components that are necessary for the $3f-$ locking technique to work. Finally, in order to satisfy Item 2, it is desirable that the reflectivity of the arm cavities for the PM sidebands satisfy $\arg(r_A(f_2)) = 5\arg(r_A(f_1))$. *An arm cavity length of* $\underline{L_{\mathrm{arm}} 37.795\,\mathrm{m}}$ *is the only length compatible with these requirements and constraints of the vacuum envelope in the lab.*

2. The carrier, $f_1$, and $f_2$ sidebands must be resonant in the PRC when the carrier is resonant in the arm cavities. Applying Equation (D.1) to determine the com-

[1] The term refers to the cavity length $L$ correct to approximately the nearest millimeter which is the precision of placing optics in the vacuum enclosure that is practically possible. For the fields to be resonant in the cavity, smaller positional changes at the wavelength scale ()1 $\mu$m) need to be made about this macroscopic separation between optics, which are called *microscopic* length changes in the LIGO parlance.

plex reflectivities of the arm cavities for the sidebands and then substituting into Equation (D.2a), we get a requirement on $L_{\mathrm{PRC}}$:

$$L_{\mathrm{PRC}} = \left(n + \frac{\theta_1}{2\pi}\right)\frac{c}{2f_1}, \quad n \in \mathbb{Z}_{\geq 0}, \tag{D.3}$$

where $\theta_1$ is the complex argument of the arm cavity's reflectivity for the $f_1$ sideband[2]. *The only value of n compatible with the constraints of the 40m vacuum envelope is* $n = 0$*, yielding* $\underline{L_{\mathrm{PRC}} = 6.753\,\mathrm{m}}$.

3. The SRC length must be such that the $f_2$ sideband is resonant when the carrier is resonant in the arm cavities. The resonant field enhancement of the $f_2$ sideband is necessary for sensing SRCL with low noise. At the same time, the $f_1$ sideband should not be resonant in the SRC as it is primarily used to sense changes in the symmetric DoFs of the interferometer, namely CARM and DARM, and so it is desirable to make the PDH signals derived from the $f_1$ sideband insensitive to changes in SRCL.

   Two modes of operation, called "Resonant Sideband Extraction (RSE)" and "Signal Recycling (SR)" are commonly used, and they correspond to different propagation phases for the carrier field in the SRC. The former is the nominal configuration of the 40m interferometer at the time of writing, and corresponds to the carrier being *anti-resonant in the SRC while being resonant in the arm cavities*. Applying Equation (D.1) and Eq. (D.2b),

$$L_{\mathrm{SRC}} = \left(n + \frac{1}{2} + \frac{\theta_2}{2\pi}\right)\frac{c}{2f_2}, \quad n \in \mathbb{Z}_{\geq 0}, \text{ and} \tag{D.4a}$$

$$L_{\mathrm{SRC}} \neq \left(m + \frac{1}{2} + \frac{\theta_1}{2\pi}\right)\frac{c}{2f_1}, \quad \forall m \in \mathbb{Z}_{\geq 0}. \tag{D.4b}$$

   *The only value of n compatible with the constraints of the 40m vacuum envelope is* $n = 1$*, yielding* $\underline{L_{\mathrm{SRC}}^{\mathrm{RSE}} = 5.399\,\mathrm{m}}$.

   For the Ponderomotive Squeezing experiment described in Chapter 4, it was determined that the SR configuration was more appropriate. This configuration corresponds to the carrier being *resonant in the SRC while being resonant in the arm cavities*. Applying Equation (D.1) and Eq. (D.2a), Equation (D.4)

[2] In Item 1, the requirement that $\arg(r_{\mathrm{A}}(f_2)) = 5\arg(r_{\mathrm{A}}(f_1))$ guarantees that the $f_2$ sideband will also be resonant.

gets modified to

$$L_{\mathrm{SRC}} = \left(n + \frac{\theta_2}{2\pi}\right)\frac{c}{2f_2}, \quad n \in \mathbb{Z}_{\geq 0}, \text{ and} \tag{D.5a}$$

$$L_{\mathrm{SRC}} \neq \left(m + \frac{\theta_1}{2\pi}\right)\frac{c}{2f_1}, \quad \forall m \in \mathbb{Z}_{\geq 0}. \tag{D.5b}$$

*The only value of n compatible with the constraints of the 40m vacuum envelope is* $n = 1$*, yielding* $L_{\mathrm{SRC}}^{\mathrm{SR}} = 4.044\,\mathrm{m}$.

4. The $f_2$ sideband must be critically coupled from the PRC to the SRC, so that it can sense the SRC length with low noise. This is done by adjusting the Schnupp asymmetry [145] appropriately. The analytic expression for transmission from the symmetric port of the interferometer to the anti-symmetric side is

$$t = \frac{e^{-i(\phi_{\mathrm{PRC}}+\phi_{\mathrm{SRC}}-\theta)}|r_A|t_P t_S \sin(2\phi_-)}{1 + |r_A|^2 r_P r_S e^{-i(2\phi_{\mathrm{SRC}}-\theta)} - |r_A|(r_P + r_S e^{-i(2\phi_{\mathrm{SRC}}-\theta)})\cos(2\phi_-)}, \tag{D.6}$$

where $\phi_i = \Omega L_i/c$ with $i$ denoting either the PRC or the SRC, the "$P$" subscript denotes the PRM, and the "$S$" subscript denotes the SRM, and $\theta = \theta(\Omega)$ is the complex argument of the arm cavity reflectivity, $r_{\mathrm{A}} \equiv |r_{\mathrm{A}}|\,e^{i\theta}$ for the $\Omega_{1,2} = 2\pi f_{1,2}$ sideband. *The value of* $l_- = \frac{\Omega\phi_-}{c}$ *compatible with the constraints of the 40m vacuum envelope is* $l_-^{RSE} = 34.2\,\mathrm{mm}$*, and* $l_-^{SR} = 23.2\,\mathrm{mm}$[3].

The analytic relations Eqs. (D.3) and (D.6) and Eqs. (D.4) and (D.5) were all validated with numerical models, from which the important results are collected in Figure D.1

## D.2 Recycling cavity folding mirrors

At the time of writing, the recycling cavities at the 40m have to contend with an additional difficulty that the folding mirrors used to form the cavity as procured turned out [146] to have a slightly convex RoC[4]. These optics are called PR2, PR3, SR2 and SR3, and are necessary to realize cavities of a suitable length within the confines of the vacuum envelope available in the lab. An excellent summary of the

[3] Note that the optimal Schnupp asymmetry depends on whether the SR or RSE configuration is used. A larger Schnupp asymmetry of $\approx 400\,\mathrm{mm}$ also realizes high $f_2$ transmission to the anti-symmetric port (see Figure D.1(f)), but is incompatible with space constraints in the 40m vacuum envelope.

[4] Ironically, one of the touted advantages of the folded design [147] is that it is more tolerant to manufacturing errors and yields a geometrically stable cavity. Howver, the original 40m recycling cavity design, that specified flat folding mirrors, was not based on any detailed tolerance analysis.

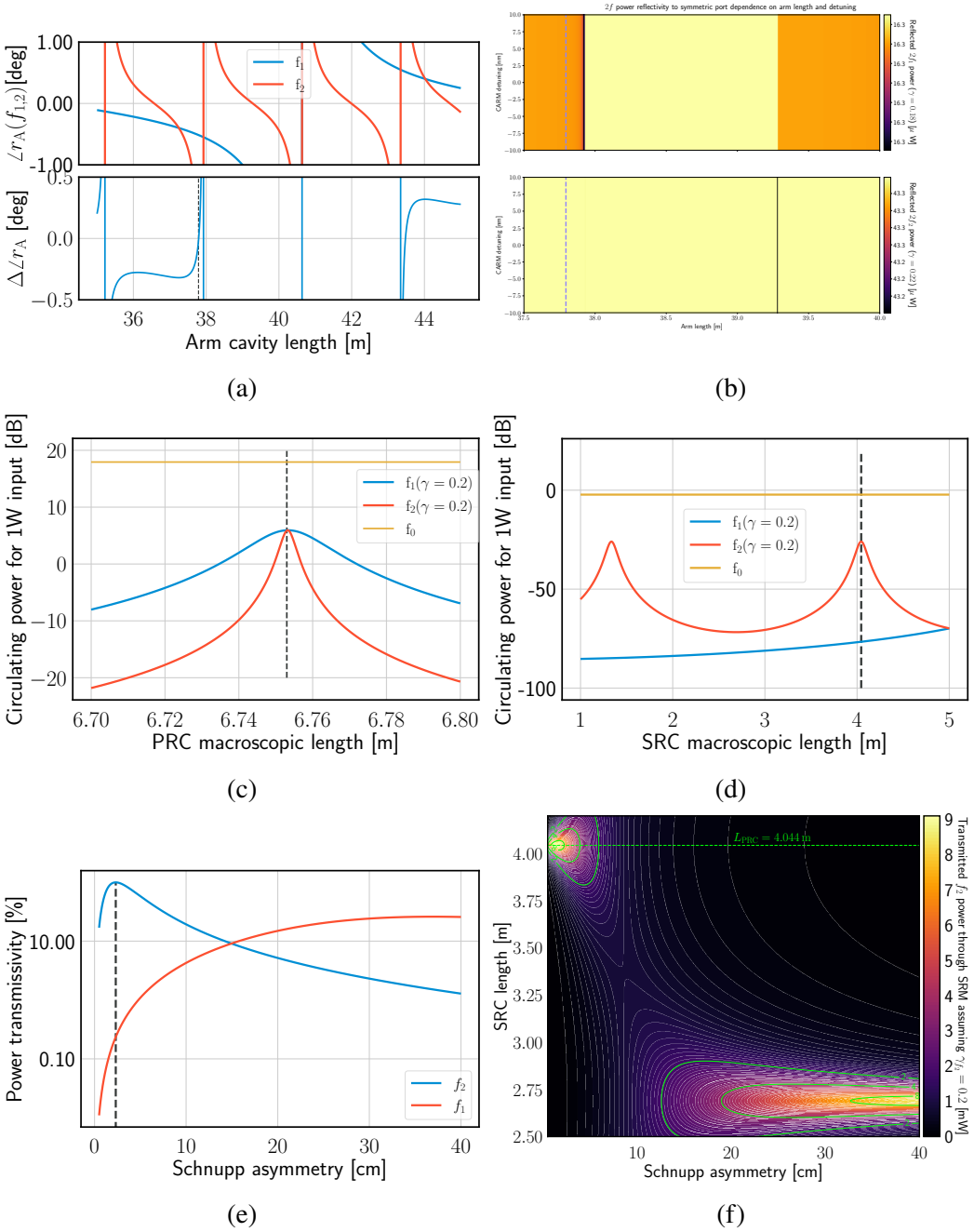


Figure D.1: Numerical validation of suitability of macroscopic cavity lengths. (a) and (b) show that for $L_A = 37.795\,\text{m}$, the considerations in Item 1 are satisfied. (c) and (d) show that $L_{PRC} = 6.753\,\text{m}$ and $L_{SRC} = 4.044\,\text{m}$ satisfy the considerations in Items 2 and 3 respecively. (e) and (f) show that a Schnupp asymmetry of $l_- = 23.2\,\text{mm}$ results in maximal transmission of $f_2$ sideband power to the anti-symmetric port of the interferometer. In these plots, $\gamma_{1,2}$ denote the modulation depths for the $f_{1,2}$ PM sidebands.

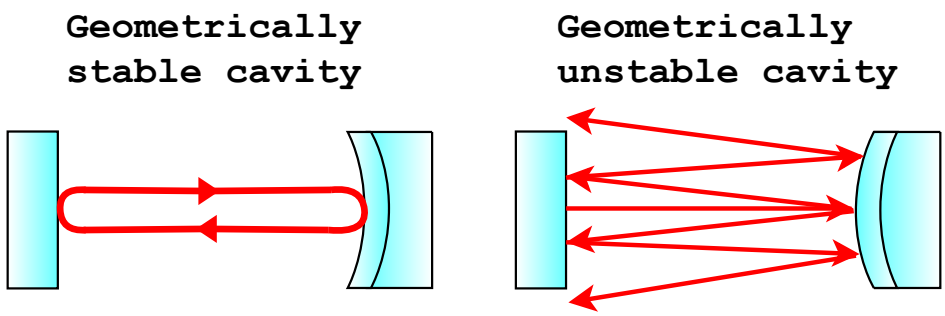


Figure D.2: Geometric visualization of stable and unstable optical cavities. These illustrations are for two mirror cavities, but the concept is the same for folded cavities like the 40m interferometer's Power Recycling Cavity (PRC). In the geometrically stable case, the concave end mirror serves to keep paraxial rays confined to the resonator, allowing stable optical power buildup. In the unstable case, the convex end mirror has the opposite effect, and the resonant enhancement cannot be realized as there is little or no spatial overlap (and hence no scope for constructive interference) of the laser field with itself as it traverses the cavity.

conditions determining the geometric stability of an optical cavity can be found in [148], but the language of Gaussian beam optics isn't necessary to understand the important concept for this discussion - a simple geometric argument using ray optics is presented in Figure D.2.

The mild convexity of the 40m PRC folding mirrors (the radii of curvature was $\approx -600\,\mathrm{m}$, with the negative sign denoting convexity) made the cavity marginally stable, which is an intermediate case between the two extremes shown in Figure D.2. The mode-confinement was sub-optimal, leading to low power enhancement in the cavity. Furthermore, the non-ideal transverse mode spacing meant that higher order $\mathrm{TEM}_{mn}$ spatial modes co-resonated with the fundamental $\mathrm{TEM}_{00}$ mode, since including the Gouy-phase effect, they too picked up a round-trip phase of $2\pi$ after traversing the cavity as described in Equation (D.2a). Even though the IMC cavity serves as a spatial mode filter[5], the input beam to the PRC has some higher order content due to imperfect mode-matching and misalignment between the beam and cavity axes. The net result was that the PDH error signal in reflection became polluted and it was no longer possible to use it as a cavity length error signal, an effect which has been seen in interferometric detectors in the past [149].

[5] In practise, if one chooses a $\mathrm{TEM}_{mn}$ mode with large enough $m+n$, a co-resonance cannot be avoided. When undertaking a design study, a reasonable rule-of-thumb is to ensure that co-resonances are avoided for $m+n \leq 15$, as spatial mode cleaning cavities usually ensure that there is negligible power in modes of higher order than this.

In order to realize a geometrically stable cavity that allowed somewhat robust locking of the interferometer, a decision was taken to flip the folding mirrors such that the reflecting surfaces forming the optical cavity became concave rather than convex. However, in this configuration, the mirror substrate and anti-reflection (AR) coating are inside the cavity, and act as sources of optical loss, thereby reducing the achievable recycling gain. These losses are estimated to be $\approx 0.5\%$ per mirror, and in a round trip, the beam encounters each of the two folding mirrors twice, for a total round-trip loss of $\approx 2\%$. The mode-matching between the RC and the arm cavities is also slightly degraded, but this compromise at least permitted repeatable locking of the interferometer, and was therefore deemed reasonable. Once this change was effected, it was possible to lock the recycling cavities repeatably and reliably.

## D.3 Design study for stable recycling cavities

To mitigate the limited optical power buildup due to increased losses in the recycling cavity, it was decided that new folding mirrors would be procured. In order to avoid a repeat of the experience with the first set of mirrors that were ordered, a more rigorous design study was undertaken. The objective of the study was to determine an RoC specification for a folding mirror such that (i) a single specification could be used in both the Power and Signal recycling cavities, (ii) the design had adequate transverse mode spacing, and allowed $> 99\,\%$ mode matching between the recycling and arm cavities, (iii) the specification was such that it is technologically feasible to manufacture, and (iv) the design be tolerant to manufacturing errors in the RoC and errors in the positioning of the optic in the propagation path, keeping the cavity geometrically stable and the mode-matching efficiency to the arm cavity high.

A combination of analytic and numerical [142, 150] tools were employed in the study.

### D.3.1 Power Recycling Cavity

In summary, it was found that an optic with RoC of $\underline{R = 1000 \pm 150\,\mathrm{m}}$, when used as the PR3 optic, with the PR2 optic flipped back such that it is seen as a convex optic by the cavity, would satisfy all of our requirements. The $\pm 150\,\mathrm{m}$ tolerance on the nominal specification was deemed sufficiently wide that a manufacturer would be able to meet this specification with high confidence, while also being tolerant to measurement uncertainty in our characterization of the convexity of the PR2 optic and positioning of these optics in the vacuum envelope. This qualitative statement is quantified in the corner plot Figure D.4(a).

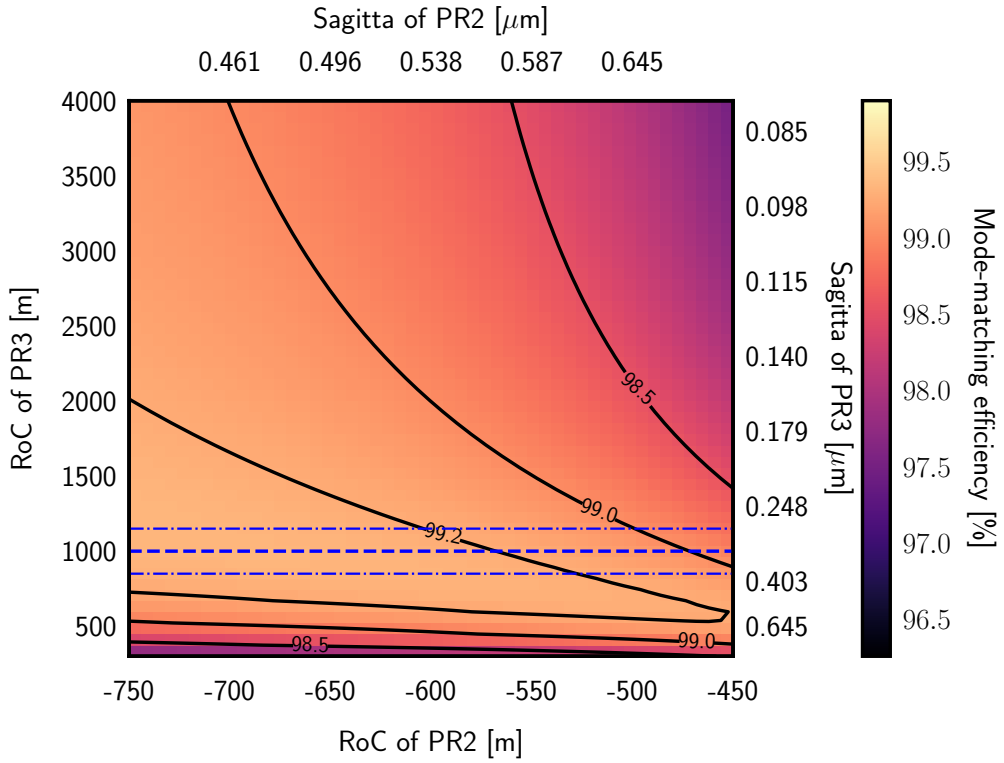


Figure D.3: Numerical model of the (average) mode overlap between the PRC and the arm cavities. It was decided that the in-hand, convex PR2 optic would be flipped back the "correct" way around, and PR3 would be designed to have the appropriate concavity to guarantee cavity stability.

### D.3.2 Signal Recycling Cavity

The original design study assumed that the RSE configuration of the interferometer would be retained. However, it was later decided that the SR configuration would be more appropriate for the Ponderomotive Squeezing experiment described in Chapter 4. By the considerations of Appendix D.1, the macroscopic length had to be appropriately shortened by $\approx 1.5\,\mathrm{m}$. The specification of $R = 1000 \pm 150\,\mathrm{m}$ for the RoC of the new optic to be procured was originally chosen such that it would also serve as a suitable SR3 optic. However, with the shortened cavity length, it was found that a stable SRC could be realized using only a single folding mirror (called SR2) that had a nominal RoC of $R = -700\,\mathrm{m}$. This specification was compatible with the existing SR2 optic, once flipped back with the convex side of the optic facing the cavity. The robustness of the geometric stability (for which the Transverse Mode Spacing is a proxy) and the mode overlap between the SRC and the arm cavities to errors in the assumed RoCs of the SRC optics and their positioning, is quantified in the corner plot Figure D.4(b).

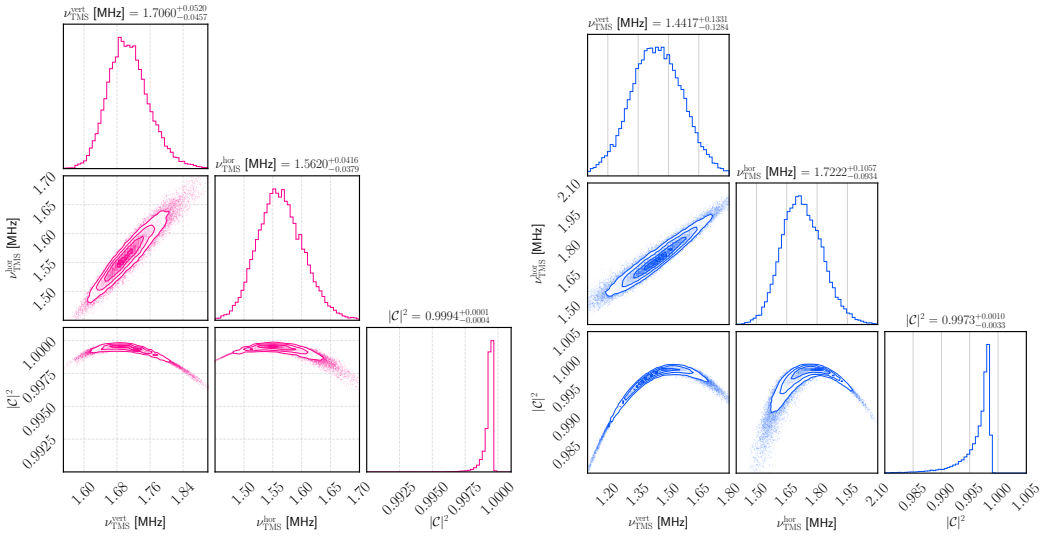


(a) (b)

Figure D.4: Robustness of PRC [(a)] and SRC [(b)] designs to errors in optic RoC and positions. $\nu^{\text{vert, hor}}$ denotes the vertical/horizontal Transverse Mode Spacing (TMS) of the cavity and is a proxy for the cavity's geometric stability, while $|C|^2$ is the average mode overlap efficiency between the recycling cavity and the arm cavities. `corner` plots [119] allow visualization of correlations in a high-dimensional parameter space, by plotting the marginalized distributions between pairs of performance metrics. In the 2D histograms, a value with a darker shade indicates a higher probability of the metric taking on that value. To generate these plots, the `emcee` package [118] was used to perturb about their nominal values (i) RoC of the optics by ±5%, (ii) separation between the optics by ±5 mm, and (iii) angles of incidence on the folding mirrors by ±1°. Perturbations were drawn from i.i.d. zero mean Gaussian distributions, with standard deviations being the ± values quoted, all of which were deemed to be reasonable from a manufacturing / optic placement point of view. $10^5$ samples were generated, and the median value of $\nu$, $|C|^2$ are indicated in the histogram titles.

*Appendix E*

# SUSPENDED OPTIC CLEANING PROCEDURE

For the most part, we followed the guidelines set out in [151] to clean the in-vacuum suspended mirrors. By doing so, we were able to realize the lowest ever measured optical loss in the C1 interferometer, with the $\approx$ 1 cm beam size in the Fabry-Pérot arm cavities. Where they differ from the procedure in [151], some particular details of the cleaning procedure for the C1 interferometer are documented in this Appendix.

## E.1 Solvents

For the most pristine optical surfaces, the actual cleaning agent used is a commercial polymer-based product, First Contact [50] (in favor of other traditional cleaning techniques like drag-wiping using methanol or isopropanol). Per the guidance set out in [151], First Contact is not compatible to be mixed in any form with methanol or isopropanol. At C1, First Contact is "painted on" to the optic using a brush. To keep the brush from drying out and stiffening between successive applications, it is immersed in a beaker filled with acetone (the only compatible solvent approved for use with First Contact). We found that it was necessary to use spectroscopic grade acetone[1] from a freshly opened bottle (100 mL bottles are best suited to avoid wastage and the remaining acetone can be used for general laboratory use such as wiping down surfaces). Lower grade acetone (or spectroscopic grade acetone that has been exposed to ambient air for more than a few hours) has higher water content and was empirically found to leave water-mark residues on the optic, as shown in Fig. E.1.

## E.2 Preparation for in-situ cleaning

The core optics are suspended from single wire loop pendulums inside the vacuum chambers. For the cleaning to be effective, we make every reasonable effort to keep the environment to which the optic is exposed during the process as clean as possible. A portable HEPA filter unit, with Ameristat®film draped around is placed adjacent to the vacuum chamber door as shown in Fig. E.2(a). All cleaning is done within this temporary "clean-room".

[1] We used "Acetone, 99.8%, Extra Dry, AcroSeal™", which has a purity of 99.8% and a maximum of 0.005% water content.

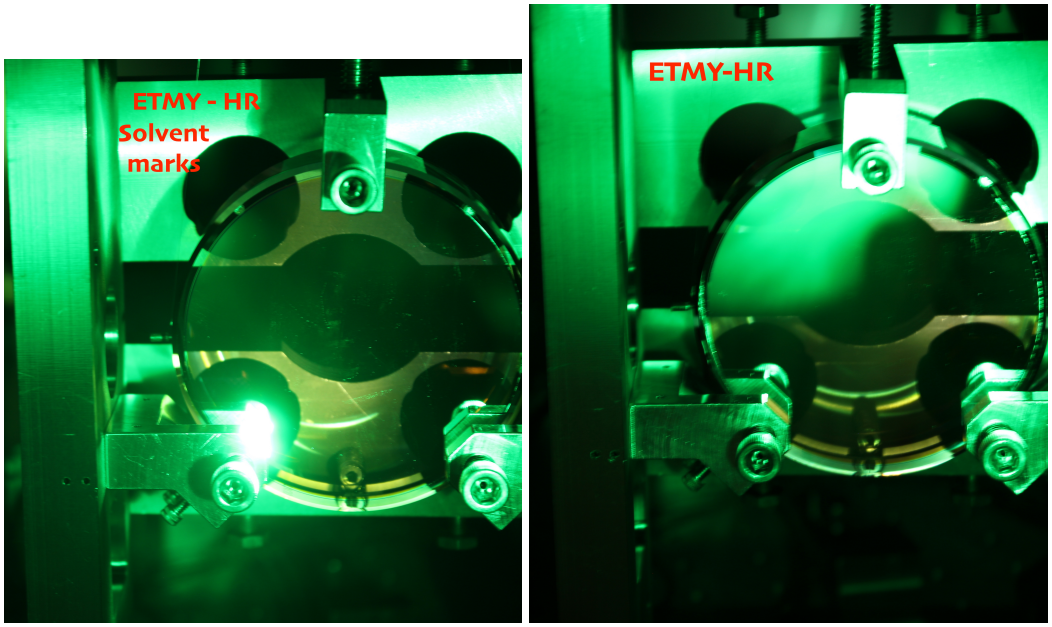


(a) (b)

Figure E.1: HR optic surface after cleaning with First Contact. Fig. E.1(a) shows residual water marks in the central clear aperture that persist on the optic even after multiple rounds of cleaning (it may be necessary to zoom in to the image to see these). We hypothesized that these were due to using insufficiently dehydrated acetone for cleaning the applicator brushes. Fig. E.1(b) shows the same optic, after multiple rounds of cleaning, this time only using spectroscopic grade acetone in the process.

It is easier to work with an optic that is fixed relative to the inertial coordinate system rather than suspended and freely swinging. The suspension cage has several "earthquake-stops" in close proximity to the optic. These are screws in threaded holes that have soft viton pieces at their tips. Normally, these screws are in a "withdrawn" position such that their viton tips are $> 5$ mm from the optic. For the cleaning, we adjust the position of these screws such that the soft viton tips clamp the optic fixed, without scratching / damaging the optic. 4 stops are also situated at the bottom of the optic, which support the weight of the optic and mildly unload the suspension wire loop. The wire is 42 $\mu$m in diameter and extremely fragile - this step helps to avoid accidentally breaking the wire during the cleaning procedure, which would then necessitate a time and labour intensive re-suspension procedure. Similarly, clamping the optic fixed using the face earthquake stops helps avoid accidentally bumping the optic against the suspension cage and knocking off magnets glued onto the AR face of the optic for actuation purposes. For this purpose, and also to allow greater freedom of movement for the suspension tower, OSEMs,

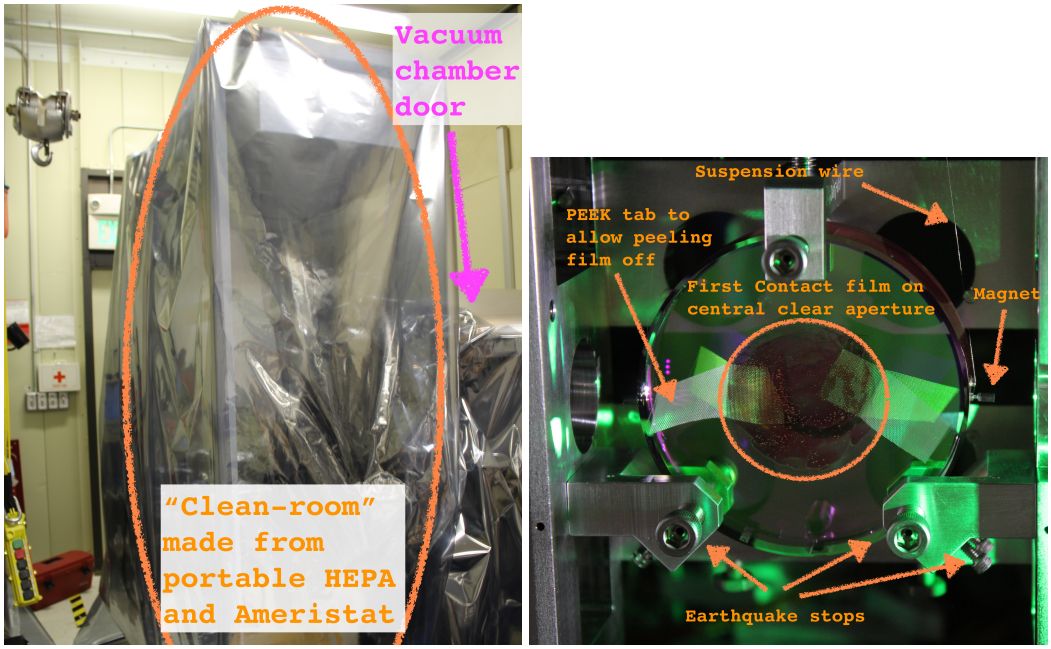


(a) (b)

Figure E.2: Preparation for cleaning a suspended optic. Fig. E.2(a) shows a portable clean environment set up next to the vacuum chamber housing a suspended optic, to keep the environment the optic is exposed to as clean as reasonably possible. Fig. E.2(b) shows a suspended optic, clamped fixed with earthquake stops, with a film of First Contact applied to the HR face.

which are normally in close proximity to the optic, are also removed. Sometimes, it is necessary to un-suspend an optic, such as when an earthquake event causes one of the actuation magnets to be knocked off. In such cases, these steps do not have to be followed exactly, as we have the freedom to remove the optic and clean it ex-situ.

Now the optic is ready to have First Contact applied, following the guidelines in [151], as shown in Fig. E.2(b).

### E.3 Suspension cage and AR face cleaning

With the HR face of the optic protected by a film of First Contact, we wiped down the metal surfaces using clean wipes soaked in acetone. Additionally, we cleaned the barrel of the suspended optic using optical grade wipes soaked in acetone. The idea was that having these surfaces as clean as possible would prevent the migration of dirt / dust / other impurities onto the HR face of the optic over time. Finally, the AR side of the optic was also cleaned. As shown in Fig. E.2(b), access to the AR face is much more restricted than the HR face, due to metal structures on the suspension cage for holding the OSEMs. Nevertheless, it is possible to apply First

Contact using a small brush. If access is deemed too restrictive, the AR face may be cleaned using traditional drag-wiping techniques using a methanol-soaked optical grade wipe.

### E.4 First-contact removal, inspection, and pumpdown

After waiting for the prescribed time for the First Contact film to dry, we are ready to remove the film and inspect the optical surface for cleanliness. During the First Contact application, one or more PEEK tabs are embedded in the film (the solvent evaporates while the PEEK tab gets embedded in the polymer matrix). By pulling on these, the dried film can be removed. A flow of ionized gas is maintained over the HR surface during the peeling for discharging and preventing ambient charged dust particles from being attracted to it. A green flashlight is used to illuminate the surface of the optic, which is visually inspected. Some high-resolution photographs are taken for documentation purposes. The appearance of residual dirt is extremely sensitive to the angle of illumination, so it is hard to definitively set a criterion for this step by which the optic is judged "clean-enough". We have found that even with the optic appearing like in Fig. E.1(a), the round-trip loss in the Fabry-Pérot cavity was as low as 50 ppm (only $\approx$ 50% worse c.f. the best measured value of $\approx$ 30 ppm, whereas before cleaning, the loss was as high as 500 ppm) at the operating wavelength of 1064 nm. Nevertheless, best effort is made to have the HR face as clean as possible. The prescription from the LIGO engineering group is to repeatedly apply First Contact until the optical surface is deemed sufficiently clean. Empirically, we found that after 3 successive rounds of application, we found no visual improvement to the surface cleanliness.

Finally, it is desirable to restore the optic to a position that recovers the nominal optical cavity alignment, re-install the OSEMs, release the earthquake stops, and pump down the vacuum envelope to nominal pressure levels, as soon as possible after the last coat of First Contact is peeled off. Since the C1 interferometer has a continuous vacuum envelope, if multiple optics are cleaned in multiple chambers, the entire process can take several hours, or even multiple days. Therefore, this prescription is more a qualitative guideline rather than a quantitative one. We were able to observe losses as low as 30 ppm round trip by pumping the vacuum envelope down within 14 hours of the last coat of First Contact being removed.